High Force Density Linear Permanent Magnet Motors:

"Electromagnetic Muscle Actuators"

by

Bryan Paul Ruddy

S.B. in Mechanical Engineering
Massachusetts Institute of Technology (2004)
S.M. in Mechanical Engineering
Massachusetts Institute of Technology (2006)

Submitted to the Department of Mechanical Engineering
in partial fulfillment of the requirements for the degree of

Doctor of Philosophy in Mechanical Engineering

at the

MASSACHUSETTS INSTITUTE OF TECHNOLOGY

September 2012

Author .....
Department of Mechanical Engineering
August 7, 2012

Certified by .....
Ian W. Hunter
Hatsopoulos Professor of Mechanical Engineering
Thesis Supervisor

Accepted by .....
David E. Hardt
Ralph E. and Eloise F. Cross Professor of Mechanical Engineering
Graduate Officer

High Force Density Linear Permanent Magnet Motors:
"Electromagnetic Muscle Actuators"

by

Bryan Paul Ruddy

Submitted to the Department of Mechanical Engineering
on August 7, 2012, in partial fulfillment of the
requirements for the degree of
Doctor of Philosophy in Mechanical Engineering

Abstract

Actuator performance represents a key constraint on the capability of many engineered devices. Performance of these devices is often exceeded by their muscle-powered natural counterparts, inspiring the development of new, "active material" actuators. This thesis reconsiders a traditional actuator, the linear permanent magnet motor, as a form of active material actuator, and presents new, unified scaling and magnetic field models for its performance. This active material motor model predicts that motors composed of large numbers of very small, actively-cooled repeat units, similar to the architecture of biological muscles, can provide greatly enhanced force density over extant designs.

Our model is constructed by considering the motor winding as an active material, with its performance limited by the diffusion of waste heat. This allows a quantitative scaling model for the motor constant and force-to-mass ratio to be built for the case of a winding immersed in a homogeneous magnetic field. This model is then modified with a small set of dimensionless parameters to describe the performance penalties imposed by the use of practical sources of magnetic field, specifically periodic arrays of permanent magnets. We explain how to calculate these parameters for a variety of different types of magnet arrays using analytical magnetic field and heat transfer models, and present a new field model for tubular linear motors having improved numerical stability and accuracy. We illustrate the use of our modeling approach with two design case studies, a motor for flapping-wing flying and an actuator for high-performance controllable needle-free jet injection. We then validate our predictions by building and testing a novel water-cooled motor using a tubular double-sided Halbach array of magnets, with a mass of 185 g, a stroke of 16 mm, and a magnetic repeat length of 14.5 mm. This motor generates a continuous force density of 140 N/kg, and has a motor constant of nearly $6\,\mathrm{N}/\sqrt{\mathrm{W}}$, both higher than any previously reported motor in this size class.

Thesis Supervisor: Ian W. Hunter
Title: Hatsopoulos Professor of Mechanical Engineering

Acknowledgments

This thesis bookends a higher education process as long as the combined elementary and secondary education that came before it, and as such was made possible through the help and guidance of far more people than I can hope to thank properly in this space. Central in this process, of course, have been my teachers, from high school through today. Before college, the opportunities and encouragement provided by Betty Manion, Norman Passmore, Gwen Sharp and Bill Geppert were particularly instrumental in bringing me to MIT from a small-town environment where I had never even heard of engineering. Once here, I benefited greatly from the mentorship and experiences given me by Kip Hodges, Sam Bowring, Mary Boyce, Barbara Hughey, Jung-Hoon Chun, Gang Chen, Alex Slocum, and Doug Hart, and from the advice of Igor Paul and Neville Hogan, my undergraduate academic advisors, as well as John Lienhard and Jack Kirtley. I must also offer my sincerest thanks to Dave Trumper, Jeff Lang, and Gill Pratt, for their guidance and welcome criticism as members of my doctoral thesis committee—your influence helped bring my project from the germ of an idea to a full, well-rounded body of work.

It has been an honor and a privilege to work with Ian Hunter in the BioInstrumentation Laboratory these past eight years. Ian has provided me with an embarrassing wealth of opportunity both within and without the lab, and our shared broad passion for science and technology has served as the foundation of a friendship and partnership that I hope continues long into the future. Ian has also gathered an amazing group of researchers, and I have truly enjoyed working with the members of the lab. While I have worked with more excellent students and staff here than I can practically list, I would particularly (and in no particular order) like to thank Rachel Pytel, Ellen Chen, Cathy Hogan, Adam Wahab, Kate Melvin, Lynette Jones, Miguel Saez, Craig Forest, Mike del Zio, Andrew Taberner, Nate Ball, Brian Hemond, Bryan Schmid, and Lynette Jones for their friendship, assistance, and guidance. I must also thank the talented group of undergraduate students I had the privilege of mentoring over my time in graduate school: Kim Harrison, Zach Reynolds, Chris Benson, Ashley Brown, Matt Rosario, Ross Wendell, and Christine Hsieh.

My life and experience through this time has been tremendously enriched by my friends, both inside and outside the office. I must offer special thanks to Dawn Wendell, who inspired me to start work on the subject that ultimately formed this thesis, and Lael Odhner, with whom I have had many informative discussions and who was one of the people most responsible for my initial interest in mechanical engineering. I would also like to thank my family, for their long years of unwavering love and support even as I have been far from home.

Finally, I would be remiss were I not to thank my funding partners: the Department of Defense, the Dupont-MIT Alliance, IARPA, and the MIT Mechanical Engineering department.

Table of Contents

List of Figures

List of Tables

Nomenclature

Chapter 1

Introduction

1.1 Motivation

Actuator technology is a key enabler of our modern society. Actuator development, from manual labor and draft animals, through waterwheels and windmills, to steam engines and electric motors, has supported our transition from subsistence farming to the post-industrial service economy. Today, the United States consumes an average of 150 W of electricity per person just to actuate industrial machinery [1], seven times what would be produced if every person in the country were employed to run the machines using muscle power (under humane working conditions) [2]. Transportation consumes over twenty times as much power; discounting for the inefficiency of fuel-burning engines, this means that every American has the equivalent of nearly thirty-five people, or a stable of three horses [3], working to move them and their belongings.

The actuators that so effectively multiply human capability consist primarily of rotary electric motors, reciprocating internal combustion engines, and gas turbines. These actuator technologies are well-suited to high-power steady-state operation, vastly outperforming biological actuators in sheer power level, power density, and endurance. However, there are many tasks that are still beyond the capability of machines and remain powered by biological muscle, or are performed by technological means but at a lower performance level than biological systems. In particular, standard actuation technology is poorly-suited to tasks requiring intermittent motion [4], such as moving through variable terrain [5, 6] or dexterously manipulating objects in a human environment [7]. In general, such tasks fall under the umbrella of robotics, as the need for intermittent, non-repetitive motion is often closely coupled to the need for planning and control strategies for that motion.

At present, most robotic systems rely on two actuator classes: fluidic actuators and rotary electric motors [4, 8]. These actuators must produce linear forces and motions for most environmental interactions, and in uncertain environments the linear motion is best produced within the robot itself (i.e. not by wheels on flat ground). Unfortunately, these actuators have serious limitations: fluidic actuators are very inefficient and require considerable support equipment, while rotary electric motors require complex and limited-power reduction drives or "clockwork" mechanisms.

Neither fluidic [9] nor rotary electric [10] actuators are yet capable of matching the performance of human muscle.

Biological muscle has several properties that make it particularly difficult to mimic with conventional actuators[1] [12]. Muscle has a variable stiffness, allowing it to passively stabilize a joint, and is generally associated with compliant tendons capable of efficient mechanical energy storage. It has very low inertia, yet it can generate a very high force, sustained across a displacement of up to 40% of the muscle's length. Muscle does this while remaining relatively efficient and powerful, with efficiency during cyclic motion estimated between 10% and 40% [13] and power density near 100 W/kg.

A common approach to the problem of making robotic actuators behave more like biological muscle has been the development of artificial muscle materials, capable of undergoing shape change in response to electrical, thermal, or chemical stimulus [14, 15]. Examples include piezoelectric ceramics, shape-memory alloys, and conducting polymers. Despite the widely varying physical principles on which these materials operate, all can be characterized by the production of a microscopic mechanical strain by the applied stimulus, which works against the constraints on the material to generate a force[2]. Like muscle, these materials can produce very high forces, and some can also provide a variable stiffness, either intrinsically [16] or by actuating a variable proportion of the material [17].

Unfortunately, while artificial muscle materials do offer intriguing properties, they are generally not able to reach the performance of biological muscle, and rarely exceed the performance of even conventional actuators. The main success stories (e.g. [18]) have been in meso- and micro-scale actuation, where conventional actuators are extremely difficult to build and the actuator requirements are better-matched to the capabilities of artificial muscles. Even in the highest-performing materials, the coupling between energy input and actuation is weak enough to make their use challenging at best [4]. More troubling, improvement in the performance of artificial muscle materials will require fundamental advances in materials science and chemistry, rather than new application and design strategies.

While artificial muscle materials are not yet a practical reality, a closer look at conventional actuators and biological muscles may suggest ways to bridge their gap in performance. A key feature of muscle is that it has structure at many different size scales; in fact, at the nanoscale, biological muscles have more in common with stepping motors than with strain-based artificial muscles. A biological muscle is a massively series and parallel combination of molecular linear stepping motors, with myosin heads moving along actin chains [12]. This free motion along structurally independent units allows muscle to undergo such large strains. At the microscale, these actin-myosin motors are closely coupled to transport systems that deliver chemical energy and remove waste, both chemical and thermal. At the mesoscale, the muscle is divided into many individually-controlled motor units, which in turn are connected in series and

[1] Portions of this discussion are reproduced from our previously published work [11].

[2] While dielectric elastomer actuators are commonly classified as artificial muscle materials, the physical mechanism they exploit is more analogous to an electric motor with a transmission than to that of a muscle.

parallel at the macroscale to the joint being actuated. The nature of the attachment depends a great deal on the type of motion in the joint; muscles that must work against large inertias include series elastic elements (i.e. tendons) to store mechanical energy, while muscles that primarily deliver mechanical power lack tendons [19].

Some of these aspects of biological muscles have been imitated with great success, particularly the use of compliant elements as in series elastic actuators [20]. The mesoscale structure has also been mimicked with cellular actuation approaches in artificial muscle actuators [17, 21], although the problems it solves (particularly lack of actuator controllability) are not typically problems with conventional actuators. The microscale transport network and nanoscale actuation mechanism, however, have seen less application.

In this thesis we seek to discover whether, perhaps inspired by the structure of biological muscle, it would be possible to make major improvements to the performance of conventional actuators for robotic applications such that they could out-perform muscles. We examine permanent magnet (PM) linear electric motors as the class of actuators to improve, by first developing a theoretical model for their maximum possible performance and by then seeking design strategies to more closely approach this theoretical potential, with an emphasis on designs with improved heat transport.

1.2 Permanent Magnet Linear Motors

Linear electric motors, in general, have a history extending back to the earliest days of electromagnetic experimentation [22, 23], with an early example built by Wheatstone in 1841. Wheatstone's motor was what we now call a reluctance motor, with force generated by the attraction of iron to an electromagnet. From this point, development of linear motors split in two different directions. Linear motors employing a single coil were developed in the 1870s, and employed as voice coil loudspeakers in telephones [24]. Voice coils made use of permanent magnets from their earliest inception, despite the extremely weak fields available at the time; eventually, voice coils with wound fields were also commonly produced [25]. Meanwhile, multi-coil linear motors like Wheatstone's original motor remained little more than curiosities until the 1940s, when a linear induction motor developed by Laithwaite was proposed for use as an aircraft catapult. Interest further picked up during the 1960s and 1970s, when maglev transportation became a popular concept and numerous linear motor designs involving superconductors and/or the newly-available rare earth permanent magnets [26] were developed. Independent of this development, the reluctance principle used by Wheatstone was refined in rotary form to create the stepping motor [27], then returned to linear form as a multi-axis planar actuator [28] in the 1960s and 1970s.

Based on this historical development, linear electric motors can be grouped into four main categories: reluctance motors, voice coils, induction motors, and synchronous motors. Reluctance motors generate a magnetic field using coils in one element of the motor, and produce force from the interaction of this field and iron on the other element of the motor. Induction motors use an alternating current in a set of coils on one element of the motor to induce a current in conductors in the other element,

and produce force based on the interaction of the magnetic field produced by these coils and the induced current. Voice coils and synchronous motors instead operate by generating a magnetic field on one element of the motor, using coils or permanent magnets, and then producing force in coils on the other element of the motor, thereby separating the field generation from the provision of current to interact with that field. Voice coils have a limited stroke, typically with only a single force-producing coil, and can be driven by a direct current. Synchronous motors have many coils, and can have an arbitrarily long stroke (as would be needed in a maglev train, for instance), but those coils must be driven by an alternating current synchronized to the motion of the motor. Both of these motor types can use permanent magnets, which generate the necessary magnetic field without requiring any power. Our interest will be in voice coils and synchronous linear motors, due to their ability to employ permanent magnets and their resulting very favorable scaling properties [29]. Despite their historical differences, voice coils can simply be considered as a subset of linear synchronous motors, consisting of those that have been built with a single coil.

An example of a linear synchronous motor is given in Figure 1-1, illustrating the major components of these motors. A periodic array of coils can move relative to a periodic array of magnets, which may use iron to guide its magnetic fields. In a planar motor, as is pictured, end-turns must be provided to allow the coils to form loops in which current can flow. A voice coil can be imagined as a single period of this structure, with only a single coil.

1.2.1 Permanent Magnet Material Properties

Despite their increasing prevalence in every-day life, permanent magnets see relatively little discussion in introductory courses on electricity and magnetism. Thus, we felt it prudent to give a brief review of their properties and mathematical description here. In short, permanent magnets can contain a positive magnetic flux density B even when the magnetizing field[3] H has a negative value, as shown in Figure 1-2. This can be described by the relationship

$$\boldsymbol{B} = \mu_0 \left(\boldsymbol{H} + \boldsymbol{M} \right), \tag{1.1}$$

where μ_0 is the permeability of free space, $4\pi \times 10^{-7}\,(\mathrm{T \cdot m})/\mathrm{A}$, and $\boldsymbol{M}$ is the magnetization, shown in Figure 1-2 using solid lines. (Bold symbols refer to vector quantities.)

The magnetization curve defines two key parameters that can describe the strength of the magnet. The first, the remanence[4] B_{rem}, is the value of the magnetization (and B-field) when there is no applied H-field. The second, the intrinsic coercivity H_{ci}, is the value of the H-field at which the magnetization drops to zero. At this point, we

[3]There is considerable pedagogical debate about the precise nomenclature and relative primacy of the two field quantities used to describe magnetism; rather than fully engage in this debate, we will henceforth simply refer to them as the B-field and H-field.

[4]To avoid confusion with the B-field in the radial direction, we have adopted this slightly non-standard symbol for the remanence throughout this work.

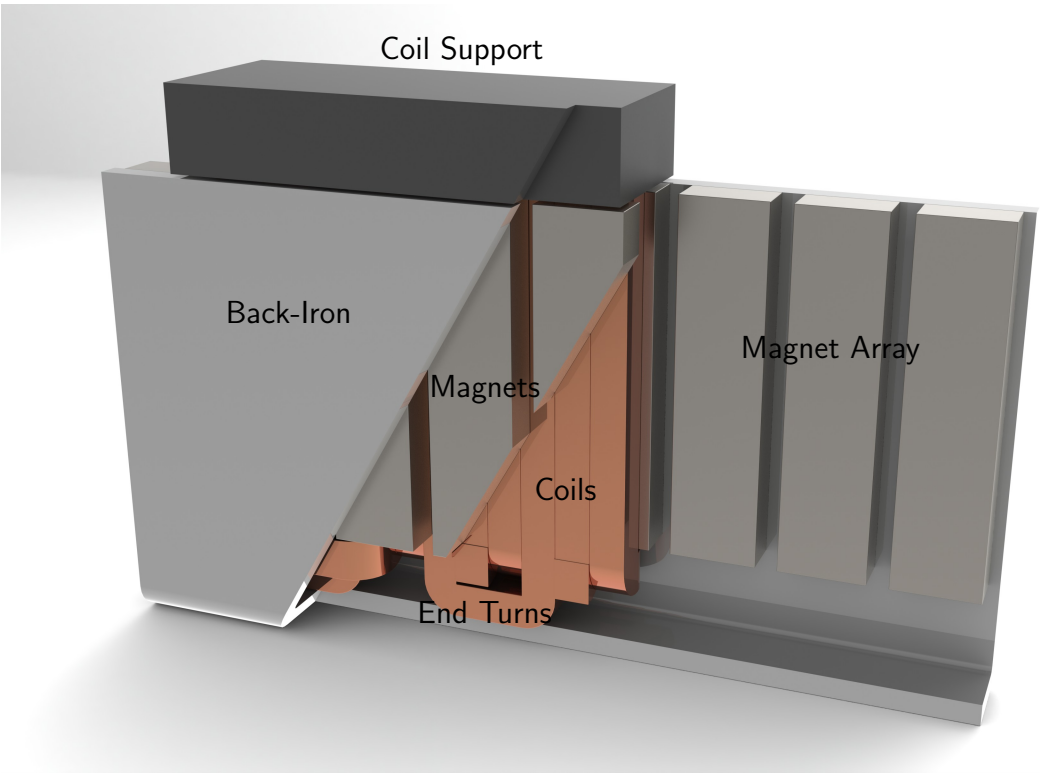

Figure 1-1: This cut-away rendering of a typical linear synchronous motor illustrates its major features: a periodic array of coils lies between two periodic arrays of magnets. In this case, the magnets would all be oriented through their thickness, alternating in direction along the array. The magnets are mechanically supported by a channel of back-iron, which also helps to guide the magnetic field. The coils have end-turns outside the magnet array, allowing them to form complete loops; the end-turns outside the channel are embedded in a support, used to make mechanical and electrical connections. Typically, a motor like this has the coil as the moving element.

can consider the magnet as having been completely demagnetized; if the H-field were brought to this level then removed, the magnetization would not recover to its original value. These parameters are functions of temperature; in rare earth magnets, both B_{rem} and H_{ci} decrease with temperature, as illustrated in the figure. The (reversible) slope of the B-H curve is given by the recoil permeability; in rare earth magnets, the recoil permeability is very close to the permeability of free space, and is typically ignored [30].

In early permanent magnets, such as hard steel and Alnico, the magnetization was strongly dependent on the applied H-field, and the magnets could be demagnetized easily. This made magnets difficult to use in motors, and special efforts were required to maintain their strength [31]. Such magnets were also very difficult to model, and tedious iterative methods were often required to calculate the fields they generated. Modern permanent magnets such as rare earth magnets and ferrites, on the other hand, behave as shown in Figure 1-2, with almost constant magnetization over a wide

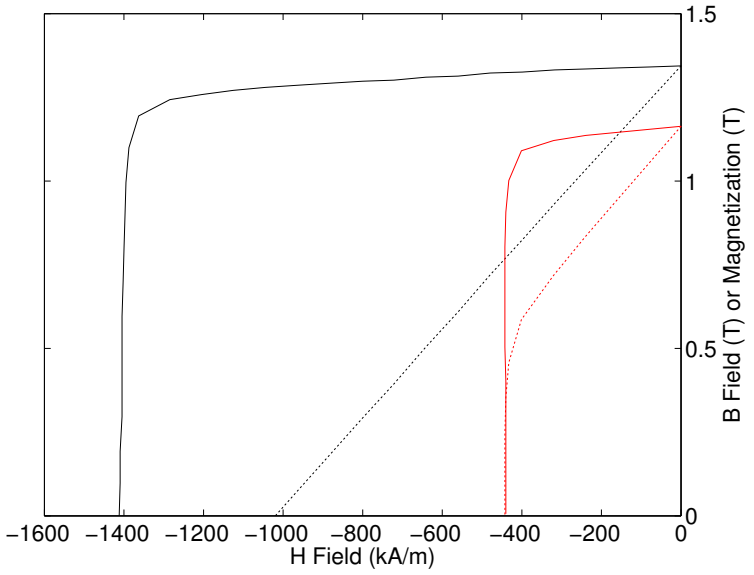

Figure 1-2: The B-H curve (dotted lines) is plotted from manufacturer's test data for a neodymium iron boron magnet (VACODYM 633 HR) at 20 °C (black) and at 150 °C (red). The magnetization (times the permeability of free space) is also given (solid lines); the magnetization is almost constant until the H-field reaches a critical value, at which it drops sharply and the magnet is demagnetized.

range of H-fields. Thus, they are relatively easy to model [32,33], and can be described by linear equations. These materials are also very difficult to demagnetize, making them useful in the development of compact, high-power and high-efficiency motors.

1.3 Thesis Overview

In order to explore the potential for improvement in linear permanent magnet motors, it is helpful to have some idea of their theoretical maximum potential. To date, no quantitative models for the maximum force output from such motors have been available, and so in Chapter 2 we develop a quantitative scaling model for permanent magnet linear motor performance. We find that the physics underlying motor operation allow for extremely high force densities to be produced, limited primarily by heat removal. We then apply principles from dimensional analysis to account for some of the practical (and inescapable) details of motor construction, including magnet structures, coil windings, and temperature-dependent material properties. Even accounting for these effects, we find that it should be possible to construct motors with force densities, powers, and efficiencies exceeding those seen in muscles. We also briefly investigate a similar scaling model for gear drives, to complete the picture for motor scaling and performance. A major lesson from this model is that, in order to achieve muscle-like performance, an active cooling system must be closely coupled to the magnetic structure, and that the motor may need to be built as a hierarchical collection of sub-units much like muscle itself.

To support our performance model, we found it necessary to develop magnetic field models for linear permanent magnet motors, in Cartesian and in cylindrical coordinates. These models, presented in Chapter 3, offer improvements in computational speed and accuracy over the models found in the literature, while describing motor performance in a form compatible with our scaling model. Our models, based on Fourier series solutions to Maxwell's equations, can be used to describe any linear motor structure with continuous layers of magnet, air, coil, or iron, and can handle saturation effects in iron at high fields. We use the field models to compare the performance of cylindrical and tubular linear motors with a wide variety of shapes, and determine the limits of design flexibility beyond which motor performance drops sharply.

Equipped with performance scaling and magnetic field models, we were able to find motor designs with performance close to the theoretical limits. In particular, as we discuss in Chapter 4, we can use the field model to optimize the relative shape of the motor subject to the design requirements, and then use the performance model to determine the overall scale of the motor. Often, this must be an iterative process, as some design constraints fix absolute motor dimensions. To assist with this process, we present a library of optimized motor designs for several common design goals. The design process is illustrated by two design case studies: a motor to operate the wing of a pigeon-sized flying machine, with performance specifications based on the specifications of real pigeon muscles and which must produce a high force density in continuous operation, and a motor to operate a needle-free injection system for drug delivery, which must provide an extremely high force under pulsed conditions.

Based loosely on the flying machine case study, we built a prototype motor to validate our models for magnetic field and motor performance. This motor, described in Chapter 5, uses water cooling and a novel double-layer tubular Halbach array magnetic design to provide more force for its mass than any commercially-available motor. We determine in this process the extent to which practical considerations in motor construction, such as structural components and cooling system design, influence motor performance relative to our predictions. Ultimately, our motor exhibits performance very close to that predicted by our models, with the mass of the motor structure and accessories amounting to just 30% of the total motor mass.

The lessons learned from this prototype, as well as throughout the development of our models and design strategies, are summarized in Chapter 6. Here, we also discuss promising avenues for further investigation, both in improved modeling and in the construction of high-performance motors.

Chapter 2

Scaling Models

This chapter presents a framework[1] for understanding the fundamental capabilities of linear permanent-magnet (PM) motors, and for examining and exploiting their scaling behavior. At each phase of the analysis, one analytically convenient motor configuration will be discussed; details of the computation of magnetic fields and performance parameters are presented in Chapter 3.

2.1 Background

The literature on electric machinery contains relatively few treatments of the general capabilities of linear motors; in most textbooks on the subject (e.g. [34]), motor theory is derived starting with the concept of slotted stators and discrete coils, with any general expressions given in terms of terminal inductance and flux linkage rather than geometric or material properties. Laithwaite [23, 35] described linear machines in terms of a "goodness factor", but used a magnetic circuit-based approach poorly suited to describing permanent magnets. More recently, Cugat et al. [29] presented a scaling analysis of motors based on fundamental physical laws, but only in terms of broad scaling relations rather than quantitatively. Cavarec et al. [36] provided a more detailed scaling analysis in order to compare a novel linear motor design to conventional leadscrew-based linear motion systems, though it could only be used for comparison rather than prediction. Outside the electric machinery community, others [8, 37, 38] have investigated scaling relations for direct-drive motors, though also without admitting quantitative links to specific motor designs.

One contributing factor, perhaps, to the paucity of generalized, yet quantitative motor models is the importance of "nuisance" effects in determining the energy losses in motors during typical steady-state operation. These effects, such as magnetic hysteresis, eddy currents, and air resistance, are strongly dependent on the fine geometric and micro-structural details of the motor design, and scale with the velocity of the motor's motion. The magnitude of their influence is difficult to even estimate without first specifying the overall design of the motor, frustrating efforts to produce general models for motor performance. Furthermore, high-speed motors are coupled

[1] Much of the content of this chapter has been published by the author in [11].

to the world through reduction drives, which as will be discussed briefly in Section 2.7 have scaling properties dominated by mechanical wear and cyclic fatigue rather than simple physics. In direct-drive motors, however, the nuisance losses are completely dominated by the basic Joule losses in the windings, which are far easier to calculate, and there is no reduction drive.

Our approach will be to define a set of quasi-static performance parameters for the linear PM motor at the most basic possible level, derived directly from fundamental physical laws and scaled by the motor mass and the magnet pole pitch, embodying the overall scale and the degree of fabrication complexity, respectively. We will also explain the consequences of various physical constraints that might be applied to the operation of a linear motor. We will then show that the effects of the practical details of motor construction can be embodied largely by a set of dimensionless parameters penalizing performance as compared to the basic model. Finally, we will discuss the scaling and performance implications of the performance parameters and of any practical details that cannot be effectively non-dimensionalized.

2.2 0-D Active Material Model

In essence, we can consider a PM motor as an active material actuator in which a body force is produced on a conductor (the "active material") proportional to the surrounding magnetic flux density, B, and to the applied current density, J. For this basic model, we will assume that the magnetic field is produced "for free", consider it as a material property, and neglect the mass and size of the magnets necessary to produce it in a real motor. We will likewise ignore any practical restrictions on the provision of current, and assume that the conductor can be excited by a spatially uniform current density. Thus, the 0-D motor model consists of a bare conductor carrying a uniform current density immersed in a uniform magnetic field that is exactly perpendicular to the current. While this model can describe rotary and linear motors equally well, we will restrict our analysis to that of linear motors.

The force production and power consumption of a PM actuator, its basic input-output relations, are given by the Lorentz force law and by Ohm's law,

$$F = BJV \text{ and} \tag{2.1}$$

$$P = \frac{J^2 V}{\sigma}, \tag{2.2}$$

where F is the force produced by the motor, V is the volume of active material, P is the electrical power converted by the motor into heat, and σ is the conductivity of the active material. (Here, we do not consider superconducting motors, which have zero Ohmic losses but instead have numerous other drawbacks, particularly at small scales.) Both of these quantities are directly proportional to the amount of active material—depending on the application, it may be preferable to describe this amount in terms of volume or in terms of mass. For this analysis, we will consider mass-sensitive applications; an alternative formulation in terms of volume can be

derived straightforwardly.

We would like to describe motor performance in terms of parameters that do not couple the motor size and the drive current. One such parameter is the ratio of the force generated to the square root of the power consumed ϵ, commonly known as the motor constant and listed on motor datasheets as K_m. The force generated per unit mass F', which we will call the force density, is another such parameter:

$$F' = \frac{BJ}{\rho_c}, \tag{2.3}$$

$$\epsilon \equiv \frac{F}{\sqrt{P}} = B\sqrt{\frac{\sigma M}{\rho_c}}. \tag{2.4}$$

Here, ρ_c is the mass density of the active material and M is the total mass of the motor. (In this case, the total mass is simply the mass of the conductor.) As we will see later in Section 2.2.2, both performance parameters have an impact on the overall efficiency of a motor driving a load.

Note that each performance parameter is independently related to a single motor design parameter: the force density achievable depends on the maximum allowable current density, while the motor constant depends on the size of the motor. The maximum current density, in turn, is restricted either by the maximum amount of heat that can be removed from and tolerated by the motor or by non-thermal damage mechanisms (demagnetization and electromigration).

2.2.1 Performance Constraints

By specifying F' and ϵ, along with the constraint on current density, one can calculate the size and potentially the aspect ratio of the required motor. The utility of this process depends on the nature of the constraint.

If the volumetric power density is constrained, we must fix the value of J, and in terms of the performance parameters

$$P/V = \frac{F'^2}{\sigma B^2}. \tag{2.5}$$

Thus, a constraint on volumetric power density directly constrains F', and it may not be possible to achieve the desired force density. A volumetric power density constraint is appropriate for conductors of thick cross-section with internal cooling channels providing for heat removal, as in a large-scale utility generator. A similar expression governs motor performance if electromigration directly limits the current density, or if adiabatic heating during low-duty-cycle pulsed operation constrains performance.

If the surface heat flux is instead constrained, and we assume a rod-shaped motor,

$$P/A = \frac{r_o F'^2 \rho_c^2}{2\sigma B^2}, \tag{2.6}$$

with A denoting the motor's surface area and r_o indicating its outer radius. In this

case, the heat flux constraint combined with the performance specifications gives the motor's aspect ratio as well as its size. A surface heat flux constraint is appropriate when the heat flow out of the motor is limited by the heat transfer coefficient $\bar{h}$ on its surface. As will be seen later in Sections 2.3 and 2.4.1, similar expressions govern motor behavior when we consider demagnetization, or when heat flow is limited by thermal conduction within the motor. Note that, under this constraint, the force density is a free parameter—any force density is achievable, so long as the aspect ratio is chosen appropriately.

Finally, a constraint on the total heat dissipation, which might be appropriate if heat removal from the motor is limited by the capability of an external cooling system, can be shown to couple the maximum available motor constant ϵ to the force density:

$$P = \left(F'\epsilon\right)^2 \frac{\rho_c^2}{\sigma^2 B^4}. \tag{2.7}$$

Under these conditions, there is necessarily a trade-off between the motor constant and the force density, and it is impossible to construct a motor that is simultaneously capable of both high force density and high motor constant.

2.2.2 Efficiency

In order to find the energy efficiency of a linear PM actuator, we need to define the work loop on which it operates. Consider perhaps the simplest situation, in which an actuator of total stroke ℓ_s sinusoidally drives an ideal dashpot at a frequency ω, with a resulting peak force amplitude of F_0. In this case, the instantaneous mechanical power P_m and electrical power P_e are given by

$$P_m = \frac{\omega \ell_s F_0}{2} \cos^2 \omega t, \tag{2.8a}$$

$$P_e = P_m + \frac{F_0^2}{\epsilon^2} \cos^2 \omega t. \tag{2.8b}$$

We can then integrate over one period in time to find the work per cycle W_m and W_e, calculate the efficiency $\eta = W_m/W_e$, and define an efficiency parameter $\hat{\eta}$:

$$\eta = \frac{1}{1+\hat{\eta}}, \tag{2.9a}$$

$$\hat{\eta} \equiv \frac{2F_0}{\omega \ell_s \epsilon^2} = \underbrace{\frac{\rho_c}{\sigma B^2}}_{\text{materials}} \times \underbrace{\frac{2}{\omega \ell_s}}_{\text{velocity}} \times \underbrace{F_0'}_{\substack{\text{force} \\ \text{density}}}. \tag{2.9b}$$

Here, we have broken out the components of ϵ to explain the scaling of $\hat{\eta}$, and F_0' denotes the peak force amplitude F_0 divided by the actuator mass M. Note the inverse relationship between $\hat{\eta}$ and the efficiency—lower values of the dimensionless efficiency are better. Three factors are seen to contribute to the efficiency parameter: the first is related to the material properties of the actuator, the second is equal to the inverse

of the peak actuator velocity, and the third is equal to the peak force density required by the work loop.

2.2.3 Numerical Values

We can calculate some rough values for the performance parameters and the efficiency to provide a sense of scale for the behavior of copper as an actuator material. For copper, the most commonly-used conductor, the conductivity $\sigma = 5.8 \times 10^7\,\mathrm{S/m}$ at room temperature and the density $\rho_c = 8940\,\mathrm{kg/m^3}$. The most powerful magnets currently commercially available [39] have a remanence[2] of approximately 1.5 T, which we will assume is equal to the field available in the conductor. Based on these material properties, a 1 kg "motor" would have a motor constant of $\epsilon = 120\,\mathrm{N}/\sqrt{\mathrm{W}}$. Typical motor design guidelines [23, 34] call for a maximum current density $J \approx 10^7\,\mathrm{A/m^2}$; under these conditions, the force density $F' = 1700\,\mathrm{N/kg}$.

At first glance, the expression for $\hat{\eta}$ in Equation 2.9b is disappointing, as it links an increase in force density directly to a decrease in efficiency. However, using the properties of copper and the best available magnets, and aggressive work loop parameters similar to those in bird flight muscles [40] ($2/\omega\ell_s = 1$ m/s, $F_0' = 1000$ N/kg) gives $\hat{\eta} = 7.1 \times 10^{-2}$, and thus an efficiency of 94%. It is therefore reasonable to expect usable efficiency from a linear motor operating at force densities characteristic of muscle, though the actual achievable efficiency will depend on just how far from this 0-D motor model the real motor happens to be.

2.3 1-D Slab Model

In a real motor, both the magnetic field and the current must form closed loops; thus, an analysis capable of incorporating these effects must take place in at least two-dimensional space. However, the thermal behavior of a planar 2-D motor can be studied with a simple one-dimensional slab model, which will prove useful in discussing the influence of conductive thermal resistance on motor scaling in analogy to Section 2.2.1.

A slab model of a planar motor is depicted in Figure 2-1. Here, we define t_c to be the coil thickness, g to be the air gap thickness and t_m as the magnet thickness. The three materials in the motor (conductor, air, and magnet) have thermal conductivities κ_c, κ_a, and κ_m, respectively, and heat is transferred to the outside world with a heat transfer coefficient $\bar{h}$. Furthermore, we define T_0 to be the temperature at the mid-plane of the conductor, and T_∞ to be the temperature of the ambient environment. The operating temperature difference, then, is given by $\Delta T \equiv T_0 - T_\infty$. The conductor is assumed to carry a uniform current density J, which can vary in time. (Note that iron may be included in the magnetic structure of this model with trivial additions of terms.)

[2] See Section 1.2.1 for definitions of permanent magnet properties.

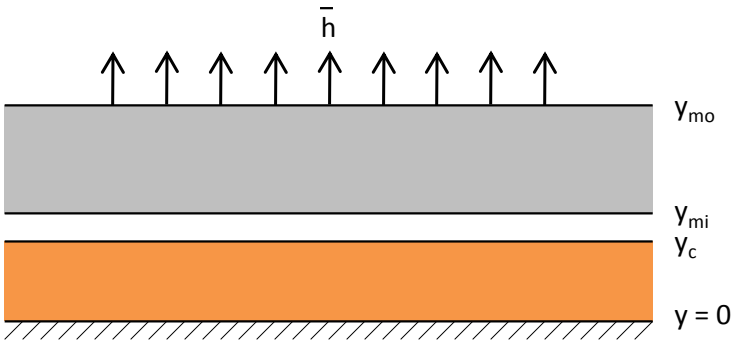

Figure 2-1: A schematic of a one-dimensional motor, with the active conductor in orange and magnets in gray. The motor is assumed to be symmetric, and the mid-plane is located at $y = 0$. The conductor extends to $y = y_c = t_c/2$, where t_c is the conductor thickness, and the magnets range from $y = y_{mi} = y_c + g$ to $y = y_{mo} = y_c + g + t_m$, where g is defined to be the air gap thickness and t_m is the magnet thickness. $\bar{h}$ is the heat transfer coefficient.

From elementary heat transfer theory [41], we can calculate a thermal resistance, R_{th} from the mid-plane to the ambient according to

$$R_{th} = \frac{1}{2}\left(\frac{t_c}{4\kappa_c} + \frac{g}{\kappa_a} + \frac{t_m}{\kappa_m} + \bar{h}^{-1}\right). \tag{2.10}$$

We could also consider a frequency-dependent thermal impedance, though in order to account for the varying temperature gradients within the motor materials such an expression would need to be quite complex. Instead, if we assume that any temporal variations in the current density are fast compared to the thermal response of the motor, we can proceed to calculate the motor temperature as a function of the time-average (RMS) current density $\bar{J}$,

$$\Delta T = \frac{R_{th} t_c \bar{J}^2}{\sigma}, \tag{2.11a}$$

and solve for the maximum RMS current density for a given acceptable temperature rise,

$$\bar{J} = \sqrt{\frac{\sigma \Delta T}{R_{th} t_c}}. \tag{2.11b}$$

We find that the thermally-limited scaling behavior of the current density $\bar{J}$ depends on whether heat conduction or convection is the limiting process; if convection limits, $\bar{J} \propto \ell^{-\frac{1}{2}}$, where ℓ is the length scale for the motor, while if conduction limits, $\bar{J} \propto \ell^{-1}$. We will refrain from non-dimensionalizing the thermal resistance until a suitable length scale arises in the analysis of Section 2.4.

2.3.1 Numerical Values

Some typical values for thermal conductivities and heat transfer coefficiencts may help provide context for this calculation. The conductor's thermal conductivity κ_c can range from that of copper ($398\,\mathrm{W/(m\cdot K)}$) to almost as low as that of air ($\kappa_a = 0.026\,\mathrm{W/(m\cdot K)}$), depending on coil construction, and is very sensitive to the copper packing fraction. For instance, if the packing fraction is 50% and the material between the wires has the thermal conductivity of air, possible values for κ_c range from $0.052\,\mathrm{W/(m\cdot K)}$ to $199\,\mathrm{W/(m\cdot K)}$ depending on the wire shape and packing structure. (See Section 2.6.1 for a detailed discussion.) For this example, we will assume $\kappa_c = 5\,\mathrm{W/(m\cdot K)}$. Neodymium iron boron (NdFeB) magnets, in turn, have a thermal conductivity of $\kappa_m = 9\,\mathrm{W/(m\cdot K)}$ [42]. If the surface of the motor is to be cooled by natural convection, we might expect $\bar{h} = 10\,\mathrm{W/(m^2\cdot K)}$ [41], while a plausible active cooling strategy involving laminar water flow through 0.5 mm tubes covering half of the outer magnet surface gives $\bar{h} = 2200\,\mathrm{W/(m^2\cdot K)}$.

Consider a motor with $t_c = t_m = 1\,\mathrm{mm}$, and $g = 10\,\mu\mathrm{m}$; with natural convection, $R_{th} = 0.1\,\mathrm{(m^2\cdot K)/W}$, while with the water cooling $R_{th} = 10^{-3}\,\mathrm{(m^2\cdot K)/W}$. If the motor is made of copper and the maximum temperature difference $\Delta T = 100\,^\circ\mathrm{C}$, the acceptable current densities would be $\bar{J} = 7.6\times10^6\,\mathrm{A/m^2}$ and $\bar{J} = 7.6\times10^7\,\mathrm{A/m^2}$ for natural and forced convection, respectively. These current densities result in force densities F' of 1,250 and 12,500 N/kg for natural and forced convection, respectively, based on the mass of the conductor alone. Note that forced convection allows for much higher force densities than does the $10^7\,\mathrm{A/m^2}$ rule of thumb.

2.4 Planar 2-D Model

A real motor must contain magnetic fields and current density fields that form closed loops. This can be achieved in one of two ways: either the structure of the motor can be finite, with flux return paths in free space (or ferrous materials) outside the motor boundaries, or the motor structure can be periodic. The simplest sort of motor that meets these restrictions is a flat, periodic motor of infinite extent, with a sheet of conductors sandwiched between ferromagnetic materials. The magnetic fields within and resulting performance of such a motor have been analyzed in numerous ways [43–45]; a complete study using the magnetic vector potential and Fourier analysis can be found in Chapter 3. The results for a simple motor will be presented here to illustrate the implications of the field solutions on motor scaling.

Perhaps the simplest flat motor configuration is an infinite periodic motor with an iron-free conductor layer between two ideal Halbach[3] arrays [46]. This motor is shown schematically in Figure 2-2, with conductor thickness t_c, magnet thickness t_m, and clearance gap g. The magnet layer has a remanence B_{rem}, recoil permeability equal to the permeability of free space μ_0, intrinsic coercivity H_{ci}, and density ρ_m,

[3]Named for Klaus Halbach, who discussed the design process for permanent magnet arrays generating highly uniform fields suitable for particle physics applications [30]. More significantly, he pioneered the practice of approximating the magnetization of rare earth magnets as field-independent, allowing the fields produced to be described by linear partial differential equations [33].

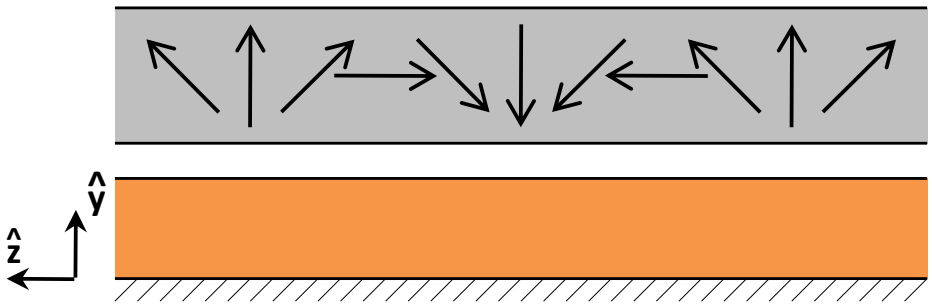

Figure 2-2: A schematic of a flat Halbach motor, with the active conductor in orange and magnets in gray. The motor is assumed to be symmetric, and the mid-plane is located at $y = 0$. The conductor has total thickness t_c, the magnets on each side have thickness t_m, and an air gap g separates the conductor from the magnets. The magnetization varies sinusoidally in space with period p, and the current density varies in step with the y-direction magnetization.

and magnetization varying with period p. More precisely, the magnetization vector $\boldsymbol{M}$ is given by

$$\boldsymbol{M} = \frac{B_{rem}}{\mu_0}\left[\cos(kz)\,\hat{\boldsymbol{y}} + \sin(kz)\,\hat{\boldsymbol{z}}\right]. \tag{2.12}$$

Here, for convenience we have defined the wavenumber $k \equiv 2\pi/p$. The conductor has conductivity σ and density ρ_c; the current density in the conductor is arranged to lie in phase with the y-direction magnetization:

$$\boldsymbol{J} = J\cos(kz)\,\hat{\boldsymbol{x}}. \tag{2.13}$$

The full solution for the field in this motor configuration is derived in Section 3.3.1; the force produced can be described as an average shear stress $\langle\sigma_{yz}\rangle$ on the surface of the conductor,

$$\langle\sigma_{yz}\rangle = \frac{B_{rem}J}{2k}\,\mathrm{e}^{-kg}\left(1-\mathrm{e}^{-kt_c}\right)\left(1-\mathrm{e}^{-kt_m}\right). \tag{2.14}$$

The form of the shear stress suggests a natural non-dimensionalization of the geometry, with k^{-1} as the length scale. We can then instead write

$$\langle\sigma_{yz}\rangle = \frac{B_{rem}J}{2k}\hat{f}, \tag{2.15a}$$

$$\hat{f} \equiv \mathrm{e}^{-kg}\left(1-\mathrm{e}^{-kt_c}\right)\left(1-\mathrm{e}^{-kt_m}\right), \tag{2.15b}$$

where $\hat{f}$ is a dimensionless force.

2.4.1 Performance Parameters and Constraints

Assuming the motor has finite length L and width W, and neglecting any effect these finite dimensions might have on the magnetic fields, we can use the magnetic shear stress from Equation 2.15a to write an expression for the total force F,

$$F = \frac{B_{rem} J L W}{k} \hat{f}. \tag{2.16a}$$

We can more conveniently express the force in terms of the total actuator mass M,

$$F = \frac{B_{rem} J M}{\rho_c} \frac{\hat{f}}{\hat{m}}, \tag{2.16b}$$

using a dimensionless mass factor $\hat{m}$:

$$M = WL\left(\rho_c t_c + 2\rho_m t_m\right) = \frac{\rho_c W L}{k} \hat{m}, \tag{2.17a}$$

$$\hat{m} \equiv k t_c + 2\frac{\rho_m}{\rho_c} k t_m. \tag{2.17b}$$

We can also find and nondimensionalize the total power dissipation P in the motor,

$$P = \frac{J^2 W L t_c}{2\sigma} = \frac{J^2 M}{\rho_c \sigma} \frac{\hat{P}}{\hat{m}}, \tag{2.18a}$$

$$\hat{P} \equiv \frac{k t_c}{2}. \tag{2.18b}$$

Note the factor of $1/2$ that arises in P when spatially averaging the power dissipation, and is carried into $\hat{P}$. For a non-sinusoidal current density, this factor may be different. Finally, we can use the expressions for force and power to calculate the performance parameters F' and ϵ,

$$F' = \frac{B_{rem} J}{\rho_c} \frac{\hat{f}}{\hat{m}}, \tag{2.19}$$

$$\epsilon = B_{rem} \hat{\epsilon} \sqrt{\frac{\sigma M}{\rho_c}}, \quad \hat{\epsilon} \equiv \frac{\hat{f}}{\sqrt{\hat{P}\hat{m}}}. \tag{2.20}$$

Note that the expressions for the force density and motor constant are almost identical to those presented in Section 2.2, Equations 2.3 and 2.4, with the addition of dimensionless correction factors $\hat{f}/\hat{m}$ and $\hat{\epsilon}$ representing the effects of the spatially varying magnetic fields and currents, as well as the mass of the magnets. The functional form of Equations 2.19 and 2.20 does not depend on the details of the magnet and conductor configuration; the motor configuration and geometry affect only the values of the dimensionless correction factors.

We can also examine the impact of the dimensionless correction factors on the

motor efficiency,

$$\hat{\eta} = \underbrace{\frac{\rho_c}{\sigma B_{rem}^2}}_{\text{materials}} \times \underbrace{\frac{2}{\omega \ell_s}}_{\text{velocity}} \times \underbrace{F_0'}_{\substack{\text{force} \\ \text{density}}} \times \underbrace{\hat{\epsilon}^{-2}}_{\substack{\text{motor} \\ \text{geometry}}} . \tag{2.21}$$

Here, we can see that $\hat{\epsilon}$ is a dimensionless efficiency parameter that can be used to compare the efficiencies of different motor configurations and geometric ratios at any size scale.

We can also nondimensionalize the expressions for the thermal constraint derived in Section 2.3 using the characteristic length k^{-1}. (The full field solution can be used to estimate the demagnetization constraint in terms of a dimensionless current density $\hat{J}$, as explained in Section 3.3.4.) The thermal resistance R_{th} and its constraint on RMS current density, Equation 2.11b, nondimensionalize as follows:

$$\bar{P} = \frac{J^2 M}{\rho_c \sigma} \frac{\hat{P}}{\hat{m}} \leq \frac{WL\Delta T}{R_{th}} = \frac{kM\Delta T}{\rho_c R_{th} \hat{m}}; \tag{2.22a}$$

$$\bar{J} \leq k\sqrt{\sigma \kappa_c \Delta T} \sqrt{\frac{1}{\hat{P}\hat{R}_{th}}}, \tag{2.22b}$$

$$\hat{R}_{th} \equiv k\kappa_c R_{th} = \frac{1}{2}\left(\frac{kt_c}{4} + kg\frac{\kappa_c}{\kappa_a} + kt_m\frac{\kappa_c}{\kappa_m} + 2\pi \mathrm{Bi}^{-1}\right), \tag{2.22c}$$

$$\mathrm{Bi} \equiv \frac{p\bar{h}}{\kappa_c}, \tag{2.22d}$$

where $\bar{P}$ is the time-average power dissipation, $\hat{R}_{th}$ is the dimensionless thermal resistance, and Bi is a Biot number for the motor, expressed in terms of the pole pitch p. The scaling relationships remarked upon earlier still hold—for large Bi, internal conduction resistance dominates, $\hat{R}_{th}$ is unchanged by length scaling, and $\bar{J} \propto p^{-1}$. For small Bi, when convection resistance dominates, $\bar{J} \propto p^{-1}\sqrt{\mathrm{Bi}} \propto p^{-1/2}$.

We can now combine these non-dimensionalized constraints with the force density expression (Equation 2.19) to yeld expressions for the scale of the motor. First, consider a demagnetization constraint, which sets a maximum value $\hat{J}_{\max}$ for the dimensionless current density. This implies that the pole pitch

$$p \leq \frac{2\pi B_{rem}^2}{\mu_0 \rho_c F'} \times \frac{\hat{f}}{\hat{m}} \hat{J}_{\max}. \tag{2.23}$$

While a similarly straightforward expression cannot be written for the general thermal constraint, because the Biot number depends on the scale of the motor, simple expressions are possible in the limits $\mathrm{Bi} \to \infty$ and $\mathrm{Bi} \to 0$ in terms of the RMS force density $\bar{F}'$:

$$\mathrm{Bi} \to \infty : \quad p \leq \frac{2\pi B_{rem}}{\rho_c \bar{F}'} \sqrt{\sigma \kappa_c \Delta T} \times \frac{\hat{\epsilon}}{\sqrt{\hat{m}\hat{R}_{th}}}, \tag{2.24a}$$

$$\text{Bi} \to 0: \quad p \leq \frac{4\pi\sigma\bar{h}B_{rem}^2\Delta T}{\rho_c^2\bar{F}'^2} \times \frac{\hat{\epsilon}^2}{\hat{m}}. \tag{2.24b}$$

Ultimately, both the thermal and the demagnetization constraints behave in the same way, constraining the pole pitch to be inversely proportional to the required force density. If the pole pitch could be reduced arbitrarily, then, an arbitrarily high force density could be available! The reality of this prospect is tempered by two major constraints, however. First, the overall efficiency of the motor, as illustrated by Equation 2.21, is inversely proportional to the force density. Our hypothetical infinite-force-density motor would require an infinite amount of input energy to produce any useful work. Second, while the mass of motor needed to reach a given force decreases linearly with the pole pitch, the mass of each repeat unit of magnets and coils decreases with the cube of the pole pitch, assuming the width scales similarly; in other words, for a given output force, the number of individual magnet segments and coil phases in the motor scales as the inverse square of the pole pitch. Our hypothetical infinite-force-density motor would also contain an infinite number of parts, and presumably also have an infinite cost. Practically, a balance must be found between the desired motor size, the desired efficiency, and the cost and complexity of the motor.

2.4.2 Numerical Values

The expression for $\hat{\epsilon}$ suggests that it may have a maximum value as a function of the dimensionless geometry kt_c, kg, and kt_m. If the conductor is solid copper and the magnet is NdFeB with a density of $\rho_m = 7600\,\text{kg/m}^3$, we can find numerically that this occurs for $kt_c \approx 0.89$, $kg = 0$,[4] and $kt_m \approx 1.7$. Thus, the best possible $\hat{\epsilon}$ for a motor of the ideal Halbach topology shown in Figure 2-2 is $\hat{\epsilon} \approx 0.37$. In the best Halbach motor, the efficiency parameter $\hat{\eta}$ is a factor of 7.2 worse (lower is better) than in the ideal model of Section 2.2.3; for the scenario presented there, the efficiency would be reduced to $\eta \approx 67\%$. This is a much lower efficiency, but still very reasonable for many applications.

We are also now in a position to illustrate the thermal scaling process for a motor. Consider the heat transfer situations presented in Section 2.3.1, with $\bar{h} = 10\,\text{W}/(\text{m}^2 \cdot \text{K})$ under natural convection or $\bar{h} = 2200\,\text{W}/(\text{m}^2 \cdot \text{K})$ under forced convection conditions, along with the work loop used in Section 2.2.2 with a target peak force density $F_0' = 1000\,\text{N/kg}$. (The RMS force density, then, is $\bar{F}' = 707\,\text{N/kg}$.)

We will use the ideal Halbach configuration in a geometry optimized for efficiency. First, assume that in each case $\text{Bi} \ll 1$. The dimensionless geometry tells us the maximum pole pitch in each situation,

$$\text{Natural Convection:} \quad p \leq 1.5 \text{ mm}, \quad \text{Bi} \approx 1.5 \times 10^{-3} \tag{2.25a}$$

$$\text{Forced Convection:} \quad p \leq 330 \text{ mm}, \quad \text{Bi} \approx 73. \tag{2.25b}$$

[4] In a practical motor, a nonzero gap is required to permit motion.

Clearly the forced convection case does not have Bi $\ll 1$, so we need to account for internal conduction resistance; by iterating a few times to find the correct value for the Biot number we find

$$\text{Forced Convection:} \quad p \leq 58 \text{ mm}, \quad \hat{R}_{th} \approx 1.4, \quad \text{Bi} \approx 13. \tag{2.26}$$

This example makes clear the vital importance of good heat transfer in supporting a high force density in a reasonably-scaled motor.

We can also examine the demagnetization constraint, as presented in Section 3.3.4. The highest-remanence grade of NdFeB magnet currently available [39] has an intrinsic coercivity $H_{ci} = 875\,\text{kA/m}$ at room temperature. (This grade is actually anisotropic, an ideal Halbach magnetization pattern cannot be produced in an anisotropic material, and coercivity at elevated temperature is more relevant to constraining performance, but this number will suffice for purposes of example.) By numerically solving Equations 3.39a and 3.38, we find $\hat{J}_{\max} \approx 1.3$, and $p \leq 210\,\text{mm}$. Clearly heat transfer is a much more significant constraint than demagnetization in this kind of motor.

Finally, we can check the actual value of required current density for electromigration concerns. From the expression for force density, Equation 2.19, we find that $J \approx 4.7 \times 10^7\,\text{A/m}^2$, well below typical electromigration current densities [47].

2.5 Axisymmetric 2-D Model

A real flat motor does not have infinite dimensions, and the effects of its edges can be substantial. In the $\hat{\boldsymbol{x}}$-direction, some provision must be made to ensure continuity in the current density at the edge of the motor, and there will thus be end-turns that make minimal contribution to force production but can have significant mass and power dissipation. There are also fringing effects in the magnetic field that reduce its magnitude around all of the edges but spread its extent beyond that of the magnets themselves. (These phenomena are discussed in detail in Section 3.3.6 and Section 3.6.)

One common approach [48] to remedying these problems is to build a tubular motor, eliminating end turns and greatly reducing fringing effects. Conceptually, this is equivalent to rolling the motor around the $\hat{\boldsymbol{z}}$-axis, placing the inner edge of the conductor sheet at a radius $r_{c,i}$. Analysis of a tubular motor is complicated by the loss of the symmetry enjoyed in the planar configuration, as well as by the properties of the solutions to Maxwell's equations in cylindrical coordinates.

A schematic of one possible tubular motor configuration is shown in Figure 2-3. This configuration uses quasi-Halbach [49] magnet arrays, with uniformly magnetized blocks rather than the continuous sinusoidal magnetization pattern of Figure 2-2. As discussed in [46], the quasi-Halbach configuration provides approximately 90% of the field of the ideal Halbach magnet array, but is considerably easier to construct. Unlike the planar motor, the tubular motor lacks symmetry, and the best geometry may require that the inner and outer magnet layers have different thicknesses from each other. The two magnet arrays may also be differently-proportioned between radial

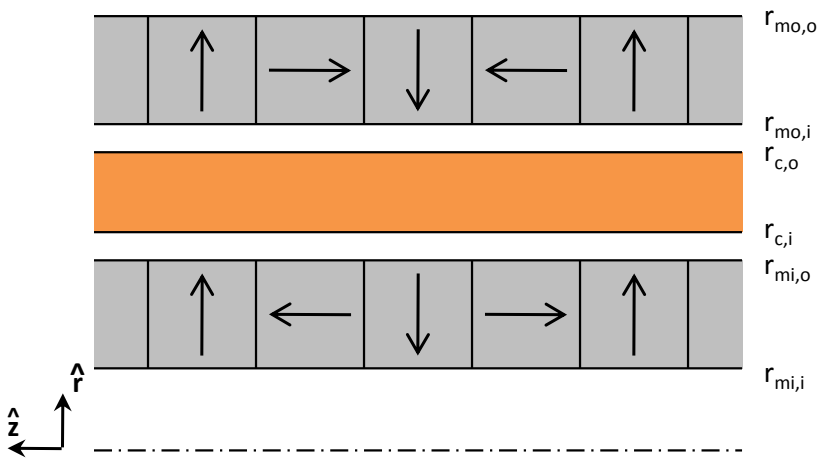

Figure 2-3: A schematic of a double-sided tubular quasi-Halbach motor, with the active conductor in orange and magnets in gray. The magnet arrays on the inside and outside may, in general, have different thicknesses and different relative block widths. The radial dimensions of the magnet and conductor layers are defined as shown in the figure. The magnet arrays have period p, and the current density varies sinusoidally in phase with the fundamental component of the $\hat{\boldsymbol{r}}$-direction magnetization.

and axial magnets; let δ_{ri} and δ_{ro} be the ratio of the width of the radial magnets to the pole pitch for the inner and outer magnet arrays, respectively.

It is worth noting that motors of the specific configuration shown in Figure 2-3 have only appeared in the literature recently, with field analyses only appearing in 2011 [50]. Nonetheless, there have been a number of general approaches to magnetic field analysis for tubular motors reported in the literature [51–53]. (The double-layered tubular Halbach array has a longer history in the magnetic bearing literature [54, 55]; high-performance voice coils have been reported [56–59] using a single period of this double-sided quasi-Halbach geometry, and magnetic springs [60] have been developed with multiple periods of this magnet configuration.) A complete analysis of this motor configuration is presented in Chapter 3, and the design, construction, and testing of an prototype motor with this configuration are discussed in Chapters 4 and 5.

Without performing the detailed field analysis to calculate the dimensionless parameters, we can still find the overall form of the motor model. By wrapping the geometry into a tube, we eliminate the independence of the motor "width" from the parameters that effect the field. Thus, the force can now be nondimensionalized as

$$F \equiv \frac{B_{rem} J L}{k^2} \hat{f}. \tag{2.27}$$

We can find the mass of the tubular motor, using the dimensions as defined in

Figure 2-3,

$$M = \pi\rho_c L\left(\left(r_{c,o}^2 - r_{c,i}^2\right) + \frac{\rho_m}{\rho_c}\left(r_{mo,o}^2 - r_{mo,i}^2 + r_{mi,o}^2 - r_{mi,i}^2\right)\right) \equiv \frac{\rho_c L}{k^2}\hat{m}, \tag{2.28a}$$

$$\hat{m} = \pi\left(\left(kr_{c,o}\right)^2 - \left(kr_{c,i}\right)^2\right) + \pi\frac{\rho_m}{\rho_c}\left(\left(kr_{mo,o}\right)^2 - \left(kr_{mo,i}\right)^2 + \left(kr_{mi,o}\right)^2 - \left(kr_{mi,i}\right)^2\right), \tag{2.28b}$$

and we can also find the power dissipation

$$P = \frac{\pi J^2 L}{2\sigma}\left(r_{c,o}^2 - r_{c,i}^2\right) \equiv \frac{J^2 L}{\sigma k^2}\hat{P}, \tag{2.29a}$$

$$\hat{P} = \pi\frac{\left(kr_{c,o}\right)^2 - \left(kr_{c,i}\right)^2}{2}. \tag{2.29b}$$

The mass and power dissipation have similar functional forms to those of the planar motor, though the more complex geometry requires slightly more complicated forms for the dimensionless parameters.

These expressions imply that we will see the same expressions for the performance parameters as were derived in Section 2.4.1:

$$F' = \frac{B_{rem} J}{\rho_c}\frac{\hat{f}}{\hat{m}}; \quad \epsilon = B_{rem}\sqrt{\frac{\sigma L}{k^2}} \times \frac{\hat{f}}{\sqrt{\hat{P}}} = B_{rem}\hat{\epsilon}\sqrt{\frac{\sigma M}{\rho_c}}. \tag{2.30}$$

Thus, the performance parameters of tubular motors scale the same way as they do for planar motors, as does the efficiency.

2.5.1 Performance Constraints

In order to find the limits to tubular motor performance, we need to find the thermal resistance in a tubular geometry. (The dimensionless current relevant to demagnetization is unchanged by the move to cylindrical coordinates.) To do this, we will also need to determine the cooling configuration of the motor; cooling may be applied on either or both the exterior or the interior of the motor, and the choice will change the thermal resistance.

First, we must find the form of the temperature equation (Equation 2.11a) for a tubular motor. In this case,

$$\Delta T = \frac{\pi\left(r_{c,o}^2 - r_{c,i}^2\right) R_{th} J^2}{2\sigma} = \frac{J^2}{\sigma\kappa_c k^2}\hat{P}\hat{R}_{th}, \quad \hat{R}_{th} = \kappa_c R_{th}. \tag{2.31}$$

The thermal resistance can be found by solving the heat diffusion equation [41]. If only the outside or the inside of the motor is cooled, the dimensionless thermal resistance

is as follows:

$$\hat{R}_{th,\text{inside}} = \frac{1}{2\pi}\left[\left(\frac{\ln\frac{kr_{c,o}}{kr_{c,i}}}{1-\left(\frac{kr_{c,o}}{kr_{c,i}}\right)^2}-\frac{1}{2}\right)+\frac{\kappa_c}{\kappa_a}\ln\frac{kr_{c,i}}{kr_{mi,o}}+\frac{\kappa_c}{\kappa_m}\ln\frac{kr_{mi,o}}{kr_{mi,i}}+\frac{1}{kr_{mi,i}\text{Bi}}\right], \tag{2.32a}$$

$$\hat{R}_{th,\text{outside}} = \frac{1}{2\pi}\left[\left(\frac{1}{2}-\frac{\ln\frac{kr_{c,o}}{kr_{c,i}}}{\left(\frac{kr_{c,o}}{kr_{c,i}}\right)^2-1}\right)+\frac{\kappa_c}{\kappa_a}\ln\frac{kr_{mo,i}}{kr_{c,o}}+\frac{\kappa_c}{\kappa_m}\ln\frac{kr_{mo,o}}{kr_{mo,i}}+\frac{1}{kr_{mo,o}\text{Bi}}\right]. \tag{2.32b}$$

The Biot number here is the same as that defined in Equation 2.22d. If both the inside and the outside of the motor are cooled, the expression for the thermal resistance is more complicated, as given below:

$$\hat{R}_{th} = \frac{(kr_0)^2\left(\ln\frac{(kr_0)^2}{kr_{c,o}kr_{c,i}}+\text{Bi}_o^{-1}+\text{Bi}_i^{-1}-1\right)+\frac{1}{2}\left((kr_{c,i})^2+(kr_{c,o})^2\right)}{4\pi\left((kr_{c,o})^2-(kr_{c,i})^2\right)} - \\ - \frac{(kr_{c,o})^2\left(\text{Bi}_o^{-1}+\frac{(kr_{c,i})^2}{(kr_{c,o})^2}\text{Bi}_i^{-1}\right)}{4\pi\left((kr_{c,o})^2-(kr_{c,i})^2\right)}, \tag{2.33a}$$

$$(kr_0)^2 = \frac{2(kr_{c,o})^2\left(\frac{(kr_{c,i})^2}{(kr_{c,o})^2}\text{Bi}_i^{-1}-\text{Bi}_o^{-1}+\frac{1}{2}\right)-(kr_{c,i})^2}{2\left(\text{Bi}_i^{-1}-\text{Bi}_o^{-1}+\ln\frac{kr_{c,o}}{kr_{c,i}}\right)}, \tag{2.33b}$$

$$\text{Bi}_i^{-1} \equiv \frac{\kappa_c}{\kappa_a}\ln\frac{kr_{c,i}}{kr_{mi,o}}+\frac{\kappa_c}{\kappa_m}\ln\frac{kr_{mi,o}}{kr_{mi,i}}+\frac{\kappa_c}{r_{mi,i}\bar{h}_i}, \tag{2.33c}$$

$$\text{Bi}_o^{-1} \equiv \frac{\kappa_c}{\kappa_a}\ln\frac{kr_{mo,i}}{kr_{c,o}}+\frac{\kappa_c}{\kappa_m}\ln\frac{kr_{mo,o}}{kr_{mo,i}}+\frac{\kappa_c}{r_{mo,o}\bar{h}_o}. \tag{2.33d}$$

In these expressions, $\bar{h}_i$ and $\bar{h}_o$ are the inner and outer convection coefficients, respectively, Bi_i and Bi_o are effective Biot numbers for the inside and outside of the motor that include conduction and convection resistances, and r_0 is the radius at which the maximum temperature occurs.

From this point, the expressions for the heat transfer constraints (Equations 2.24a

and 2.24b) are largely unchanged:

$$\text{Bi} \to \infty: \quad p \leq \frac{2\pi B_{rem}}{\rho_c F'} \sqrt{\sigma \kappa_c \left(T_0 - T_\infty\right)} \times \frac{\hat{\epsilon}}{\sqrt{\hat{m}\hat{R}_{th}}} \tag{2.34a}$$

$$\text{Bi} \to 0: \quad p \leq \frac{8\pi^3 \sigma \bar{h}_x B_{rem}^2 \left(T_0 - T_\infty\right)}{\rho_c^2 F'^2} \times \frac{\hat{\epsilon}^2}{\hat{m}} k r_x, \tag{2.34b}$$

where r_x refers to either the outside or the inside radius of the motor, whichever has a heat transfer coefficient $\bar{h}_x$. (Equation 2.34b applies only if a single motor surface is cooled, rather than both.)

2.5.2 Numerical Values

We are now in a position to discuss the quantitative performance of tubular linear PM motors, using the particular example of the ironless configuration shown in Figure 2-3. As will be shown in Chapter 3, this motor configuration performs best as a flat plate; rolling it to form a tubular motor degrades the efficiency. The efficiency penalty can be quite small, however.

Consider a planar motor of the optimal proportions discussed in Section 2.4.2; using quasi-Halbach magnets, it would have $\hat{\epsilon} \approx 0.334$ (see Section 3.3.2). If this motor were wrapped into a tube with the mid-plane located at a radius equal to the pitch length, the efficiency parameter $\hat{\epsilon}$ would decrease only slightly, with $\hat{\epsilon} \approx 0.329$, and its efficiency driving the load of Section 2.2.3 goes from 62% to 61%. Even if the planar motor is wrapped so tightly that the inner magnets become solid rather than ring-shaped (i.e. $r_{mi,i} = 0$), the efficiency parameter only decreases to $\hat{\epsilon} \approx 0.280$, with a corresponding efficiency of 53%.

We can also determine the optimum motor proportions for any given "wrapping" radius. For example, the optimum motor with a solid core ($r_{mi,i} = 0$) has dimensionless radii $kr_{mi,o} = kr_{c,i} = 3.30$, $kr_{mo,i} = kr_{c,o} = 4.18$, and $kr_{mo,o} = 5.59$, with $\delta_i = 0.409$ and $\delta_o = 0.531$. This motor has $\hat{\epsilon} \approx 0.324$, almost as good as that of the planar motor.

2.6 Further Deviations from Ideality

The analysis of Sections 2.4 and 2.5 considered the effect of motor geometry on performance, but a periodic arrangement of magnets and coils is not the sole deviation from the active material model needed to construct a practical motor. Here, we will consider four major effects: the replacement of the ideal "conductor" layer with insulated wires, the non-sinusoidal and potentially mis-aligned current distribution created by building the real "conductor" from discrete coils, the finite length of the motor in the direction of periodicity, and variation in the properties of motor materials with temperature.

2.6.1 Copper Packing Density

We have assumed a perfectly anisotropic ideal "conductor" in the analyses up to this point. However, the best conductors available to us with current technology are isotropic metals, such as copper and aluminum. In order to contain the spatially-varying current density demanded by the motor, then, the "conductor" must actually be made up of discrete, insulated wires. The insulation takes up space, reducing the effective current density and the effective conductivity.

While the exact effect of making the motor with insulated wires is difficult to calculate due to possible changes in current distribution, we can make a first-order lumped-parameter estimate of the effect on performance. To be specific, let the fill factor X denote the fraction of the "conductor" volume that is occupied by metal, and let ρ_i be the density of the insulator. We can then write the performance parameters by replacing the current density and conductivity by their reduced values as follows:

$$F' = \frac{B_{rem} X J}{\rho_c} \frac{\hat{f}}{\hat{m}}, \tag{2.35}$$

$$\epsilon = B_{rem} \hat{\epsilon} \sqrt{\frac{X \sigma M}{\rho_c}}, \tag{2.36}$$

$$\hat{\eta} = \frac{\rho_c}{\sigma B^2} \times \frac{2}{\omega \ell_s} \times F_0' \times \frac{1}{X \hat{\epsilon}^2}. \tag{2.37}$$

To account for the different densities of metal and insulation, we also need to change the expression for $\hat{m}$. For the simple planar ironless motor, it becomes

$$\hat{m} = \left((1 - X) \frac{\rho_i}{\rho_c} + X \right) k t_c + 2 \frac{\rho_m}{\rho_c} k t_m. \tag{2.38}$$

From these expressions, we can see that the fill factor has a rather direct impact on the efficiency; the $\hat{\eta}$ parameter is inversely proportional to the fill factor, which for large values of $\hat{\eta}$ is equivalent to the efficiency being directly proportional to the fill factor. It has a secondary effect on the dimensionless mass parameter, especially since insulation is typically far less dense than metal. (e.g. polyimide insulation has a density of approximately $1430\,\mathrm{kg/m^3}$ [41] compared to the $8940\,\mathrm{kg/m^3}$ density of copper.)

Numerically, the optimized motor configuration from Section 2.4.2 ordinarily has a mass parameter of $\hat{m} \approx 3.78$. Let us assume we will use 28 AWG magnet wire with heavy-build insulation [61]; in a square-packed array, similar to that encountered in a coil, the fill factor is $X = 0.6$. If the wire has polyimide insulation, the mass parameter drops to $\hat{m} \approx 3.48$. The net effect on the efficiency under the conditions of Section 2.4.2 is a decrease from 67% to 56% efficiency.

The effect of the fill factor on the thermal conductivity of the coil is more complex. Consider two limiting cases: in the upper bound on thermal conductivity, the metal is arranged in cylinders parallel to the heat flow direction, while in the lower bound it is arranged in sheets perpendicular to the heat flow. We can easily find that the bounds

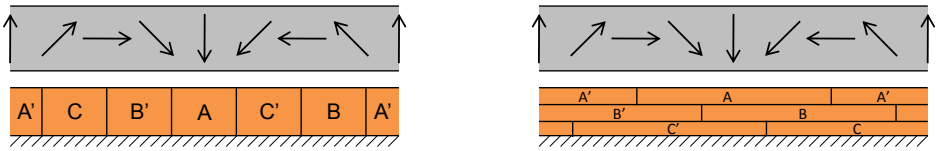

Figure 2-4: Two example three-phase windings, illustrated on a planar linear motor: a concentrated winding (left) and a layered distributed winding (right). In each case, the three phases are labeled A, B, and C, and the primed windings have current flowing in the opposite direction from the unprimed windings.

on the effective thermal conductivity of the conductor κ_{eff} are

$$\frac{\kappa_c \kappa_i}{X\kappa_i + (1-X)\kappa_c} \leq \kappa_{\text{eff}} \leq \left(X\kappa_c + (1-X)\kappa_i\right), \tag{2.39}$$

where κ_i is the thermal conductivity of the insulation. For copper metal, polyimide insulation ($\kappa_i = 0.35$ W/(m $\cdot$ K) [41]), and $X = 0.6$, the effective thermal conductivity is $0.87 \leq \kappa_{\text{eff}} \leq 240$ W/(m $\cdot$ K). While these bounds are very broad, unfortunately the real configuration is close to that of the lower bound on conductivity—heat must flow perpendicular to the wires to exit the motor. A much closer estimate can be derived from the known analytical solution for the conductivity of a square array of conductors in a matrix [62,63], which gives a value of $\kappa_{\text{eff}} \approx 1.5$ W/(m $\cdot$ K). In special winding configurations, such as edge-wound ribbons, the effective thermal conductivity of the coil can be greatly enhanced to closely approach that of the metal itself.

2.6.2 Winding Factors

Even with the use of insulation to produce an effectively anisotropic conductor, it is still not practical to produce an arbitrary current distribution in the conductor region. When building a real motor, we can only produce regions of uniform current density (i.e. apply current to wires), each of which requires a separate power amplifier. There is a trade-off, then, between the provision of an ideal current distribution aligned with the magnetic field and the complexity of the associated power electronics. The usual compromise is to arrange the winding as three phases, which require the minimum set of power amplifiers for a current distribution that can produce force in any motor position. However, the conventional analytical approach [34] to determining motor performance with a realistic winding begins from an assumed ideal concentrated winding, rather than the ideal distributed winding of the present analysis.

Thus, to fit our modeling approach we need to derive the phase currents and motor performance directly from analytical motor models. The full derivation is given in Section 3.3.2; there, we examine two winding configurations: a single-layer concentrated winding and a multi-layer distributed winding, as shown in Figure 2-4.

We can account for the winding structure using an average winding factor K_w, to be multiplied with the motor constant found with an ideal sinusoidal current distribution,

$\hat{\epsilon}_{tot} = K_w \hat{\epsilon}$. The results of the Section 3.3.2 analysis are given below:

$$\text{Concentrated Winding:} \qquad K_w = \frac{N_\phi}{\pi \alpha^{1/2}} \sin\left(\frac{\pi\alpha}{N_\phi}\right), \tag{2.40a}$$

$$\text{Layered Winding:} \qquad K_w = \frac{2}{\pi \alpha^{1/2}} \sin\left(\frac{\pi\alpha}{2}\right), \tag{2.40b}$$

where N_ϕ is the number of phases (or twice the number of phases if there are an odd number of phases) and α is the fraction of the width of each winding group occupied. The winding factors are averaged over the stroke; if there is a substantial amount of coil left unoccupied, the mass parameter will also have to be adjusted to yield accurate results.

For example, a planar motor produced with a quasi-Halbach magnet array has a value of the dimensionless motor constant $\hat{\epsilon} = 0.33$ when the current distribution is assumed to be ideal and sinusoidal, implying an efficiency of 61% under the conditions of Section 2.4.2. If instead a concentrated three-phase winding like that shown in Figure 2-4 is employed, we find that the average motor constant drops 4.5%, to $\hat{\epsilon} = 0.32$, and the overall efficiency decreases only slightly, to 58%.

If the layered distributed winding is instead employed, first note that the three phases do not necessarily see the same magnetic flux density, and thus need to be of different thicknesses in order to operate at optimum efficiency. Also, rather than being completely composed of conductor with areas of oppositely-directed current directly adjacent, as shown in Figure 2-4, each such boundary (A-A', B-B', etc.) instead should have a buffer of non-conducting material such that $\alpha = 0.85$.. Even with these adjustments, we find that the layered distributed winding can only achieve a motor constant $\hat{\epsilon} \approx 0.23$, implying an overall efficiency of only 44%. While the distributed winding is far simpler to manufacture, it is not capable of approaching the performance of concentrated windings.

2.6.3 Finite Length

The finite length of a real motor has two major impacts on its performance. The most obvious effect is the reduction of magnetic flux density near the ends of the motor, where it can spread out into the adjoining air. It is possible to calculate the magnitude of this effect analytically for the planar ironless motor [64, 65]; for motors arranged symmetrically (i.e. half-length magnets at the ends), $\hat{\epsilon}$ is reduced to 95% of its infinite-motor value when only two pole-pitches of magnets are used, as shown in Section 3.6. Even a motor employing just a single period of magnets, like a voice coil, has a value for $\hat{\epsilon}$ that is over 90% of the infinite-motor ideal. Thus, we can conclude that the effect of finite length on the magnetic field is actually very small for practical motors.

The other way in which the finite length of a motor can impact its performance is somewhat more subtle, but ultimately has much more influence on motor performance. If the magnet array and the "conductor" have equal lengths, the force that the motor

can produce using a given current will drop as it moves away from a neutral, centered position. This happens as portions of the conductor leave the magnetic field and cease to produce force. The power the motor consumes, on the other hand, does not change with its position. In order to provide consistent performance over a finite stroke length, then, there are three possible approaches: de-rate the performance so that the motor only operates at its thermal limits at the ends of the stroke, make the magnets longer than the conductor by the stroke length, or make the conductor longer than the magnets by its stroke length. To the best of the author's knowledge, these effects are rarely considered in published optimizations, particularly in the case of de-rated performance.

First, consider the case where the magnets are longer than the conductor, a condition often described as "underhung". We can introduce a parameter $Y < 1$ equal to the ratio of the coil length to the magnet length, and study its effect on the performance parameters. Our analysis takes place in the context of a spatially-averaged motor, so in this case the Y parameter has precisely the same effect on the performance parameters as the fill factor Y. We can thus write

$$F' = \frac{B_{rem} XYJ}{\rho_c} \frac{\hat{f}}{\hat{m}}, \tag{2.41}$$

$$\epsilon = B_{rem} \hat{\epsilon} \sqrt{\frac{XY\sigma M}{\rho_c}}, \tag{2.42}$$

$$\hat{\eta} = \frac{\rho_c}{\sigma B^2} \times \frac{2}{\omega L_0} \times F_0' \times \frac{1}{XY\hat{\epsilon}^2}. \tag{2.43}$$

The effect of the underhung geometry on the dimensionless mass is also similar to that of the fill factor, except that the missing conductor is not replaced by insulator:

$$\hat{m} = Y \left((1 - X) \frac{\rho_i}{\rho_c} + X \right) k t_c + 2 \frac{\rho_m}{\rho_c} k t_m. \tag{2.44}$$

For the analysis of this section, assume the motor has the planar Halbach geometry, a fill factor of $X = 0.6$, and that we require a stroke-to-length ratio of 40%, or $Y = 0.60$. The mass parameter drops to $\hat{m} \approx 3.29$, and the efficiency drops to 45%.

Next, consider the situation arising when the conductor is longer than the magnets, or the motor is "overhung". We now introduce a parameter $Y' < 1$, defined as the ratio of the magnet length to the coil length. In this case, the force density is unchanged, but the power dissipation is increased by a factor of $1/Y'$. This implies that

$$F' = \frac{B_{rem} XJ}{\rho_c} \frac{\hat{f}}{\hat{m}}, \tag{2.45}$$

$$\epsilon = B_{rem} \hat{\epsilon} \sqrt{\frac{XY'\sigma M}{\rho_c}}, \tag{2.46}$$

$$\hat{\eta} = \frac{\rho_c}{\sigma B^2} \times \frac{2}{\omega L_0} \times F_0' \times \frac{1}{XY'\hat{\epsilon}^2}. \tag{2.47}$$

The expression for the dimensionless mass is similar to that from the underhung case:

$$\hat{m} = \frac{1}{Y'}\left((1-X)\,\frac{\rho_i}{\rho_c} + X\right) kt_c + 2\frac{\rho_m}{\rho_c} kt_m. \tag{2.48}$$

To achive the same stroke as for the underhung geometry, we require $Y' = 0.71$. This increases the mass parameter to $\hat{m} \approx 3.82$, and also reduces the efficiency to 46%. If we instead require the same ratio of stroke to length, we need $Y' = 0.60$, and we find that $\hat{m} \approx 4.00$ and the efficiency drops further to 40%.

Finally, consider de-rating the motor for operation with the coil partially exposed. In this case, the force is reduced but the power dissipation is not. Defining $Y'' < 1$ as the stroke-to-length ratio, we can compute the performance parameters at the end of the stroke as follows:

$$F' = \frac{B_{rem} X J \left(1 - Y''\right)}{\rho_c} \frac{\hat{f}}{\hat{m}}, \tag{2.49}$$

$$\epsilon = B_{rem}\hat{\epsilon}\left(1 - Y''\right)\sqrt{\frac{X\sigma M}{\rho_c}}. \tag{2.50}$$

The dimensionless mass, of course, is unchanged by this operating arrangement. We cannot use the derivation of efficiency from Section 2.2.2, however, as in this case the motor constant ϵ varies with the motor position. Instead, let the motor constant with the coil centered in the motor be ϵ_0, and the position of the coil relative to the center be z_0. We thus have

$$\epsilon(z_0) = \epsilon_0\left(1 - \frac{2\,|z_0|}{L}\right). \tag{2.51}$$

As in Section 2.2.2, the motor moves sinusoidally, with $z_0 = \frac{\ell_s}{2}\sin(\omega t)$. Integrating and averaging over time, we find that

$$W_m = \frac{\ell_s F_0}{4}, \tag{2.52}$$

$$W_e = W_m + \frac{F_0^2}{\omega\epsilon_0^2}\frac{\pi\left(1 - \sqrt{1-Y''^2}\right) + 2Y''\sqrt{1-Y''^2} + 2\tan^{-1}\frac{Y''}{\sqrt{1-Y''^2}}}{\pi Y''^2\sqrt{1-Y''^2}}. \tag{2.53}$$

These expressions for the work per cycle of motion can now be used to find the dimensionless efficiency $\hat{\eta}$:

$$\hat{\eta} = \frac{\rho_c}{\sigma B^2} \times \frac{2}{\omega\ell_s} \times F_0' \times \frac{Y''_{\text{eff}}}{X\hat{\epsilon}^2}, \tag{2.54}$$

$$Y''_{\text{eff}} \equiv 2\frac{\pi\left(1 - \sqrt{1-Y''^2}\right) - 2Y''\sqrt{1-Y''^2} + 2\tan^{-1}\frac{Y''}{\sqrt{1-Y''^2}}}{\pi Y''^2\sqrt{1-Y''^2}}. \tag{2.55}$$

Here, the effects of varying motor constant are embodied by Y''_{eff}. For a stroke-to-length

ratio $Y'' = 0.40$, $Y''_{\text{eff}} \approx 1.53$, and the overall efficiency is 44%.

It is evident, then, that each of the three ways to address the problem of providing a finite stroke from a finite motor reduces the efficiency by about the same amount from the infinite-motor situation. The difference, then, lies in the thermal properties and moving mass of each configuration. The underhung motor has the lowest possible moving mass and the smallest physical size, but also operates at the highest thermal power density. The de-rated motor has an intermediate mass and size, but must be controlled to compensate for its varying motor constant and may have highly variable thermal behavior as portions of the coil enter and exit the magnet structure. The overhung motor is larger and heavier, and operates at the lowest average thermal power density, but also must be designed to handle heat transfer conditions that vary over the surface of the coil.[5]

2.6.4 Material Property Variation

The maximum operating temperature of a motor is not set arbitrarily—in general, it is determined by a combination of the softening temperature of the adhesives and insulation in the coil, the demagnetization point of the magnets, and thermal expansion of the motor components. Furthermore, at high temperatures the electrical conductivity of the coil and the remanent magnetization of the magnets both drop, reducing the motor's relative performance. Thus, even with the use of exotic, high-temperature materials, there may be a point of diminishing returns in attempting to increase force and power density by increasing the maximum operating temperature.

To initially examine these thermal effects, we can neglect the demagnetizing field created by the coil and look at pure thermal demagnetization. (Choice of coil insulation has little bearing on performance, excepting the associated temperature limits, and it is possible to accommodate thermal expansion with very modest air gaps within the motor, so the associated thermal effects can be neglected.) In the equations for the efficiency parameter (Equation 2.21) and the thermally-limited maximum pole pitch (Equation 2.24a), we can identify two groups of temperature dependent variables as figures of merit:

$$FOM_\eta = \sigma B_{rem}^2, \quad FOM_F = B_{rem}\sqrt{\sigma\,(T - T_\infty)}, \tag{2.56}$$

where FOM_η is the efficiency figure of merit, FOM_F is the force density figure of merit, and T is the operating temperature at which B_{rem} and σ are measured. There is once again a trade-off between efficiency and force density, as FOM_η is a decreasing function of temperature and FOM_F may be an increasing function of temperature. For example, FOM_F for one magnet material, VACODYM 669 [66] is plotted in Figure 2-5.

The maximum allowable temperature is given by the thermal demagnetization limit, which in turn depends on the properties of the magnet material (temperature

[5] If it is possible to electrically de-energize exposed portions of the coil, the overhung motor can provide nearly ideal efficiency and much more consistent thermal performance, at the expense of adding complex power electronics to the coil.

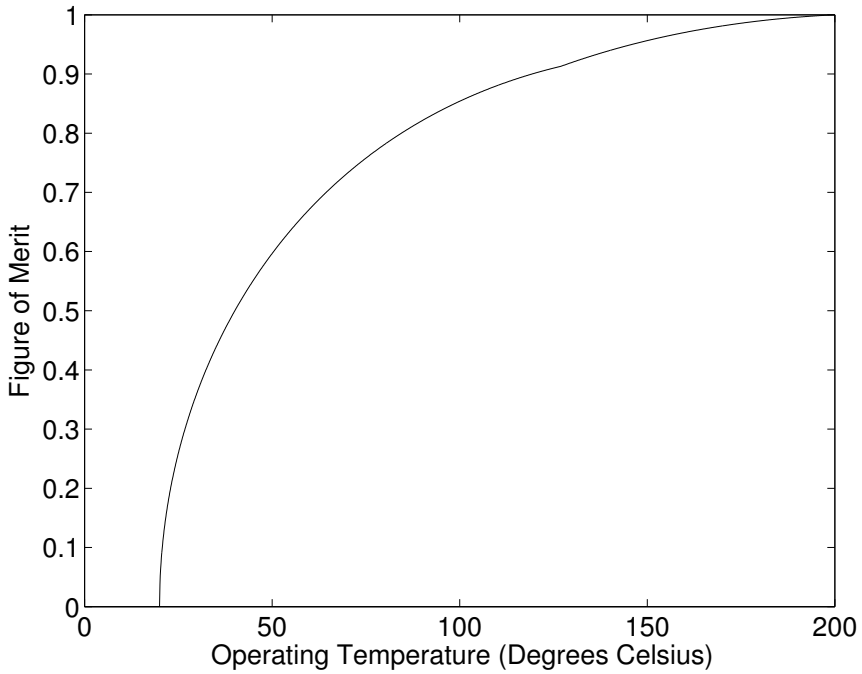

Figure 2-5: A plot of the force density figure of merit for VACODYM 669 magnet material, normalized to the maximum value in this temperature range. Note that demagnetization becomes an increasing hazard at higher temperatures.

dependence of H_{ci}) and on the strength of the demagnetizing field, commonly given as the permeance coefficient P_c of the magnet geometry. The permeance coefficient is equal to the ratio of the $\boldsymbol{B}$-field to the demagnetizing field within the magnets, taken at the point of greatest demagnetization, and may vary dramatically for different geometries. For example, an ideal Halbach array like that analyzed in Section 3.3.1 has a permeance coefficient of about -0.072, indicating powerful demagnetization, while an ideal iron-backed planar magnet array has a permeance coefficient of -2, a much milder condition. For a typical magnet material used in motors, VACODYM 669 [66], the resulting temperature limits are 130° C and 195° C, respectively.

The actual temperature limit of the motor, however, may be lower than the thermal demagnetization limit depending on the quality of heat transfer. The temperature is elevated, after all, by the application of current to the windings, which produces a demagnetizing field of its own in addition to that of the magnets themselves. In order to make a full evaluation of the temperature limit, then, the heat transfer and demagnetization constraints must be solved as a coupled system. While such an analysis is beyond the scope of the discussion here, its necessity illustrates the close design coupling required in detailed modeling of motors.

2.7 Scaling of Gears and Reduction Drives[6]

[6]The analysis of this section was inspired by an email discussion with Gill Pratt.

One of the greatest challenges in the development of small and/or complex robots is the miniaturization of actuators. Most often, the actuators in question are permanent magnet rotary motors (brushed or brushless) coupled to multi-stage gearboxes, or gearmotors. As discussed in [37, 67], the motors in these actuators have favorable power density scaling, but unfavorable torque density scaling:

$$P_m \propto \ell^{2.5}, \quad \tau_m \propto \ell^{3.5}, \tag{2.57}$$

where ℓ is the characteristic length scale and τ_m is the motor torque output.

Most loads in robotics, however, take the form of torque loads (such as gravity or grip force) rather than constant-power loads (typically fans and pumps). For purposes of this analysis, we will consider the load to be a given torque, τ_{tot}, at a given speed, ω_{out}, for a total output power P_m. In order to exploit the power scaling for this load, the motors need to operate at an increasing speed as they grow smaller, and the gearboxes in turn require increasing reduction ratios:

$$\omega_m \propto \ell^{-1}, \quad N \propto \ell^{-1}, \tag{2.58}$$

where ω_m is the motor angular velocity and N is the overall gear ratio. The utility of miniaturized gearmotors, then, depends entirely on the scaling performance of gearboxes, which must improve with decreasing size to offset the need for more reduction, and thus more gears.

Gears, in general, are primarily limited by the torque they can transmit without breaking and while maintaining an acceptable lifetime. To calculate the maximum torque, we can use the American Gear Manufacturers Association (AGMA) standard stress calculation equations for gears [68], although they are empirical in nature and have only been verified for a limited set of standard gear sizes. Nonetheless, we can consider their basic scaling:

$$\sigma_b \propto \tau_g \ell^{-3} K_v K_s, \tag{2.59a}$$

$$\sigma_c \propto \sqrt{\tau_g \ell^{-3} K_v K_s}, \tag{2.59b}$$

where σ_b is the bending stress, σ_c is the contact stress, τ_g is the gear torque, K_v is the AGMA dynamic factor, K_s is the size factor [68], and the other AGMA factors have been omitted as they are scale-invariant. The lack of speed dependence implies that the output gear will limit the overall performance, an implication borne out by the ratings of real gearboxes. The size factor K_s scales as $\ell^{0.107}$, but the behavior of the dynamic factor is more subtle, depending on the precision of the gear with scaling between unity and $\ell^{0.541}$ for the best and worst precision classes, respectively. The maximum permissible surface speed also depends on the gear precision, though this results in a scaling of $\omega_m \propto \ell^{-1}$, analogous to that of the motor.

It is worth briefly discussing the problem of gear precision here. According to the most recent AGMA standard [69], the allowable tolerance on the tooth profile of a gear is proportional to the square root of the feature size, plus a constant factor. While this implies a minimum tolerance of about 3 micrometers, in practice the standard was only

written for gears as small as 0.5 mm module, which are thus given relative tolerances of about 0.2%. This approach cannot extend to significantly smaller gears; sub-millimeter gears would require sub-micrometer precision and the associated expensive production techniques. Scaling the gear down further thus would, by necessity, reduce its precision and thereby reduce the maximum speed and torque more than the above scaling analysis suggests.

Assembling the AGMA relationships, we find that for a constant maximum stress, the maximum allowable gear torque τ_g scales as

$$\tau_g \propto \ell^{2.352} \quad \text{to} \quad \ell^{2.893}. \tag{2.60}$$

This implies both that gears increase in strength relative to motors at small scales, and that the torque-to-mass ratio of gears should improve as the gears shrink. However, if we examine real gearheads (such as Faulhaber's offerings [70]), we instead find a decrease in torque-to-mass ratio for small gears. What could explain this discrepancy?

One possible foil to the gear scaling argument is the nature of wear. In general, wear between metal surfaces that slide on each other can be described by the Archard equation [68],

$$\dot{V}_w = \frac{K F_c v}{H_s}, \tag{2.61}$$

where $\dot{V}_w$ is the volumetric wear rate, K is the dimensionless wear coefficient, F_c is the contact force, v is the sliding velocity, and H_s is the surface hardness. Ignoring scale-free parameters and assuming a constant lifetime, we can determine the scaling of the wear equation as

$$w \propto \left(\tau \ell^{-3}\right)(\omega \ell) = P \ell^{-2}, \tag{2.62}$$

where w is the linear amount of material wear. The acceptable wear presumably scales with the characteristic length, implying that $P \propto \ell^3$. Thus, the wear-limited power density of gears is scale-invariant, if the wear can be assumed to obey the Archard equation. In practice, the speed dependence may vary depending on the lubrication conditions, and wear rates may be reduced at higher speeds with elasto-hydrodynamic lubrication [71]. If this is the case, the situation becomes dire for miniaturized gearboxes, whose output stages run at a lower linear speed for a given rotational speed as their scale shrinks. This result helps to explain the drop in torque density seen for small gearmotors.

Using these relationships, we can now examine the scaling of the entire motor. For a given output power, the gearmotor mass M_{tot} can be given by

$$M_{tot} = \frac{P}{p_m} + \frac{P}{p_g} \cdot \frac{N}{N_s}, \tag{2.63}$$

where p_m is the motor power density ($\propto \ell^{-0.5}$), p_g is the gearbox power density ($\propto 1$), and N_s is the gear ratio of a single stage (which does not change with scale). Substitution of the scaling of the power densities and gear ratio yields an overall mass

scaling for a given power,

$$\frac{M}{P} \propto \ell^{0.5} + \ell^{-1}, \text{ or } p_{tot} \propto \frac{\ell}{1 + \ell^{1.5}}, \tag{2.64}$$

with p_{tot} denoting the overall power-to-mass ratio. It follows that there is actually an optimum scale for any given gearmotor power output, with a sharp ($\propto \ell$) penalty for being too small and a more gradual penalty ($\propto \ell^{-0.5}$) for being too large. Thus, we have found the reason for the poor scaling of gearmotors: the increased number of reduction stages required for smaller motors at a given torque and speed output.

While we have not established the scaling for a pure torque requirement, only a combined torque and speed (power) requirement, it is clear that a small gearmotor will likely have a poor power density, limiting the actuator's ability to move against the torque load. Furthermore, it is important to note that the only reason there is a favorable power density scaling is the enhancement of heat transfer at small size scales. Exploitation of this property requires operation at lower efficiency, as we saw in Section 2.2.3, and so the "penalty" for large size is accompanied by an efficiency improvement.

2.8 Limits to Scaling

The favorable implications of reducing the magnetic pole pitch suggest that the highest-performance motors should push this dimension to the limits of manufacturing technology. While the structures needed in a motor can be produced very small indeed via MEMS technology (e.g. [72]), there are a few limits that go beyond those of geometric precision.

At the highest level, the overall motor structure must still be capable of withstanding the applied loads—an extremely long, slender motor may be prone to buckling under compressive load, and at high force densities could also fail under tension simply due to the limited strength of the materials. For instance, Joseph and Cronje [73] describe the design of a utility-scale linear generator whose performance is limited by the tensile strength of iron, and thus could not produce a higher force density through pole-pitch reduction. Avoiding this problem requires replacing a single coarse-pitch motor with an array of smaller, short-pitch motors.

Another problem that arises when scaling to very small pole pitches relates to the microstructure and materials science of rare earth permanent magnets. Neodymium magnets smaller than a few millimeters in smallest dimension begin to show degradation in their magnetic properties due to machining processes [74], which require further treatment to recover their original properties [75]. At smaller scales still, magnet production via conventional pressing, sintering, and machining processes is no longer practical, particularly as a single motor with sub-millimeter magnet pitch might require hundreds or even thousands of individual magnets. Parallel processing of rare-earth magnets for micromanufacturing remains an active field of research, and while recent results are promising (e.g. [76]) microscale magnets are very challenging to produce and offer inferior properties to their macroscale brethren.

Finally, in order to scale to very small pole pitches the running clearance between moving elements must also be scaled to a very small level. At the millimeter scale, the air gap must be kept to below $100\,\mu$m to avoid significant loss of performance, as will be shown in Chapter 4. Just below this size scale, the gap becomes small enough that precautions must be taken to avoid jamming or wearing out the motor with particle contamination. As the goal is to apply relatively large forces and motions to the outside world, it may become difficult to maintain a clean enough environment without incurring friction and stiffness from the necessary seals. Scaling limitations of this sort will be discussed further in Section 3.7.2, where reference can be made to the results of electromagnetic modeling.

2.9 Summary and Discussion

This chapter has presented a broad modeling architecture for linear permanent-magnet motors, establishing the highest theoretical performance available and describing the effects of the major deviations from theoretical perfection required to build a working motor. We are thus now in a position to describe the best *practical* performance of such an actuator, and to discuss the implications of the efficiency and thermal constraint equations for actuator capabilities.

2.9.1 Efficiency

From the basic model of a conductor in a magnetic field, were able to derive an expression for the energy efficiency of a linear motor sinusoidally driving a pure viscous damper, Equation 2.9b, without reference to the specific geometry or design of the motor. With additional factors to describe the influence of geometry and design, we can represent the efficiency η as follows,

$$\eta = \frac{1}{1+\hat{\eta}}, \tag{2.65a}$$

$$\hat{\eta} = \underbrace{\frac{\rho_c}{\sigma B_{rem}^2}}_{\text{materials}} \times \underbrace{\frac{2}{\omega \ell_0}}_{\text{velocity}} \times \underbrace{F_0'}_{\substack{\text{force}\\\text{density}}} \times \underbrace{\frac{1}{XY\hat{\epsilon}^2}}_{\substack{\text{motor}\\\text{geometry}}}. \tag{2.65b}$$

Here, $X \leq 1$ is the conductor packing density (Section 2.6.1), $Y \leq 1$ describes the compromise required to provide a finite stroke from a finite motor (Section 2.6.3), and $\hat{\epsilon}$ represents the effect of the specific magnet and coil configuration used. Smaller values for $\hat{\eta}$ lead to improved efficiencies, though with diminishing returns for $\hat{\eta} < 1$.

Note that none of the factors influencing the motor efficiency directly depend on the size of the motor under these conditions—the efficiency of the motor instead depends on the required performance, represented as the force density, and the required velocity. The benefits of using a reduction drive instead of direct-drive are also readily apparent, as any increase in velocity allowed by such a mechanism simultaneously reduces the force. Indeed, if we represent the reduction ratio from motor motion to

load motion by N, neglect the mass of the reduction drive, and assume the drive is perfectly efficient we find that

$$\hat{\eta} = \underbrace{\frac{\rho_c}{\sigma B_{rem}^2}}_{\text{materials}} \times \underbrace{\frac{2}{\omega L_0}}_{\text{velocity}} \times \underbrace{F_0'}_{\substack{\text{force} \\ \text{density}}} \times \underbrace{\frac{1}{XY\hat{\epsilon}^2}}_{\substack{\text{motor} \\ \text{geometry}}} \times \underbrace{N^{-2}}_{\substack{\text{reduction} \\ \text{ratio}}} . \tag{2.66}$$

This is, of course, the reason for the ubiquity of rotary motors with reduction gearing in modern engineering—until the motor velocity becomes so fast that frictional losses or breakdowns in the quasi-static analysis assumption occur and dominate the energetics of the motor, increasing the velocity increases the efficiency and the mechanical power available. Direct-drive motors are only advantageous in situations where reduction drive is impractical, either due to a desire for low motor inertia (as in a haptic interface or positioning stage) or due to a small overall size (which makes friction and wear dominate the force and energy balance of a reduction drive).

Similar relationships apply under other loading conditions, though energy efficiency may cease to be the appropriate metric. For example, under static loading conditions, the motor constant itself becomes the most important metric for energy usage, leading to an expression for the power consumed P:

$$P = \underbrace{\frac{\rho_c}{\sigma B_{rem}^2}}_{\text{materials}} \times \underbrace{F}_{\text{force}} \times \underbrace{F'}_{\substack{\text{force} \\ \text{density}}} \times \underbrace{\frac{1}{XY\hat{\epsilon}^2}}_{\substack{\text{motor} \\ \text{geometry}}} . \tag{2.67}$$

In this case, the relationship between force density (i.e. motor compactness) and power consumption is even more clear.

2.9.2 Thermal Constraints

While our modeling approach has clearly demonstrated the link between increased force density and reduced efficiency, some applications (e.g. high-speed positioning and locomotion) may demand high direct-drive force density without regard to efficiency. These applications are instead likely to be constrained by the thermal power the motor can handle. Even in high-efficiency motors, thermal management issues limit the maximum mechanical power output.

By considering an abstract active material model (Section 2.2.1), we found that heat removal from the surface of a motor (the most commonly used pathway) constrains the motor's overall aspect ratio. In our subsequent, more detailed analysis, we found that in practical motors the aspect ratio constraint is equivalent to a constraint on the feature scale of the magnets and coils. Specifically, found that the features within the magnets and coils all scaled with the pole pitch p.

If the coil is entirely within the magnet array, we can write an expression for its

maximum pole pitch:

$$p \leq 2\pi \underbrace{\frac{B_{rem}\sqrt{\sigma\kappa_{\text{eff}}}}{\rho_c}}_{\text{materials}} \times \underbrace{\sqrt{\Delta T}}_{\text{thermal limits}} \times \underbrace{\frac{1}{\bar{F}'}}_{\substack{\text{force} \\ \text{density}}} \times \underbrace{\hat{\epsilon} Y \sqrt{\frac{X}{\hat{m}\hat{R}_{th}}}}_{\substack{\text{motor} \\ \text{geometry}}}. \tag{2.68}$$

Here, $\hat{R}_{th}$ is a dimensionless thermal resistance, and we assume the coil does not move. If the coil is not entirely contained within the magnets, then the motor does not experience uniform heat transfer conditions, and a more careful modeling approach should be used.

Unfortunately, we cannot assess the thermal capabilities of a motor without at least making some assertions about its shape, in order to calculate the thermal resistance. In general, achievement of force densities in excess of 1000 N/kg while keeping the pole pitch above the millimeter scale requires low thermal resistances commensurate with liquid cooling, as discussed in Section 2.4.2.

2.9.3 Discussion

Our model for motor performance can be distinguished from previously reported motor scaling models by three key features: the explicit coupling between thermal performance and pole pitch, simple break-out of the influence of motor design, and consideration of the influence of stroke length on motor performance. Some scaling models [37, 77, 78] include thermal performance, but with only one overall scale for the motor. Cugat et al. [29] acknowledge that the thermal length scale may differ from the electromagnetic length scale, but do not explore the relationship between the two. None of these scaling models admit quantitative motor descriptions, including the effects of electromagnetic motor design or stroke length, and so they cannot be used to predict the performance of a real motor at a particular scale.

Given approximate values for the dimensionless parameters, we are for the first time in a position to predict the realistic performance of a motor at arbitrary overall sizes and pole pitches. In Chapter 3, we will lay the groundwork for a library of optimized designs, satisfying a variety of optimization criteria and with corresponding values for the dimensionless parameters, which could be used to allow custom motor design without requiring detailed electromagnetic modeling. It is up to the user of our models to determine what the acceptable trade-offs are between cost and complexity, which increase as pole pitch shrinks, and raw performance, which improves at smaller pole pitches.

Chapter 3

Analytical Field Solutions

This chapter presents a series of analytical models for the magnetic fields in linear permanent magnet motors, and explains how the models can be used to compute the dimensionless performance parameters defined in Chapter 2. Planar motors are first considered, to explain the modeling approach and allow easy comparison to established solutions. The approach is then extended to tubular motors, using a numerically stable analytical solution to Maxwell's equations. The effects of field-related performance details, particularly demagnetization and finite length effects, are considered throughout. Where appropriate, the analytical models are verified with finite element analysis.

3.1 Introduction and Literature Review

Fundamentally, electric motors are devices that produce force via the interaction of electrical currents with magnetic fields. As such, in order to assess the performance of a motor geometry, its three-dimensional magnetic fields must be calculated from the appropriate form of Maxwell's equations and from the constitutive relations for the materials used. (In this work, we will use the term "geometry" to refer to the shape and relative size of the components of a particular motor, and "configuration" to refer to the set of all geometries that can be described by the same parameterization and contain the same number, kind, and orientation of components. For example, each motor configuration may have an optimum geometry.)

There is a rich history of this kind of calculation, extending back over 125 years to the earliest mathematical modeling approaches [79]. Over this time, a number of different approaches to magnetic field calculation have been developed, which can be broadly broken down into three categories: techniques using spatial discretization, techniques operating in the spatial frequency domain, and techniques employing explicit, exact field solutions. Spatial discretization was the earliest type of technique developed, in the form of magnetic circuit modeling. In this approach, iron components are assumed to have infinite (or near-infinite) permeabilities, and the user estimates the loops of magnetic flux that will be present accordingly. These loops are in turn broken down into lumped reluctance elements and modeled using an electric circuit

analogy. For simple geometries, this is a straightforward and accurate approach, taught routinely in undergraduate electromagnetics classes. In some situations, this method can even account for nonlinear behaviors in the iron, such as saturation.

In motors with wide air gaps, or structures containing no iron at all, no simple magnetic circuit model can be constructed. In these situations, the usual approach is to abandon analytical modeling and use finite element analysis (FEA), which can be considered as a sort of grid-based magnetic circuit model. FEA can solve the fields and forces to good accuracy in arbitrary motor configurations, but at the expense of very high computational effort. All but the simplest FEA models require too much computational effort for use in optimization or design synthesis.

Frequency-domain (i.e. Fourier) solution methods are considerably more accurate than magnetic circuit models, while also being far less computationally expensive than FEA. In this family of models, the motor structure is broken down into regions with uniform properties, and Maxwell's equations are solved in each region using separation of variables. While the mathematics behind this approach also have roots in the 19$^{\text{th}}$ century, Fourier techniques (and any form of rigorous analysis, for that matter) were slow to catch on in the electrical engineering community, with the first comprehensive publications on the subject appearing in the 1920s [80]. Until the advent of rare-earth magnets [30], Maxwell's equations could not be approached analytically in machines employing permanent magnets due to the magnets' intrinsically nonlinear material properties. Once it was recognized that modern materials are essentially linear within their safe operating conditions, Fourier solutions were obtained for a number of permanent magnet linear motors. Deng et al. [43] wrote what appears to be the first such paper in 1986, describing a single-sided planar motor with a slotted stator and a simple magnet structure. Trumper et al. [46] first discussed the use of Halbach's magnet arrays in motors, and solved the fields in an ironless planar motor. More recently, Gysen et al. wrote a comprehensive review of the use of Fourier techniques for electric machines [81], covering the approach for moderately complex structures in Cartesian, polar, and cylindrical coordinates.

While Fourier series field solutions work well for many motor configurations and coordinate systems, they are more challenging in cylindrical coordinates, as would be appropriate for a tubular motor. The solutions to Maxwell's equations in cylindrical coordinates cannot be expressed in terms of elementary functions, and in regions containing currents or radial permanent magnets are not even described by any of the common special functions. The earliest solutions to this problem in motors were approximations to the magnetization and current density distributions in the motor that could allow the fields to be expressed in terms of elementary functions and Bessel functions, as developed by Kim et al. [82] and Bianchi [52]. These approximations are least accurate in the situations where curvature is most pronounced, however, rendering the use of a cylindrical solution moot. For instance, if a radial magnet has an outside diameter equal to twice its inside diameter, the approximation used by Bianchi is 5% off of the true magnetization.

The most popular solution, initially given by Halbach without commentary [83] but re-introduced in the linear motor context by Wang et al. in 1999 [51], is to express the fields in terms of Bessel functions and their integrals, using a Green's function approach

to the solution of Maxwell's equations in the current-carrying and/or magnetized regions. While mathematically exact, this approach requires the numerical evaluation of definite integrals of rapidly-varying functions, which are difficult and expensive to evaluate accurately. Only recently, after the work described in this thesis commenced, was it recognized in the motor literature that magnetic fields in cylindrical coordinates can be solved in terms of named special functions with efficient numerical behavior, the modified Struve functions [53]. (The integrals encountered when using Green's functions can also be expressed analytically in terms of the modified Struve function.) Even with the benefit of a named function, however, the reports to date [50, 84, 85] do not offer numerically stable solutions, instead giving field equations that suffer from severe cancellation errors and are thus only usable for low harmonic orders.

Fourier series methods can require extensive calculations if high spatial resolution is desired, reducing their advantage over FEA. In Cartesian coordinates, the exact fields caused by individual magnet segments can be calculated, via solution of superposition integrals, and can then be added together to find global solutions for the fields in a motor. This approach has a long history as well, and was presented as a simple solution method in Hague's 1929 textbook [80]. In the linear motor literature, Xiong and Nasar presented an early superposition integral analysis in 1989 [44], though not in explicit analytical form. Konkola [86] presented an in-depth superposition analysis for linear motors, in terms of the explicit analytical expressions for multipole fields. Superposition integral-based techniques were limited to Cartesian (planar) motors until much later, with Kim and Murphy giving an implicit, integral-based solution to the problem in cylindrical coordinates in 2004 [87], and no explicit solutions given until the work of Ravaud et al. in 2009 [88]. These solutions are appealing in machines with relatively few magnets, but are difficult to calculate when many magnet segments are present. Furthermore, the explicit solutions in cylindrical coordinates involve calculating a large number of elliptic integrals, which are computationally expensive.

In special cases, other approaches have been applied; for instance, in motor structures with iron, conformal mappings can be used to calculate the field. Carter's classic analysis of slotted stators [89, 90] was an early example of this approach, but it was used relatively little afterwards due to the analytical intractability of complex conformal maps. More recently, Spooner and Haydock [91] used Schwartz-Christoffel mapping to analyze variable reluctance motors, and Gysen et al. [92] used the same technique to study complex slotted stators in tubular linear motors, though their geometry was complex enough to demand numerical evaluation of the map.

We chose to focus on the Fourier analysis approach to the magnetic field problem, and to address the flaws in the existing analyses through careful analytical calculations and by maintaining numerical stability wherever possible. We focused on the problems with tubular motor analyses, as tubular motors have promising properties but did not yet have easily-computed solutions. We also examined the standard planar motor configurations, to develop the modeling approach and investigate numerical methods and tricks.

3.2 Analytical Framework

To begin, it will be helpful to carefully define the context of the magnetic field analysis. The model used in Chapter 2 is designed to predict the static and low-speed behavior of motors. Throughout this work, then, we will strive to solve the magnetoquasistatic (MQS) form of Maxwell's equations,

$$\nabla \cdot \boldsymbol{B} = 0, \tag{3.1a}$$

$$\nabla \times \boldsymbol{H} = \boldsymbol{J}, \tag{3.1b}$$

where $\boldsymbol{B}$ is the magnetic field, $\boldsymbol{H}$ is the magnetizing field, and $\boldsymbol{J}$ is the electrical current density. An alternative way to interpret Equation 3.1a is to define the $\boldsymbol{B}$ field as the curl of a magnetic vector potential $\boldsymbol{A}$,

$$\nabla \times \boldsymbol{A} \equiv \boldsymbol{B}. \tag{3.2}$$

To solve Maxwell's equations, we also need to know the relationship between $\boldsymbol{B}$ and $\boldsymbol{H}$ within the materials of the motor. We will consider motors made up of four fundamental kinds of material: air, conductor, magnet, and iron. We can consider air to have the constitutive relations of a vacuum, and conductor to be non-magnetic and to otherwise behave according to Ohm's law. We will restrict the magnet materials under consideration to "modern" materials, i.e. rare-earth and ferrite magnets. The constitutive behavior of these materials can be closely approximated by a constant intrinsic magnetization and permeability equal to that of vacuum [33]. (In practice, values of the effective relative permeability in these permanent magnet materials range between 1.05 and 1.1.) Finally, we will consider iron to be an isotropic material with saturation, but no hysteresis, which can therefore be described by a nonlinear, single-valued scalar magnetic permeability function. These constitutive relations are summarized below:

Air: $$\boldsymbol{B} = \mu_0 \boldsymbol{H}, \quad \boldsymbol{J} = 0 \tag{3.3a}$$

Conductor: $$\boldsymbol{B} = \mu_0 \boldsymbol{H}, \quad \boldsymbol{J} \text{ specified} \tag{3.3b}$$

Magnet: $$\boldsymbol{B} = \mu_0 \left(\boldsymbol{H} + \boldsymbol{M}\right), \quad \boldsymbol{J} = 0 \tag{3.3c}$$

Iron: $$\boldsymbol{B} = \mu_0 \mu\left(\left|\boldsymbol{H}\right|^2\right) \boldsymbol{H}, \quad \boldsymbol{J} = 0. \tag{3.3d}$$

Here, $\boldsymbol{M}$ is the magnetization vector, and μ is the relative magnetic permeability, given as a function of the magnitude of the $\boldsymbol{H}$-field. Values for the remanence of permanent magnets are readily available from suppliers (e.g. [66]), and permeability curves for iron can be derived from manufacturers' data, such as that in [93].

With the constitutive relations, we are equipped to write a single partial differential equation for the magnetic vector potential in each material. Using basic vector calculus

identities, and defining the divergence of the vector potential to be zero (i.e. setting the Coulomb gauge), we find the following governing relations:

$$\text{Air:} \qquad \nabla^2 \boldsymbol{A} = \boldsymbol{0} \tag{3.4a}$$

$$\text{Conductor:} \qquad \nabla^2 \boldsymbol{A} = -\mu_0 \boldsymbol{J} \tag{3.4b}$$

$$\text{Magnet:} \qquad \nabla^2 \boldsymbol{A} = -\nabla \times \boldsymbol{M} \tag{3.4c}$$

$$\text{Iron:} \qquad \nabla^2 \boldsymbol{A} = -\frac{1}{\mu}\left(\frac{\partial \mu}{\partial \left|\boldsymbol{H}\right|^2}\right) \nabla\left(\boldsymbol{H} \cdot \boldsymbol{H}\right) \times \left(\nabla \times \boldsymbol{A}\right). \tag{3.4d}$$

In the absence of iron, Equations 3.4 are linear Poisson's equations, and superposition principles can be used to solve the overall problem. Superposition allows the magnet and coil structures to be analyzed separately, and grants considerable flexibility in the calculation of fields for each component. The behavior of iron is, in general, formidably nonlinear, but if μ is constant the right-hand side of Equation 3.4d becomes zero and the solution is the same as that seen in air. Thus, if we are willing to approximate each iron region as having constant permeability, superposition can still be used if the iron's B-H curve is linearized and the equations are solved iteratively.

In practice, linear motors have a periodic structure in their direction of actuation; we will base our analysis on the period of the magnet structure, the pole pitch p. Linear motors also are finite in length, with a magnet structure containing N_p periods. Note that N_p need not be integral—a voice coil can be considered as having $N_p = 1/2$, for instance.

The finite-but-periodic structure of a motor results in a choice of analysis approaches: the known solutions for the fields produced by isolated magnets and coils may be added together for each element in the motor [94, 95], or the field solutions for infinitely long periodic motor structures may be found via Fourier analysis, and then modified via convolution to account for the actual finite length [64, 96]. It is our view that the Fourier series approach to magnetic field calculation is considerably more flexible than the isolated-element approach, and provides a better intuitive understanding of the motor's behavior. It also allows the mathematically simpler behavior of an infinite motor to be determined separately from the mathematically complex end effects encountered in a finite motor. Note that the general calculation approach employed in this work is not new—the overall dimensionless parameter framework of Chapter 2 is novel, and novel features of the field analyses will be noted as they appear.

3.3 Planar Motors

Planar motors are the earliest linear motors developed [23], and their magnetic fields can be described in terms of elementary functions (trigonometric functions

and exponentials). We will thus begin by applying our framework to motors of this topology, developing the concepts from the simplest possible configuration to more complex designs. Our discussion will closely follow the results in [46] for the ironless motors, but new analytical approaches will be required to deal with motors containing iron, and to accurately assess demagnetization.

3.3.1 Simple Halbach

Here, we will consider perhaps the simplest flat motor configuration, an infinite periodic motor with an iron-free conductor layer between two ideal Halbach-magnetized magnet layers, as shown in Figure 3-1. This configuration has been described in detail by Trumper et al. in [45] and [46][1], but its analysis will be described here for illustration. The magnet layer (region 3) has intrinsic coercivity H_{ci}, density ρ_m, and both axial (z-direction) and transverse (y-direction) magnetization varying sinusoidally with period p. More precisely, the magnetization vector is given by

$$\mu_0 \boldsymbol{M} = B_{rem} \left(\cos(kz)\, \hat{\boldsymbol{y}} + \sin(kz)\, \hat{\boldsymbol{z}} \right), \tag{3.5}$$

where B_{rem} is the remanence of the magnet material, and for convenience we have defined the wavenumber $k \equiv 2\pi/p$. As was described by Halbach [83], this magnetic structure concentrates all of its flux on one side, increasing the achievable magnetic field over other arrangements. The current density in the conductor (Region 1) is arranged to lie in phase with the y-direction magnetization:

$$\boldsymbol{J} = J \cos(kz)\, \hat{\boldsymbol{x}}. \tag{3.6}$$

The relevant Poisson equations are now readily solved in Cartesian coordinates for the vector potentials, which take the form:

$$\boldsymbol{A} = \Big[A_m(y) \sin(kz) + A_c(y) \cos(kz) \Big] \hat{\boldsymbol{x}}, \tag{3.7}$$

where A_m and A_c are scalar functions of the y-coordinate only. These functions can be determined for the materials in the Halbach motor:

$$A_{m,\,\text{magnet}} = \frac{B_{rem}}{k} \left(a\, \mathrm{e}^{ky} + b\, \mathrm{e}^{-ky} + 1 \right), \tag{3.8a}$$

$$A_{c,\,\text{coil}} = \frac{\mu_0 J}{k^2} \left(\frac{a}{k}\, \mathrm{e}^{ky} + \frac{b}{k}\, \mathrm{e}^{-ky} + 1 \right), \tag{3.8b}$$

$$A_{m,\text{other}} = \frac{B_{rem}}{k} \left(a\, \mathrm{e}^{ky} + b\, \mathrm{e}^{-ky} \right), \tag{3.8c}$$

$$A_{c,\text{other}} = \frac{\mu_0 J}{k^2} \left(a\, \mathrm{e}^{ky} + b\, \mathrm{e}^{-ky} \right). \tag{3.8d}$$

[1] Strictly speaking, Trumper et al. only describe the case of a single magnet layer and a single coil layer, but their analysis can cover the present case with a simple change of boundary condition.

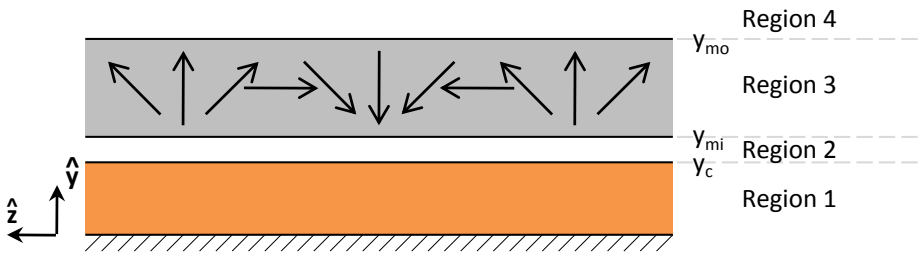

Figure 3-1: A schematic of a flat Halbach motor, with the active conductor in orange and magnets in gray. The motor is assumed to be symmetric, and the mid-plane is located at $y = 0$. The conductor extends to $y = y_c = t_c/2$, where t_c is the conductor thickness, and the magnets range from $y = y_{mi} = t_c/2 + g$ to $y = y_{mo} = t_c/2 + g + t_m$, where g is defined to be the air gap thickness and t_m is the magnet thickness. The magnetization varies sinusoidally in space with period p, and the current density varies sinusoidally in step with the y-direction magnetization. Note that positive x points out of the page.

Here, a and b are arbitrary constants that must be found in each region by matching boundary conditions. As the constants a and b are arbitrary, we have taken the liberty of factoring the magnet and coil particular solutions out and rendering the constants dimensionless. We will use numerical subscripts to denote the motor region, as shown in Figure 3-1.

There are a number of approaches available to find the arbitrary constants; one popular option is to use the transfer relations concept advocated by Melcher [46, 97]. We will simply use the brute-force approach, making use of the definition of the magnetic vector potential (Equation 3.2) and the constitutive relations to find the magnetic field $\boldsymbol{B}$ and the magnetizing field $\boldsymbol{H}$. We can then find the general expression for the $\boldsymbol{B}$-field,

$$\boldsymbol{B} = \left[kA_m \cos(kz) - kA_c \sin(kz)\right]\hat{\boldsymbol{y}} - \left[\frac{\partial A_m}{\partial y}\sin(kz) + \frac{\partial A_c}{\partial y}\cos(kz)\right]\hat{\boldsymbol{z}}. \tag{3.9}$$

Substituting the appropriate derivatives of the vector potential yields the following specific equations for the $\boldsymbol{B}$-fields in each region:

$$\boldsymbol{B}_1 = \left[B_{rem}\left(a_{m,1}\,\mathrm{e}^{ky} + b_{m,1}\,\mathrm{e}^{-ky}\right)\cos(kz) - \frac{\mu_0 J}{k}\left(a_{c,1}\,\mathrm{e}^{ky} + b_{c,1}\,\mathrm{e}^{-ky} + 1\right)\sin(kz)\right]\hat{\boldsymbol{y}} - \left[B_{rem}\left(a_{m,1}\,\mathrm{e}^{ky} - b_{m,1}\,\mathrm{e}^{-ky}\right)\sin(kz) + \frac{\mu_0 J}{k}\left(a_{c,1}\,\mathrm{e}^{ky} - b_{c,1}\,\mathrm{e}^{-ky}\right)\cos(kz)\right]\hat{\boldsymbol{z}}, \tag{3.10a}$$

$$\boldsymbol{B}_2 = \left[B_{rem} \left(a_{m,2}\, \mathrm{e}^{ky} + b_{m,2}\, \mathrm{e}^{-ky} \right) \cos(kz) - \frac{\mu_0 J}{k} \left(a_{c,2}\, \mathrm{e}^{ky} + b_{c,2}\, \mathrm{e}^{-ky} \right) \sin(kz) \right] \hat{\boldsymbol{y}} - \left[B_{rem} \left(a_{m,2}\, \mathrm{e}^{ky} - b_{m,2}\, \mathrm{e}^{-ky} \right) \sin(kz) + \frac{\mu_0 J}{k} \left(a_{c,2}\, \mathrm{e}^{ky} - b_{c,2}\, \mathrm{e}^{-ky} \right) \cos(kz) \right] \hat{\boldsymbol{z}}, \tag{3.10b}$$

$$\boldsymbol{B}_3 = \left[B_{rem} \left(a_{m,3}\, \mathrm{e}^{ky} + b_{m,3}\, \mathrm{e}^{-ky} + 1 \right) \cos(kz) - \frac{\mu_0 J}{k} \left(a_{c,3}\, \mathrm{e}^{ky} + b_{c,3}\, \mathrm{e}^{-ky} \right) \sin(kz) \right] \hat{\boldsymbol{y}} - \left[B_{rem} \left(a_{m,3}\, \mathrm{e}^{ky} - b_{m,3}\, \mathrm{e}^{-ky} \right) \sin(kz) + \frac{\mu_0 J}{k} \left(a_{c,3}\, \mathrm{e}^{ky} - b_{c,3}\, \mathrm{e}^{-ky} \right) \cos(kz) \right] \hat{\boldsymbol{z}}, \tag{3.10c}$$

$$\boldsymbol{B}_4 = \left[B_{rem} \left(a_{m,4}\, \mathrm{e}^{ky} + b_{m,4}\, \mathrm{e}^{-ky} \right) \cos(kz) - \frac{\mu_0 J}{k} \left(a_{c,4}\, \mathrm{e}^{ky} + b_{c,4}\, \mathrm{e}^{-ky} \right) \sin(kz) \right] \hat{\boldsymbol{y}} - \left[B_{rem} \left(a_{m,4}\, \mathrm{e}^{ky} - b_{m,4}\, \mathrm{e}^{-ky} \right) \sin(kz) + \frac{\mu_0 J}{k} \left(a_{c,4}\, \mathrm{e}^{ky} - b_{c,4}\, \mathrm{e}^{-ky} \right) \cos(kz) \right] \hat{\boldsymbol{z}}. \tag{3.10d}$$

The $\boldsymbol{H}$-fields can then be found simply via the constitutive relations.

The boundary condition at infinity can be used to immediately find two of the arbitrary constants:

$$a_{m,4} = 0, \quad a_{c,4} = 0. \tag{3.11}$$

At each boundary between regions, the y-component of the $\boldsymbol{B}$ field and the z-component of the $\boldsymbol{H}$ field must be continuous. On the symmetry plane at $y = 0$, the z-components of both the $\boldsymbol{B}$ and the $\boldsymbol{H}$ fields must be zero. This leads to a system of linear equations for the 16 unknown coefficients, with the following solutions:

$$\begin{aligned}
a_{m,1} &= \mathrm{e}^{-\left(\frac{kt_c}{2} + kg\right)} \left(1 - \mathrm{e}^{-kt_m} \right) & b_{m,1} &= a_{m,1} \\
a_{c,1} &= -\frac{1}{2}\, \mathrm{e}^{-\frac{kt_c}{2}} & b_{c,1} &= a_{c,1} \\
a_{m,2} &= a_{m,1} & b_{m,2} &= a_{m,1} \\
a_{c,2} &= 0 & b_{c,2} &= b_{c,4} \\
a_{m,3} &= -\,\mathrm{e}^{-\left(\frac{kt_c}{2} + kg\right)}\, \mathrm{e}^{-kt_m} & b_{m,3} &= a_{m,1} \\
a_{c,3} &= 0 & b_{c,3} &= b_{c,4} \\
a_{m,4} &= 0 & b_{m,4} &= a_{m,1} \\
a_{c,4} &= 0 & b_{c,4} &= -\sinh\left(\frac{kt_c}{2} \right).
\end{aligned} \tag{3.12}$$

With the magnetic fields known, we are almost ready to determine the force produced by the motor. To calculate the force per unit area of motor, we need to find the yz component of the Maxwell Stress Tensor, σ_{yz}, on the surface of the conductor, and average it over space. We can find the Maxwell Stress Tensor as follows:

$$\begin{aligned}\sigma_{yz} &= \frac{1}{\mu_0} B_y B_z \Big|_{y=t_c/2} \\ &= \frac{2B_{rem}J}{k} a_{m,1} b_{c,4} \, \mathrm{e}^{-\frac{kt_c}{2}} \left[\cosh\left(\frac{kt_c}{2}\right) \cos^2(kz) + \sinh\left(\frac{kt_c}{2}\right) \sin^2(kz) \right] - \\ &\quad \left[\frac{B_{rem}^2}{\mu_0} a_{m,1}^2 \sinh(kt_c) + \frac{\mu_0 J^2}{2k^2} b_{c,4}^2 \, \mathrm{e}^{-kt_c} \right] \sin(2kz) \,.\end{aligned} \tag{3.13}$$

We can then find the spatial average magnetic shear stress and nondimensionalize:

$$\left\langle \sigma_{yz} \right\rangle = \frac{B_{rem}J}{k} a_{m,1} b_{c,4} = \frac{B_{rem}J}{2k} \hat{f}, \tag{3.14a}$$

$$\hat{f} \equiv \mathrm{e}^{-kg} \left(1 - \mathrm{e}^{-kt_c}\right) \left(1 - \mathrm{e}^{-kt_m}\right). \tag{3.14b}$$

The remaining dimensionless parameters do not depend directly on the field, and are given by Equations 2.17b and 2.18b.

3.3.2 Block Halbach with Windings

In practice, ideal Halbach arrays are difficult to construct, and can only be made from bonded or isotropic sintered magnet materials, which offer relatively low remanence (0.7 T [98] and 1.0 T [99], respectively, in the NdFeB system) compared to available anisotropic sintered magnets. Instead, the array is assembled from a series of blocks of uniform magnetization, as illustrated in Figure 3-2. These arrays can be handled by representing the magnetization as an infinite Fourier series instead of the pure sinusoids of the ideal Halbach magnet [83]:

$$\boldsymbol{M} = \frac{B_{rem}}{\mu_0} \sum_{n=1}^{\infty} \left[\hat{M}_{yn} \cos(nkz) \, \hat{\boldsymbol{y}} + \hat{M}_{zn} \sin(nkz) \, \hat{\boldsymbol{z}} \right], \tag{3.15a}$$

$$\hat{M}_{yn} = \frac{2}{n\pi} \sin\left(\frac{n\pi\delta_y}{2}\right) \left((-1)^{n+1} + 1\right), \tag{3.15b}$$

$$\hat{M}_{zn} = \frac{2}{n\pi} \sin\left(\frac{n\pi\delta_z}{2}\right) \left((-1)^{n+1} + 1\right), \tag{3.15c}$$

where $\hat{M}_{yn}$ and $\hat{M}_{zn}$ represent nondimensionalized Fourier coefficients for the vertical and axial magnets, respectively, at harmonic order n, δ_y and δ_z represent the fraction of the array made up of each magnet type, there are four of blocks per period, and the symmetry of the array eliminates even harmonics. The fractional widths δ_y and δ_z should sum to one for an array with no gaps between magnets; a lower sum

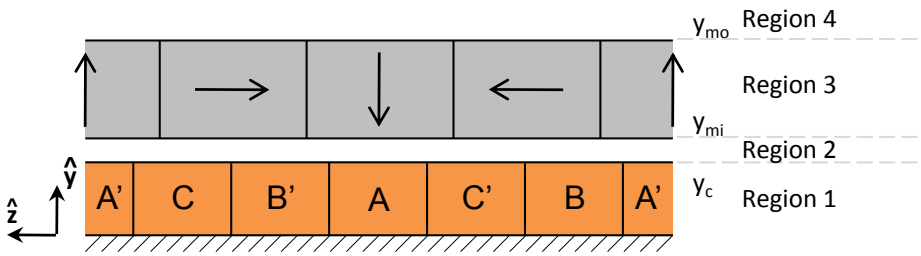

Figure 3-2: A schematic of a flat block Halbach motor, with the active conductor in orange and magnets in gray. The motor is assumed to be symmetric, and the mid-plane is located at $y = 0$. The conductor extends to $y = y_c = t_c/2$, where t_c is the conductor thickness, and the magnets range from $y = y_{mi} = t_c/2 + g$ to $y = y_{mo} = t_c/2 + g + t_m$, where g is defined to be the air gap thickness and t_m is the magnet thickness. The magnet array has four blocks per period p, and the winding has three phases.

allows for gaps, while a higher sum is physically unrealistic. Only odd harmonics are present, due to the inherent symmetry of the magnet array. For a four-block array with $\delta_y = \delta_z = 1/2$, as shown in Figure 3-2, the fundamental component of the magnetization is about 90% of that in an ideal Halbach array of the same remanence. Arrays with more blocks can approach the ideal Halbach array more closely, but are correspondingly more difficult to manufacture; the formula for their magnetization is given in [83].

Similarly, it is difficult to arrange for an exactly sinusoidal current density distribution, and instead winding regions of uniform current density must be provided. The simplest way to do this is to divide the whole coil thickness into three or more equal winding groups per period. These winding groups are powered by three or more distinct currents, or phases; if there are an even number of coil groups, half that number of phases can be used, with the two groups per phase arranged symmetrically and wound in opposite directions. Figure 3-2 shows a six-group, three-phase winding. Let N_ϕ be the number of coil groups, and α be the fraction of the coil occupied by winding groups; the current density can be represented by the following Fourier series:

$$\boldsymbol{J} = \sum_{i=0}^{N_\phi - 1} \sum_{n=1}^{\infty} J_{ni} \cos\left(nk\left(z - z_0\right) - \frac{2\pi n i}{N_\phi} \right) \hat{\boldsymbol{x}}, \tag{3.16}$$

$$J_{ni} = \frac{2J_i}{n\pi} \sin\left(\frac{n\pi\alpha}{N_\phi} \right), \tag{3.17}$$

where J_i is the current density in group i , J_{ni} is the Fourier coefficient of order n for coil group i, and z_0 is the displacement of the coil from the position in which phase 0 and the y-direction magnetization are aligned.

The overall behavior of the motor is determined by the set of phase current densities, which are in turn determined by the commutation pattern employed. The

most efficient pattern is sinusoidal commutation, which places the fundamental of the overall current density waveform in phase with that of the magnetization:

$$J_i = J_{cmd} \cos\left(kz_0 + \frac{2\pi i}{N_\phi}\right), \tag{3.18}$$

where J_{cmd} is an overall commanded current density. With this commutation pattern in place, and after some trigonometric manipulation, the first harmonic of the overall current density $\boldsymbol{J}_1$ is given as follows:

$$\boldsymbol{J}_1 = J_{cmd} \frac{N_\phi}{\pi} \sin\left(\frac{\pi\alpha}{N_\phi}\right) \cos(nkz)\, \hat{\boldsymbol{x}}. \tag{3.19}$$

(Expressions for the remaining harmonics are too complex to warrant writing out explicitly.) Thus, a typical six-group winding like the one shown in Figure 3-2 produces a sinusoidal current density 95% as strong as the "ideal". The power required is given by

$$P = \frac{\alpha J_{cmd}^2 W L t_c}{\sigma N_\phi} \sum_{i=0}^{N_\phi - 1} \cos^2\left(kz_0 + \frac{2\pi i}{N_\phi}\right) = \frac{\alpha J_{cmd}^2 L W t_c}{2\sigma}, \tag{3.20}$$

where the final equality is true only if $N_\phi > 2$. Comparing with Equation 2.18b, we see that this winding scheme with sinusoidal commutation has the same dimensionless power as the ideal winding, except for the coil group width factor α:

$$\hat{P} = \frac{\alpha k t_c}{2}. \tag{3.21}$$

With the magnetization and current density now expressed as Fourier series, the field solutions derived for the ideal Halbach array can be used with a few small modifications:

$$\boldsymbol{A} = \sum_{n=1}^{\infty} \left[A_{mn} \sin(nkz) + \sum_{i=0}^{N_\phi - 1} A_{cni} \cos\left(nk\,(z - z_0) - \frac{2\pi n i}{N_\phi}\right) \right] \hat{\boldsymbol{x}}, \tag{3.22}$$

with A_{mn} giving the n$^{\text{th}}$ harmonic coefficient of the magnetization's vector potential and A_{cni} giving the n$^{\text{th}}$ harmonic of the vector potential from coil group i. Rather than finding a single set of coefficients, we now must find one for every order n. The vector potential functions are given as follows in the motor regions:

$$A_{mn,\,3} = \frac{B_{rem}}{nk} \left(a\, \mathrm{e}^{nky} + b\, \mathrm{e}^{-nky} + \hat{M}_{yn} \right), \tag{3.23a}$$

$$A_{cni,\,1} = \frac{\mu_0 J_{ni}}{n^2 k^2} \left(a\, \mathrm{e}^{nky} + b\, \mathrm{e}^{-nky} + 1 \right), \tag{3.23b}$$

$$A_{mn,\,\text{other}} = \frac{B_{rem}}{nk} \left(a\, \mathrm{e}^{nky} + b\, \mathrm{e}^{-nky} \right), \tag{3.23c}$$

$$A_{mn,\text{ other}} = \frac{\mu_0 J_{ni}}{n^2 k^2} \left(a\, \mathrm{e}^{nky} + b\, \mathrm{e}^{-nky} \right). \tag{3.23d}$$

Analogous modifications can be made to the field expressions (Equations 3.9 and 3.10) to account for the Fourier series and different current spatial phase. The constants a and b now have the following values:

$$\begin{aligned}
a_{mn,1} &= \frac{1}{2}\left(\hat{M}_{yn} + \hat{M}_{zn}\right)\left(1 - \mathrm{e}^{-nkt_m}\right)\mathrm{e}^{-\frac{nkt_c}{2}}\,\mathrm{e}^{-nkg} & b_{mn,1} &= a_{mn,1} \\
a_{cni,1} &= -\frac{1}{2}\,\mathrm{e}^{-\frac{nkt_c}{2}} & b_{cni,1} &= a_{cni,1} \\
a_{mn,2} &= a_{m,1} & b_{mn,2} &= a_{mn,1} \\
a_{cni,2} &= 0 & b_{cni,2} &= b_{cni,4} \\
a_{mn,3} &= -\frac{1}{2}\left(\hat{M}_{yn} + \hat{M}_{zn}\right)\mathrm{e}^{-\frac{nkt_c}{2}}\,\mathrm{e}^{-nkg}\,\mathrm{e}^{-nkt_m} & & \\
b_{mn,3} &= -\frac{1}{2}\left(\hat{M}_{yn}\,\mathrm{e}^{-nkt_m} - \hat{M}_{zn}\left(1 - \mathrm{e}^{-nkt_m}\right)\right)\mathrm{e}^{-\frac{nkt_c}{2}}\,\mathrm{e}^{-nkg} & & \\
a_{cni,3} &= 0 & b_{cni,3} &= b_{cni,4} \\
a_{mn,4} &= 0 & b_{mn,4} &= \frac{1}{2}\left(\hat{M}_{yn}\sinh\left(nkt_m\right) + \hat{M}_{zn}\left(1 - \cosh\left(nkt_m\right)\right)\right)\mathrm{e}^{-\frac{nkt_c}{2}}\,\mathrm{e}^{-nkg} \\
a_{cni,4} &= 0 & b_{cni,4} &= -\sinh\left(\frac{nkt_c}{2}\right).
\end{aligned} \tag{3.24}$$

To calculate the force produced by the motor, one could compute the Maxwell stress tensor for the total field, using many harmonics. However, only those field harmonics produced by the magnets and coils that line up in phase actually contribute to the spatially-averaged shear stress, and the strengths of the higher harmonics of field decay rapidly away from their sources. Furthermore, only the fundamental of the current density is commanded to be in phase with the magnetization; the higher harmonics can move in and out of phase as the coil moves. Thus, it is conventional to calculate the force using only the first harmonics of the field; in this case, Equation 3.14a is unchanged except for the substitution of J_{cmd} for J, and the total dimensionless force $\hat{f}_{tot}$ is given by

$$\hat{f}_{tot} = \frac{N_\phi}{2\pi}\left(\hat{M}_{z1} + \hat{M}_{y1}\right)\mathrm{e}^{-kg}\left(1 - \mathrm{e}^{-kt_c}\right)\left(1 - \mathrm{e}^{-kt_m}\right)\sin\left(\frac{\pi\alpha}{N_\phi}\right). \tag{3.25}$$

We are now able to calculate all of the performance parameters for a realistic motor design. Combined with Equation 3.21 for the dimensionless power, we can define a winding factor and a magnet-specific force parameter:

$$\hat{f} = \frac{1}{2}\left(\hat{M}_{z1} + \hat{M}_{y1}\right)\mathrm{e}^{-kg}\left(1 - \mathrm{e}^{-kt_c}\right)\left(1 - \mathrm{e}^{-kt_m}\right), \tag{3.26}$$

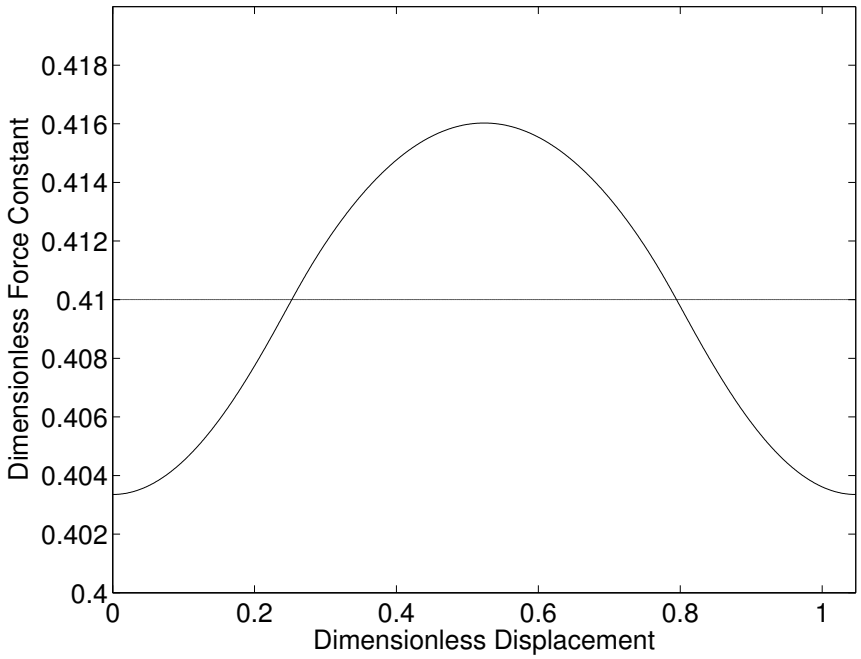

Figure 3-3: The dimensionless force $\hat{f}$ is plotted against the dimensionless displacement kz_0 for a block Halbach motor with the geometric parameters described in the text. The force parameter varies by approximately $\pm 1.5\%$ over the stroke.

$$K_w = \frac{N_\phi}{\pi \alpha^{1/2}} \sin\left(\frac{\pi \alpha}{N_\phi}\right). \tag{3.27}$$

Using this approach, the details of the winding strategy can be almost completely separated from the design of the magnet array, with the only design coupling appearing in the expression for the mass parameter. If $\alpha < 1$, the mass parameter must be adjusted accordingly, depending on what is to be done with the empty space.

We will optimize the geometry of this motor in Section 3.7.1, but for the moment consider a motor with $\alpha = 1$, $\delta_y = \delta_z = 1/2$, $N_\phi = 6$, $kt_c = 0.89$, $kg = 0.01$, and $kt_m = 1.7$. The differences between the ideal Halbach motor and the block Halbach motor with windings are reflected in the $\hat{f}$ parameter and in the winding factor; the ideal Halbach motor with this geometry has $\hat{f} = 0.477$, while the block Halbach motor has $\hat{f} K_w = 0.410$. Figure 3-3 compares the dimensionless force estimated using Equation 3.26 for this particular motor to that obtained using 99 harmonics of the fields, over one-sixth of the stroke. As can be seen, the first-harmonic estimate represents the average force, and the higher harmonics appear as ripple. This configuration has a a small amount of ripple, but it can be almost eliminated by adjusting δ_y and δ_z at the expense of a reduction in average dimensionless force; specifically, the ripple drops to under 0.1% for $\delta_y = 0.347$ and $\delta_z = 0.653$.

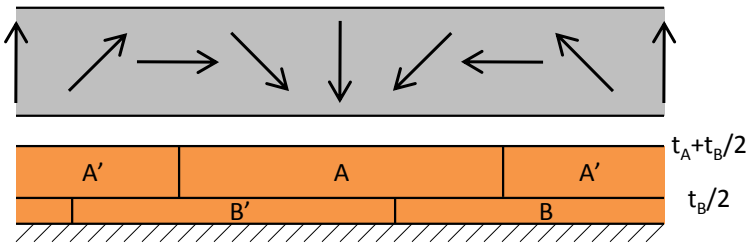

Figure 3-4: This layered winding arrangment allows each phase to be wound continuously within the coil, without external connecting leads. There are three phases labeled A, B, and C, and the primed windings have current flowing in the opposite direction from the unprimed windings. (Phase C lies on the opposite side of the center line, and is not shown here.) Layers A and C have thickness t_A, while layer B has a thickness of t_B.

Layered Coil Windings

The winding structure depicted in Figure 3-2 is only one possible structure; alternatively, the different phases could be arranged to each occupy a layer of the coil in the y-direction, as shown in Figure 3-4. This arrangement is much easier to manufacture [23], but will require a slightly different analysis to model. Significantly, note that the y-direction magnetic field varies as $\cosh(nky)$, so the different layers will not see equal magnetic fields, unlike the situation seen with concentrated windings. This means that, even using just the first harmonic of the field to calculate force, there must be ripple in either the force (if the layers have equal thicknesses) or the power (if the layer thicknesses are chosen to eliminate force ripple). For analytical convenience, we will choose the layer thicknesses for equal force production.

Let us consider a three-phase motor, with layer thicknesses t_A and t_B, and layer C equal in thickness to layer A. To enforce equal force production, the field integrated over each layer must be one-third of the field integrated over the total coil thickness. Thus, we can determine the thickness of the central layer, then find the outer layer thickness from the remainder of the total coil thickness. We have

$$\begin{aligned}\frac{1}{3}\int_{-t_c/2}^{t_c/2} \boldsymbol{B}\cdot\hat{\boldsymbol{y}}\,dy &= \int_{-t_B/2}^{t_B/2} \boldsymbol{B}\cdot\hat{\boldsymbol{y}}\,dy \\ &= 4B_{rem}a_{mn,1}\cos(kz)\int_0^{t_B/2}\cosh(ky) \\ &= \frac{4B_{rem}a_{mn,1}}{k}\cos(kz)\sinh\left(\frac{kt_B}{2}\right), \end{aligned} \tag{3.28a}$$

and comparing the integrals leads to the result

$$\frac{1}{3}\sinh\left(\frac{kt_c}{2}\right) = \sinh\left(\frac{kt_B}{2}\right);$$
$$kt_B = 2\sinh^{-1}\left(\frac{1}{3}\sinh\left(\frac{kt_c}{2}\right)\right). \tag{3.28b}$$

For our model geomtetry, with $kt_c = 0.89$, the resulting center layer thickness is $kt_B = 0.30$, and thus $kt_A = 0.29$. The difference is small here, but can be more substantial if the coil is thicker.

With the layer thicknesses thus chosen, we can calculate the force as though the current were uniform through the thickness, then divide by the number of phases. The current density harmonics are given by

$$J_{ni} = \frac{2J_i}{n\pi}\sin\left(\frac{n\pi\alpha}{2}\right), \tag{3.29}$$

with the notation as before, and the commutation pattern is identical. The dimensionless power is thus given by

$$\hat{P} = \alpha\left(kt_A\cos^2(kz_0) + kt_B\cos^2\left(kz_0 + \frac{2\pi}{3}\right) + kt_A\cos^2\left(kz_0 + \frac{4\pi}{3}\right)\right), \tag{3.30}$$

which has the expression given by Equation 3.21 as its average value over z_0. Finally, this implies an average winding factor

$$K_w = \frac{2}{\pi\alpha^{1/2}}\sin\left(\frac{\pi\alpha}{2}\right). \tag{3.31}$$

3.3.3 Block Halbach with Back-Iron

Halbach motors are relatively uncommon, due to challenges that can arise in their assembly and to their relatively high usage of historically expensive permanent magnets. (In smaller motors and under the economic conditions of the past decade, the cost of magnets has been far less significant.) More often, simple magnets directed in the $\hat{\boldsymbol{y}}$-direction are used, mounted on an iron sheet (referred to as back-iron) to complete the flux path. To maintain generality, we will consider a motor of the structure shown in Figure 3-5, with an iron layer supporting a Halbach array.

As was discussed in Section 3.2, iron is a highly nonlinear material, and approximations are required to model magnetic fields when it is present. The most common approximation is to assume that the iron simply has infinite permeability [43], and recognize that the $\boldsymbol{H}$-field must be entirely perpendicular to the boundary of infinite-permeability regions. However, we are left with the question of how thick the iron must be made to avoid deleterious saturation effects, especially in weight-sensitive and space-sensitive applications. Alternatively, we can include the iron as a layer of

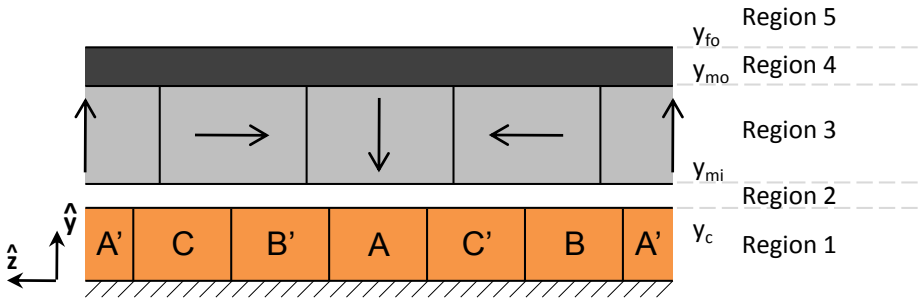

Figure 3-5: A schematic of a flat iron-backed block Halbach motor, with the coil in orange, iron in dark gray, and magnets in light gray. The motor is assumed to be symmetric, and the mid-plane is located at $y = 0$. The conductor extends to $y = y_c = t_c/2$, where t_c is the conductor thickness, and the magnets range from $y = y_{mi} = t_c/2 + g$ to $y = y_{mo} = t_c/2 + g + t_m$, where g is defined to be the air gap thickness and t_m is the magnet thickness. The iron extends from $y = y_{mo}$ to $y = y_{fo} = t_c/2 + g + t_m + t_f$, where t_f is the iron thickness. The magnet array has four blocks per period p, and the winding has three phases.

finite permeability in the motor, and approximate its permeability as constant. In this case, we will have to solve iteratively, finding the field in the iron, determining the appropriate permeability, and re-solving until convergence is achieved. In a more discretized sense, this is also the approach followed by finite element and boundary element methods. We will consider both approaches here; the latter approach appears not to have been reported in conjunction with Fourier analysis in the modern linear motor literature, despite lying at the heart of finite element approaches to magnetic field modeling [32].

Infinite Permeability

If we assume the iron to be infinitely permeable, we can solve for the field in just regions 1 to 3. The boundary conditions at $y = y_{mo}$ become

$$b_{cni,3} = a_{cni,3}\, \mathrm{e}^{2nky_{mo}}\,, \tag{3.32a}$$

$$b_{mn,3} = a_{mn,3}\, \mathrm{e}^{2nky_{mo}} + B_{rem}\hat{M}_{zn}\, \mathrm{e}^{nky_{mo}}\,, \tag{3.32b}$$

and the constants can be solved for in the usual manner. The results are as follows:

$$a_{mn,1} = \frac{1}{2}\left[\hat{M}_{yn}\frac{\sinh(nkt_m)}{\sinh(nky_{mo})} + \hat{M}_{zn}\frac{\cosh(nkt_m) - 1}{\sinh(nky_{mo})}\right] \qquad b_{mn,1} = a_{mn,1}$$

$$a_{cni,1} = -\frac{1}{2}\frac{\sinh(nkg + nkt_m)}{\sinh(nky_{mo})} \qquad b_{cni,1} = a_{cni,1}$$

$$a_{mn,2} = a_{mn,1} \qquad b_{mn,2} = a_{mn,1}$$

$$a_{cni,2} = a_{cni,3} \qquad\qquad b_{cni,2} = b_{cni,3}$$

$$a_{mn,3} = -\frac{1}{2}\left[\hat{M}_{yn}\,\mathrm{e}^{-nky_{mo}}\,\frac{\sinh\left(nky_{mi}\right)}{\sinh\left(nky_{mo}\right)} + \hat{M}_{zn}\frac{1-\mathrm{e}^{-nky_{mo}}\cosh\left(nky_{mi}\right)}{\sinh\left(nky_{mo}\right)}\right]$$

$$b_{mn,3} = -\frac{1}{2}\left[\hat{M}_{yn}\,\mathrm{e}^{nky_{mo}}\,\frac{\sinh\left(nky_{mi}\right)}{\sinh\left(nky_{mo}\right)} + \hat{M}_{zn}\frac{1-\mathrm{e}^{nky_{mo}}\cosh\left(nky_{mi}\right)}{\sinh\left(nky_{mo}\right)}\right]$$

$$a_{cni,3} = \frac{1}{2}\,\mathrm{e}^{-nky_{mo}}\,\frac{\sinh\left(\frac{nkt_c}{2}\right)}{\sinh\left(nky_{mo}\right)}$$

$$b_{cni,3} = \frac{1}{2}\,\mathrm{e}^{nky_{mo}}\,\frac{\sinh\left(\frac{nkt_c}{2}\right)}{\sinh\left(nky_{mo}\right)}. \tag{3.33}$$

The first-harmonic dimensionless force (with winding effects excluded) for this configuration is thus

$$\hat{f} = \sinh\left(\frac{kt_c}{2}\right)\left[\hat{M}_{y1}\frac{\sinh\left(kt_m\right)}{\sinh\left(ky_{mo}\right)} + \hat{M}_{z1}\frac{\cosh\left(kt_m\right)-1}{\sinh\left(ky_{mo}\right)}\right]. \tag{3.34}$$

This expression is a bit more complicated than that encountered in the ironless motors. The $\hat{\boldsymbol{z}}$-directed magnets are relatively ineffective when the magnets are thin, since it is actually easier for the flux produced to simply pass through the back-iron than to cross the air gap and interact with the coil.

Using the same geometric parameters as in Section 3.3.2, we find the dimensionless force to be $\hat{f} = 0.416$. If the axial magnets are omitted to make a "conventional" magnet array, we can calculate the force parameter by simply setting $\delta_z = 0$. If the Halbach array is replaced by just $\hat{\boldsymbol{y}}$-directed magnets, with $\delta_y = 1$, we find $\hat{f} = 0.348$.

Our work is not done, however—we need to determine the mass of the iron in the motor to calculate $\hat{m}$. This is a step not often taken in the linear motor literature; the closest thing appears to be the tactic employed by Wang et al. [100] of calculating the flux density in the iron adding a fictitious airgap based on the iron's B-H curve. We will instead employ a more direct method, based on an assumed value of saturation flux density B_{sat} in the iron; the iron thickness t_f will be set to limit the maximum flux density in the iron to B_{sat}. In doing so, we also assume that the B-field in the iron is uniform across the thickness. While less accurate than using the B-H curve, we can employ that data more directly in the finite-permeability analysis.

To determine the iron thickness, then, we must determine the total flux through the iron and divide by the saturation flux density. For simplicity, we will neglect the field produced by the current in the motor. From the periodicity of the motor, we can identify that the flux through the iron at $kz = 0$ must be zero. The maximum flux, then, would occur at $kz = \pi/2$. By continuity, the flux Φ is given by the following

integral:

$$\begin{aligned}\Phi(z) &= \int_0^z \boldsymbol{B}\left(z'\right)\cdot\hat{\boldsymbol{y}}dz' \\ &= B_{rem}\sum_{n=1}^{\infty}\left[\hat{M}_{yn}\frac{\sinh\left(nky_{mo}\right)-\sinh\left(nky_{mi}\right)}{nk\sinh\left(nky_{mo}\right)}+\right. \\ &\qquad\left.\hat{M}_{zn}\frac{\cosh\left(nky_{mo}\right)-\cosh\left(nky_{mi}\right)}{nk\sinh\left(nky_{mo}\right)}\right]\sin\left(nkz\right). \end{aligned} \tag{3.35}$$

Note the additional factor of $1/n$ in the sum—the flux integral converges rapidly, and it will be possible to use relatively few terms to calculate it. If we assume the iron layer is to have a uniform thickness, based on just reaching B_{sat} at the maximum flux point, then we can determine the dimensionless thickness kt_f as follows:

$$\begin{aligned}kt_f &= \frac{k\Phi\left(\pi/2k\right)}{B_{sat}} \\ &= \frac{B_{rem}}{B_{sat}}\sum_{n=1}^{\infty}\left[\hat{M}_{yn}\frac{\sinh\left(nky_{mo}\right)-\sinh\left(nky_{mi}\right)}{n\sinh\left(nky_{mo}\right)}+\right. \\ &\qquad\left.\hat{M}_{zn}\frac{\cosh\left(nky_{mo}\right)-\cosh\left(nky_{mi}\right)}{n\sinh\left(nky_{mo}\right)}\right]\left(-1\right)^{(n-1)/2}. \end{aligned} \tag{3.36}$$

Finally, the dimensionless mass $\hat{m}$ is given by

$$\hat{m} = kt_c + 2\frac{\rho_m}{\rho_c}\left(\delta_y+\delta_z\right)kt_m + 2\frac{\rho_f}{\rho_c}kt_f, \tag{3.37}$$

where ρ_f is the density of the iron.

We can now calculate the dimensionless motor constant for an iron-backed motor; assuming a value of $B_{sat} = 2\,\mathrm{T}$, we find that $\hat{\epsilon} = 0.262$, a much lower value than for the pure Halbach motor, which has $\hat{\epsilon} = 0.316$. If the iron were massless, we would have $\hat{\epsilon} = 0.320$, so the mass of the iron has a strong effect on the overall performance. Using only the first harmonic of the field in the iron thickness calculation very slightly overestimates the required mass, giving $\hat{\epsilon} = 0.261$; for rapid calculation purposes, the first harmonic alone should suffice.

Of course, the introduction of iron changes the optimal motor geometry, so the reduction in performance seen here is not necessarily representative of the best motors. In Section 3.7.1 we will calculate optimized geometries to allow for a fair comparison. This calculation method also relies heavily on the choice of the effective saturation flux density; next, we will explore a finite-permeability calculation that does away with the need to specify saturation flux, at the expense of computer time.

Finite Permeability

The field equations are readily solved if the iron is assumed to have a finite, linearized relative permeability μ, though we now must account for all five regions. In this case, the field coefficients do not have simple expressions, and are given in Appendix A.1. Unfortunately, these expressions suffer from loss of precision due to cancellation error, and are difficult to re-write to avoid the error. Nonetheless, they are easily calculated numerically for low harmonic orders.

We are left with the problem of determining the appropriate value of permeability to use with the model. We can find the maximum field in the iron B_{max}, which will often appear in the same location as in the infinite-permeability case. When a Halbach array lies directly against an iron surface, the peak field will instead appear at the corners of the magnets, but be far more localized. We account for this by checking the field at the outer surface of the iron, but the corner of the magnet, and at the inner surface of the iron, at $kz = \pi/2$, then using the higher of the two values of field.

The field magnitude is used to find a new linearized permeability from the B-H curve of the iron, and the process is then repeated until convergence is achieved. (Note that the correct permeability is not given by the derivative of the B-H curve, but rather by dividing B by $\mu_0 H$.) We re-used the MATLAB implementation of Brent's method [101] to perform the permeability iterations, with slight modifications. Convergence is rapid, typically taking fewer than ten iterations.

We will refrain from comparing this requation to the infinite permeability solution or to FEA here, and instead discuss the merits of the two methods when applied to the more analytically challenging tubular configurations.

3.3.4 Demagnetization

We can now also derive the constraint imposed by avoidance of magnet demagnetization. Permanent magnets may be damaged if they are exposed to $\boldsymbol{H}$ fields of magnitude greater than H_{ci}, the intrinsic coercivity of the magnet. Anisotropic magnets, like sintered NdFeB, are only harmed by the component of $\boldsymbol{H}$ fields directly opposed to their magnetization, while isotropic magnets can be damaged by any $\boldsymbol{H}$ field not directly aligned with their magnetization.

For simplicity, we consider the demagnetization constraint for the ideal Halbach motor, with isotropic magnets:

$$|\boldsymbol{H}| < H_{ci}. \tag{3.38}$$

Using Equations 3.10 and 3.12, we can find the magnitude of the $\boldsymbol{H}$-field:

$$\begin{aligned}
|\mu_0 \boldsymbol{H}|^2 &= \left[B_{rem} \left(a_{m,3}\, \mathrm{e}^{ky} + b_{m,3}\, \mathrm{e}^{-ky} \right) \cos(kz) - \frac{\mu_0 J}{k} b_{c,4}\, \mathrm{e}^{-ky} \sin(kz) \right]^2 + \\
&\quad \left[B_{rem} \left(a_{m,3}\, \mathrm{e}^{ky} - b_{m,3}\, \mathrm{e}^{-ky} - 1 \right) \sin(kz) + \frac{\mu_0 J}{k} b_{c,4}\, \mathrm{e}^{-ky} \cos(kz) \right]^2 \\
&= B_{rem}^2 \left[\left(a_{m,3}\, \mathrm{e}^{ky} + b_{m,3}\, \mathrm{e}^{-ky} \right) \cos(kz) - \hat{J} b_{c,4}\, \mathrm{e}^{-ky} \sin(kz) \right]^2 + \\
&\quad B_{rem}^2 \left[\left(a_{m,3}\, \mathrm{e}^{ky} - b_{m,3}\, \mathrm{e}^{-ky} - 1 \right) \sin(kz) + \hat{J} b_{c,4}\, \mathrm{e}^{-ky} \cos(kz) \right]^2, \qquad (3.39a) \\
\hat{J} &\equiv \frac{\mu_0 J}{k B_{rem}}, \qquad (3.39b)
\end{aligned}$$

where a dimensionless current density $\hat{J}$ has been defined. It would be possible to analytically find the maximum value of the demagnetizing field, but the result is a transcendental equation and it is expedient to just numerically evaluate the demagnetization constraint throughout the magnet region instead. For a given set of dimensionless geometry kt_c, kg, and kt_m, and material properties, the constraint in Equation 3.38 will dictate a maximum value for $\hat{J}$, $\hat{J}_{max}$, with $J = kB_{rem}\hat{J}_{max}/\mu_0 \propto p^{-1}$. This scaling is identical to that demanded by thermal conduction resistance.

For anisotropic magnets, the demagnetization constraint instead takes the following form:

$$-\frac{\boldsymbol{H} \cdot \boldsymbol{M}}{|\boldsymbol{M}|} < H_{ci}. \qquad (3.40)$$

This expression is more difficult to work with analytically, but is also easy to evaluate numerically; the scaling behavior is similar to that seen in the isotropic case. In block Halbach arrays, the strongest demagnetizing fields appear near the corners of the magnets, and the field needs to be calculated to high harmonic order to obtain accurate results. In small motors, the dependence on k and the orthogonality of the magnet-induced field and the current-induced field lead to $\hat{J}$ only having a weak effect on the demagnetizing field; instead, the demagnetizing field can be used to estimate the motor's temperature limit, as H_{ci} has a strong negative temperature dependence in rare-earth magnets.

Figure 3-6 illustrates the demagnetizing field in a block Halbach array with back-iron. The field obtained via direct summation of the Fourier series is shown on the left, and exhibits a major limitation of Fourier series approaches: the Gibbs phenomenon [102]. This causes the fields to be over-estimated at the edge of the magnets, precisely where we need to evaluate them for demagnetization! While this problem is not addressed in the motor literature (Gysen et al. [81] show some particularly egregious examples), there are a number of techniques available for smoothing Fourier series convergence.

Here, we have employed Lanczos' sigma-factors [102] to smooth convergence. Each term of the Fourier series is multiplied by a factor σ_n that depends on the total number

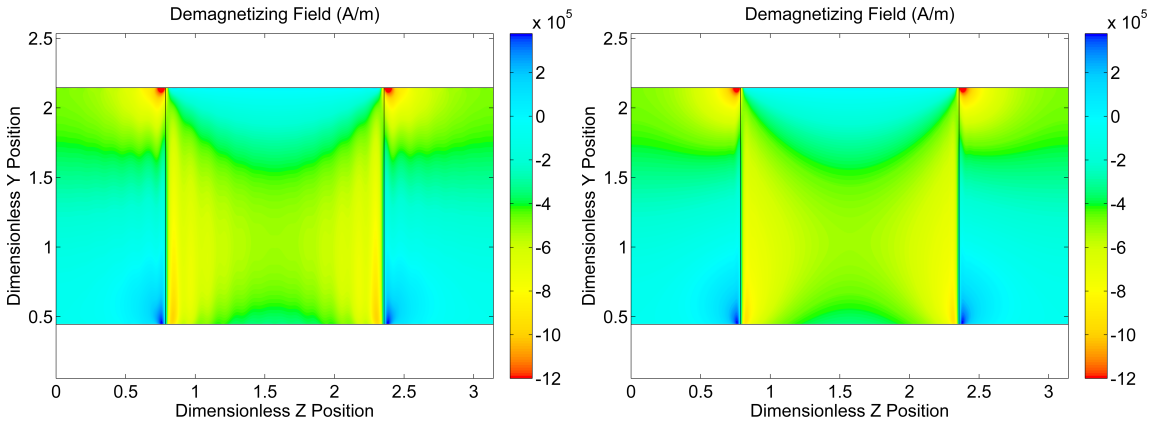

Figure 3-6: The demagnetizing field in a Halbach motor with back-iron but no current flow ($\delta_y = \delta_z = 1/2$, $kt_c = 0.89$, $kg = 0.01$, and $kt_m = 1.7$) field harmonics is shown in both images. The left and right of each plot contain vertical magnets, while the center contains a z-directed magnet. On the left, the field has been computed from direct summation of the Fourier series with 49 harmonics, and significant ringing is visible in the z magnet. On the right, the field has been computed using Lanczos' sigma factors and 99 harmonics, and the oscillations have been nearly eliminated.

of harmonics to be used N_h:

$$\sigma_n = \frac{N_h + 1}{n} \sin\left(\frac{n}{N_h + 1}\right). \tag{3.41}$$

The effect is to reduce the Gibbs phenomenon by an order of magnitude, but to also reduce the spatial resolution by about a factor of two. The reduction in peak demagnetizing field seen in Figure 3-6 when using the sigma factors stems from the loss of spatial resolution; doubling the number of harmonics restores the resolution and yields the same peak. The strongest demagnetizing field in this array is present in the corners of the vertical magnets, and is not significantly affected by the Gibbs phenomenon. However, the demagnetizing field in the axial magnets is afflicted with the Gibbs phenomenon, and at equivalent spatial resolution the use of Lanczos' sigma factors reduces the apparent demagnetizing field by 10%.

3.3.5 Flux-Concentrating Magnets and Slotted Stators

The Fourier series approach used for the preceding analyses has an important limitation: we cannot examine motors in which the iron permeability varies in the axial direction. This prevents us from directly studying coils in slotted iron structures or magnet arrays that use iron to concentrate their magnetic flux. While we did not develop any new techniques in this area, Gysen et al. [81] wrote an excellent discussion of one approach, that of using local Fourier series with different wavenumbers k to describe the areas in these periodic iron arrays, then patching the Fourier series together on the boundaries. This paper also reviews most of the techniques employed up to this point

in our discussion; in Cartesian two-dimensional motor analysis, our main contribution is the use of the sigma-approximation to evaluate the Fourier series, and the different saturation strategies in iron.

For some situations, conformal mapping can yield simple analytical results; for instance, F. W. Carter's seminal analysis of the slotted stator [89, 90] continues in use today. Most often, however, these structures are modeled using lumped-parameter magnetic circuits. In Section 4.3, we will use such a basic magnetic circuit analysis to examine a voice coil with a flux-concentrating magnet array.

3.3.6 End-Turns and Attraction Force

One major effect not accounted for in this analysis is that of the finite length and width of the motor. It has been demonstrated [23, 64] (and will be verified in Section 3.6) that the finite size effects on the actual fields within linear permanent magnet motors are very minor. More significant, however, can be the power lost in the portions of the windings needed to complete the coils, the "end-turns". Here we will consider a simple model for the end-turns in a motor with concentrated windings, to motivate the move to tubular motor configurations.

Neglecting the effects of turning the current flow around a corner, or of making space for the end-turns of other phases, the minimum volume required for the end turns on a single phase can be considered as a trapezoidal region connecting one region to the next. Assuming there are an even number of coil groups, the end-turns for each phase have an effective volume

$$V_{et} = \frac{p^2 t_c}{2N_\phi}. \tag{3.42}$$

The total conductor volume, then, becomes

$$V = \frac{L}{p} \cdot N_\phi V_{et} + WLt_c \tag{3.43}$$

$$= Lt_c \left(W + \frac{p}{2} \right), \tag{3.44}$$

where p is the pole pitch, and we can define an end-turn factor K_{et},

$$K_{et} = \left(1 + \frac{p}{2W} \right)^{-1/2}, \tag{3.45}$$

applied to the motor constant in the same manner as the winding factor K_w. To get 95% of the expected motor constant, we would require $W \geq 4.6p$. In practice, a wide variety of winding strategies are employed to further reduce the end-turn burden, and most linear motors are wide and flat to minimize the end-turn factor.

A final effect, with important implications for the mechanical construction of the motor, is the attractive force between the magnets on both sides of the coil. This can be calculated using the normal stress term σ_{yy} of the Maxwell stress tensor at $y = 0$

in the absence of applied current:

$$\begin{aligned}\sigma_{yy} &= \sum_{n \text{ odd}}^{\infty} \left[\frac{1}{\mu_0} \left(\boldsymbol{B} \cdot \hat{\boldsymbol{y}} \right)^2 - \frac{1}{2\mu_0} \boldsymbol{B} \cdot \boldsymbol{B} \right] \\ &= \frac{1}{\mu_0} \sum_{n \text{ odd}}^{\infty} a_{mn,1}^2 \cos^2 \left(nkz \right), \end{aligned} \tag{3.46}$$

$$\left\langle \sigma_{yy} \right\rangle = \frac{1}{2\mu_0} \sum_{n \text{ odd}}^{\infty} a_{mn,1}^2. \tag{3.47}$$

For the model ironless block Halbach motor geometry that has been studied throughout this section, the resulting attractive force amounts to 160 kPa. If the magnet array were 25 mm wide, and 100 mm long, supported along one edge, the total force would be 400 N, applying a bending moment of 5 N · m to the support. If the support were made of aluminum, and the mechanical air gap g, and thus the allowable deflection, were 20 μm, the support would have to be at least 4 mm thick; if the motor had a pitch length of 12 mm, the motor itself would only be about 8 mm thick! The support material needed to maintain the air gaps against magnetic attraction in a planar motor can thus amount to a large fraction of the mass of the electromagnetic components.

3.4 Tubular Ironless Motors

Planar linear motors lose performance due to end-turns, and must be built robustly to resist the attractive force between the magnets (in a double-sided motor) or between the magnets and slotted stator (in a single-sided motor). An appealing strategy to mitigate these effects is to wrap the magnetic structure into a cylindrical shape, with ring magnets and circular coils.

3.4.1 General Field Solution

The tubular topology comes at an analytical cost, however, as the field equations (Equations 3.4) must now be solved in cylindrical coordinates. The Poisson equation can still be solved by separation of variables for the magnetic vector potential:

$$\boldsymbol{A} = \sum_{n=1}^{\infty} \Big[A_{mn}(r) \sin \left(nkz \right) + A_{cn}(r) \cos \left(nkz + \phi_n \right) \Big] \hat{\boldsymbol{\theta}}, \tag{3.48}$$

$$\begin{aligned} \boldsymbol{B} = &- \left[nkA_{mn} \cos \left(nkz \right) - nkA_{cn} \sin \left(nkz + \phi_n \right) \right] \hat{\boldsymbol{r}} + \\ &\left[\left(\frac{A_{mn}}{r} + \frac{\partial A_{mn}}{\partial r} \right) \sin \left(nkz \right) + \left(\frac{A_{cn}}{r} + \frac{\partial A_{cn}}{\partial r} \right) \cos \left(nkz + \phi_n \right) \right] \hat{\boldsymbol{z}}. \end{aligned} \tag{3.49}$$

where ϕ_n is the phase offset of the n^{th} current harmonic from the relevant radial magnetization harmonic. The radial vector potential functions A_{mn} and A_{cn} are more difficult to calculate and work with, however. The homogeneous solutions (i.e. in air) are given by the well-known modified Bessel functions [97, 103]:

$$A_{\text{other}} = \frac{a}{nk}\,\mathrm{I}_1(nkr) + \frac{b}{nk}\,\mathrm{K}_1(nkr)\,, \tag{3.50}$$

where I_0 and I_1 refer to modified Bessel functions of the first kind and K_0 and K_1 refer to modified Bessel functions of the second kind. The particular solutions to Poisson's equation in cylindrical coordinates, however, are not given by any named functions in common use. Specifically, let us assume the following forms for the current density and magnetization, for arbitrary current and block magnets:

$$\boldsymbol{J} = \sum_{n=1}^{\infty} \left[J_n \cos\left(nkz + \phi_n\right)\right] \hat{\boldsymbol{\theta}}, \tag{3.51a}$$

$$\boldsymbol{M} = \frac{B_{rem}}{\mu_0} \sum_{n=1}^{\infty} \left[\hat{M}_{rn} \cos\left(nkz\right) \hat{\boldsymbol{r}} + \hat{M}_{zn} \sin\left(nkz\right) \hat{\boldsymbol{z}}\right], \tag{3.51b}$$

$$\hat{M}_{rn} = \frac{2}{n\pi} \sin\left(\frac{n\pi\delta}{2}\right)\left(\left(-1\right)^{n+1} + 1\right), \tag{3.51c}$$

$$\hat{M}_{zn} = \frac{2}{n\pi} \sin\left(\frac{n\pi\delta_z}{2}\right)\left(\left(-1\right)^{n+1} + 1\right), \tag{3.51d}$$

where J_n is the amplitude of the n^{th} current harmonic, $\hat{M}_{rn}$ is the dimensionless radial magnetization, and δ is the fractional width of the radial magnets, defined in the same manner as in the planar motor. (Note that the magnetization only has odd harmonics.) To determine the vector potential, we will need the curl of the magnetization:

$$\nabla \times \boldsymbol{M} = -\frac{B_{rem}}{\mu_0} \sum_{n=1}^{\infty} nk\hat{M}_{rn} \sin\left(nkz\right) \hat{\boldsymbol{\theta}}. \tag{3.52}$$

Separation of variables applied to Poisson's equation then yields inhomogeneous differential equations of the following form:

$$\frac{\partial^2 A_p}{\partial r} + \frac{1}{r}\frac{\partial A_p}{\partial r} - \left(c^2 + \frac{1}{r^2}\right) A\left(r\right) = d, \tag{3.53}$$

where A_p is a function of the radial coordinate only and c and d are constants. Specifically, $c = nk$, and d is the $\hat{\boldsymbol{\theta}}$-component of the right-hand side of Poisson's equation.

Equation 3.53 is not a "standard" differential equation, despite being simply the inhomogeneous form of the Bessel differential equation, and most literature discussions of its solution either give a solution in terms of convolution integrals [51, 83, 97] or use an approximation to the radial magnetization that yields a more tractable

equation [52, 82]. We instead seek a solution that would be both exact and easy to calculate numerically.

We initially used the Frobenius method [104] to solve for A_p, yielding as a particular solution

$$A_p(r) = 2dr^2 \sum_{m=0}^{\infty} \frac{(2cr)^{2m}\, m!\,(m+1)!}{(2m+1)!\,(2m+3)!} + c_1 r \sum_{m=0}^{\infty} \frac{(2cr)^{2m}}{2^{2m} m!\,(m+1)!}, \tag{3.54}$$

where c_1 is an arbitrary constant, and which converges for all positive, real values of r. A bit of inspection identified the second series as simply the Taylor series for the modified Bessel function of the first kind $\mathrm{I}_1(cr)$, but the first series was considerably more obscure. The Bessel function is also part of the homogeneous solution, and could therefore be discarded from the particular solution, but we ultimately found it to be very useful in achieving a numerically stable computation.

While we initially used this particular solution to derive field solutions, the Taylor series expansion is difficult to use for large values of nkr. After further research, via the identification of Equation 3.53 as a form of the Lommel differential equation [105] and investigation of related functions, we identified the first series as belonging to the modified Struve function [103,106]. The Struve functions have surprisingly little history in electromagnetics, but have seen more uses in optics [107, 108] and acoustics [109]. The modified Struve function was originally developed to describe integrals of modified Bessel functions [110], and has seen little use in the solution of partial differential equations. (After this work commenced, a handful of papers were published using the modified Struve function in low-frequency electromagnetics, namely work by Wijono et al. [53, 84] and Yan et al. [50].) More importantly, there exist efficient numerical techniques for the calculation of the modified Struve function, as described by Zhang and Jin [111, 112] and by MacLeod [113, 114].

In terms of the modified Struve function of order ν, $\mathrm{L}_\nu(x)$, the particular solution is given by

$$A_p(r) = \frac{\pi d}{2c^2}\,\mathrm{L}_1(cr) + c_1\,\mathrm{I}_1(cr)\,. \tag{3.55}$$

While it is common to set $c_1 = 0$, examination of the magnetic field equations will suggest an improved approach. Consider, for instance, the radial component of the field in the coil, neglecting any contribution from magnets. This is given by

$$\boldsymbol{B}\cdot\hat{\boldsymbol{r}} = \sum_{n=1}^{\infty} \frac{\mu_0 J_n}{nk}\Bigg(-a_{cn}\,\mathrm{I}_1(nkr) - b_{cn}\,\mathrm{K}_1(nkr) + \\ + \frac{\pi}{2}\,\mathrm{L}_1(nkr) - \frac{n^2k^2}{\mu_o J_n} c_1\,\mathrm{I}_1(nkr)\Bigg)\sin\left(nkz+\phi_n\right). \tag{3.56}$$

Here, we have not yet modified the arbitrary field constant c_1 to make it dimensionless. The modified Struve function and the modified Bessel function of the first kind both grow asymptotically at the same rate [103], and we might anticipate a problem subtracting them for large values of nkr. In fact, their difference approaches the

constant value of $2/\pi$, even as the individual functions grow exponentially! This suggests that, if we choose the correct value for c_1, the problem can be eliminated:

$$c_1 \equiv -\frac{\pi d}{2c^2}, \tag{3.57}$$

$$A_p(r) = -\frac{\pi d}{2c^2}\left(\mathrm{I}_1(cr) - \mathrm{L}_1(cr)\right). \tag{3.58}$$

For large values of r, $A_p(r)$ will now approach d/c^2, the same as the particular solution encountered in the planar case (Equation 3.23), and no loss of precision during calculations will be incurred. To give a specific example, explicitly calculating the difference between functions begins to give a different result from the asymptotic expansion of the difference [112] near $nkr \approx 20$; by $nkr \approx 30$, it differs by 0.0072%, and by $nkr \approx 40$, the explicit difference is zero using double-precision arithmetic.

Thus, we will formulate the field solutions in terms of auxillary functions

$$\Lambda_\nu(x) \equiv \frac{\pi}{2}\Big(\mathrm{I}_\nu(x) - \mathrm{L}_\nu(x)\Big), \tag{3.59}$$

which possess efficient series representations for all real values of the argument x. The fields can thus be found as follows:

$$\begin{aligned}\boldsymbol{B}_{\text{magnet}} = \sum_{n=1}^{\infty}\Bigg[& B_{rem}\Big(\ \ a_{mn}\,\mathrm{I}_1(nkr) + b_{mn}\,\mathrm{K}_1(nkr) + \hat{M}_{rn}\,\Lambda_1(nkr)\Big)\,\hat{\boldsymbol{r}}\cos(nkz) + \\ & \frac{\mu_0 J_n}{nk}\Big(-a_{cn}\,\mathrm{I}_1(nkr) - b_{cn}\,\mathrm{K}_1(nkr)\Big)\,\hat{\boldsymbol{r}}\sin(nkz+\phi_n) + \\ & B_{rem}\Big(-a_{mn}\,\mathrm{I}_0(nkr) + b_{mn}\,\mathrm{K}_0(nkr) - \hat{M}_{rn}\,\Lambda_0(nkr)\Big)\,\hat{\boldsymbol{z}}\sin(nkz) + \\ & \frac{\mu_0 J_n}{nk}\Big(-a_{cn}\,\mathrm{I}_0(nkr) + b_{cn}\,\mathrm{K}_0(nkr)\Big)\,\hat{\boldsymbol{z}}\cos(nkz+\phi_n)\Bigg],\end{aligned} \tag{3.60a}$$

$$\begin{aligned}\boldsymbol{B}_{\text{coil}} = \sum_{n=1}^{\infty}\Bigg[& B_{rem}\Big(\ \ a_{mn}\,\mathrm{I}_1(nkr) + b_{mn}\,\mathrm{K}_1(nkr)\Big)\,\hat{\boldsymbol{r}}\cos(nkz) + \\ & \frac{\mu_0 J_n}{nk}\Big(-a_{cn}\,\mathrm{I}_1(nkr) - b_{cn}\,\mathrm{K}_1(nkr) - \Lambda_1(nkr)\Big)\,\hat{\boldsymbol{r}}\sin(nkz+\phi_n) + \\ & B_{rem}\Big(-a_{mn}\,\mathrm{I}_0(nkr) + b_{mn}\,\mathrm{K}_0(nkr)\Big)\,\hat{\boldsymbol{z}}\sin(nkz) + \\ & \frac{\mu_0 J_n}{nk}\Big(-a_{cn}\,\mathrm{I}_0(nkr) + b_{cn}\,\mathrm{K}_0(nkr) - \Lambda_0(nkr)\Big)\,\hat{\boldsymbol{z}}\cos(nkz+\phi_n)\Bigg],\end{aligned} \tag{3.60b}$$

$$\boldsymbol{B}_{\text{air, iron}} = \sum_{n=1}^{\infty} \Big[B_{rem} \Big(\quad a_{mn}\, \mathrm{I}_1(nkr) + b_{mn}\, \mathrm{K}_1(nkr) \Big) \hat{\boldsymbol{r}} \cos(nkz) + \frac{\mu_0 J_n}{nk} \Big(-a_{cn}\, \mathrm{I}_1(nkr) - b_{cn}\, \mathrm{K}_1(nkr) \Big) \hat{\boldsymbol{r}} \sin(nkz + \phi_n) + B_{rem} \Big(-a_{mn}\, \mathrm{I}_0(nkr) + b_{mn}\, \mathrm{K}_0(nkr) \Big) \hat{\boldsymbol{z}} \sin(nkz) + \frac{\mu_0 J_n}{nk} \Big(-a_{cn}\, \mathrm{I}_0(nkr) + b_{cn}\, \mathrm{K}_0(nkr) \Big) \hat{\boldsymbol{z}} \cos(nkz + \phi_n) \Big]. \tag{3.60c}$$

Here, a_{cn}, a_{mn}, b_{cn}, and b_{mn} are the dimensionless field constants, and depend on the harmonic order. (The form of the field is the same in air and iron regions, so long as the permeability has been linearized.) These solutions must then patched together using appropriate boundary conditions for the magnetic field and the magnetizing field to find values for the constants in each region, just as in the planar motor. The solution process is greatly aided by an identity for the modified Bessel functions[2]:

$$\mathrm{I}_0(x)\, \mathrm{K}_1(x) + \mathrm{I}_1(x)\, \mathrm{K}_0(x) = x^{-1}, \tag{3.61}$$

where x is the arbitrary argument of the functions. This identity allows the boundary conditions for the radial and axial fields to be used together.

To calculate the force produced by the motor, we can once again compute the Maxwell stress tensor at the inner and outer surfaces of the coil region, and find their spatial averages. However, we no longer have a symmetry plane in the center of the coil, so we must multiply the shear stress at the inner and outer coil surfaces by the appropriate circumferences and add the results to find the force per unit length generated by the motor. As before, we can approximate the force production as being done by only the first spatial harmonics of the current and magnetic field distributions [46], greatly simplifying the calculation process.

3.4.2 Field Solution for Ironless Motors

The general configuration of an ironless tubular motor is shown in Figure 3-7. The symmetry of the planar case has been removed by the change to tubular geometry, so there are more regions of analysis and more geometric parameters to contend with. To keep the field finite everywhere in space, we will require $b_{mn,1} = b_{cn,1} = 0$ and $a_{mn,7} = a_{cn,7} = 0$. Thanks to the linearity of the materials, we can recognize that there will only be three distinct sets of coil field parameters and five distinct sets of magnet field parameters. The magnet arrays are described by four sets of harmonic parameters, $\hat{M}_{rni}$ and $\hat{M}_{zni}$ for the inner magnet array and $\hat{M}_{rno}$ and $\hat{M}_{zno}$ for the outer magnet array. Simpler configurations, with some of the magnets removed, can be readily modeled by simply zeroing out the relevant magnetization parameters.

[2]This identity is not applied by one of the major research groups publishing on tubular linear motors, e.g. [49].

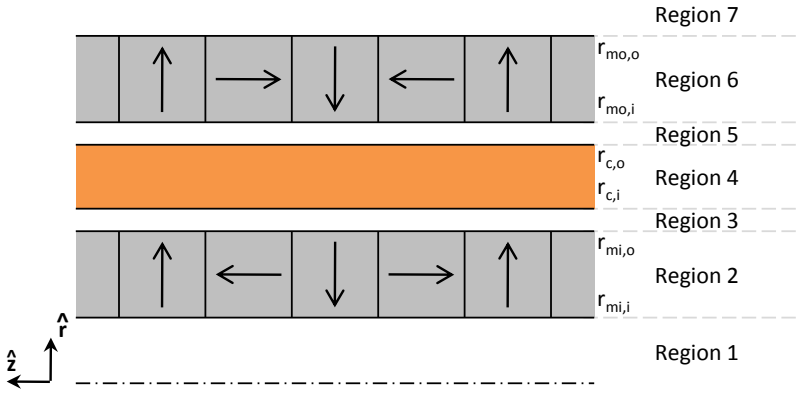

Figure 3-7: A schematic of a tubular, double-sided block Halbach motor. The inner magnet array extends from $r_{mi,i}$ to $r_{mi,o}$, the coil extends from $r_{c,i}$ to $r_{c,o}$, and the outer magnet array extends from $r_{mi,i}$ to $r_{mi,o}$. The magnet array has four blocks per period p, with relative radial magnet widths δ_{ri} and δ_{ro} and relative axial magnet widths δ_{zi} and δ_{zo} in the inner and outer arrays, respectively.

After a great deal of algebraic manipulation, we can solve for all of the field parameters. To simplify the solutions, we introduce the following additional auxillary functions:

$$\mathcal{L}_{\mathrm{I}}(x) \equiv x\left(\Lambda_1(x)\,\mathrm{I}_0(x) - \Lambda_0(x)\,\mathrm{I}_1(x)\right), \tag{3.62}$$

$$\mathcal{L}_{\mathrm{K}}(x) \equiv x\left(\Lambda_1(x)\,\mathrm{K}_0(x) + \Lambda_0(x)\,\mathrm{K}_1(x)\right), \tag{3.63}$$

which appear repeatedly and are closely related to the integrals of the modified Bessel functions [103]. These functions are numerically stable, and no additional tricks are required to calculate them beyond those needed for the modified Struve functions. The dimensionless coil parameters are given as follows:

$$\begin{aligned}
a_{cn,1} &= a_{cn,3} & b_{cn,1} &= 0 \\
a_{cn,2} &= a_{cn,3} & b_{cn,2} &= 0 \\
a_{cn,3} &= \mathcal{L}_{\mathrm{K}}\left(nkr_{c,i}\right) - \mathcal{L}_{\mathrm{K}}\left(nkr_{c,o}\right) & b_{cn,3} &= 0 \\
a_{cn,4} &= -\mathcal{L}_{\mathrm{K}}\left(nkr_{c,o}\right) & b_{cn,4} &= -\mathcal{L}_{\mathrm{I}}\left(nkr_{c,i}\right) \\
a_{cn,5} &= 0 & b_{cn,5} &= \mathcal{L}_{\mathrm{I}}\left(nkr_{c,o}\right) - \mathcal{L}_{\mathrm{I}}\left(nkr_{c,i}\right) \\
a_{cn,6} &= 0 & b_{cn,6} &= b_{cn,5} \\
a_{cn,7} &= 0 & b_{cn,7} &= b_{cn,5}.
\end{aligned} \tag{3.64}$$

The dimensionless magnet parameters are slightly more complex, due to the four unique magnetization harmonic parameters:

$$\begin{aligned}
a_{mn,1} = a_{mn,5} + \hat{M}_{rni}&\left(\mathcal{L}_{\mathrm{K}}\left(nkr_{mi,i}\right) - \mathcal{L}_{\mathrm{K}}\left(nkr_{mi,o}\right)\right) + \\
&\hat{M}_{zni}\left(nkr_{mi,i}\,\mathrm{K}_1\left(nkr_{mi,i}\right) - nkr_{mi,o}\,\mathrm{K}_1\left(nkr_{mi,o}\right)\right)
\end{aligned}$$

$$
\begin{aligned}
b_{mn,1} &= 0 \\
a_{mn,2} &= a_{mn,5} - \hat{M}_{rni}\,\mathcal{L}_{\mathrm{K}}\big(nkr_{mi,o}\big) - \hat{M}_{zni} nkr_{mi,o}\,\mathrm{K}_1\big(nkr_{mi,o}\big) \\
b_{mn,2} &= \hat{M}_{rni}\,\mathcal{L}_{\mathrm{I}}(nkr_{mii}) + \hat{M}_{zni} nkr_{mi,i}\,\mathrm{I}_1\big(nkr_{mi,i}\big) \\
a_{mn,3} &= a_{mn,5} \\
b_{mn,3} &= \hat{M}_{rni}\left(\mathcal{L}_{\mathrm{I}}\big(nkr_{mi,i}\big) - \mathcal{L}_{\mathrm{I}}\big(nkr_{mi,o}\big)\right) + \\
&\qquad \hat{M}_{zni}\left(nkr_{mi,i}\,\mathrm{I}_1\big(nkr_{mi,i}\big) - nkr_{mi,o}\,\mathrm{I}_1\big(nkr_{mi,o}\big)\right) \\
a_{mn,4} &= a_{mn,5} \\
b_{mn,4} &= b_{mn,3} \\
a_{mn,5} &= \hat{M}_{rno}\left(\mathcal{L}_{\mathrm{K}}\big(nkr_{mo,i}\big) - \mathcal{L}_{\mathrm{K}}\big(nkr_{mo,o}\big)\right) + \\
&\qquad \hat{M}_{zno}\left(nkr_{mo,i}\,\mathrm{K}_1\big(nkr_{mo,i}\big) - nkr_{mo,o}\,\mathrm{K}_1\big(nkr_{mo,o}\big)\right) \\
b_{mn,5} &= b_{mn,3} \\
a_{mn,6} &= -\hat{M}_{rno}\,\mathcal{L}_{\mathrm{K}}\big(nkr_{mo,o}\big) - \hat{M}_{zno} nkr_{mo,o}\,\mathrm{K}_1\big(nkr_{mo,o}\big) \\
b_{mn,6} &= b_{mn,3} + \hat{M}_{rno}\,\mathcal{L}_{\mathrm{I}}\big(nkr_{mo,i}\big) + \hat{M}_{zno} nkr_{mo,i}\,\mathrm{I}_1\big(nkr_{mo,i}\big) \\
a_{mn,7} &= 0 \\
b_{mn,7} &= b_{mn,3} + \hat{M}_{rno}\left(\mathcal{L}_{\mathrm{I}}\big(nkr_{mo,i}\big) - \mathcal{L}_{\mathrm{I}}\big(nkr_{mo,o}\big)\right) + \\
&\qquad \hat{M}_{zno}\left(nkr_{mo,i}\,\mathrm{I}_1\big(nkr_{mo,i}\big) - nkr_{mo,o}\,\mathrm{I}_1\big(nkr_{mo,o}\big)\right).
\end{aligned}
\tag{3.65}
$$

Note that the inner and outer magnets are effectively independent, as expected.

With the field fully determined, we can compute the Maxwell stress tensor and determine the force. After performing the algebra, we find

$$F = \frac{B_{rem} J_1 L}{k^2}\hat{f}, \tag{3.66a}$$

$$\hat{f} \equiv \pi\left(a_{c1,3} b_{m1,5} + a_{m1,3} b_{c1,5}\right), \tag{3.66b}$$

where L is the overall length of the motor, J_1 is the first harmonic of the current density, and we have used only the first harmonic of the field. The remaining dimensionless parameters are given by Equations 2.28b and 2.29b, and the winding factor K_w is unchanged by the move to a tubular configuration. Thus, we now have everything necessary to calculate the dimensionless motor constant $\hat{\epsilon}$ for tubular ironless motors.

3.4.3 Finite Element Validation

In order to check the accuracy of our analytical solution for the motor magnetic fields, we performed finite element analysis (FEA) using ANSYS, with a magnet remanence of 1.47 T and magnet relative permeability of $\mu = 1.05$. We considered two different geometries: a motor with only inner magnets, with $kr_{mi,i} = 0.86$, $kr_{mi,o} = 3.0$, $kr_{c,i} = 3.03$, $kr_{c,o} = 3.87$, $\delta_{ri} = 0.41$, and $\delta_{zi} = 0.59$; and a full double-sided motor,

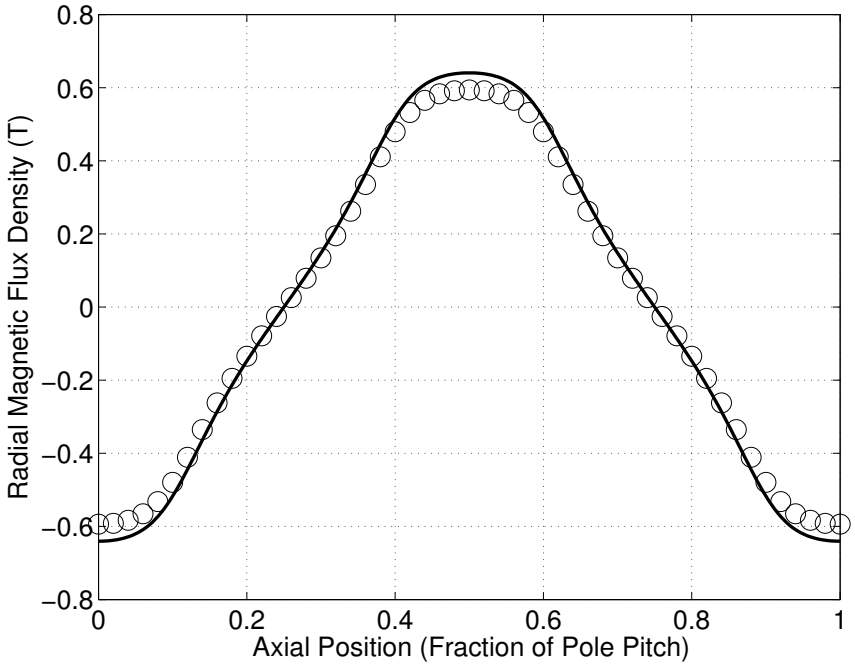

Figure 3-8: A comparison of the radial magnetic flux density in the center of the coil of the single-sided tubular motor depicted in Figure 3-9 between the 149-harmonic analytical model (solid line) and the FEA model (open circles) The maximum deviation occurs near the peak of the flux waveform, where the analytical solution is approximately 8% greater in magnitude than the FEA result.

with $kr_{mi,i} = 0$, $kr_{mi,o} = 2.5$, $kr_{c,i} = 2.52$, $kr_{c,o} = 2.77$, $kr_{mo,i} = 2.8$, $kr_{mo,o} = 3.79$, $\delta_{ri} = 0.365$, $\delta_{zi} = 0.635$, $\delta_{ro} = 0.545$, and $\delta_{zo} = 0.455$. Both motors were analyzed with no current applied, and were specified with a pitch length of $p = 10\,\text{mm}$.

Contour plots of the radial magnetic flux density in the single-sided motor are shown in Figure 3-9, for both the analytical model of Equations 3.60 using Lanczos' sigma-factors and the FEA model. These plots show good qualitative agreement, primarily differing due to the lower spatial resolution of the analytical model. More quantitatively, Figure 3-8 shows a comparison of the radial flux density in the middle of the air gap between the analytical and FEA models, with approximately 8% discrepancy. This difference can be explained primarily by the non-unity relative permeability of the magnets in the FEA model.

The double-sided motor is similarly characterized in Figures 3-10 and 3-11. In this case, the analytical model actually matches the finite element result more closely than for the single-sided motor; we suspect this is due to the more enclosed flux path, and corresponding reduction of the influence of magnet permeability. The air-gap flux density agrees to within 2%, with the discrepancy appearing at the peaks of the waveform. We also computed the force for this motor geometry using a square wave of current (akin to having $N_\phi = 2$); the analytical model and FEA agreed within 3%.

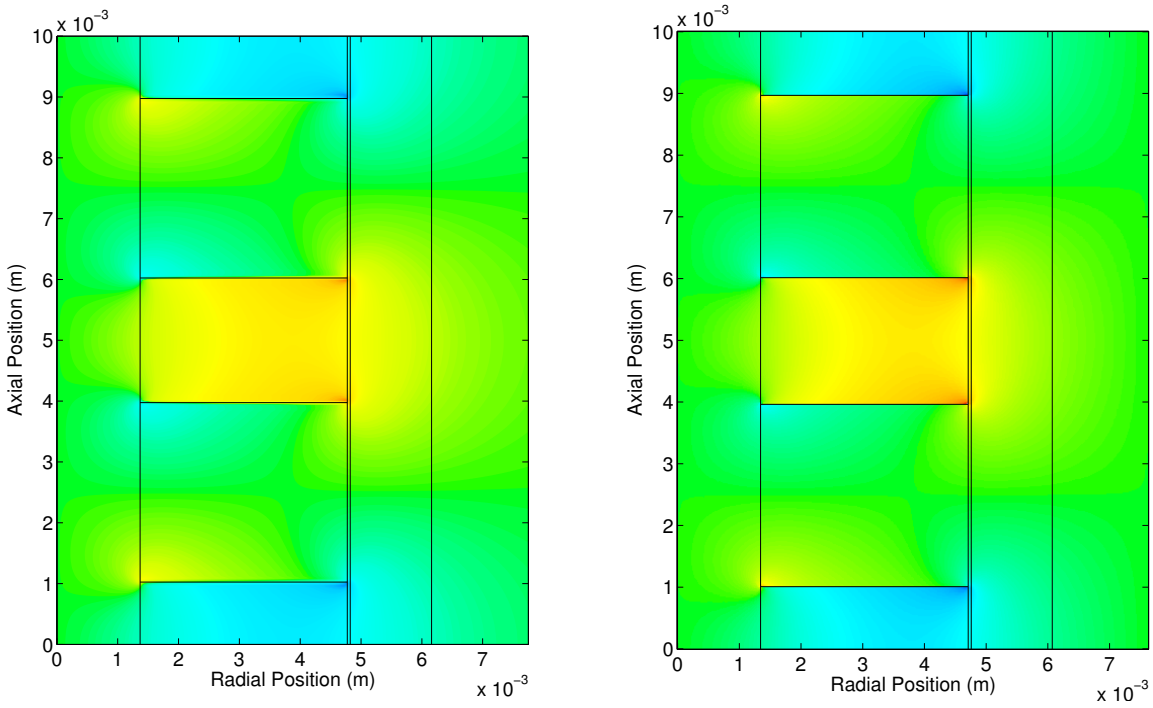

Figure 3-9: A plot of the radial magnetic flux density for a single-sided ironless tubular motor ($kr_{mi,i} = 0.86$, $kr_{mi,o} = 3.0$, $kr_{c,i} = 3.03$, $kr_{c,o} = 3.87$, $\delta_{ri} = 0.41$, and $\delta_{zi} = 0.59$) as computed using ANSYS finite element software (right) and using the analytical model of Equations 3.60 with 149 harmonics (left). Qualitative agreement between the analytical and numerical flux plots is excellent, primarily differing in the sharpness of the boundaries between radial and axial magnets.

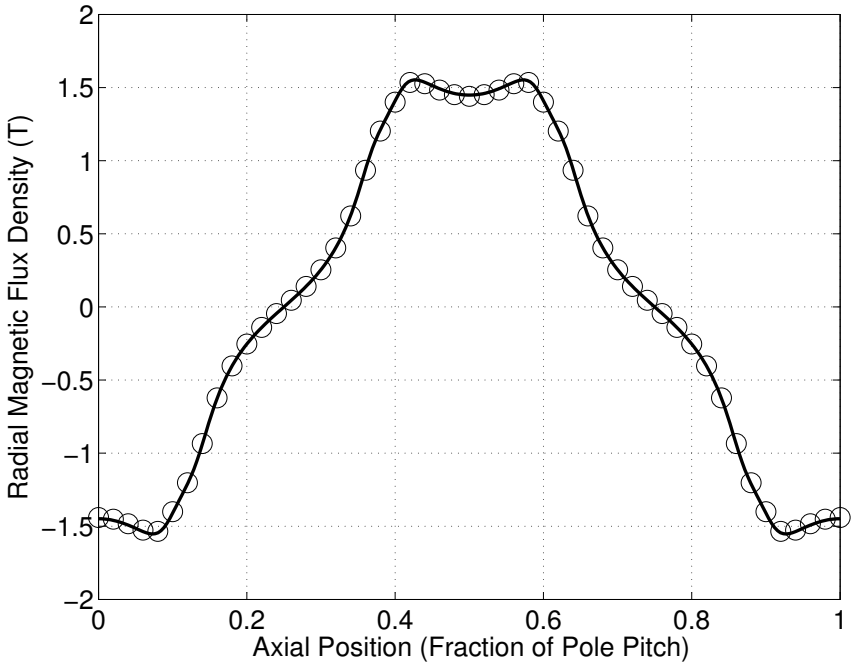

Figure 3-10: A comparison of the radial magnetic flux density in the center of the air gap of the double-sided ironless tubular motor depicted in Figures 3-7 and 3-11 between the 149-harmonic analytical model (solid line) and the FEA model (open circles) The maximum deviation occurs near the corners of the flux waveform, where the analytical solution is approximately 2% greater in magnitude than the FEA result.

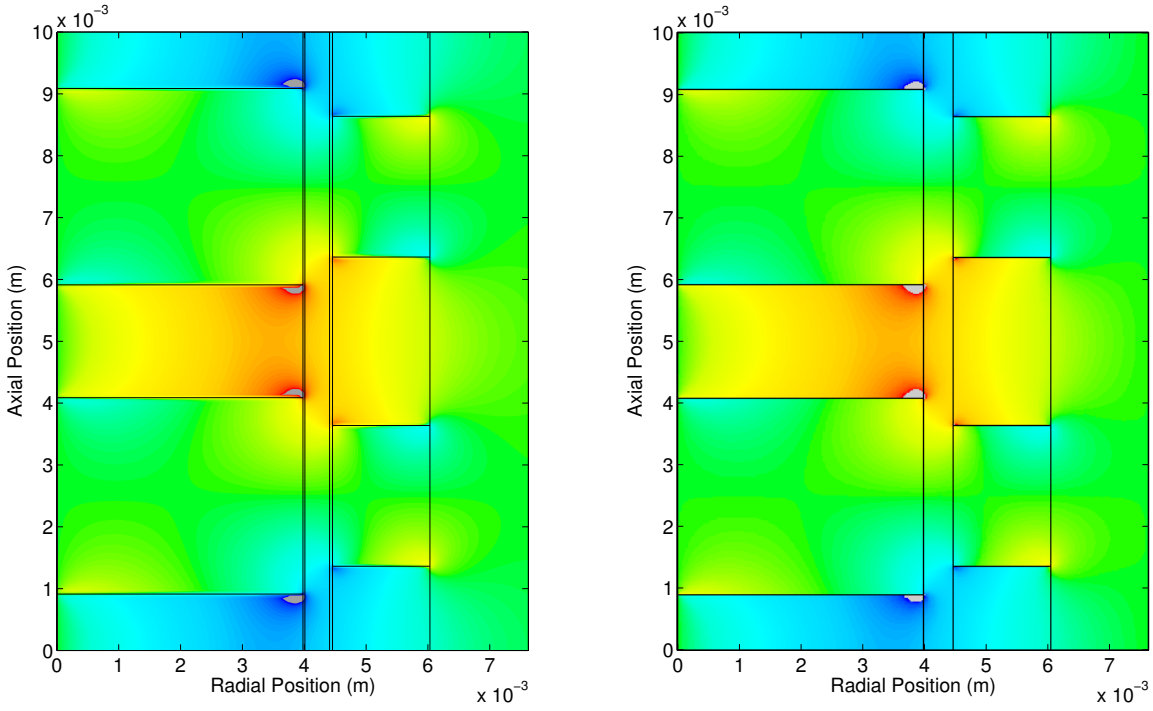

Figure 3-11: A plot of the radial magnetic flux density for a double-sided ironless tubular motor ($kr_{mi,i} = 0$, $kr_{mi,o} = 2.5$, $kr_{c,i} = 2.52$, $kr_{c,o} = 2.77$, $kr_{mo,i} = 2.8$, $kr_{mo,o} = 3.79$, $\delta_{ri} = 0.365$, $\delta_{zi} = 0.635$, $\delta_{ro} = 0.545$, and $\delta_{zo} = 0.455$) as computed using ANSYS finite element software (right) and using the analytical model of Equations 3.60 with 149 harmonics (left). Regions of flux density greater than 2 T have been removed from the plots, and are shown in gray. Qualitative agreement between the analytical and numerical flux plots is excellent, primarily differing in the sharpness of the boundaries between radial and axial magnets.

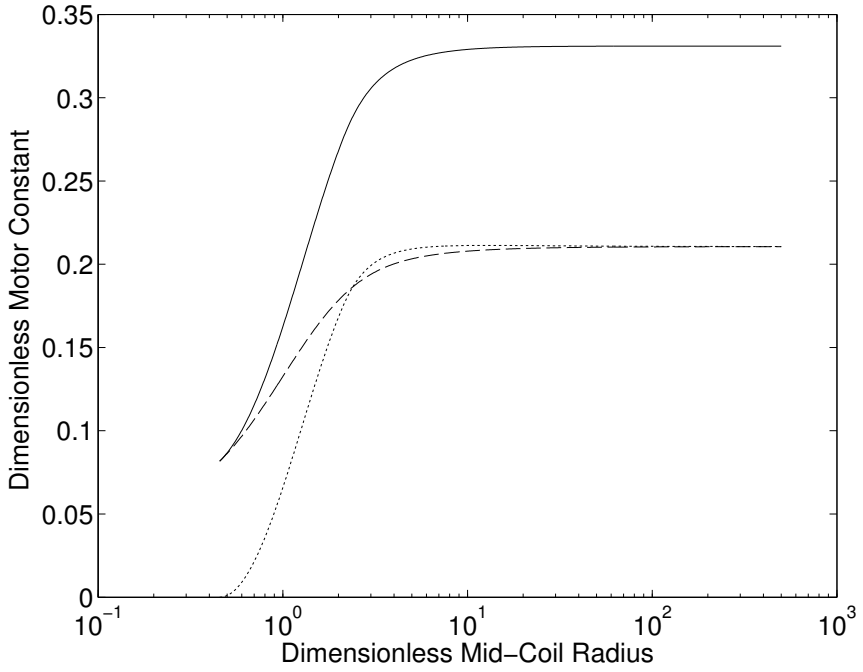

Figure 3-12: The motor constant is plotted for a motor with $kt_c = 0.87$, $kg = 0.01$, $kt_m = 1.7$, and $\delta_y = \delta_z = 0.5$ that has been formed into a tube, as a function of the dimensionless mean coil radius kr_m. For mean coil radii that would require a negative radius for the inside of the inner magnets, that radius is instead set to zero. A double-sided motor is indicated by the solid line, a motor with only inner magnets is indicated by the dotted line, and a motor with only outer magnets is shown with a dashed line. The performance of the double-sided motor remains within 1% of the planar performance for dimensionless radii above approximately 8; a motor with only inner magnets sees maximum performance at a dimensionless radius of 12.7, though this is only 0.3% better than the planar performance.

3.4.4 Performance and Radial Scaling

While we will derive optimized geometries for ironless tubular motors in Section 3.7.1, we can still examine their performance, and the influence of the radial scale, based on the geometry of the model planar motor. Figure 3-12 shows the dimensionless motor constants of tubular motors over several orders of magnitude of radial scaling.[3] The plot was generated by taking the geometry of our model planar motor ($kt_c = 0.87$, $kg = 0.01$, $kt_m = 1.7$, and $\delta_y = \delta_z = 0.5$) and forming it into a tubular shape, with mean coil radius $r_m = 0.5r_{c,i} + 0.5r_{c,o}$.

The performance of the double-sided motor remains very close to the planar performance, only dropping by 1% at $kr_m = 7.8$, and 5% at $kr_m = 3.6$. Compared to the end-turn loss in a planar motor, this corresponds to a width of $W = 3.6p$, so we are able to use a "narrower" motor to achieve the same performance. As the loss of field to edge-effects was not considered in that calculation, the benefits are even more

[3]Note that this plot is impossible to construct using the models extant in the literature!

pronounced than this suggests. Furthermore, this geometry may not be the optimal geometry at each value of the effective radius, and as we will see optimization can move these performance thresholds to even tighter radii.

3.4.5 Radial Magnets

In practice, it is very difficult to fabricate high-performance radially-oriented rare earth magnets. If the magnets are radially thick, fabrication becomes completely impossible. Instead, radially-oriented magnet rings are produced by assembling a number of ring segments, with each segment uniformly magnetized. These arrays are no longer axisymmetric, and any circumferential magnetization does not contribute to force production.

While the prospect of three-dimensional solution of the Poisson equation may seem intimidating, the circumferential solutions are simple sinusoids [97]. Curiously, there do not appear to be any analytical treatments of segmented, uniformly-magnetized ring magnets prior to that by Meessen et al. in 2011 [115], contemporaneous with our own work. The effect of segmentation is quite simple—the segmented ring can be treated as a uniform, radially-magnetized ring with magnetization equal to the average magnetization of the segmented array in the radial direction; the higher harmonics in the circumferential direction cannot contribute to force production in the motor. Mathematically speaking, we have

$$\hat{M}'_{rn} = \hat{M}_{rn} \frac{N_{seg}}{\pi} \sin \frac{\pi}{N_{seg}}, \tag{3.67}$$

where N_{seg} is the number of (equal) segments in the ring and the primed version of the magnetization includes the segmentation effect. A four-segment ring achieves about 90% of the strength of an ideal radially-magnetized ring, and six segments bring the performance to 95%. In Halbach arrays, the loss of performance is less severe, as segmentation does not have any noticeable effect on axially-oriented ring magnets.

This approach can also be used to account for segmented rings with gaps between segments, although for any reasonable number of segments the effect is extremely similar to a simple reduction in magnetization by a factor of the missing area fraction. In ironless structures, the circumferential field has no influence on motor performance, and Equation 3.67 is all that is necessary to exactly account for segmentation. In motors with back-iron, the circumferential field may contribute slightly to satuation of the iron, but any effect should be small as the circumferential field has no effect when averaged over the entire motor.

3.5 Tubular Motors with Back-Iron

As in the planar case, we can solve for the properties of an iron-bearing tubular motor by assuming an infinite permeability, and setting the iron thickness to achieve a target peak flux density, or by assuming a constant, finite linearized permeability and iterating on the nonlinear B-H curve of the iron. The first approach is computationally

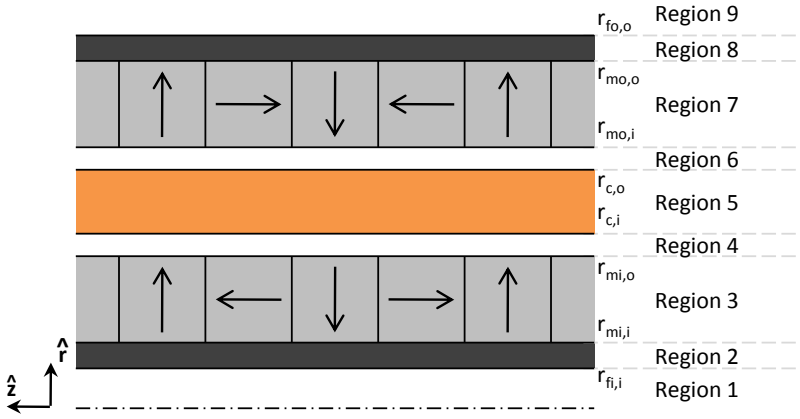

Figure 3-13: A schematic of a tubular, double-sided block Halbach motor with back-iron layers. The inner magnet array extends from $r_{mi,i}$ to $r_{mi,o}$, the coil extends from $r_{c,i}$ to $r_{c,o}$, and the outer magnet array extends from $r_{mi,i}$ to $r_{mi,o}$. The iron layers (if present) extend from $r_{fi,i}$ to $r_{mi,i}$ and from $r_{mo,o}$ to $r_{fo,o}$. The magnet array has four blocks per period p, with relative radial magnet widths δ_{ri} and δ_{ro} and relative axial magnet widths δ_{zi} and δ_{zo} in the inner and outer arrays, respectively.

easier, but relies on the setting of an arbitrary flux density target, while the second is much more expensive to calculate but potentially more accurate. We will present the results obtained with both approaches here, and compare to finite element results.

Due to the loss of symmetry in cylindrical coordinates, there are now three distinct iron-bearing motor configurations to consider. There can be iron outside the coil, iron inside the coil, or iron on both sides. (We considered only iron on both sides for the planar case, though a single-sided motor with iron behind the magnets and a coreless winding would have required a different field solution.) The general configuration is shown in Figure 3-13; if one of the iron layers is missing, that region number will be omitted from the list of field parameters, but the layer beyond will be included.

3.5.1 Infinite Permeability

If the iron permeability is assumed to be infinite, it is straightforward to solve the field parameters subject to the new set of boundary conditions. In the case with iron outside, omitting region 2, we find the following field parameters for the coil field:

$$
\begin{aligned}
a_{cn,1} &= a_{cn,4} & b_{cn,1} &= 0 \\
a_{cn,3} &= a_{cn,4} & b_{cn,3} &= 0 \\
a_{cn,4} &= a_{cn,6} + \mathcal{L}_{\mathrm{K}}\left(nkr_{c,i}\right) - \mathcal{L}_{\mathrm{K}}\left(nkr_{c,o}\right) & b_{cn,4} &= 0 \\
a_{cn,5} &= a_{cn,6} - \mathcal{L}_{\mathrm{K}}\left(nkr_{c,o}\right) & b_{cn,5} &= -\mathcal{L}_{\mathrm{I}}\left(nkr_{c,i}\right) \\
a_{cn,6} &= b_{cn,6}\frac{\mathrm{K}_0\left(nkr_{mo,o}\right)}{\mathrm{I}_0\left(nkr_{mo,o}\right)} & b_{cn,6} &= \mathcal{L}_{\mathrm{I}}\left(nkr_{c,o}\right) - \mathcal{L}_{\mathrm{I}}\left(nkr_{c,i}\right)
\end{aligned}
$$

$$a_{cn,7} = a_{cn,6} \qquad\qquad b_{cn,7} = b_{cn,6}. \tag{3.68}$$

The dimensionless magnet parameters are then as follows:

$$\begin{aligned}
a_{mn,1} &= a_{mn,6} + \hat{M}_{rni}\left(\mathcal{L}_{\mathrm{K}}\left(nkr_{mi,i}\right) - \mathcal{L}_{\mathrm{K}}\left(nkr_{mi,o}\right)\right) + \\
&\qquad \hat{M}_{zni}\left(nkr_{mi,i}\,\mathrm{K}_1\left(nkr_{mi,i}\right) - nkr_{mi,o}\,\mathrm{K}_1\left(nkr_{mi,o}\right)\right) \\
b_{mn,1} &= 0 \\
a_{mn,3} &= a_{mn,6} - \hat{M}_{rni}\,\mathcal{L}_{\mathrm{K}}\left(nkr_{mi,o}\right) - \hat{M}_{zni} nkr_{mi,o}\,\mathrm{K}_1\left(nkr_{mi,o}\right) \\
b_{mn,3} &= -\hat{M}_{rni}\,\mathcal{L}_{\mathrm{I}}\left(nkr_{mi,i}\right) + \hat{M}_{zni} nkr_{mi,i}\,\mathrm{I}_1\left(nkr_{mi,i}\right) \\
a_{mn,4} &= a_{mn,6} \\
b_{mn,4} &= \hat{M}_{rni}\left(\mathcal{L}_{\mathrm{I}}\left(nkr_{mi,o}\right) - \mathcal{L}_{\mathrm{I}}\left(nkr_{mi,i}\right)\right) - \\
&\qquad \hat{M}_{zni}\left(nkr_{mi,o}\,\mathrm{I}_1\left(nkr_{mi,o}\right) - nkr_{mi,i}\,\mathrm{I}_1\left(nkr_{mi,i}\right)\right) \\
a_{mn,5} &= a_{mn,6} \\
b_{mn,5} &= b_{mn,4} \\
a_{mn,6} &= a_{mn,7} + \hat{M}_{rno}\,\mathcal{L}_{\mathrm{K}}\left(nkr_{mo,i}\right) + \hat{M}_{zno} nkr_{mo,i}\,\mathrm{K}_1\left(nkr_{mo,i}\right) \\
b_{mn,6} &= b_{mn,4} \\
a_{mn,7} &= \frac{b_{mn,7}\,\mathrm{K}_0\left(nkr_{mo,o}\right) - \hat{M}_{rno}\,\Lambda_0\left(nkr_{mo,o}\right) - \hat{M}_{zno}}{\mathrm{I}_0\left(nkr_{mo,o}\right)} \\
b_{mn,7} &= b_{mn,4} - \hat{M}_{rno}\,\mathcal{L}_{\mathrm{I}}\left(nkr_{mo,i}\right) + \hat{M}_{zno} nkr_{mo,i}\,\mathrm{I}_1\left(nkr_{mo,i}\right).
\end{aligned} \tag{3.69}$$

While the parameters have not been written out explicitly, these expressions do not suffer from cancellation and are numerically stable. The resulting dimensionless force is given by

$$\hat{f} \equiv \pi\left(\left(a_{c1,4} - a_{c1,6}\right) b_{m1,6} + a_{m1,4} b_{c1,6}\right). \tag{3.70}$$

This reduces to the same form as in Equation 3.66b, and physically speaking the coil coefficients actually represent the result of integrating the magnet field over the coil, rather than the field the coil produces. The dimensionless force and winding factor are unchanged from the ironless motor.

As we did in the planar case, we can use the total flux in the iron and the saturation flux density to determine the iron thickness required. The flux integral is given as follows:

$$\begin{aligned}\Phi(z) &= 2\pi r_{mo,o}\int_0^z \boldsymbol{B}\left(r_{mo,o},\ z'\right)\cdot\hat{\boldsymbol{r}}\,dz' \\ &= 2\pi r_{mo,o}B_{rem}\sum_{n=1}^{\infty}\left[\frac{b_{mn,7}+\hat{M}_{rno}\,\mathcal{L}_{\mathrm{I}}\left(nkr_{mo,o}\right)-\hat{M}_{nzo}nkr_{mo,o}\,\mathrm{I}_1\left(nkr_{mo,o}\right)}{n^2k^2r_{mo,o}\,\mathrm{I}_0\left(nkr_{mo,o}\right)\csc\left(nkz\right)}+\right. \\ &\qquad\left.+\ \hat{J}_n\frac{\mathcal{L}_{\mathrm{I}}\left(nkr_{c,o}\right)-\mathcal{L}_{\mathrm{I}}\left(nkr_{c,i}\right)}{n^2k^2r_{mo,o}\,\mathrm{I}_0\left(nkr_{mo,o}\right)}\cos\left(nkz+\phi\right)\right], \quad (3.71)\end{aligned}$$

where for completeness we have included the effect of current and re-introduced the dimensionless current,

$$\hat{J}_n \equiv \frac{\mu_0 J_n}{nkB_{rem}}. \quad (3.72)$$

The iron thickness can then be determined as follows:

$$\begin{aligned}k^2r_{fo,o}^2 &= k^2r_{mo,o}^2+\frac{k^2\Phi\left(\pi/2k\right)}{\pi B_{sat}} \\ &= k^2r_{mo,o}^2+\frac{2B_{rem}}{B_{sat}}\sum_{n=1}^{\infty}\left[\frac{b_{mn,7}+\hat{M}_{rno}\,\mathcal{L}_{\mathrm{I}}\left(nkr_{mo,o}\right)-\hat{M}_{nzo}nkr_{mo,o}\,\mathrm{I}_1\left(nkr_{mo,o}\right)}{(-1)^{(n-1)/2}\,n^2\,\mathrm{I}_0\left(nkr_{mo,o}\right)}+\right. \\ &\qquad\left.+\,\hat{J}_n\frac{\mathcal{L}_{\mathrm{I}}\left(nkr_{c,o}\right)-\mathcal{L}_{\mathrm{I}}\left(nkr_{c,i}\right)}{n^2\,\mathrm{I}_0\left(nkr_{mo,o}\right)}\cos\left(\frac{n\pi}{2}+\phi\right)\right], \quad (3.73)\end{aligned}$$

where terms that would be imaginary (even harmonics for magnet part) should be discarded. At high current loadings, the maximum flux will appear at a different location, but to be conservative one could set $\phi=-\pi/2$ so that the field produced by the current reinforces that of the magnets. For brevity, we will define the dimensionless flux in the outer iron

$$\begin{aligned}\hat{\Phi}_o \equiv \sum_{n=1}^{\infty}\left[\frac{b_{mn,7}+\hat{M}_{rno}\,\mathcal{L}_{\mathrm{I}}\left(nkr_{mo,o}\right)-\hat{M}_{nzo}nkr_{mo,o}\,\mathrm{I}_1\left(nkr_{mo,o}\right)}{(-1)^{(n-1)/2}\,n^2\,\mathrm{I}_0\left(nkr_{mo,o}\right)}+\right. \\ \left.+\,\hat{J}_n\frac{\mathcal{L}_{\mathrm{I}}\left(nkr_{c,o}\right)-\mathcal{L}_{\mathrm{I}}\left(nkr_{c,i}\right)}{n^2\,\mathrm{I}_0\left(nkr_{mo,o}\right)}\cos\left(\frac{n\pi}{2}+\phi\right)\right]. \quad (3.74)\end{aligned}$$

Equipped with these relations, and accounting for all of the relevant effects, the

dimensionless mass is given by

$$\hat{m} = \pi \left(x\alpha + \frac{\rho_i}{\rho_c}(1-x)(1-\alpha) \right) \left(\left(kr_{c,o}\right)^2 - \left(kr_{c,i}\right)^2 \right) + \\ + \pi \frac{\rho_m}{\rho_c} \left(\left(kr_{mo,o}\right)^2 - \left(kr_{mo,i}\right)^2 + \left(kr_{mi,o}\right)^2 - \left(kr_{mi,i}\right)^2 \right) + 2\frac{\rho_f}{\rho_c}\frac{B_{rem}}{B_{sat}}\hat{\Phi}_o, \quad (3.75)$$

where ρ_f is the density of the iron, and the fill factor and coil width have been accounted for. (Further accounting for the stroke-to-length ratio is trivial, but must be done differently for each of the scenarios of Section 2.6.3.)

A motor with interior iron can be analyzed in the same manner, with regions 1, 2, and 8 excluded from the analysis. The magnets produce a field with the following coefficients:

$$\begin{aligned}
a_{mn,3} &= a_{mn,6} - \hat{M}_{rni}\,\mathcal{L}_{\mathrm{K}}\left(nkr_{mi,o}\right) - \hat{M}_{zni} nkr_{mi,o}\,\mathrm{K}_1\left(nkr_{mi,o}\right) \\
b_{mn,3} &= \frac{a_{mn,3}\,\mathrm{I}_0\left(nkr_{mi,i}\right) + \hat{M}_{rni}\,\Lambda_0\left(nkr_{mi,i}\right) + \hat{M}_{zni}}{\mathrm{K}_0\left(nkr_{mi,i}\right)} \\
a_{mn,4} &= a_{mn,6} \\
b_{mn,4} &= b_{mn,3} + \hat{M}_{rni}\,\mathcal{L}_{\mathrm{I}}\left(nkr_{mi,o}\right) - \hat{M}_{zni} nkr_{mi,o}\,\mathrm{I}_1\left(nkr_{mi,o}\right) \\
a_{mn,5} &= a_{mn,6} \\
b_{mn,5} &= b_{mn,4} \\
a_{mn,6} &= \hat{M}_{rno}\left(\mathcal{L}_{\mathrm{K}}\left(nkr_{mo,i}\right) - \mathcal{L}_{\mathrm{K}}\left(nkr_{mo,o}\right)\right) + \\
&\quad \hat{M}_{zno}\left(nkr_{mo,i}\,\mathrm{K}_1\left(nkr_{mo,i}\right) - nkr_{mo,o}\,\mathrm{K}_1\left(nkr_{mo,o}\right)\right) \\
b_{mn,6} &= b_{mn,4} \\
a_{mn,7} &= -\hat{M}_{rno}\,\mathcal{L}_{\mathrm{K}}\left(nkr_{mo,o}\right) - \hat{M}_{zno} nkr_{mo,o}\,\mathrm{K}_1\left(nkr_{mo,o}\right) \\
b_{mn,7} &= b_{mn,4} - \hat{M}_{rno}\,\mathcal{L}_{\mathrm{I}}\left(nkr_{mo,i}\right) + \hat{M}_{zno} nkr_{mo,i}\,\mathrm{I}_1\left(nkr_{mo,i}\right) \\
a_{mn,9} &= 0 \\
b_{mn,9} &= b_{mn,4} + \hat{M}_{rno}\left(\mathcal{L}_{\mathrm{I}}\left(nkr_{mo,o}\right) - \mathcal{L}_{\mathrm{I}}\left(nkr_{mo,i}\right)\right) - \\
&\quad \hat{M}_{zno}\left(nkr_{mo,o}\,\mathrm{I}_1\left(nkr_{mo,o}\right) - nkr_{mo,i}\,\mathrm{I}_1\left(nkr_{mo,i}\right)\right).
\end{aligned} \quad (3.76)$$

The coil, in turn, generates a field described by these coefficients:

$$\begin{aligned}
a_{cn,3} &= a_{cn,4} & b_{cn,3} &= a_{cn,4}\frac{\mathrm{I}_0\left(nkr_{mi,i}\right)}{\mathrm{K}_0\left(nkr_{mi,i}\right)} \\
a_{cn,4} &= \mathcal{L}_{\mathrm{K}}\left(nkr_{c,i}\right) - \mathcal{L}_{\mathrm{K}}\left(nkr_{c,o}\right) & b_{cn,4} &= b_{cn,3} \\
a_{cn,5} &= -\mathcal{L}_{\mathrm{K}}\left(nkr_{c,o}\right) & b_{cn,5} &= b_{cn,3} - \mathcal{L}_{\mathrm{I}}\left(nkr_{c,i}\right) \\
a_{cn,6} &= 0 & b_{cn,6} &= b_{cn,3} + \mathcal{L}_{\mathrm{I}}\left(nkr_{c,o}\right) - \mathcal{L}_{\mathrm{I}}\left(nkr_{c,i}\right) \\
a_{cn,7} &= 0 & b_{cn,7} &= b_{cn,6}
\end{aligned}$$

$$a_{cn,9} = 0 \qquad\qquad b_{cn,9} = b_{cn,6}, \tag{3.77}$$

and the dimensionless force is given by

$$\hat{f} \equiv \pi \left(a_{c1,4} b_{m1,6} + a_{m1,4} \left(b_{c1,6} - b_{c1,4} \right) \right). \tag{3.78}$$

Once again, the coil coefficients and form of the dimensionless force relation from the ironless case (Equation 3.66b) could be used here as well. We must derive a new dimensionless flux to cover this case, as the form of the equation is slightly different for interior iron:

$$\hat{\Phi}_i \equiv \sum_{n=1}^{\infty} \left[\frac{a_{mn,3} + \hat{M}_{rni}\, \mathcal{L}_{\mathrm{K}}\left(nkr_{mi,i}\right) - \hat{M}_{nzi} nkr_{mi,i}\, \mathrm{K}_1\left(nkr_{mi,i}\right)}{(-1)^{(n-1)/2}\, n^2\, \mathrm{K}_0\left(nkr_{mi,i}\right)} + \right.$$
$$\left. + \hat{J}_n \frac{\mathcal{L}_{\mathrm{K}}\left(nkr_{c,i}\right) - \mathcal{L}_{\mathrm{K}}\left(nkr_{c,o}\right)}{n^2\, \mathrm{K}_0\left(nkr_{mi,i}\right)} \cos\left(\frac{n\pi}{2} + \phi \right) \right]. \tag{3.79}$$

Given this relation, the dimensionless mass can be easily calculated by simply substituting $\hat{\Phi}_i$ for $\hat{\Phi}_o$ in Equation 3.75. Note that, in this case, the current in the coil contributes more strongly to the iron flux than in the motor with exterior iron. For example, consider the first harmonic flux in a motor with $kr_{c,i} = 2.52$, $kr_{c,o} = 2.77$, and either $kr_{mi,i} = 2.5$ or $kr_{mo,o} = 2.8$ (i.e. a 1% gap between coil and iron), and ignore the contribution of magnets to the dimensionless flux. The structure with inner iron would have $\hat{\Phi}_i = 0.66\hat{J}_1$, while the structure with outer iron would have $\hat{\Phi}_o = 0.46\hat{J}_1$. The contributions become more equal as the iron interfaces are moved away from the coil.

The field solutions are considerably more complex if both the inner and outer iron layers are present; the coefficients are given in Appendix A.4. Rather than being able to use the boundary conditions in sequence, starting from a point where the a or b coefficient is zero, they must be solved simultaneously. The dimensionless force is now given by

$$\hat{f} \equiv \pi \left(\left(a_{c1,4} - a_{c1,6} \right) b_{m1,6} + a_{m1,4} \left(b_{c1,6} - b_{c1,4} \right) \right). \tag{3.80}$$

The fluxes in the inner and outer iron are still given by Equations 3.79 and 3.74, respectively, and the dimensionless mass can be trivially calculated with the inclusion of both layers.

3.5.2 Finite Permeability

The finite-permeability solutions for the fields are given in the appendix, with interior iron in Appendix A.2 and exterior iron in Appendix A.3. The introduction of boundaries between different layers of finite permeability greatly complicates the expressions for the field coefficients, as the simplifying identity in Equation 3.61 becomes unavailable. Unlike the solution for the planar double-sided motor, these finite-permeability solutions do not suffer from cancellation error and can be used to very high harmonic

order, limited only by double precision overflow when calculating the Bessel functions. While they may be complex, the solutions can easily be implemented in MATLAB or other computing systems.

We do not provide a solution for a motor structure with both inner and outer iron, both due to its high complexity and due to the difficulty in accounting for saturation. Iterating on the nonlinear B-H curve in two different layers can be an unstable process, as lowering the permeability in one layer can raise the flux passing through the other layer. Careful algorithm development would be required to warrant further investigation of such configurations, which were not within the scope of our present work.

3.5.3 Finite Element Validation

To test our models for iron-bearing tubular motors, we chose to investigate motors with iron outside, as this is the most common single-sided configuration made or discussed in the literature. (Double-sided configurations were not used for comparison testing due to the lack of a finite-permeability model.) We began with the geometry investigated for the ironless model, with $kr_{mi,i} = 0.86$, $kr_{mi,o} = 3.0$, $kr_{c,i} = 3.03$, $kr_{c,o} = 3.87$, $\delta_{ri} = 0.41$, and $\delta_{zi} = 0.59$. We then added iron starting at $kr_{mo,o} = 3.91$. For the infinite-permeability model, we used $B_{sat} = 2\,\mathrm{T}$, $B_{sat} = 3\,\mathrm{T}$ and $B_{sat} = 4\,\mathrm{T}$, ranging from a conservative choice to a choice that would guarantee saturation. The model thus required $kr_{fo,o} = 4.19$, $kr_{fo,o} = 4.10$, and $kr_{fo,o} = 4.05$, respectively. All three geometries were tested with the finite-permeability model to 100^{th} harmonic order and with ANSYS FEA, using the same nonlinear B-H curve [116] for 1018 steel, given in Figure 3-14. For the finite element analyses, the coil was divided to form a "single-phase" winding, with a current density of $10^6\,\mathrm{A/m^2}$ applied as a square wave in phase with the field from the magnets.

Figure 3-15 shows the field in the middle of the coil region for the cases investigated. The finite-permeability model closely matches the magnitude of the flux density given by FEA closely, with permeabilities of $\mu = 83.2$, $\mu = 23.2$, and $\mu = 15.6$ for the three design fluxes, respectively. The analytical model predicts a slightly broader flux distribution than the finite element model. We can also see that the 2 T case posesses a flux waveform very close to that expected for a motor with infinite permeability.

We can also compare the force production estimates. There are two ways we can interpret the finite element results: we can calculate an effective dimensionless force (as per Equation 2.27) based on the first harmonic of the current distribution, with a factor of $4/\pi$ to account for the square wave, or we can consider it as produced by all harmonics. The first interpretation allows for comparison to analytical models for the first-harmonic force generation, which is easiest to compute and represents the average force over the stroke, while the second requires a more involved analytical computation but represents the FEA situation more precisely. Both approaches are presented in Table 3.1. Note that calculation of the force parameter due to higher harmonics requires each term to be scaled by a factor of n^{-2}.

On a first-harmonic basis, the results with our model are promising, with the finite-permeability model consistently over-predicting the performance by about 4%.

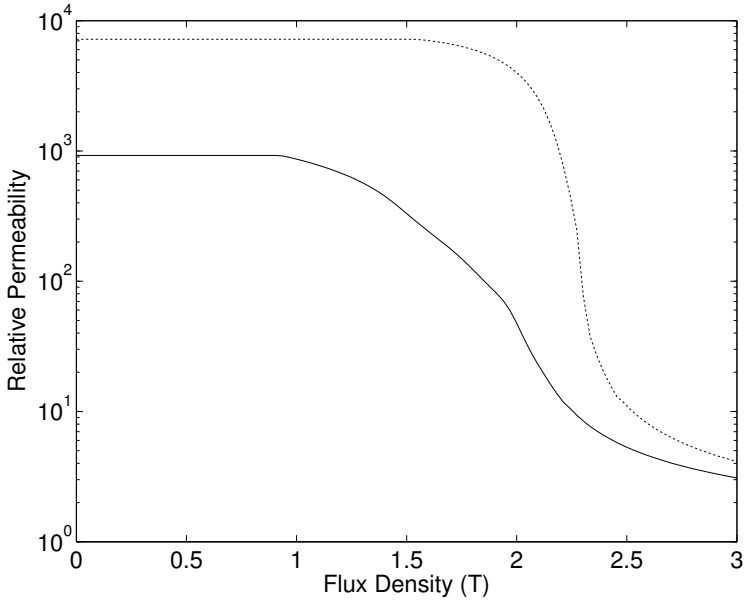

Figure 3-14: The permeability of iron used in our FEA and analytical analyses is given by the solid black curve, as a function of flux density. This is a curve for low-carbon 1018 steel, based on data from [116]. For comparison, the dotted curve gives the permeability of vanadium permendur, the magnetic alloy with the highest saturation flux density available.

More importantly, both our model and the FEA suggest that performance is best when the iron is not quite saturated, as opposed to the infinite-permeability model which blindly allows the flux density in the iron to be set at any level. The infinite-permeability model is very close, however, when the iron is minimally saturated, as in the 2 T design case. A motor with the same geometry, but no iron, is also included to show that even heavily saturated iron is preferable to none at all. The discrepancy between the FEA first-harmonic result and the model is most likely due to assuming the FEA force to be entirely from the first harmonic.

The full-harmonic force results show even closer agreement between the model and FEA. Calculating the force constant with the analytical model only requires a handful of harmonics; only the first and third are required to calculate the force constant to within 1% of the value found with 99 harmonics. Our model agrees with FEA to within 1%, which is perhaps surprising given that we do not account for the non-unity permeability of the magnets. (It would be possible to do so, but as seen here accounting for magnet permeability offers little gain for a great deal of mathematical pain.) This is likely because the two main residual errors act in opposite directions: the magnet permeability acts to decrease the force in the FEA, while the spatially nonuniform permeability acts to increase the force.

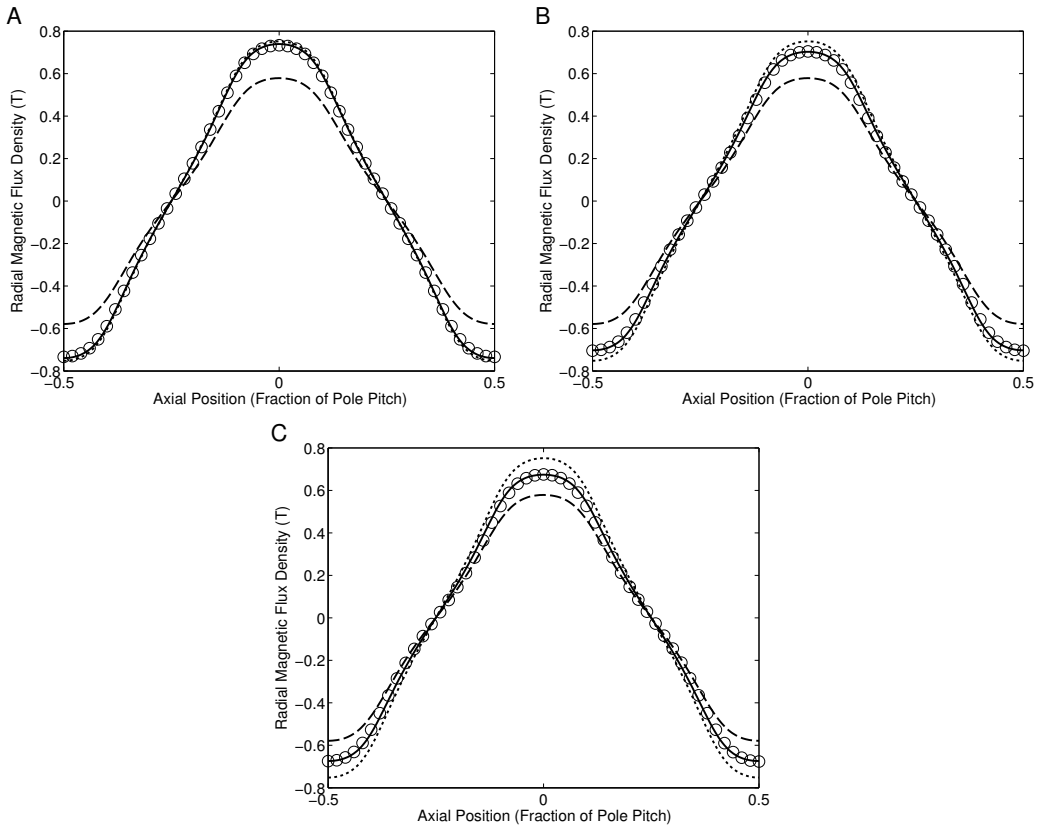

Figure 3-15: The radial B-field is plotted for motors with $kr_{mi,i} = 0.86$, $kr_{mi,o} = 3.0$, $kr_{c,i} = 3.03$, $kr_{c,o} = 3.87$, $kr_{mo,i} = kr_{mo,o} = 3.91$, $\delta_{ri} = 0.41$, and $\delta_{zi} = 0.59$, with A) $kr_{fo,o} = 4.19$, B) $kr_{fo,o} = 4.10$, and C) $kr_{fo,o} = 4.05$. The dashed lines represent the field in the absence of iron, the dotted lines show the field with infinitely-permeable iron, the solid lines indicate the field according to the finite-permeability model, and the circles show the field according to an ANSYS finite element model. In all cases, the finite-permeability analytical solution shows close agreement with the finite element analysis. In case A, the field is very close to that with assumed infinite permeability.

3.6 Finite Length Effects

The Fourier series approach to magnetic field solution allows for a straightforward accounting of finite length effects in motors. The result has been reported elsewhere, such as by Golda et al. [64], but we can present it with somewhat more specificity.

A finite length (of N_p pole pitches) can be accommodated for the motor by, conceptually, multiplying the magnetization function by a rectangle function:

$$\boldsymbol{M}'' = \boldsymbol{M} \operatorname{rect}\left(\frac{kz}{2\pi N_p}\right), \tag{3.81}$$

where $\boldsymbol{M}''$ is the finite-length magnetization and the rect function is equal to one for values of its argument between -1/2 and 1/2 and is zero elsewhere. (This formulation

Table 3.1: The performance predicted for our three iron-bearing motor geometries is compared between the infinite-permeability analytical model ($\hat{\epsilon}_\infty$ and $\hat{f}_\infty$), the finite-permeability model ($\hat{\epsilon}_{\text{finite}}$ and $\hat{f}_{\text{finite}}$), and finite element analysis ($\hat{\epsilon}_{\text{FEA}}$ and $\hat{f}_{\text{FEA}}$). The dimensionless motor constants $\hat{\epsilon}$ are determined based on the first harmonic of current (FEA force is multiplied by $\pi/4$). The dimensionless forces are based on all of the harmonics of the current square wave and the magnetic field.

Design Flux Density	$\hat{\epsilon}_\infty$	$\hat{\epsilon}_{\text{finite}}$	$\hat{\epsilon}_{\text{FEA}}$	$\hat{f}_\infty$	$\hat{f}_{\text{finite}}$	$\hat{f}_{\text{FEA}}$
2 T	0.274	0.270	0.260	6.384	6.278	6.215
3 T	0.282	0.262	0.254	6.384	5.928	5.919
4 T	0.286	0.255	0.246	6.384	5.677	5.652
No Iron	N/A	0.230	N/A	N/A	4.880	N/A

assumes the motor is centered on a radial magnet; it can be centered on an axial magnet simply by adding a factor of 1/4 to the argument of the rect function.)

This can be brought into the Fourier domain via the standard correspondence between multiplication in the time domain and convolution in the frequency domain. The result is that the magnetization is now given as follows:

$$\boldsymbol{M}'' = \frac{B_{rem}}{\mu_0} \sum_{n=1}^{\infty} \left[\int_{-\infty}^{\infty} \left[\hat{M}_{rn} \cos\left(|n+j|\, kz\right) \hat{\boldsymbol{r}} + \hat{M}_{zn} \sin\left(|n+j|\, kz\right) \hat{\boldsymbol{z}} \right] \frac{\sin\left(jN_p\pi\right)}{j\pi} \mathrm{d}j \right], \tag{3.82}$$

where j is effectively a continuous spatial frequency. This expression, despite now containing an integral, can still be used as the input to solving the field equations. Ultimately, the solutions for the field coefficients and fields are largely unchanged, but n must be replaced by $|n+j|$ (except in the expressions for $\hat{M}_{rn}$ and $\hat{M}_{zn}$). For example, in air in the tubular motor, the B-field from magnets will now be given by

$$\begin{aligned} \boldsymbol{B}_{\text{air}} = \\ B_{rem} \sum_{n=1}^{\infty} \Bigg[\int_{-\infty}^{\infty} \Bigg[& \Big(a_{mn}\, \mathrm{I}_1\big(|n+j|\, kr\big) + b_{mn}\, \mathrm{K}_1\big(|n+j|\, kr\big) \Big) \hat{\boldsymbol{r}} \cos\left(|n+j|\, kz\right) + \\ & + \Big(-a_{mn}\, \mathrm{I}_0\big(|n+j|\, kr\big) + b_{mn}\, \mathrm{K}_0\big(|n+j|\, kr\big) \Big) \hat{\boldsymbol{z}} \sin\left(|n+j|\, kz\right) \Bigg] \frac{\sin\left(jN_p\pi\right)}{j\pi} \mathrm{d}j \Bigg]. \end{aligned} \tag{3.83}$$

This expression certainly appears to be complex, but the integrals are effectively Fourier integrals, with good convergence properties for numerical integration.[4] A small amount of algebraic manipulation may be required to keep removable singularities out of the region of integration. Alternatively, the integral can be approximated by a finite sum, and the result calculated in the same manner as in the infinite motor.

[4]We were able to obtain an analytical expression for the field in a finite planar motor in terms of the exponential integral function, but its numerical properties are vastly inferior to those of simple numerical integration by quadrature.

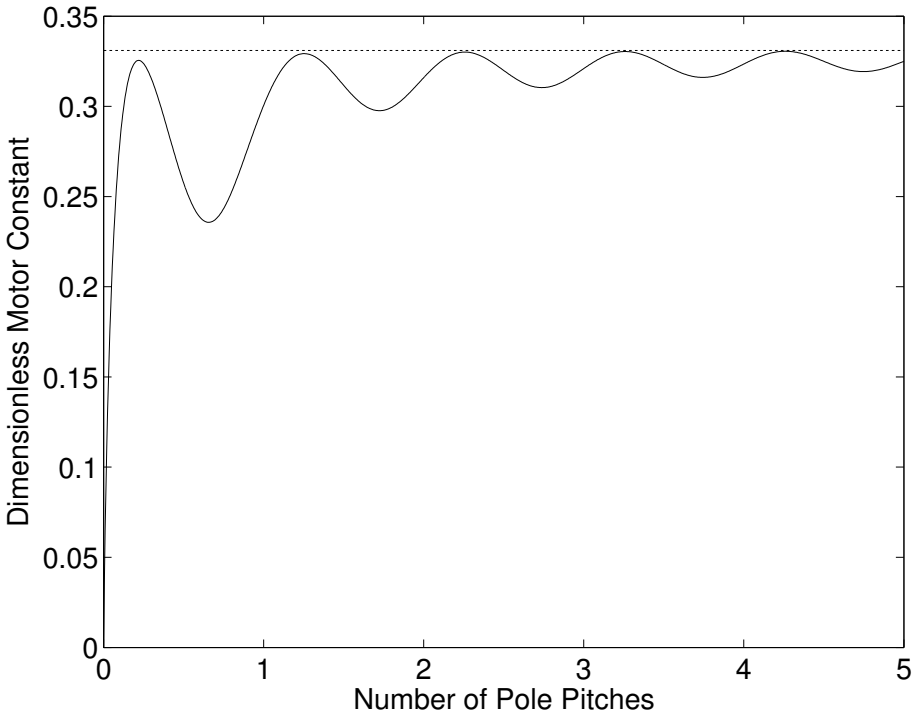

Figure 3-16: The dimensionless motor constant is plotted for a planar double-sided Halbach motor with $kt_c = 0.89$, $kg = 0.01$, $kt_m = 1.7$, and $\delta_y = \delta_z = 0.5$, for a wide range of motor lengths (in pole pitches). The coil is assumed to have the same spatial extent as the magnet array. The dashed line indicates the performance of an infinitely-long motor.

The force can be calculated from the field in the coil region, either using the Maxwell stress tensor or by direct integration of the Lorentz force density. It is more expedient to compute the force produced by integrating the Lorentz force over the volume of the coil in this case, as we no longer have the orthogonality of discrete harmonics of current and magnet fields to simplify the calculation.

We have done this calculation for the planar double-sided Halbach motor, and the results for the dimensionless motor constant are given in Figure 3-16. If there are more than two pole pitches present, the motor performance is within 95% of that of the infinite motor; eight pole pitches gives 99% of the infinite-motor performance. Note, however, that maximum performance in the finite motors is given for non-integral numbers of pole pitches, with approximately 1/4 extra pitch; this corresponds to having full-width transverse magnets on the ends, rather than half-width.

Now, in practice and as discussed in Section 2.6.3, the question of whether the motor is overhung or underhung becomes more important than the variation in field near the ends of the motor. If the motor is underhung, there will be a drop in performance near the ends of travel, while if the motor is overhung there may be extra performance due to fringing fields outside the ends of the magnet array. If the magnet array and/or coil is longer than about two pole pitches, the end-effects should be small compared to the effect of having inactive magnet or coil length.

3.7 Summary and Discussion

We have established analytical magnetic field models for a wide variety of motor configurations, which allow us to calculate most aspects of motor performance from first principles. Our focus has been on the development of formulas for the dimensionless motor parameters of Chapter 2, but the field models have broad applicability. In cylindrical coordinates, our solutions are the first explicit analytical expressions for the fields in linear motors that can be applied at large radii and high harmonic orders. We also use a distinctive approach to modeling the fields in saturable iron structures, with high accuracy and intuitive computation. The only type of motor structure our approach cannot model is that incorporating periodic iron features, as found in slotted stators. While such structures could be addressed by patching regions of different periodicity, as described by Gysen et al. [81], or by interfacing with a magnetic circuit model, we chose not to pursue them in our work.

3.7.1 Comparison of Topologies

We have derived and verified equations for the dimensionless motor constant in three broad classes of tubular motor: ironless (Equation 3.66b), interior back-iron (Equation 3.78), and exterior back-iron (Equation 3.70). With these relations, we can begin to ask the question of what motor topology will offer the best performance in a given application, and what the best choice of geometric parameters will be in each case. The most obvious basis of comparison is based on the dimensionless motor constant itself—how can we get the most force for a given input power and motor mass? (Other criteria are considered in Chapter 4.)

Thanks to the relatively easy computation of $\hat{\epsilon}$, we can use it to perform geometric optimization for each motor topology. Upon doing so, we immediately discover that most motor topologies are most effective in the planar configuration; forming the structure into a tubular motor degrades its performance even when optimized, as we saw in Figure 3-12. As we would still like to use tubular motors, we performed the optimization over a range of fixed mean coil radii r_m. We also chose to fix the physical air gaps adjacent to the coil, with $kg = 0.01$. The choice of parameterization is important to successful optimization; we used the parameters of the planar motor (kt_c, kt_m, kt_f, and δ), but with distinct parameters describing inner and outer magnet arrays.

We optimized the performance for twelve different possible topologies, based on either desirable mechanical properties or the presence of local optima in the solutions. For ironless motors, we examined motors with Halbach arrays inside the coil, Halbach arrays outside the coil, Halbach arrays on both sides of the coil, and motors with Halbach arrays outside but only axial magnets present inside, with the radial magnets replaced by empty spaces. For motors with interior iron, we examined motors with interior iron and exterior Halbach arrays, motors with interior iron-backed radial magnets and exterior Halbach arrays, and motors with interior iron-backed Halbach arrays and exterior Halbach arrays. For motors with exterior iron, we analogously examined motors with interior Halbach arrays and exterior iron,

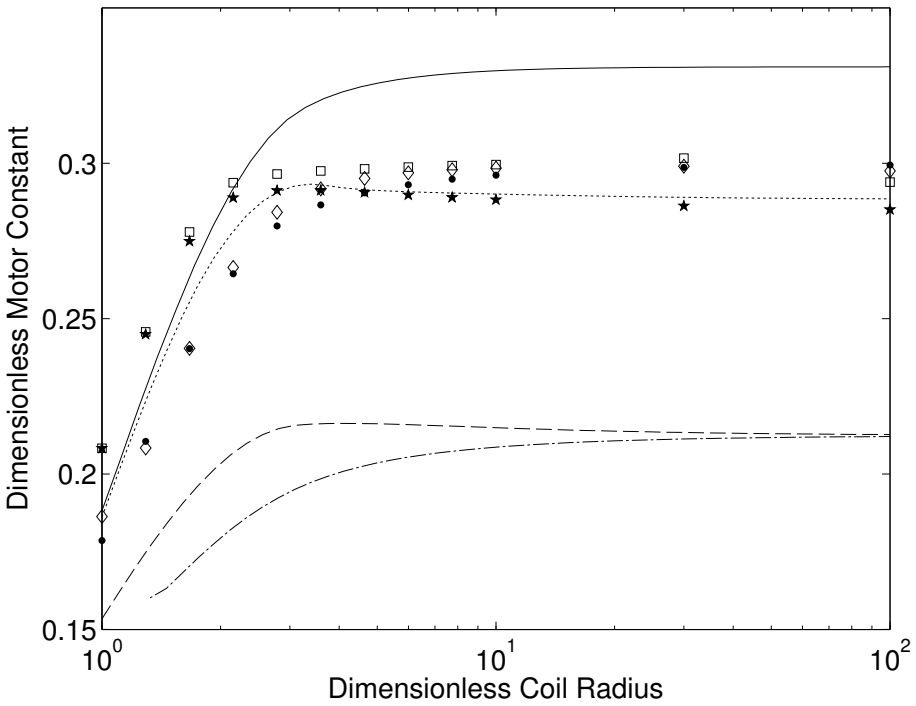

Figure 3-17: The dimensionless motor constant $\hat{\epsilon}$ is plotted against the dimensionless mean coil radius for eight different motor configurations: inner and outer Halbach arrays (solid line), inner Halbach only (dashed line), outer Halbach only (dot-dash line), inner axial magnets and outer Halbach (dotted line), inner Halbach and outer iron (dots), inner Halbach with outer radial magnets and iron (diamonds), inner iron and outer Halbach (stars), and inner iron and radial magnets with an outer Halbach array (squares). In all cases, we have fixed $kg = 0.01$.

motors with interior Halbach arrays and exterior iron-backed radial magnets, and motors with interior Halbach arrays and exterior iron-backed Halbach arrays. The results of the optimizations, performed using the finite-permeability formulations where applicable, are shown in Figure 3-17.

Of the topologies examined, the best performance by about a 10% margin is offered by the ironless double-sided Halbach motor; the iron-backed Halbach arrays are optimized into geometries that lack the iron layers. At small coil radii ($kr_m < 2$), improved performance is offered by motors with interior iron; any interior magnet array between the iron and coil is removed by the optimization process. Ironless motors with single-sided magnet arrays offer much lower performance, and substituting a pure axial array for the inner Halbach array still results in major performance loss up to the point at which interior iron becomes preferable. The iron-bearing motors show slightly erratic behavior at the largest radii, as the full set of harmonics in the field calculation used to determine saturation cannot be calculated. Relatively little deviation from the performance of the planar version of each motor is seen up to $kr_m \approx 10$, and the performance of the double-sided Halbach motor remains within 5% of its planar value until $kr_m \approx 3$.

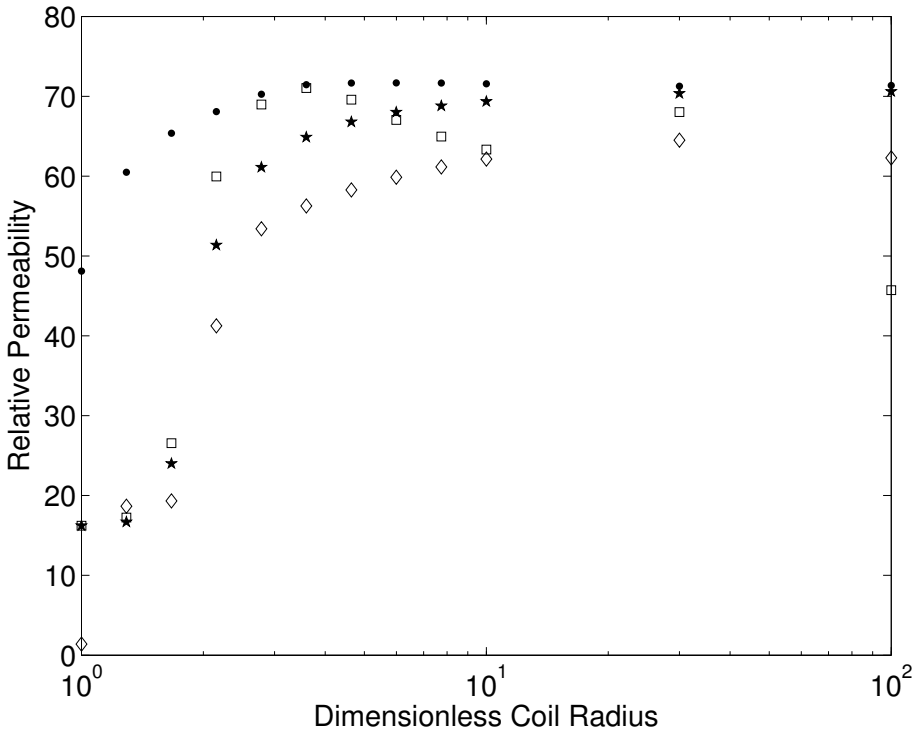

Figure 3-18: The relative permeability of the iron in the optimized motors of Figure 3-17 is shown over the range of mean coil radii. The symbols are as given in Figure 3-17. Motors with iron inside the coil transition from relatively unsaturated operation to saturated operation at small radii.

To see whether the use of the finite-permeability model was necessary, with its relatively expensive computation, we also examined the iron permeability in each iron-bearing motor geometry, as shown in Figure 3-18. At all but the smallest radii, the iron is operating relatively unsaturated, with the permeability corresponding to a field very close to 2 T. At small radii, the iron starts to become more saturated, reaching about 2.2 T. (At $kr_m = 1$, the optimization completely removes the iron from the topology with outer iron-backed radial magnets, yielding the very low effective permeability shown in the figure.) Thus, it would be reasonable to use the infinite-permeability model for optimization with a target flux density of 2 T.

If the performance at even relatively tight radii is so close to that of the planar motor, do we even need the model in cylindrical coordinates? Figure 3-19 compares the optimized double-sided Halbach motor to the planar motor wrapped around the z-axis. The performance of the planar motor drops noticeably below $kr_m = 10$, but does not suffer more than a 5% loss until $kr_m \approx 2.5$. At smaller radii, as would typically be seen in a voice coil design, the performance difference rapidly becomes more significant.

The benefit of using the model in cylindrical coordinates becomes clearer when we examine the actual optimum geometries, as shown in Figure 3-20. The optimal magnet thickness deviates wildly from the planar values, especially close to the point

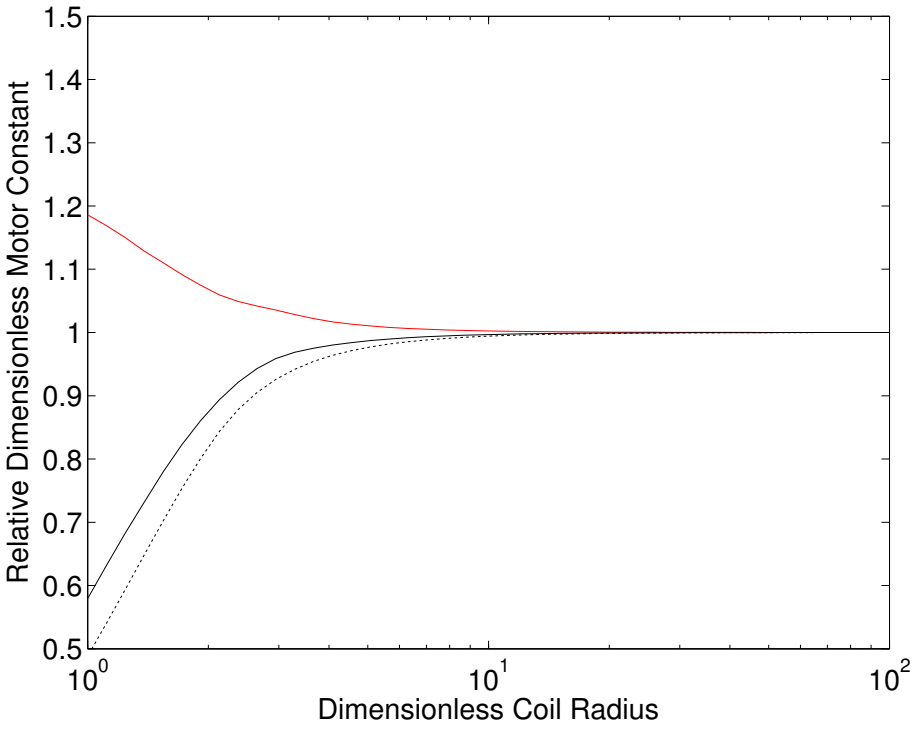

Figure 3-19: The dimensionless motor constant $\hat{\epsilon}$ of the optimum double-sided Halbach motor (solid line) is compared to that of a double sided Halbach motor using the same magnet and coil thicknesses as a planar motor (dotted line). Optimization of the geometry with respect to the mean coil radius becomes advantageous for $kr < 10$; the red line gives the ratio of optimized performance to the performance of the planar geometry.

at which the mean coil diameter equals the pole pitch ($kr_m = \pi$). At this radius, the optimal inner magnets become solid cylinders rather than rings, and in the surrounding transition region the optimal inner magnets are much thicker than the outer magnets. As the performance does not deviate nearly as much as the geometry does at these radii, the implication is that the optimum is extremely shallow—a wide variety of geometries yield similar performance in this transition zone. Rather than slavishly following the optimum geometry for the motor constant, then, we are free to enhance other performance parameters or to follow other design constraints, and simply check the resulting performance to ensure we are near the optimum.

3.7.2 Limits to Scaling

The modeling approach we have developed in Chapter 2 and in this chapter implicitly assumes that all of the motor dimensions can be scaled with the pole pitch, and otherwise be chosen arbitrarily. However, in reality manufacturing technology limits scaling on the small end, and other constraints limit the arbitrary choice of dimensions. For instance, the physical air gap must be chosen to prevent interference between the coil and magnets, to allow for a coil former if desired, and to accommodate

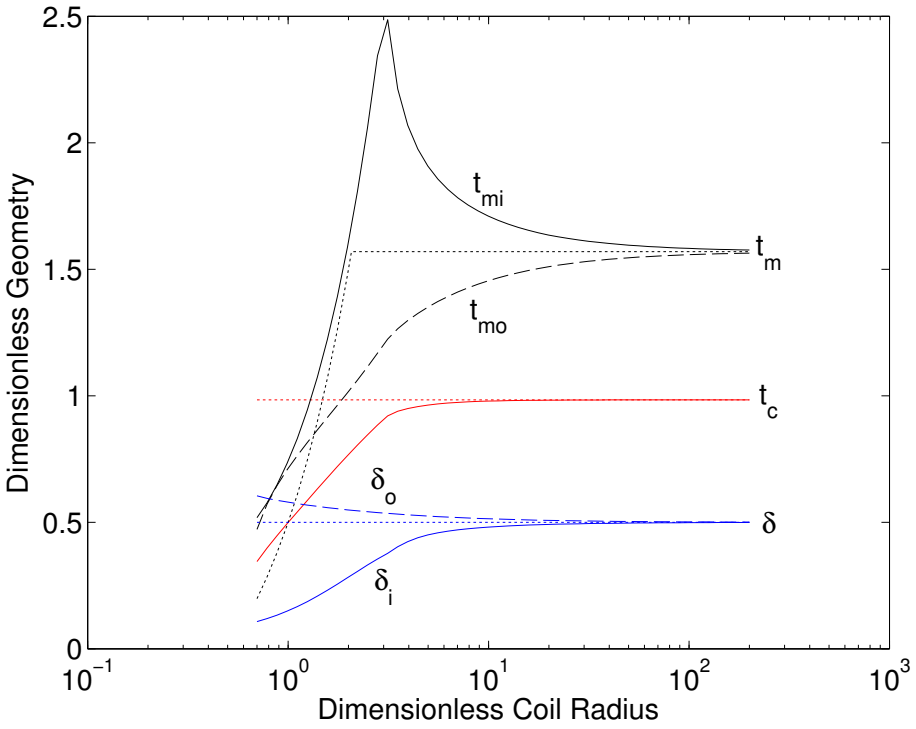

Figure 3-20: The dimensionless geometric parameters of the optimized double-sided Halbach motor are given as a function of the dimensionless mean coil radius. The optimum geometry changes dramatically at $kr_m \approx \pi$, where the mean coil diameter equals the pole pitch; below this point, the inner magnets become solid disks rather than rings. The geometry of the planar motor is given by the dotted lines; the inner magnet thickness in this case must drop at small radii when the innermost radius becomes zero.

thermal expansion of the motor components. With a copper coil and typical operating temperatures 100 °C above ambient, the linear thermal expansion of the coil could approach 1%. NdFeB magnets, on the other hand, undergo very little thermal expansion [66], and so the thermal expansion must be accommodated in the air gap.

In a tubular motor, the coil is wound into a complete circle, thus, the thermal expansion does not act proportionally on the coil thickness, but instead on the radii of the coil's inner and outer surfaces. Thus, the physical air-gap g must scale with the coil radius, not the pole pitch. Figure 3-21 gives the performance of the ironless motor designs under this constraint, with the inner and outer air-gaps equal to 1% of the radius. In this case, performance drops rapidly with dimensionless radius, and the best performance is available from $kr_m = 3$ to $kr_m = 7$ in the double-sided Halbach array motor.

The most significant limit to scaling, of course, is in miniaturization. If the magnets require a 10 μm coating to protect them from corrosion, for instance, 80 μm of axial length in each pole pitch of the magnet array will be inactive. At a pole pitch of 10 mm, this results in just a 0.6% drop in performance. At a pole pitch of 1 mm, however, the performance penalty is now 6.5%. If one wished to shrink the dimensions

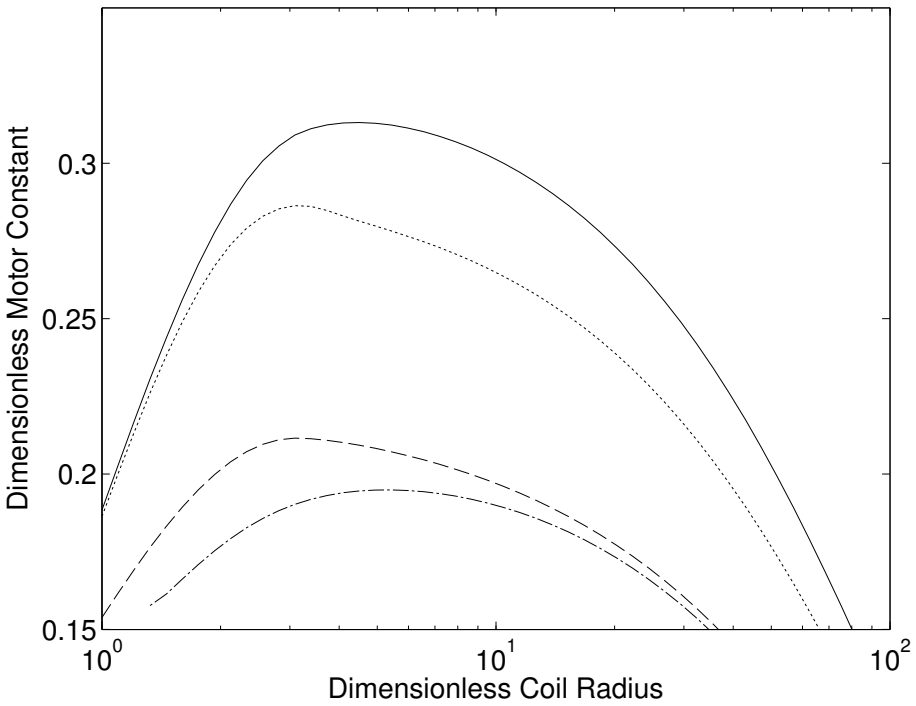

Figure 3-21: The dimensionless motor constant $\hat{\epsilon}$ is plotted against dimensionless mean coil radius for ironless motors when the physical air gap is required to be 1% of the radius at which it appears. The motor topologies shown are inner and outer Halbach arrays (solid line), inner Halbach only (dashed line), outer Halbach only (dot-dash line), and inner axial magnets and outer Halbach (dotted line). In this case, the best performance is seen at moderate radii.

even further, the performance loss is inversely proportional to pole pitch, and almost all of the force produced by the motor is gone at a pole pitch of 100 μm.

Similarly, if the physical air-gap $g = 50\,\mu$m, the performance loss with a 10 mm pole pitch ($kg = 0.03$) is 3.1%. However, as illustrated in Figure 3-22, at a pole pitch of 1 mm ($kg = 0.31$) the dimensionless motor constant is now just 73% of its value in the absence of a gap. (Optimization is not able to get around the exponential dependence on gap seen in Equation 3.14b.) Mitigating this effect requires very close tolerances and formless coils for small pole pitches.

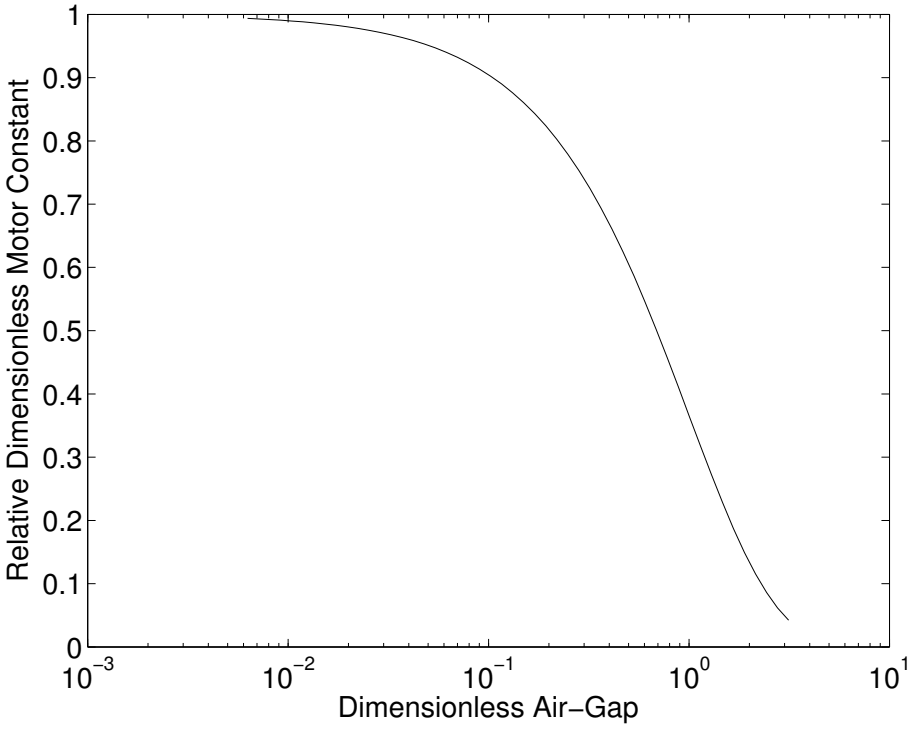

Figure 3-22: The dimensionless motor constant $\hat{\epsilon}$ is plotted relative to its zero-gap value for a range of dimensionless air-gaps kg, at a dimensionless mean coil radius $kr_m = 10$. For reference, a 50 μm air gap at a 10 mm pole pitch corresponds to $kg = 0.03$.

Chapter 4

Design Case Studies

With a modeling framework and an extensive set of analytical field solutions established, we are prepared to explore the applications of the models. This chapter describes our application approach, and explores in detail two applications for improved direct-drive linear motors: operation of bioinspired flapping-wing flying machines, and needle-free jet injection of vaccines and pharmaceuticals. Each application requires different optimization approaches, and explores different strengths and weaknesses of our modeling approach.

4.1 Application Approach

Our modeling framework, as described in Chapter 2, suggests a two-pronged approach to the design process, as illustrated in Figure 4-1. The first stage in the design process is to identify one or more sets of performance parameters to optimize. These might include the motor constant, the maximum force under a performance constraint, the maximum acceleration, the electrical or mechanical time constant, or any other desired property. One should also identify the major specifications—is there a particular value of mass, force, stroke, or power required? For instance, if we are designing a motor to apply static forces for relatively long time periods, we might wish to optimize the motor constant ϵ to minimize power consumption, or perhaps instead optimize the thermally-limited maximum continuous force output, subject to a desired mass and a desired force.

Next, we need to chose the topologies that will be considered for the motor; that is, we have to choose the identities of the layers in the motor, be they Halbach, modified Halbach, conventional transverse magnet arrays, or axial magnet arrays, with or without iron. While any number of such topologies can be optimized and compared, each is governed by a different set of equations, and some topologies can be excluded based on the application needs. (For instance, those placing iron inside the coils will have their peak force capabilities limited by saturation of that iron at high currents.) Once this has been done, the design process can be handled in two largely independent phases: optimizing the geometric ratios of magnet and coil features to improve the dimensionless performance parameters, and choosing the overall feature size (pole

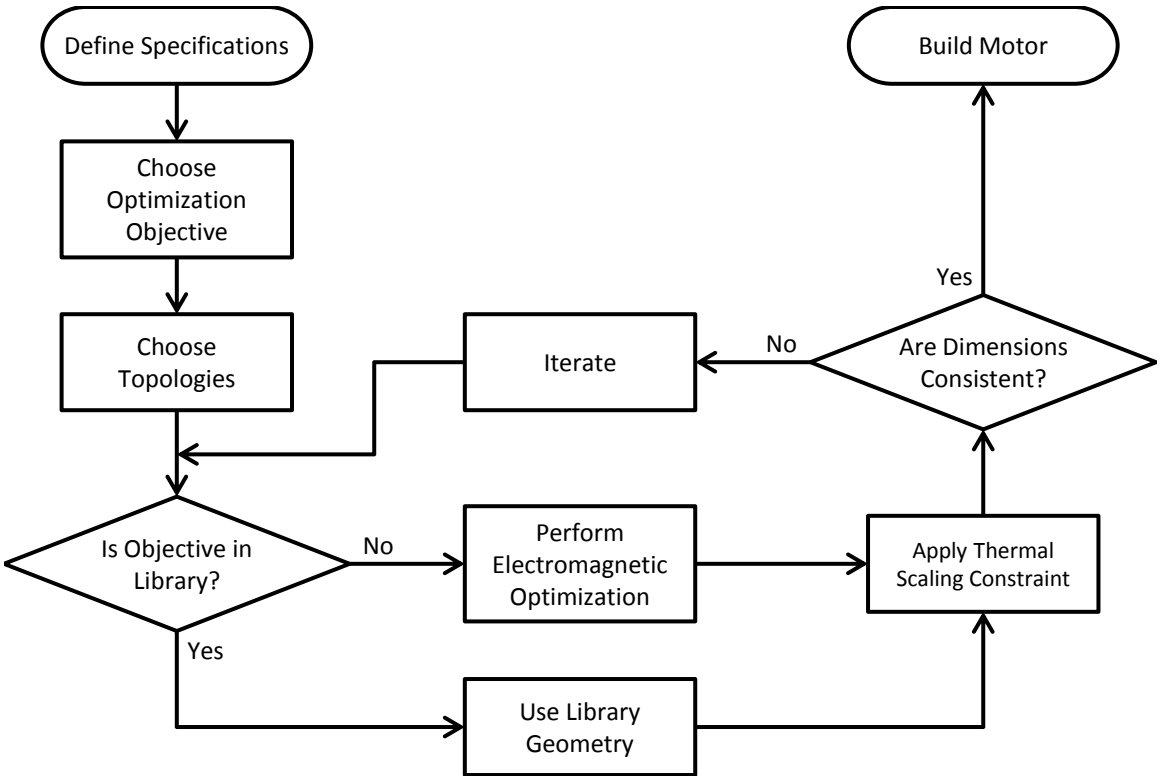

Figure 4-1: The design process using our modeling approach is illustrated in this flowchart. After choosing a set of performance properties to optimize for the desired application, the designer can then choose whether to use a tabulated magnet and coil geometry or to optimize the electromagnetics specifically for the application. Then, the scaling laws can be used to determine the overall feature size and dimensions of the motor. For some constraint and objective choices, iteration may be required to reconcile dimensionless optimization with dimensional constraints.

pitch), motor size, and cooling method. While the choice of overall properties does depend on the values of the dimensionless parameters, the magnet and coil geometry can be selected from a pre-computed library of designs with corresponding fixed parameters, without requiring specialist knowledge of electromagnetics by the design engineer. Some optimization criteria may lead to unique solutions for the geometry of the magnets and coils, obviating the need for further optimization.

4.1.1 Brief Example

As a brief example, consider the problem of designing a motor for static force production. If we seek a motor with optimized motor constant, we can choose a motor radius and use the results from Figure 3-17. If we instead wish to optimize for the thermal constraint, we first must choose the nature of the constraint. For example, if the motor is to operate under convection-dominated thermal conditions ($\mathrm{Bi} \to 0$), we can

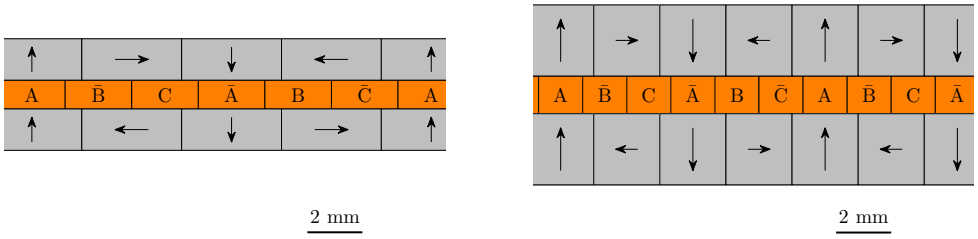

Figure 4-2: The geometry of a motor optimized for thermal performance (left) can be quite different from that optimized for efficiency (right). Both motors are planar and use the same topology, and have been sized to produce 707 N/kg with a convection heat transfer coefficient of 100 $\mathrm{W/m^2K}$.

define a dimensionless pole pitch parameter $\hat{p}_0$:

$$\hat{p}_0 \equiv \left(\frac{\hat{f}}{\hat{m}}\right)^2 \hat{P}^{-1} = \frac{\hat{\epsilon}^2}{\hat{m}}, \tag{4.1a}$$

$$p \leq \frac{4\pi\sigma\bar{h}B_r^2\Delta T}{\rho_c^2\bar{F}'^2} \times \hat{p}_0. \tag{4.1b}$$

This parameter can then be optimized, and happens to also lead to a unique solution for the geometry at every motor radius. Designs for this criterion, as well as several other optimization criteria relevant to applications, will be tabulated in Section 4.4.

For instance, consider designing a planar double-sided block Halbach motor to deliver a sinusoidal force, with a peak force density $F' = 1000\,\mathrm{N/kg}$ (average force density $\bar{F}' = 707\,\mathrm{N/kg}$), as in the scenario of Section 2.4.2. We will assume the (copper) coil has a thermal conductivity of $\kappa_c = 5\,\mathrm{W/(m \cdot K)}$, that the magnets are NdFeB with a remanence of $B_{rem} = 1.334\,\mathrm{T}$, and that the convective heat transfer coefficient is $\bar{h} = 100\,\mathrm{W/(m^2 \cdot K)}$. We will also assume a 100% fill factor and no air-gap, and neglect finite-length and finite-width effects. Under these conditions, $\hat{p}_0$ is optimized for $kt_c \approx 0.453$ and $kt_m \approx 0.651$, as illustrated in Figure 4-2. This requires $p \leq 14.5\,\mathrm{mm}$, about 50% larger than the efficiency-optimized motor, which would need $p \leq 9.6\,\mathrm{mm}$. The dimensionless motor constant, in turn, drops to $\hat{\epsilon} \approx 0.264$, as compared to $\hat{\epsilon} \approx 0.334$ for the efficiency-optimized design.

Now, in this case our neglect of a physical air-gap could be a major problem, as the air-gap offers considerable thermal resistance itself. We cannot calculate the effect of this added constraint in one pass, as specifying an air-gap requires breaking up the dimensionless geometry, but we can apply the iteration indicated in Figure 4-1 to study its effects. If we require a 50 μm air-gap, the required pole pitches drop to 12.5 mm for the thermally-optimized motor and 8.0 mm for the efficiency-optimized motor, and the dimensionless motor constants also drop somewhat. With this gap, if the heat transfer coefficient were instead $10\,\mathrm{W/(m^2 \cdot K)}$, iteration would indicate that

it is not possible to meet the specifications.

4.2 Motor Design for Continuous Motion

One major problem in robotics that has drawn considerable attention recently is that of flapping-wing, biomimetic flight [117]. While there has been considerable advancement in this field, from the rubber-band powered models of the 19$^{\text{th}}$ century to modern piezoelectric-driven micro-air vehicles [118], to date flapping-wing robots have used a single prime mover to power all of each machine's wings. In most bird-scale machines, this prime mover is a rotary electric motor coupled to the wings via a clockwork reduction drive mechanism, which can achieve high power density but provides limited control of the wing motion. Maneuverability is supplied by auxiliary control surfaces, or even lateral thrusters. In real birds [119, 120], by contrast, differential wing motions are an important source of maneuverability. To produce these motions in a robot, independent wing actuators are needed, but duplication of the currently-used clockwork mechanisms carries too high a mass penalty to be practical, and these mechanisms reflect a very high inertia to the actuator, limiting control bandwidth. Direct-drive motors could eliminate these problems, but the required motor specifications are far in excess of those commercially available.

4.2.1 Required Specifications

For the purposes of this design study, consider a flying machine built to the scale of a common pigeon. The flight actuators, then, need to meet or exceed the performance of the pigeon's flight muscles [19, 121, 122]. Roughly speaking, the pigeon pectoralis has a mass of 50 grams, produces a rectified sinusoidally-varying force of 50 N amplitude and 8.7 Hz frequency during level flight (with no force during the up-stroke), moves through a displacement of 20 mm while doing so, and moves at a peak velocity of about 0.5 m/s. Its antagonist muscle, the supracoracoideus, has a mass of 10 grams and produces a similarly varying force of 35 N amplitude, though during the up-stroke instead. The energy efficiency of the bird muscle is estimated at between 10% and 20%, operating at a mechanical power density of about 100 W/kg.

In terms of the performance parameters defined for the linear motors in this work, then, we seek a peak force density $F_0' \geq 830\,\text{N/kg}$ at a 60-gram mass scale. The actual work loop in each bird muscle is roughly triangle-shaped, but for the present purposes we can approximate the overall work loop as being made of two semi-circles, the positive one corresponding to the pectoralis and the negative one to the suparcoracoideus (shown in Figure 4-3), and use a modified form of the analysis from Sections 2.2.2 and 2.3. Equations 2.65 and 2.68 can be used as derived; however note that the RMS force density is the average of the values from the up-stroke and down-stroke, with $\bar{F}' \geq 500\,\text{N/kg}$. To complete the specifications, let us assume a maximum coil temperature of 150 °C and an ambient temperature of 40 °C. These specifications are summarized in Table 4.1.

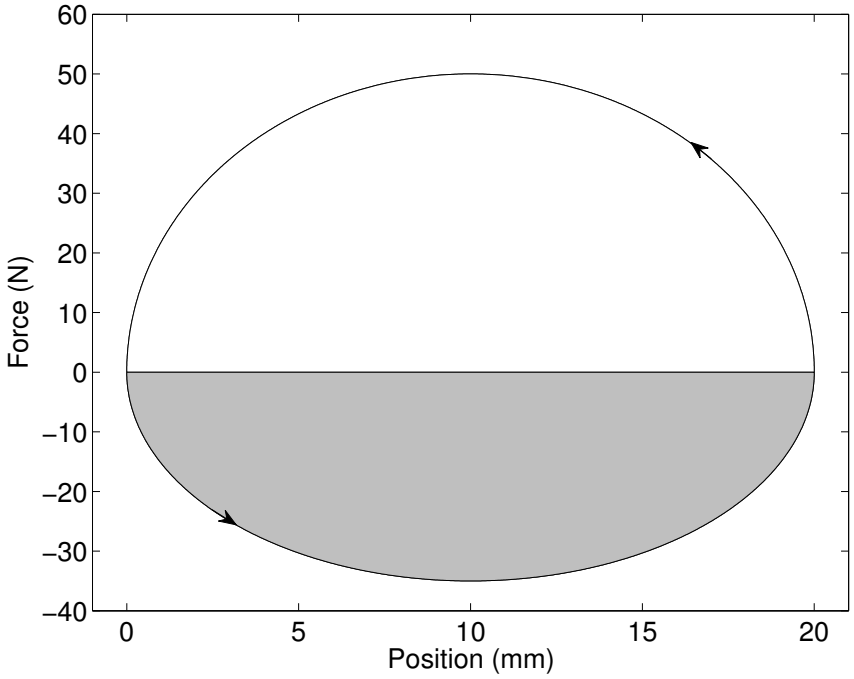

Figure 4-3: The work loop for flapping-wing flight in a pigeon is approximated as shown here; the clear region corresponds to the contribution of the pectoralis, while the shaded region corresponds to that of the supracoracoideus.

Table 4.1: The design specifications for a motor intended to operate a flapping wing propulsion system are given here.

Parameter	Value or Constraint
Mass	$M = 50\,\mathrm{g}$
Force Density	$\bar{F}' = 500\,\mathrm{N/kg}$
Stroke Length	$\ell_s = 20\,\mathrm{mm}$
Temperature Rise	$\Delta T = 110\,^\circ\mathrm{C}$

4.2.2 Optimization Criteria

Our specifications have fixed the mass, force, and stroke, leaving the pole pitch and the stroke factor Y as the only free scaling parameters. There are two distinct approaches we can take to choosing the pole pitch and corresponding electromagnetic geometry—we can optimize for efficiency, and choose the largest pole pitch allowed by the heat removal method, or we can optimize around the heat removal method to give the largest possible pole pitch. We will carry through both optimizations, to see the effect of each choice. Note that the stroke factor and pole pitch will be coupled to each other to satisfy the mass and stroke constraints, and some iteration will be required.

Mathematically speaking, the efficiency optimization criterion is to first simply maximize $\hat{\epsilon}$, then apply a thermal constraint to determine the maximum allowable pole pitch. Because the coil is moving rapidly, Equation 2.68 cannot be used directly;

instead, we must account for the stroke length parameter $Y < 1$ in the thermal resistance and use a modified form of the pole pitch equation:

$$p \leq 2\pi \underbrace{\frac{B_r\sqrt{\sigma\kappa_{\text{eff}}}}{\rho_c}}_{\text{materials}} \times \underbrace{\sqrt{\Delta T}}_{\text{thermal limits}} \times \underbrace{\frac{1}{\bar{F}'}}_{\substack{\text{force}\\\text{density}}} \times \hat{\epsilon}\underbrace{\sqrt{\frac{XY}{\hat{m}\hat{R}_{th}}}}_{\substack{\text{motor}\\\text{geometry}}}. \tag{4.2}$$

To optimize around heat removal, we must choose the manner of heat transfer. The simplest way to provide efficient heat transfer is by forced convection on the outside of the motor. It is reasonable, with liquid cooling in small channels, to achieve a heat transfer coefficient of $\bar{h} = 1000\,\text{W/m}^2\text{K}$. In this case, the dimensionless parameter to be optimized is that present in Equation 4.2:

$$\hat{p} \equiv \frac{\hat{\epsilon}}{\sqrt{\hat{m}\hat{R}_{th}}}, \tag{4.3}$$

where the fill factor X has been removed, as it is a manufacturing constraint, and the stroke factor Y will be treated as a fixed parameter used to constrain the optimization. Once the $\hat{p}$ parameter has been optimized, the pole pitch can be found, and the efficiency compared to that of the efficiency-optimal geometry.

4.2.3 Topology Selection

To optimize the chosen dimensionless parameters, we now must choose the motor topologies to examine so that we can establish the parameters' functional forms. First, let us restrict our attention to tubular motors, rather than planar motor arrangements. Next, we can anticipate that any topologies containing back-iron inside the coil will suffer from saturation at high force densities, and exclude them from consideration. This leaves three reasonable topologies, from those studied in Chapter 3: double-sided Halbach (HCH), Halbach inside and iron outside (HCI), and Halbach inside with iron-backed radial magnets outside (HCRI). As the expected performance gain from including radial magnets with iron is small, and excluding them greatly simplifies motor construction, we will exclude the HCRI topology from consideration. To avoid potential problems with iron losses, we will keep the coil in the HCI topology detached from the iron, which will instead move with the magnets. The dimensionless parameters $\hat{\epsilon}$ and $\hat{m}$ for these topologies can be found in Sections 3.4 and 3.5.

We will also need values of the dimensionless thermal resistance $\hat{R}_{th}$ for these topologies. Given that the motor should be moving rapidly in this application, we can treat each surface in the motor as isothermal, even if the surface is not always directly adjacent to its heat transfer partner. The thermal resistance can thus be calculated by averaging appropriately. For the HCH topology, the thermal resistance is given by a slight modification to Equation 2.32:

Underhung:

$$\hat{R}_{th} = \frac{1}{2\pi}\left[\frac{1}{Y}\left(\frac{1}{2} - \frac{\ln\frac{kr_{c,o}}{kr_{c,i}}}{\left(\frac{kr_{c,o}}{kr_{c,i}}\right)^2 - 1}\right) + \frac{\kappa_c}{\kappa_a}\ln\frac{kr_{mo,i}}{kr_{c,o}} + \frac{\kappa_c}{\kappa_m}\ln\frac{kr_{mo,o}}{kr_{mo,i}} + \frac{1}{kr_{mo,o}\mathrm{Bi}}\right], \tag{4.4a}$$

De-rated:

$$\hat{R}_{th} = \frac{1}{2\pi Y''_{th}}\left[\left(\frac{1}{2} - \frac{\ln\frac{kr_{c,o}}{kr_{c,i}}}{\left(\frac{kr_{c,o}}{kr_{c,i}}\right)^2 - 1}\right) + \frac{\kappa_c}{\kappa_a}\ln\frac{kr_{mo,i}}{kr_{c,o}} + \frac{\kappa_c}{\kappa_m}\ln\frac{kr_{mo,o}}{kr_{mo,i}} + \frac{1}{kr_{mo,o}\mathrm{Bi}}\right], \tag{4.4b}$$

Overhung:

$$\hat{R}_{th} = \frac{1}{2\pi}\left[\frac{1}{Y'}\left(\frac{1}{2} - \frac{\ln\frac{kr_{c,o}}{kr_{c,i}}}{\left(\frac{kr_{c,o}}{kr_{c,i}}\right)^2 - 1}\right) + \frac{\kappa_c}{\kappa_a}\ln\frac{kr_{mo,i}}{kr_{c,o}} + \frac{\kappa_c}{\kappa_m}\ln\frac{kr_{mo,o}}{kr_{mo,i}} + \frac{1}{kr_{mo,o}\mathrm{Bi}}\right], \tag{4.4c}$$

where in the derated case the value Y''_{th} is found by averaging the thermal resistance over the stroke,

$$Y''_{th} \equiv \frac{1 - \frac{2}{\pi}\arctan\frac{2Y''}{\sqrt{1-4Y''^2}}}{\sqrt{1-4Y''^2}}. \tag{4.4d}$$

Finally, we will need to stipulate the nature of the air-gap between the magnets and windings. To keep the fabrication difficulties within reason, we will stipulate that the minimum air-gap shall be $g \geq 50\,\mu$m. To allow thermal expansion, the air-gap will be set to the greater of the minimum and 1% of the radius of the gap. We will assume that the magnets do not require coatings, and neglect the glue thickness holding them together; we will further assume that a coil fill factor X of 60% can be achieved.

4.2.4 Optimization Results

These constraints and performance equations combine to require iteration in several variables. One can look at this process as first requiring iteration on pole pitch, to meet the thermal constraint, then on mean coil radius, to meet the mass specification, and finally on stroke-to-length ratio (Y) to meet the stroke length requirement. For the HCH topology optimized for motor constant, this iteration is straightforward, if tedious, and leads to a shallow optimum near a mean coil radius $kr_m = 3.03$, $Y = 0.426$ ($L = 34.8\,$mm), and $p = 11.8\,$mm, with $\epsilon = 4.04\,\mathrm{N}/\sqrt{\mathrm{W}}$. At this point, the

magnet array is very close to 3 pole pitches long, but the coil would need to be 1.26 pole pitches long. Finding a near-optimal configuration that uses a round number of magnet and coil pitches (multiples of 1/2 pole pitch are reasonable) requires a far more computationally-intensive series of iterations. Also, this approach places the design exactly on the thermal pole-pitch constraint, but it may be more advantageous to use a smaller pole pitch, greatly expanding the design search space.

To reduce the computational effort, we can compute a library of optimized geometries over a range of mean coil radii, gap thicknesses, and stroke-to-length ratios. With this library, iteration merely requires interpolation in the library, rather than re-optimization. Several cross-sections of the design libraries are presented in Section 4.4.1, though note that the libraries cover a three-dimensional parameter space that is challenging to visualize.

Using the library, we can instead look at the design process by choosing a range of possible values of Y and p, determining the mean coil radius for each design point that leads to a motor of the correct mass, and then selecting the "best" design from the resulting map, shown in Figure 4-4 for the HCH topology optimizing the geometry for $\hat{\epsilon}$. These maps were computed on a 20 by 20 grid of points in motor length and pole pitch. To choose motor designs with integral numbers of magnets and coils, we plotted the results against the total motor length $L = \ell_s / (1 - Y)$ rather than Y itself, and against the pole pitch p rather than the resulting dimensionless gap thickness. Note that, for both the coil and the magnet array to comprise integral numbers of half-pole-pitches, the stroke length itself must do so as well, with $p = 2\ell_s/N'$, where N' is an integer. The possible total lengths at each pole pitch are simply multiples of half the pole pitch, leading to the acceptable configurations indicated on the figures.

There are two further issues to consider; first, we can optimize for thermal performance instead, as shown in Figure 4-5. As might be expected, this allows larger pole pitches to be used, at the expense of a reduced motor constant. The other issue is the possibility of using several independent motor structures in parallel to accomplish the task. These smaller motors also have enhanced thermal performance, thanks to the fundamental scaling behavior of linear permanent magnet motors, potentially allowing larger pole pitches or shorter motors to be used. The results of the optimization, considering these issues, are given in Table 4.2.

We can also consider the optimum geometries for a given motor length rather than for a given pole pitch; the results cast this way are shown in Table 4.3. Here, we recognize that the best results in every case are given using a single motor structure, and optimizing for the motor constant. In some cases, the optimum may be skewed by the discretized nature of the acceptable pole pitches. At the shortest motor lengths, interpolation on the performance map does not give the true results due to the coarseness of the original grid, and instead the likely configurations must be directly re-calculated.

Other topologies also behave according to the trends in optimal dimensionless motor constant. The optimization map for the HCI topology is given in Figure 4-6; the very different mass parameter for this topology changes the shape of the map somewhat, but the behavior is broadly similar to that seen in the HCH case. Interestingly, this topology is limited more by the thermal constraint than the HCH topology.

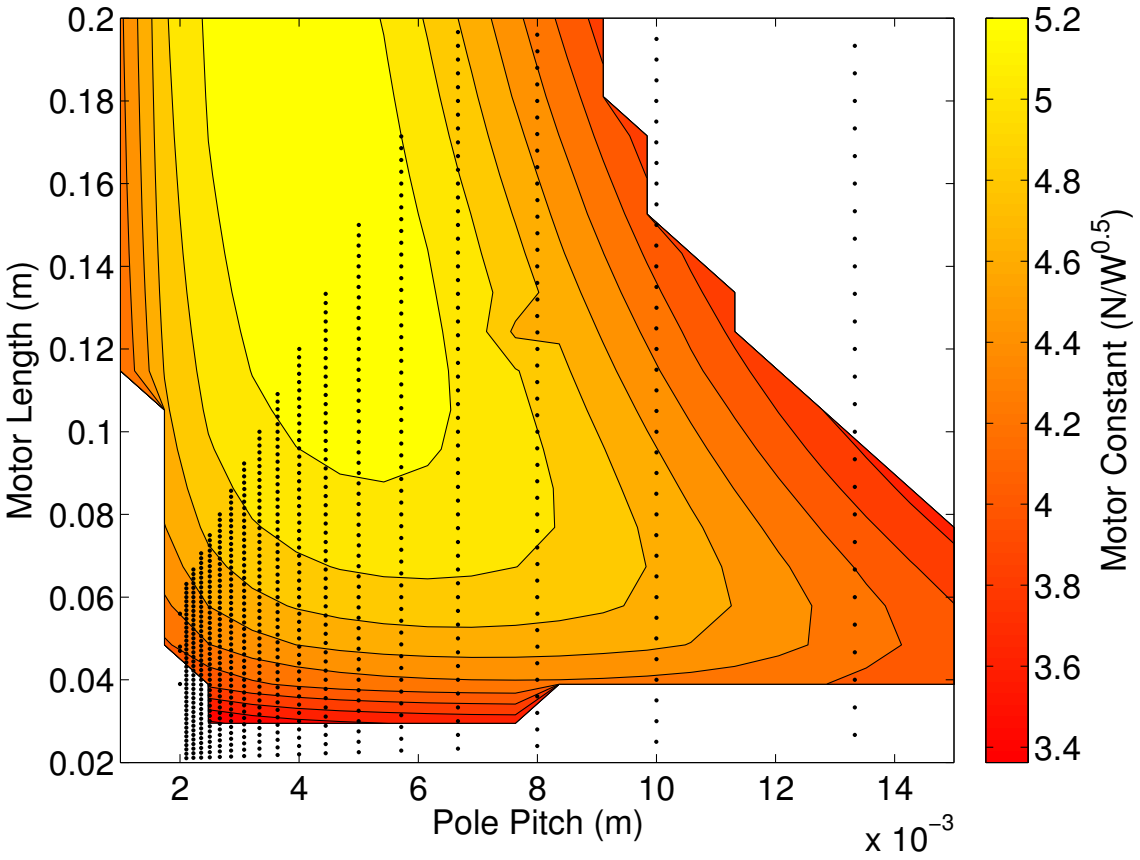

Figure 4-4: This plot gives a map of the motor constant achievable in a 50-gram tubular double-layer Halbach motor, with a stroke length of 20 mm, if it has been optimized for the dimensionless motor constant $\hat{\epsilon}$. Regions outside the contour map indicate either motors with extreme aspect ratios or motors that violate the thermal constraint. Black dots indicate combinations of pole pitch and motor length that allow the magnets and coils to include whole half-pitches of structure, up to a length of 30 pole pitches.

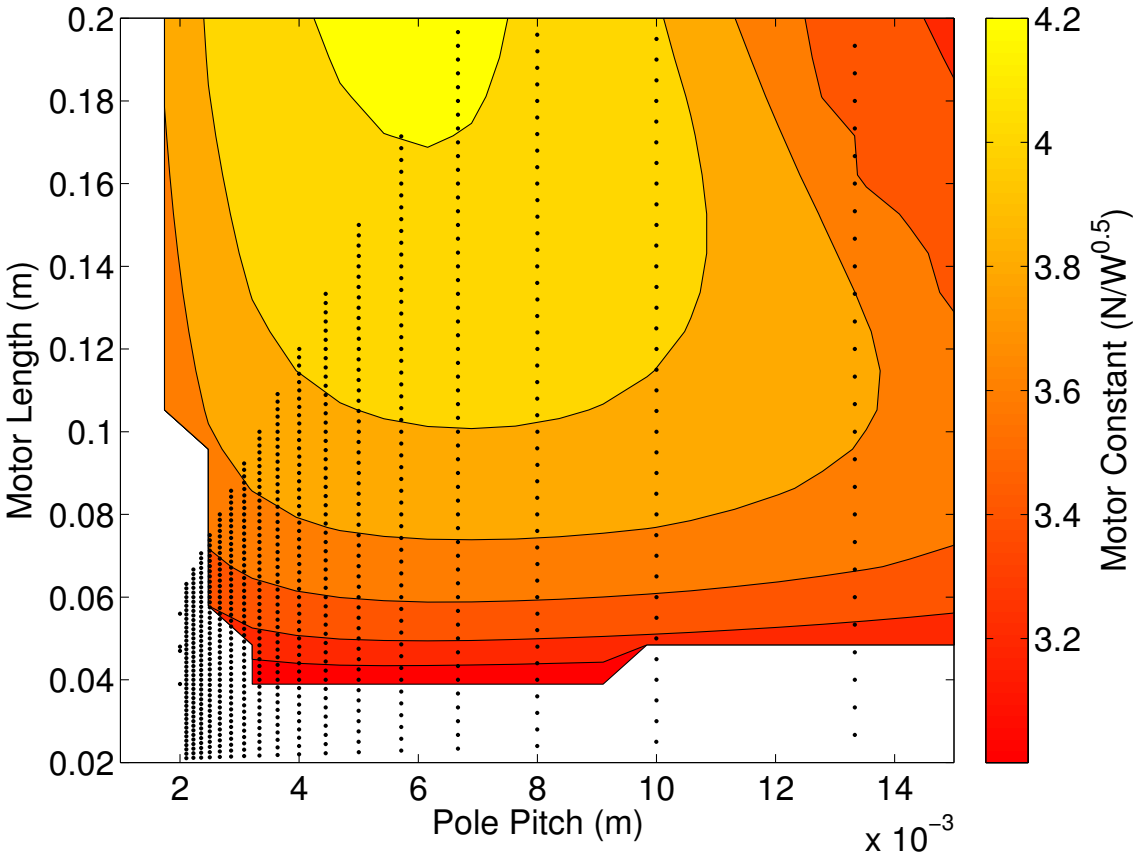

Figure 4-5: This plot gives a map of the motor constant achievable in a 50-gram tubular double-layer Halbach motor, with a stroke length of 20 mm, if it has been optimized for the dimensionless pole pitch $\hat{p}$ (Equation 4.3). Regions outside the contour map indicate either motors with extreme aspect ratios or motors that violate the thermal constraint. Black dots indicate combinations of pole pitch and motor length that allow the magnets and coils to include whole half-pitches of structure, up to a length of 30 pole pitches.

Table 4.2: The range of optimum double-layer Halbach motor geometries for several possible pole pitches and are given here, from the library-based optimization process.

Pole pitch (mm)	Optimal Length (mm)	Motor Constant ($N/\sqrt{W}$)
Optimized for Motor Constant with One Motor Structure		
13.33	53.33	4.29
10.00	65.00	4.77
8.00	84.00	5.03
6.67	106.67	5.19
5.71	125.71	5.27
5.00	145.00	5.32
Optimized for Motor Constant with Two Motor Structures		
13.33	40.00	3.55
10.00	50.00	4.14
8.00	60.00	4.52
6.67	70.00	4.77
5.71	85.71	4.93
5.00	95.00	5.04
Optimized for Pole Pitch with One Motor Structure		
20.00	80.00	3.39
13.33	113.33	3.83
10.00	160.00	4.06
Optimized for Pole Pitch with Four Motor Structures		
13.33	60.00	3.12
10.00	65.00	3.44
8.00	84.00	3.70
6.67	103.33	3.87
5.71	122.86	3.97
5.00	142.50	4.04

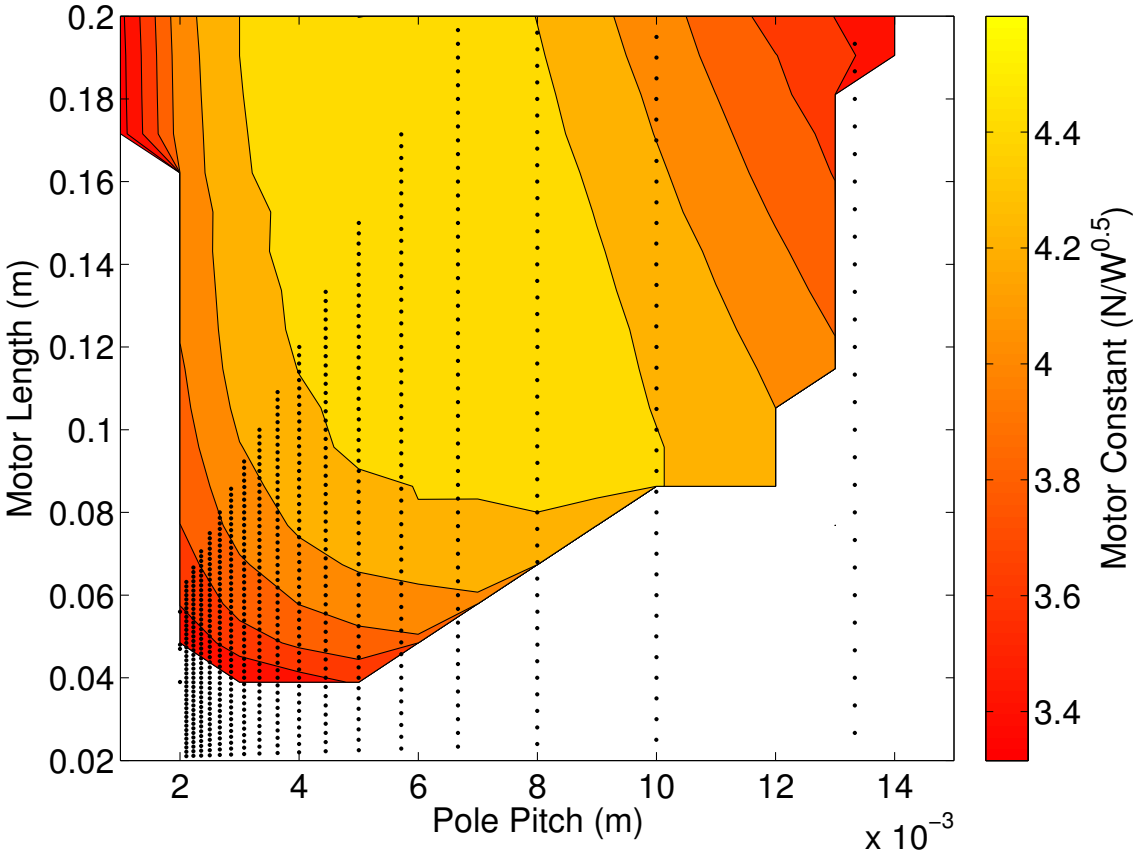

Figure 4-6: This plot gives a map of the motor constant achievable in a 50-gram inner-Halbach outer-iron motor, with a stroke length of 20 mm, if it has been optimized for the dimensionless motor constant $\hat{\epsilon}$. Regions outside the contour map indicate either motors with extreme aspect ratios or motors that violate the thermal constraint. Black dots indicate combinations of pole pitch and motor length that allow the magnets and coils to include whole half-pitches of structure, up to a length of 30 pole pitches.

Table 4.3: The range of optimum motor geometries for several possible motor lengths are given here, from the library-based optimization process for the HCH topology. The motor constant has been re-calculated at each of these configurations, rather than interpolated.

Maximum Length (mm)	Optimal Pole Pitch (mm)	Motor Constant ($N/\sqrt{W}$)
30	6.67	3.69
35	10.00	4.12
40	8.00	4.41
45	8.00	4.57
50	6.67	4.75
55	5.71	4.84
60	6.67	4.94
70	6.67	5.06
80	5.71	5.15
100	5.00	5.26

4.2.5 Design Assessment and Discussion

The optimization data computed from the design library show that, for these design criteria, the achievable motor constant is limited more by the stroke-to-length ratio and the aspect ratio than by the thermal constraint, and the double-sided ironless Halbach topology is superior to the single-sided topology with back-iron. Only if an extremely short motor (under 35 mm) is required does the thermal constraint limit the available performance. The best configurations all occur far from the edges of the allowed design space, with shorter pitches (and thus larger mean coil radii for the same mass) providing higher performance. Thus, a range of different performances are available—the coarsest pitch for the $\hat{\epsilon}$-optimized design leads to a motor with a length comparable to that of the actual pectoralis muscle in a pigeon, which typically ranges from 50 to 60 mm [121]. This motor would drive the design load at the typical 8.7 Hz wingbeat frequency with an efficiency of 22%, slightly higher than that seen in natural muscle. If a shorter pitch is acceptable, a 60 mm motor can achieve a 27% efficiency, and if longer lengths are also allowed the drive efficiency can reach as high as 30% (for $\epsilon = 5.32\,N/\sqrt{W}$). An interesting property of this design space is that the best choice of pole pitch becomes shorter as the motor gets longer; the initial iteration on the thermal constraint simply gave the intersection point between the locus of optimal pole pitches for given motor lengths and the thermal constraint.

As might have been expected, the thermal optimization was able to extend the range of usable pole pitches, with a 20 mm pitch becoming possible. This motor can only reach a 15% efficiency, however, and the motor constants and resulting efficiencies for all of the geometries investigated are much lower than for efficiency-optimized motor designs. Thermal optimization also leads to much longer motors than efficiency optimization, at the same pole pitch, due in large part to the much-reduced mass parameter under thermal optimization.

Under these design conditions, adding more motor structures mechanically in

parallel is of very limited benefit. The optimum motor length at a given pole pitch is reduced, but so is the optimum performance at that pole pitch. The effect of the stroke length parameter y dominates, and even at the same motor length the use of more motor structures requires a smaller value for the mean coil radius, and thus a smaller value of the dimensionless motor constant (as indicated by Figure 3-17). If the performance were constrained more by the thermal requirements, the benefits of using more structures might be more apparent.

4.3 Motor Design for Pulsed Force

A very different motor application is in high-performance needle-free drug delivery [123–126]. While needles have been used for over 200 years [127] to deliver drugs and vaccines, their use has major drawbacks, including hundreds of thousands of annual needle-stick injuries [128] and a massive logistical footprint for needle acquisition and disposal. A number of techniques have been developed since the middle of the 20$^{\text{th}}$ century to deliver drugs without needles, but to date none have achieved widespread clinical use. Existing devices typically use compressed gases [129] or springs [130] to pressurize an ampoule of liquid drug solution, ejecting it as a high-speed jet through a small (100 μm to 300 μm) nozzle. These devices are relatively inflexible in their usage, however, and can be adapted to different injection sites or tissue depths only through mechanical recalibration. The MIT BioInstrumentation Laboratory has developed a more flexible needle-free jet injector (the "MIT jet injector") [124] that employs an electronically-controllable voice coil motor to pressurize the drug, and can be adapted to different injection conditions by means of simple software adjustment.

While the MIT jet injector is far more controllable than other devices, it does have some limitations stemming from its use of an actuator rather than a mechanical energy storage mechanism. In particular, the maximum pressure it can develop using its 500 gram voice coil is limited, and to date a much larger device [125] with a 1.5 kg voice coil has been required for high-pressure, and thus high-velocity, injections to great depths and/or into tough tissues. This larger device requires two-handed use, limiting its suitability in clinical settings. Considerable current interest in drug and vaccine delivery focuses on the shallow tissue depths accessible to the hand-held MIT jet injector [131], but there is also building interest in the delivery of concentrated materials [132] and controlled-release formulations [133]. These materials can have high viscosities and will require very high injector pressures to reach even shallow depths. In order to successfully deliver these materials using the hand-held MIT jet injector, a linear motor in the 500-gram size class must be developed with peak force capability comparable to that of the 1.5 kg voice coil.

4.3.1 Required Specifications

The large-scale jet injector built by Hemond et al. [125] utilizes a BEI-Kimco model LA25-42-000A [134] voice coil actuator to reach fluid pressures of over 60 MPa. In follow-on (unpublished) tests, this system was able to achieve pressures of nearly

Table 4.4: The design specifications for a motor intended to operate a needle-free jet injection system for high-viscosity materials are given here.

Parameter	Value or Constraint
Mass	$M = 500\,\mathrm{g}$
Peak Force Density	$F' = 2000\,\mathrm{N/kg}$
Stroke Length	$\ell_s = 36\,\mathrm{mm}$ (30 mm used)
Number of Phases	$N_\phi = 2$
Temperature Rise	$\Delta T = 110\,^\circ\mathrm{C}$
Force Duration	$\Delta t = 10\,\mathrm{ms}$

100 MPa. The MIT jet injector uses a smaller voice coil, with a peak force of 200 N deveolped for about 10 ms, and a maximum stroke of 25 mm [124]. This force is applied to an ampoule with a cross-sectional area of $10^{-5}\,\mathrm{m}^2$, for a maximum pressure of 20 MPa. To match the capability of the large device in the hand-held system, then, we need to be able to apply 100 MPa over a piston with a cross-sectional area of $10^{-5}\,\mathrm{m}^2$, for a total peak force of 1000 N.

Due to the extremely short duration of the injection force, we can neglect heat transfer from the motor to ambient; thus, the thermal constraint consists of the temperature rise in the heat capacity of the coil alone. We will once again assume a maximum temperature of 150 °C, and an ambient temperature of 40 °C. In a hand-held device that must nonetheless deliver kilowatts of pulsed power, it is important to minimize the complexity of power electronics; we will thus require that the motor be a single-phase voice coil, not a polyphase synchronous motor. (In terms of the analysis in Section 3.3.2, this means $N_\phi = 2$, as one phase can drive two coil groups wound in opposite directions.) These specifications are summarized in Table 4.4.

While they are not specifications per se, we also can set values for our manufacturing constraints at this point. We will fix the inner radius of the inner magnets $r_{mi,i} = 1.5\,\mathrm{mm}$, to provide a channel down the center of the motor that can be used for alignment and to fasten the components of the motor together. We will require that a space of 3 mm be allowed at each end of the stroke, to allow for coil termination and mechanical parts. (This also has the side-effect of excluding the lowest-force parts of the stroke.) We will allow 500 μm of physical air-gap inside the coil, to accommodate a bobbin, and 100 μm of air-gap outside the coil as running clearance. Finally, as before, we will assume a fill factor $X = 60\%$ in the coil.

4.3.2 Optimization Criteria

These specifications and design constraints effectively leave only the stroke-to-length parameter Y as a free scaling parameter; the single-phase nature of the motor couples the pole pitch p to the stroke length ℓ_s. In a single-phase motor, there are nodes of zero motor constant located a distance $p/4$ from the position of maximum motor constant, thus limiting the stroke length to $\ell_s < p/2$ regardless of the total motor length. We do have the ability to choose the number of coils used, corresponding to

one coil per half pole pitch.

The thermal constraint for pulsed operation is equivalent to a constraint on the maximum current density; we can equate the thermal energy and electrical energy dissipated to find the exact constraint, assuming constant power dissipation:

$$\rho_c c_p V_c \Delta T = \frac{J^2 V_c \Delta t}{\sigma},$$
$$J \leq \sqrt{\frac{\sigma \rho_c c_p \Delta T}{\Delta t}}, \tag{4.5}$$

where c_p is the specific heat capacity of the conductor ($c_p = 385\,\mathrm{J/(kg \cdot K)}$ for copper). We can combine this with the expression for the force density (Equation 2.30) to connect the thermal constraint to the dimensionless parameters,

$$\frac{\hat{f}}{\hat{m}} \geq \frac{F'}{XYB_{rem}} \sqrt{\frac{\rho_c \Delta t}{\sigma c_p \Delta T}}. \tag{4.6}$$

(This expression assumes the motor is underhung.) At this point, we should check to see if we can expect to meet this constraint; if we use copper windings and magnets with $B_{rem} = 1.334\,\mathrm{T}$, and assume $Y = 1$, the constraint is $\hat{f}/\hat{m} \geq 9.0 \times 10^{-3}$. For the planar double-sided Halbach motor, optimized for motor constant, the value $\hat{f}/\hat{m} = 0.115$. Thus, we should have considerable latitude in meeting the force specification. We will likely also have to check our designs for demagnetization at this current density, as the maximum allowed current density J is $1.5 \times 10^9\,\mathrm{A/m^2}$, an extremely high value.

Given this thermal constraint, the most sensible choice of optimization criterion for the electromagnetic design is simply the dimensionless motor constant $\hat{\epsilon}$, as we would like to achieve the target force using as little power as possible. While this criterion leads to straightforward optimum designs, the interaction between pole pitch and stroke length will require iteration. We can anticipate that the best designs will have small values of dimensionless mean coil radius as a result of this coupling. An open question, however, is the location in the stroke at which $\hat{\epsilon}$ should be calculated, as calculating it at the midpoint of the stroke where it reaches a maximum may leave the force at the ends of travel too low to meet the specifications. Thus, we will perform optimizations both at the midpoint of the stroke and at the endpoint, and compare the results.

4.3.3 Topology Selection

As in the case of the wing-flapping motor, we will consider only tubular motors, and once again exclude those topologies incorporating central iron due to saturation concerns[1]. Thus, we once again have the HCH, HCI, and HCRI topologies to investigate. For simplicity of construction, in this case we will exclude the HCH topology from consideration. Most high-performance commercial voice coils (including the BEI

[1]We did investigate a topology with inner iron-backed radial magnets and outer iron, but found in FEA that it would saturate before reaching a force of even 40 N!

coil used in the large jet injector built by Hemond et al. [125]) instead use a flux-concentrating topology, with iron in place of the radial magnet in the central Halbach array of the HCI topology. We will call this an ACI topology, and derive a magnetic circuit model for its performance.

In all of the topologies under consideration, we can anticipate that the motor becomes longer and narrower as more coils are used, which pushes the performance progressively lower. Thus, we will use just one coil in our motor, equivalent to using half a pole pitch. However, as we saw in Figure 3-16, there is a performance penalty in such a short motor. We can alleviate this by using iron end-caps of thickness t_e, which in the ideal case present periodic boundary conditions for the magnetic structure and allow us to avoid time-consuming calculations of finite length effects. Doing so restricts us to the underhung configuration (coil shorter than magnets), which conveniently also allows for a strong structure that can resist the tendency of the central magnets to be pulled off-center. This gives us the following explicit relationship between pole pitch, stroke length, and stroke-to-length ratio:

$$Y = 1 - \frac{2\ell_s}{p} = 1 - \frac{k\ell_s}{\pi}. \tag{4.7}$$

We can also determine that $Y = \alpha$, where α is the fraction of the possible winding length that is occupied.

4.3.4 Magnetic Circuit Model

A basic magnetic circuit diagram for the ACI motor is shown in Figure 4-7. There are two reluctances, one in the magnet ($\mathcal{R}_M$) and one in the air gap ($\mathcal{R}_g$), and the magnet acts as a source of magnetomotive force (MMF) $\mathcal{F}_M$ in series with its own reluctance. Neglecting fringing fields, we can easily identify values for the reluctance and MMF:

$$\mathcal{R}_M = \frac{L_M}{\pi\mu_0 r_{mi,o}^2}, \tag{4.8a}$$

$$\mathcal{R}_g = \frac{1}{2\pi\mu_0 L_{conc}} \ln \frac{r_{mo,o}}{r_{mi,o}}, \tag{4.8b}$$

$$\mathcal{F}_M = \frac{L_M B_{rem}}{\mu_0}, \tag{4.8c}$$

where L_M is the length of the magnet, L_{conc} is half of the length of the iron flux concentrator, and we are using the dimensional conventions of Figure 3-13. However, this simple model gives very inaccurate results, predicting zero flux in the magnetic circuit if the flux concentrator is absent and optimal performance when the flux concentrator occupies half the length of the motor.

Instead, we can create a differential magnetic circuit model by assuming that the flux within the magnets is purely axial and the flux in the air gap is purely radial. This requires that we also attempt to account for the fact that some of the radial gap flux must come from inside the magnets; if we take an average gap reluctance across

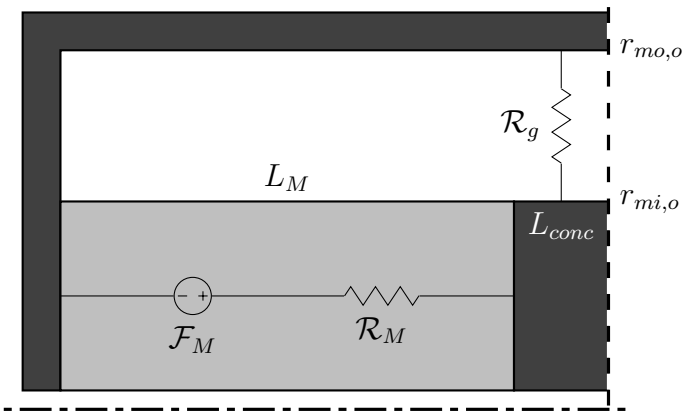

Figure 4-7: A flux-concentrating voice coil employs axial magnets (light gray) and iron (dark gray). The dashed line indicates a symmetry plane, across which no magnetic flux flows, and the dot-dashed line is the motor's centerline. The reluctance of the magnet is given by $\mathcal{R}_M$, and the reluctance of the air gap is given by $\mathcal{R}_g$; iron regions are assumed to have infinite permeability, and thus no reluctance. The magnetomotive force produced by the magnet is denoted by $\mathcal{F}_m$.

the magnet thickness, we find the differential gap reluctance to be

$$\mathrm{d}\mathcal{R}_g = \frac{1}{2\pi\mu_0 \mathrm{d}z}\left(\ln\frac{r_{mo,o}}{r_{mi,o}} + \frac{1}{2}\right), \tag{4.9}$$

A differential model with this reluctance leads to a differential equation for flux $\Phi(z)$,

$$\frac{\mathrm{d}^2\Phi}{\mathrm{d}z^2} - \frac{2}{r_{mi,o}^2\left(\ln\frac{r_{mo,o}}{r_{mi,o}} + \frac{1}{2}\right)}\Phi = -\frac{2\pi B_{rem}}{\ln\frac{r_{mo,o}}{r_{mi,o}} + \frac{1}{2}}. \tag{4.10}$$

This equation has the same form as that of the fin equation, as used in heat transfer [41], and the solutions will look very similar. Solving the differential equation with appropriate boundary conditions yields the result

$$\Phi(z) = \pi r_{mi,o}^2 B_{rem}\left(1 - \frac{\cosh\left(k'\left(L_M + L_{conc} - z\right)\right)}{k'L_{conc}\xi\sinh\left(k'L_M\right) + \cosh\left(k'L_M\right)}\right), \tag{4.11a}$$

where the "fin parameter" k' is given by

$$k' \equiv \sqrt{\frac{2}{r_{mi,o}^2\left(\ln\frac{r_{mo,o}}{r_{mi,o}} + \frac{1}{2}\right)}}, \tag{4.11b}$$

we have defined for convenience

$$\xi \equiv \frac{\ln \frac{r_{mo,o}}{r_{mi,o}} + \frac{1}{2}}{\ln \frac{r_{mo,o}}{r_{mi,o}}}, \tag{4.12}$$

and $z = 0$ lies on the motor's central symmetry plane. We can also find the radial flux density in the air gap along the surface of the magnets and flux concentrator,

$$\boldsymbol{B} \cdot \hat{\boldsymbol{r}} = \begin{cases} \frac{1}{2} B_{rem} k' r_{mi,o} \frac{\tanh\left(k' L_M\right)}{k' L_{conc} \tanh\left(k' L_M\right) + \xi^{-1}}, & z < L_{conc}, \\ \frac{1}{2} B_{rem} k' r_{mi,o} \frac{\sinh\left(k'\left(L_M + L_{conc} - z\right)\right)}{k' L_{conc} \xi \sinh\left(k' L_M\right) + \cosh\left(k' L_M\right)}, & z < L_{conc} + L_M. \end{cases} \tag{4.13}$$

Finally, we can integrate to find the total flux in the portion of the air gap occupied by the coil, Φ_c, once again assuming that the flux is purely radial:

$$\begin{aligned} \Phi_c &= 2\pi r_{mi,o} \int_{z_{bot}}^{z_{top}} \boldsymbol{B} \cdot \hat{\boldsymbol{r}} dz, \\ &= \pi B_{rem} r_{mi,o}^2 \left[2 - \frac{\cosh\left(k'\left(L_M + L_{conc} - z_{top}\right)\right) + \cosh\left(k'\left(L_M + L_{conc} + z_{bot}\right)\right)}{k' L_{conc} \xi \sinh\left(k' L_M\right) + \cosh\left(k' L_M\right)} \right], \end{aligned} \tag{4.14}$$

where z_{top} and z_{bot} are the positions of the top and bottom of the coil; we assume that the coil always covers the flux concentrator. (Larger excursions can be accommodated with a slight adjustment to this integral.) This gives a value for the force

$$F = J \Phi_c \left(r_{c,o} - r_{c,i}\right). \tag{4.15}$$

These equations can be nondimensionalized in the usual manner, if desired.

4.3.5 Electromagnetic Geometry Optimization

Equipped with a model for the flux-concentrating topology, we are ready to perform the design optimization. Our modeling assumptions require the iron in the end-caps to behave ideally, and so we will use the infinite-permeability field models to describe the HCI and HCRI motors, with a design flux density of 2.5 T in the iron. (The ACI model, of course, intrinsically assumes infinite permeability.) Since we are interested in motor constant variation over the stroke, we will find it advantageous to perform a customized optimization, rather than using design libraries. For efficient optimization, we use the outer radius of the inner magnets as a scaling parameter, to satisfy the mass constraint. We can then optimize the remaining dimensions at a variety of values for α, and map out the results.

For example, the optimal motor constants found for the ACI topology are given in Figure 4-8, based on optimizations at the end-stroke, quarter-stroke, and mid-stroke

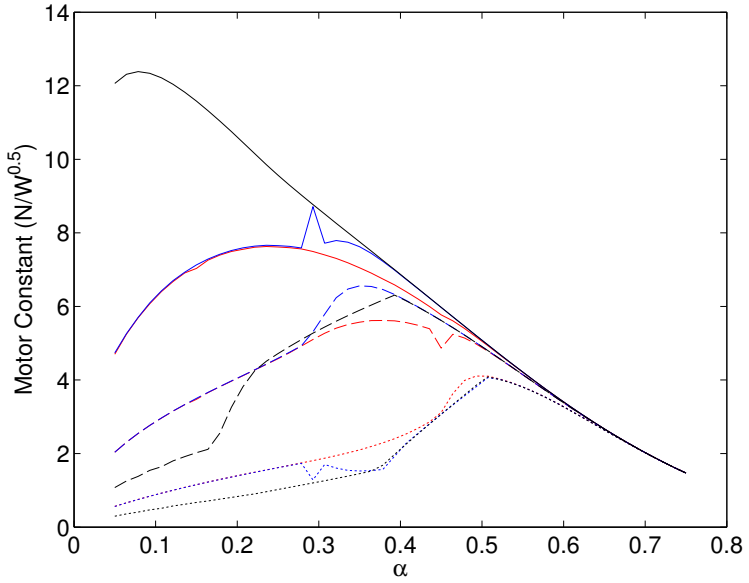

Figure 4-8: The achievable motor constant for a flux-concentrating voice coil according to our design requirements is given at three different positions in the stroke (solid lines at mid-stroke, dashed lines at 7.5 mm from mid-stroke, and dotted lines at 15 mm from mid-stroke). The performance is given for motors optimized at these same three positions, with black lines for motors optimized at mid-stroke, blue lines for motors optimized at 7.5 mm from mid-stroke, and red lines for motors optimized at 15 mm from mid-stroke.

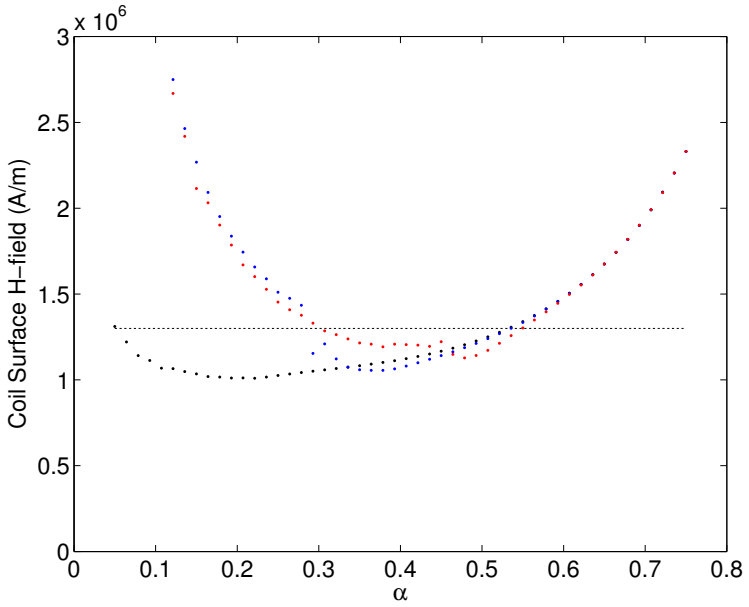

Figure 4-9: The approximate H-field on the interior surface of the coil is given for the three motors from Figure 4-8, when producing 1000 N at mid-stroke. The dotted line indicates the field for the onset of demagnetization in VACODYM 633 HR material.

positions, and measured at these same points. (Note that the model presented in Section 4.3.4 does not allow for a nonzero inner radius of the inner magnets, so $r_{mi,i} = 0$.) Here, it becomes apparent that optimization away from mid-stroke is of limited benefit, but the performance at the different positions can indeed be highly variable. For this topology, the most well-rounded results are obtained for values of α between 0.3 and 0.5. Due to the discontinuous nature of the radial B-field, the optimization misbehaves when the edge of the coil lies very close to the edge of the flux concentrator. It is also worth noting that, when the geometry is optimized at a point where the coil does not overlap the flux concentrator, the flux concentrator is optimized out of existence!

All of these motors remain far from the thermal current limits, but the current densities required are high enough to warrant evaluation of demagnetization. While doing this in detail requires FEA, rather than this magnetic circuit model, we can make an approximate demagnetization check via the thin-coil approximation. We assume the coil is long and infinitely thin, but carries a surface current equal to the current density times the coil thickness. Under these conditions, the H-field inside the coil is simply equal to the surface current density. The resulting field when the motor applies the specified 1000 N force at mid-stroke is given in Figure 4-9, for all three optimizations. All three can reach 1000 N without hitting the demagnetization constraint, though they are very close and FEA study is warranted. None can produce the specified force at the ends of the stroke, however.

The optimization results for the HCI topology follow a similar pattern to that exhibited by the concentrator-free ACI topology, as shown in Figure 4-10. These are also the results obtained if one attempts to include outer radial magnets; the optimization process removes the outer magnets, just as was seen for the periodic motors. This topology outperforms the flux-concentrating topology for $\alpha > 0.25$, especially near the ends of the stroke, and can provide the required force without demagnetizing for $0.25 < \alpha < 0.55$.

4.3.6 Design Assessment and Discussion

According to our models, the Halbach topology is capable of slightly better performance than the flux-concentrating voice coil, both with a higher motor constant and with greater resistance to demagnetization, but there is little benefit to including outer radial magnets. However, both the magnetic circuit model and the field model are approximate in this case, particularly due to the presence of iron end-caps. To confirm these results, finite element analysis is required.

We examined several optimal geometries around $\alpha = 0.4$ for both the HCI and ACI topologies in ANSYS FEA. To test the influence of saturation, we chose two different optimization results for each topology, one with $B_{sat} = 2\,\mathrm{T}$ and one with $B_{sat} = 3\,\mathrm{T}$. As shown in Table 4.5, the performance is actually improved by forcing the iron in the motor into saturation. The results for a larger range of saturation fluxes are given in Figure 4-11; the nominal mid-stroke motor constant reaches a maximum near $B_{sat} = 6\,\mathrm{T}$, and the motor constant when delivering 1000 N actually is best when the iron is entirely removed (as modeled by setting $B_{sat} = 1000\,\mathrm{T}$). Also

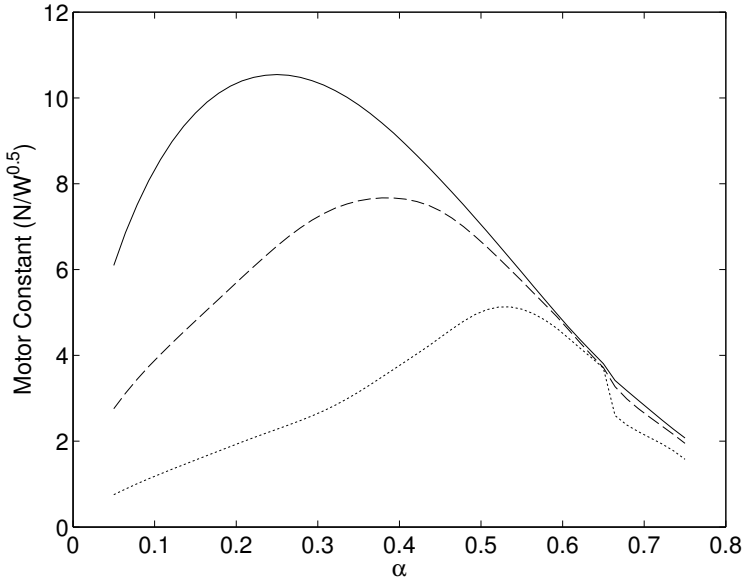

Figure 4-10: The achievable motor constant for a Halbach voice coil according to our design requirements is given at three different positions in the stroke (solid lines at mid-stroke, dashed lines at 7.5 mm from mid-stroke, and dotted lines at 15 mm from mid-stroke). The motor is optimized at the mid-stroke position.

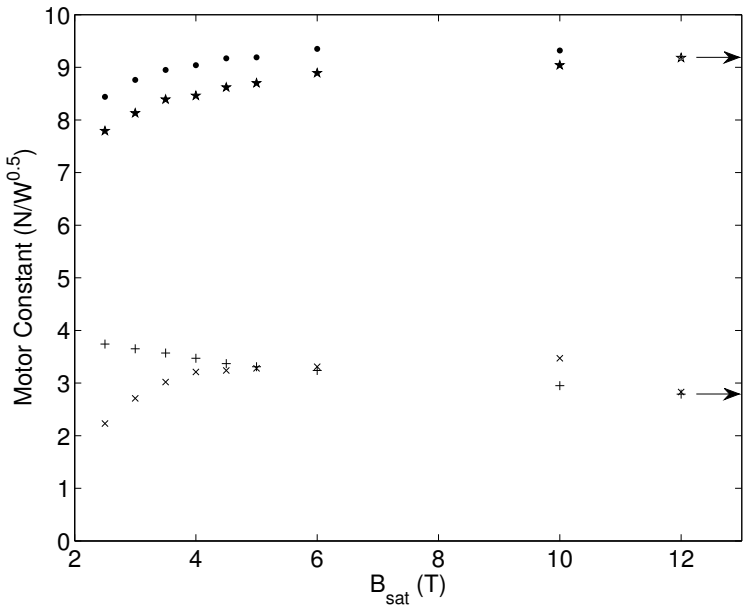

Figure 4-11: The motor constant for a Halbach voice coil (HCI topology) is given for a range of saturation flux design guidelines. Dots indicate the nominal, mid-stroke motor constant, stars the mid-stroke motor constant when delivering 1000 N, crosses the motor constant when delivering 200 N towards the near end of the motor at the end of stroke, and diagonal crosses the motor constant when delivering 200 N towards the far end of the motor at the end of stroke. The points on the right with arrows correspond to $B_{sat} = 1000$ T. In all cases, the motor constant was calculated using ANSYS FEA, and assuming a 100% fill-factor.

Table 4.5: The effect of the choice of saturation flux density is shown here in both the HCI and in the ACI topologies, in terms of the mid-stroke motor constant. Calculation of the motor constant here excludes the effect of the fill factor X.

Parameter		ACI		HCI	
		$B_{sat} = 2\,\mathrm{T}$	$B_{sat} = 3\,\mathrm{T}$	$B_{sat} = 2\,\mathrm{T}$	$B_{sat} = 3\,\mathrm{T}$
$r_{mi,i}$	(mm)	1.5	1.5	1.5	1.5
$r_{mi,o}$	(mm)	12.0	13.0	12.9	14.5
$r_{c,i}$	(mm)	12.5	13.5	13.4	15.0
$r_{c,o}$	(mm)	19.3	20.0	22.8	23.2
$r_{mo,o}$	(mm)	19.4	20.1	22.9	23.3
$r_{fo,o}$	(mm)	21.2	21.4	25.5	25.2
t_e	(mm)	2.9	2.1	4.5	3.1
δ		0.102	0.110	0.140	0.140
α		0.461	0.466	0.376	0.387
ϵ	$(\mathrm{N}/\sqrt{\mathrm{W}})$	7.93	8.21	10.2	10.9

shown here is the behavior at the ends of the stroke, when delivering 200 N of force. At the end of the stroke, variable reluctance force from the coil's proximity to the end-caps becomes important, but is entirely canceled by saturation for $B_{sat} = 5\,\mathrm{T}$.

We also used these FEA studies to assess our designs for demagnetization. In each case, a small number of magnet elements near the corners of the axial magnets reached the demagnetization threshold. However, removing the magnetization from these elements did not result in any appreciable degradation of performance, with a 2% loss of nominal motor constant in the flux-concentrating motor and less than a 1% loss of motor constant in the Halbach motor.

While the models were able to describe the motor performance relatively well, the impact of saturation was clearly very significant. Under these design requirements, the added magnet mass (effectively pushing kr_m higher) allowed by using less iron more than outweighs the loss of field from saturation. Saturation of the end-caps actually has a stronger effect on performance than saturation of the shell, so we do not expect the use of the finite-permeability motor model to significantly improve the accuracy of the design process. Nonetheless, our models have paved the way to significant improvements in pulsed force capability in voice coils, and suggest that the inclusion of radial magnets is more beneficial than the use of iron flux concentrators.

4.3.7 Prototype Development

Based on these results, and with the information gleaned from FEA studies, we chose to build a prototype voice coil employing the optimized HCI topology, with a 4 T design flux density in the iron. The target dimensions of this motor are given in Table 4.6. According to ANSYS FEA studies, we should expect this motor to operate with a mid-stroke motor constant of about $9\,\mathrm{N}/\sqrt{\mathrm{W}}$ at low forces, and $8.5\,\mathrm{N}/\sqrt{\mathrm{W}}$ at 1000 N.

Table 4.6: The major electromagnetic dimensions of our prototype motor for needle-free jet injection are given below; L_r refers to the length of the radially-oriented magnet, and L_c refers to the length of the coil.

Radial Dimensions	Axial Dimensions
$r_{mi,i} = 1.5\,\text{mm}$	$t_e = 2.2\,\text{mm}$
$r_{mi,o} = 13.1\,\text{mm}$	$L_r = 7.7\,\text{mm}$
$r_{c,i} = 13.6\,\text{mm}$	$L_c = 24.8\,\text{mm}$
$r_{c,o} = 21.4\,\text{mm}$	$L_M = 26.6\,\text{mm}$
$r_{mo,o} = 21.5\,\text{mm}$	
$r_{fo,o} = 22.8\,\text{mm}$	

This performance is plotted in Figure 4-12, and compared to the FEA-predicted performance of the motor used in the existing MIT jet injector.

The detailed design, construction, and testing of this motor is described by Brown[2] [135]. A rendering of her design is shown in Figure 4-13. While this motor has not yet been tested at very high forces, at low forces the mid-stroke motor constant is about $8.4\,\text{N}/\sqrt{\text{W}}$, only 7% below the theoretical prediction. Figure 4-14 shows the force produced by the motor over its stroke, closely matching the shape of the curve in Figure 4-12. Features used for structural support added to the mass of the motor, yielding a total of 578 g.

4.4 Library of Optimized Designs

As we have seen, it is very useful to have a pre-computed library of optimized motor designs, as it can save hours of computer time when the design requirements demand complex iteration. This section illustrates important cross-sections of several design libraries; the complete libraries are available upon request from the author. We also present the large-radius (planar) overall optimum designs for each objective function, neglecting physical air-gaps, fill factors, and stroke length effects. For brevity, only the libraries for the underhung ironless double-sided Halbach motor are presented, except in the case of motor constant optimization.

Each library contains the optimized geometries and properties of motors with three free dimensionless parameters: mean coil radius kr_m, physical air-gap kg, and stroke length parameter Y. The fill factor X is set to a reasonable value for a coil of round wire, $X = 0.6$. The material properties are set as follows: $\rho_m = 7600\,\text{kg/m}^3$, $\rho_c = 8940\,\text{kg/m}^3$, $\rho_f = 7850\,\text{kg/m}^3$, $\rho_i = 1350\,\text{kg/m}^3$, $\kappa_a = 0.026\,\text{W/(m}\cdot\text{K)}$, $\kappa_m = 9\,\text{W/(m}\cdot\text{K)}$, $\kappa_{eff} = 1.5\,\text{W/(m}\cdot\text{K)}$, and $\kappa_f = 64\,\text{W/(m}\cdot\text{K)}$. For iron-bearing motors, the iron is assumed to be 1018 steel, with the B-H curve given in Figure 3-14, and the magnet is assigned $B_{sat} = 1.344\,\text{T}$. We assume that cooling is provided on the outside of the motor only, and require that the coil be built with $\alpha = 1$.

[2]This undergraduate senior thesis was supervised by the author.

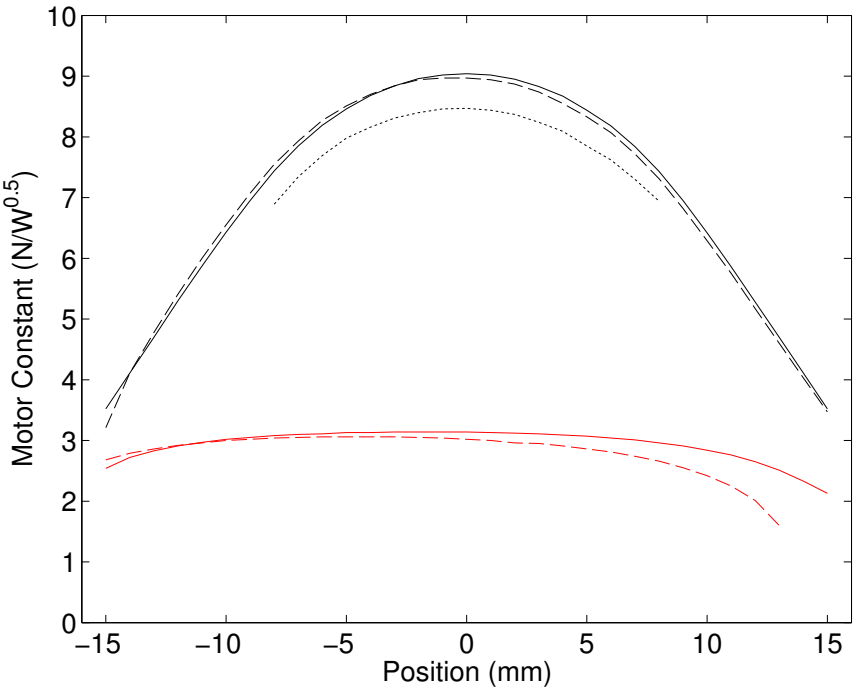

Figure 4-12: The motor constant of our proposed voice coil (black lines), as determined by ANSYS FEA, is compared to that of the motor currently used in the MIT jet injector (red lines) at several different force levels. The behavior at low force ($J = 10^6\,\mathrm{A/m^2}$) is indicated by a solid line, the behavior when delivering 200 N is indicated by a dashed line, and the motor constant at 1000 N is indicated with a dotted line (for our new design only).

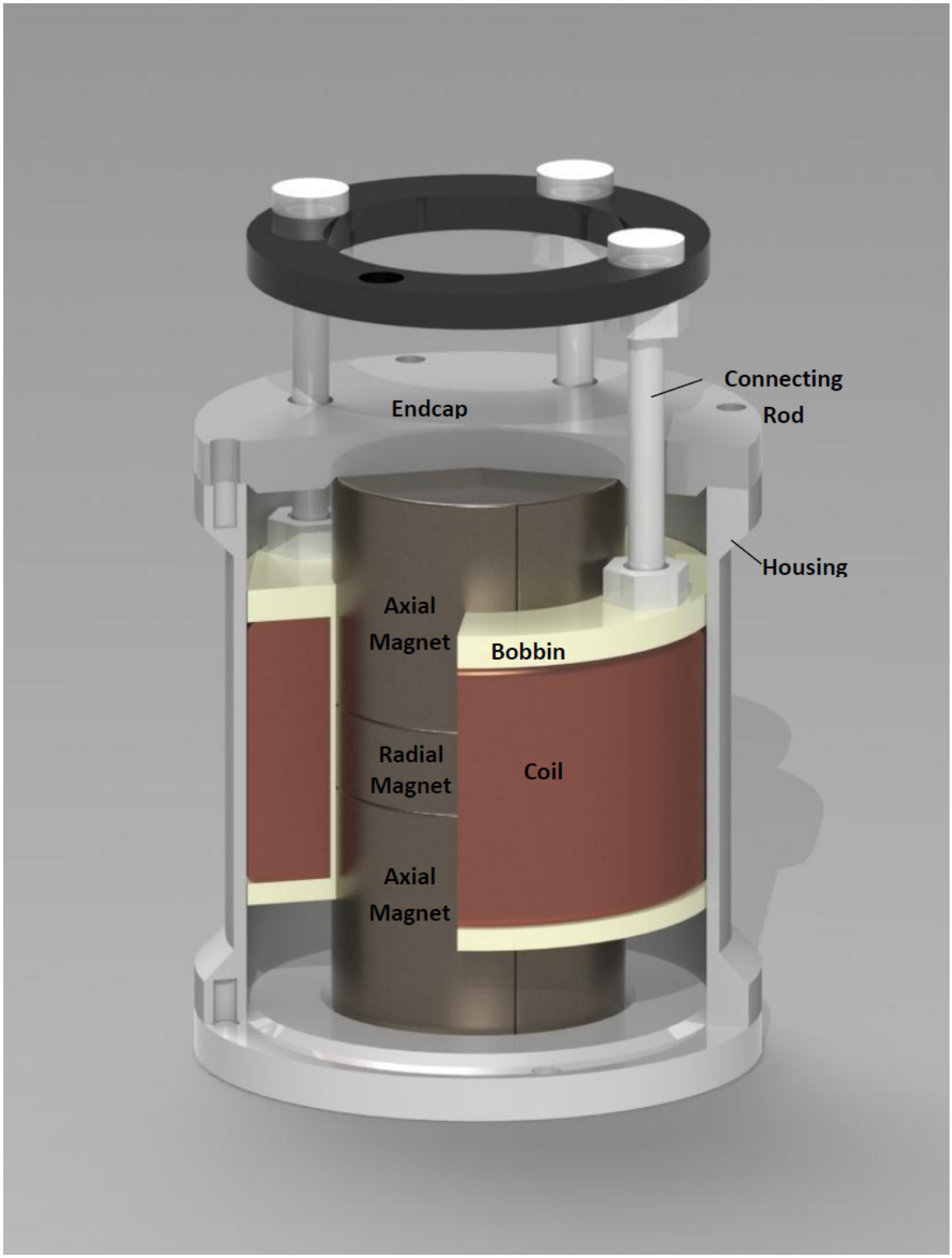

Figure 4-13: This rendering shows the major components of the high-force voice coil constructed by Brown. Figure used with permission from [135].

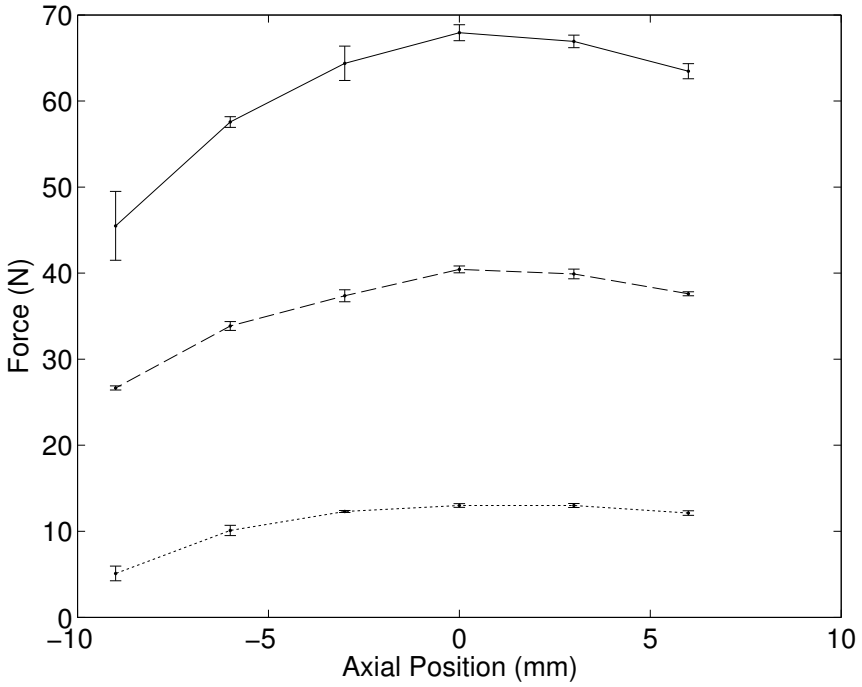

Figure 4-14: The force experimentally produced by the prototype voice coil is shown at three different applied current densities, showing agreement with the force profile illustrated in Figure 4-12. All measurements correspond to the force in the pushing direction, with the dotted line measured at 1 A (2.3×10^6 A/m^2), the dashed line measured at 3 A (6.9×10^6 A/m^2), and the solid line measured at 5 A (1.1×10^7 A/m^2). Error bars indicate 95% confidence intervals. Data are from [135] and used with permission.

4.4.1 Optimum Motor Constant

In this case, as we have previously discussed, the appropriate optimization parameter is $\hat{\epsilon}$. The behavior of the double-sided Halbach motor optimized with this parameter is given in Figure 4-15. We supply a library for the HCI configuration under these conditions, as well; this library required approximately 200 hours of computer time to calculate. The behavior of the HCI configuration is shown in Figure 4-16.

These libraries follow the trends explored in Section 3.7.1, with the double-sided Halbach motor providing the higher motor constant. As might be expected, there is a harsher penalty for air-gaps in the iron-cored motor; if one were to think in terms of the method of images, the air-gap between the coil and iron would behave as though it had twice its thickness.

4.4.2 Optimum Conductive Heat Transfer

Here, we will assume that the motor operates with a Biot number approaching infinity; i.e. active cooling is provided, and performance is limited by conduction heat transfer within the motor. We will also assume the motor to be stationary, with no axial heat transfer. Thus, the appropriate optimization parameter will be $\hat{p}$; the corresponding behavior is summarized by Figure 4-17.

Under these conditions, the thermal penalty of thick magnets outweighs the electromagnetic benefits, unless the impact of a thick, forced air-gap minimizes the effectiveness of thinning the magnets in reducing thermal resistance. Thus, the optimal performance does not occur for the planar, gap-free motor, but rather at an intermediate radius ($kr_m \approx 2.5$) with a small air-gap. However, the electromagnetic performance of motors optimized in this manner is also very poor compared with that found when efficiency is the optimization goal, and this design approach is only advantageous if a large increase in pole pitch for a set of thermal constraints is required.

4.4.3 Optimum Convective Heat Transfer

Here, we will instead neglect conduction thermal resistance within the motor, and consider only a convective thermal resistance on the motor exterior. We will once again assume the motor to be stationary, with no axial heat transfer. In this case, the appropriate optimization parameter is $\hat{p}_0$; the corresponding behavior is summarized by Figure 4-18.

In this case, the optimization works to increase the surface area of the motor, by penalizing the dimensionless mass. The performance trends are very similar to those seen with the designs optimized for motor constant, though with significantly lower motor constant values.

4.4.4 Optimum Force Constant

If the motor is to be operated under transient conditions, with little heat transfer available at all, it might be advantageous to optimize for the force per unit current

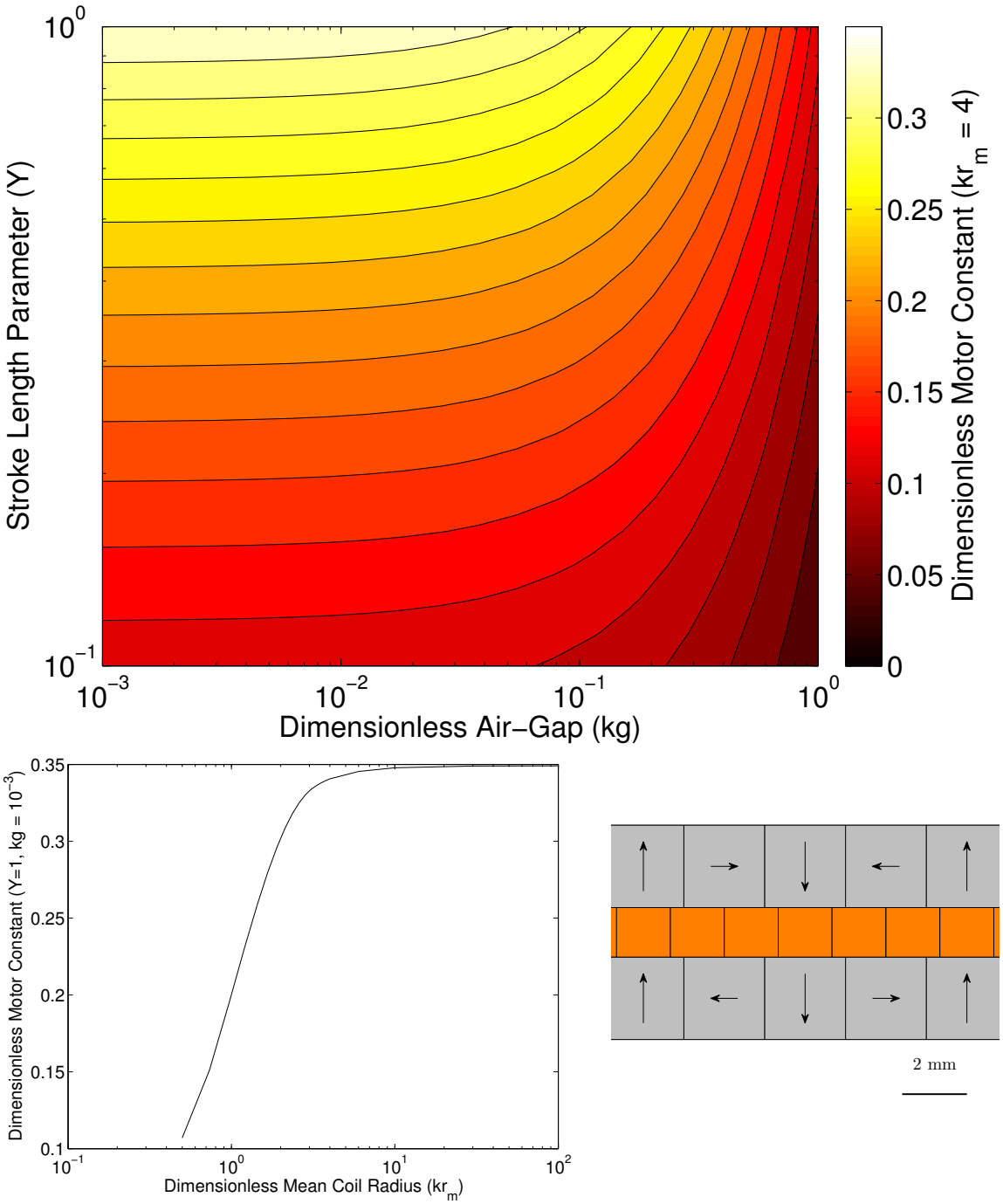

Figure 4-15: The behavior of double-sided Halbach motors optimized for motor constant is summarized here, with the influence of stroke length and air-gap (top), the influence of mean coil radius (bottom left), and the planar optimal geometry (bottom right) given. The dimensionless motor constant is adjusted for the influence of Y, as per Equation 2.42.

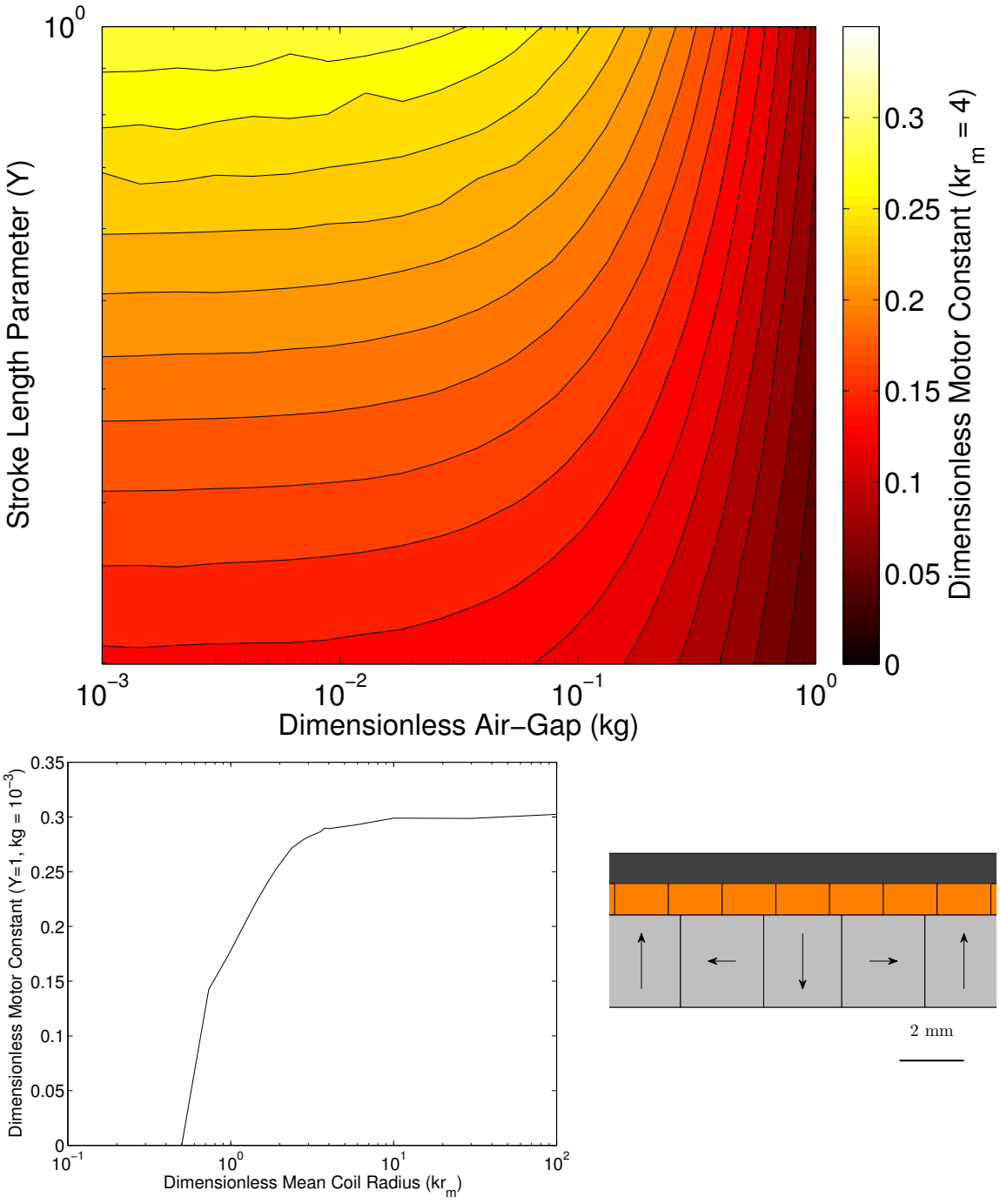

Figure 4-16: The behavior of single-sided Halbach motors with iron cores optimized for motor constant is summarized here, with the influence of stroke length and air-gap (top), the influence of mean coil radius (bottom left), and the planar optimal geometry (bottom right) given. The dimensionless motor constant is adjusted for the influence of Y, as per Equation 2.42.

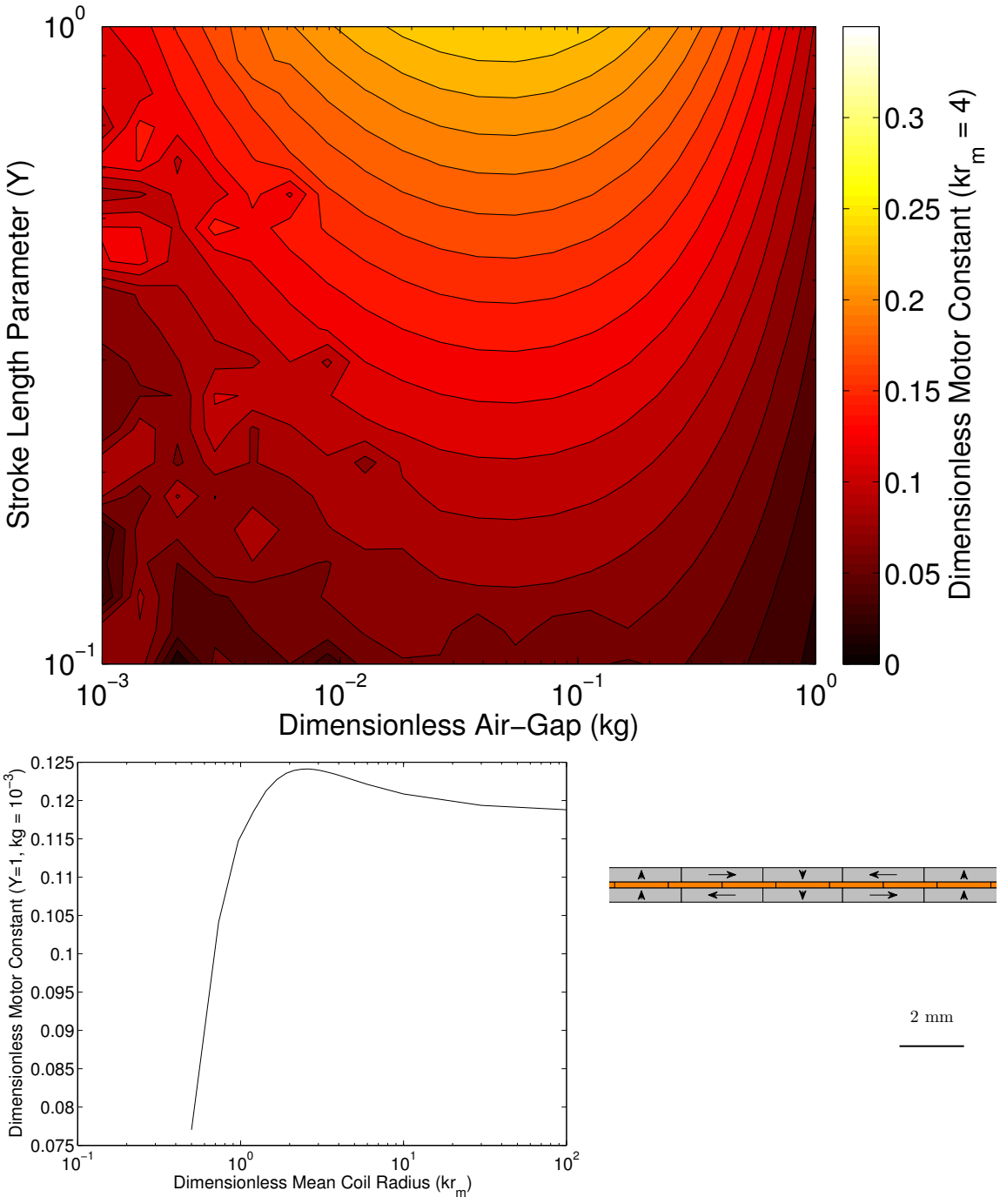

Figure 4-17: The behavior of double-sided Halbach motors optimized for conduction-limited heat transfer is summarized here, with the influence of stroke length and air-gap (top), the influence of mean coil radius (bottom left), and the planar optimal geometry (bottom right) given. The dimensionless motor constant is adjusted for the influence of Y, as per Equation 2.42.

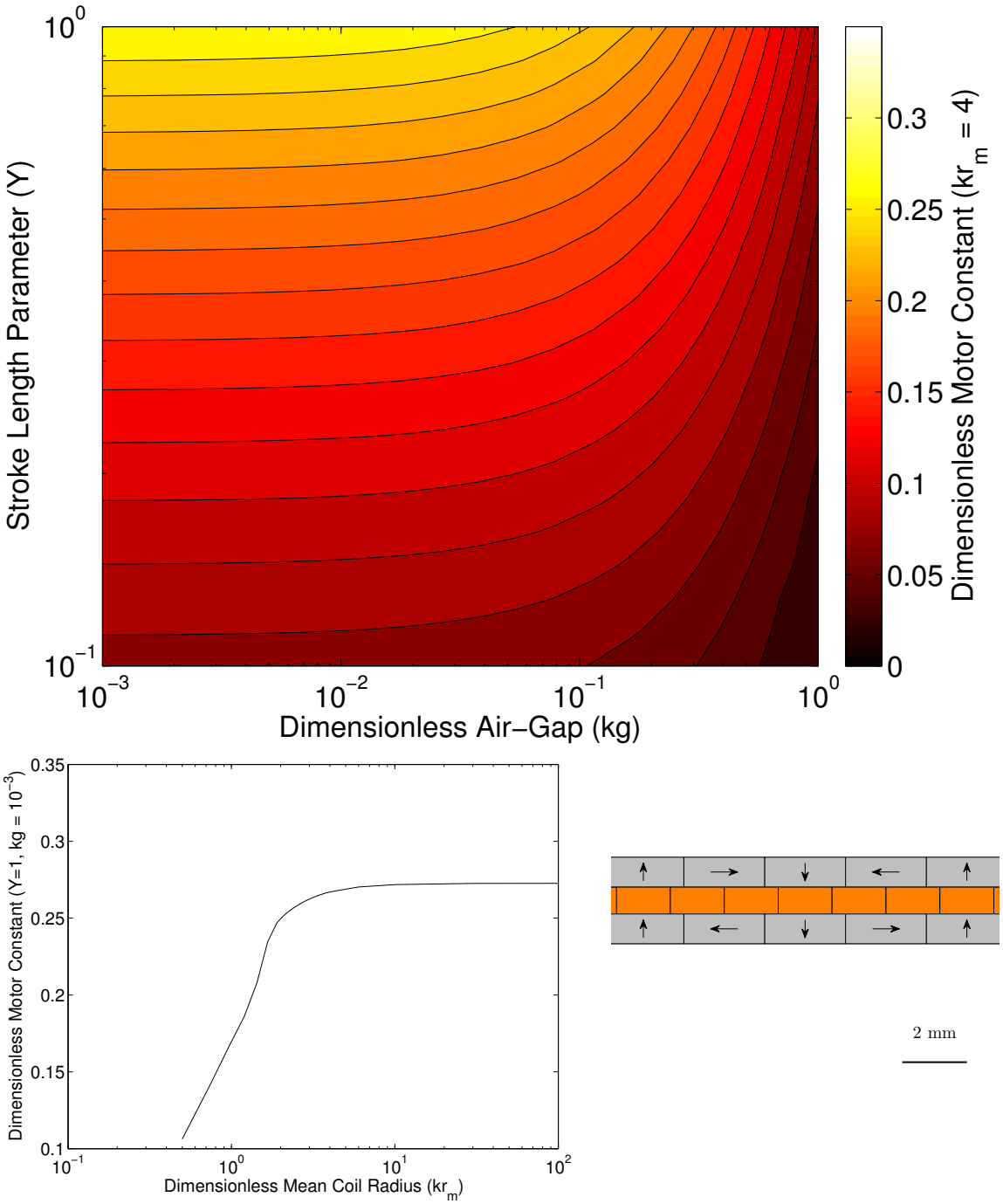

Figure 4-18: The behavior of double-sided Halbach motors optimized for convection-limited heat transfer is summarized here, with the influence of stroke length and air-gap (top), the influence of mean coil radius (bottom left), and the planar optimal geometry (bottom right) given. The dimensionless motor constant is adjusted for the influence of Y, as per Equation 2.42.

density ("force constant") rather than the motor constant. We saw this arise in our discussion of the design of the jet injector motor, though in that case the pulsed force requirement was so high as to render demagnetization more important than heat. Nonetheless, we can identify a set of dimensionless parameters to optimize for in this case, $\hat{f}/\hat{m}$, for which the results are given in Figure 4-19.

This optimization criterion favors the inclusion of more coil in the motor, relative to magnets. The reduction in motor constant from the designs optimized for it is modest, despite the large change in geometry. The greater coil thickness, however, will render motors optimized for force constant more prone to demagnetization at high current densities.

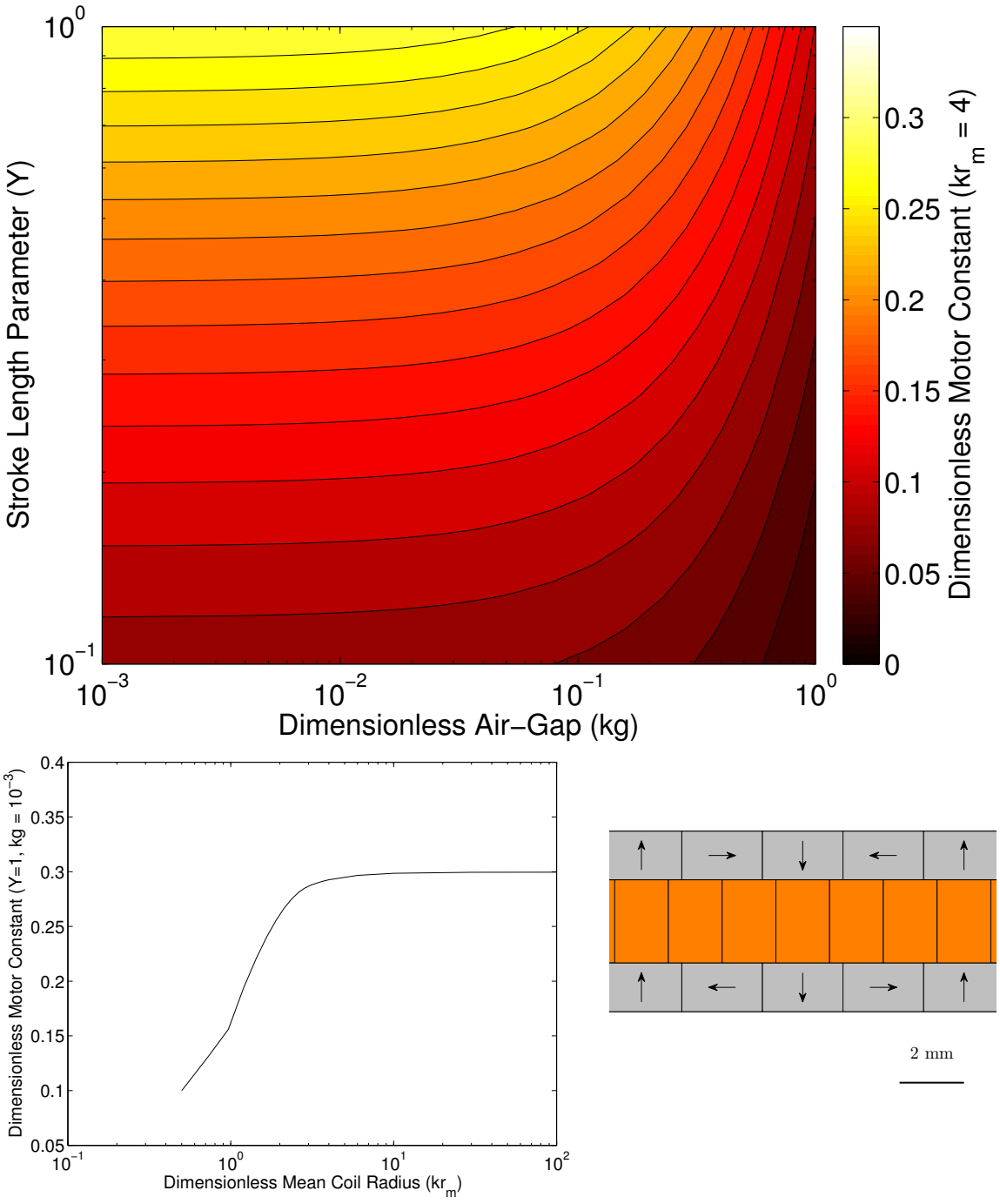

Figure 4-19: The behavior of double-sided Halbach motors optimized for maximum force per unit current density is summarized here, with the influence of stroke length and air-gap (top), the influence of mean coil radius (bottom left), and the planar optimal geometry (bottom right) given. The dimensionless motor constant is adjusted for the influence of Y, as per Equation 2.42.

Chapter 5

Experimental Realization

In order to validate our models and design approach, we set out to build a motor similar to that designed in Section 4.2 and evaluate its performance. This chapter describes the detailed design of this exemplar motor, and the changes and additional features required to turn an optimized coil and magnet geometry into a whole, manufacturable motor. Our primary means of performance evaluation will be static force testing over the entire stroke, and the design of the test system as well as the bench-top cooling system will be discussed. The performance of our motor will then be compared to that of other motors of similar mass and stroke.

5.1 Electromagnetic Design and Predicted Performance

As we showed in Section 4.2.5, optimizing the dimensionless motor constant $\hat{\epsilon}$ yields a motor with both good electromagnetic performance and reasonable thermal performance, so long as the pole pitch can be kept short. Based on the bird muscle example, we chose to make an underhung double-sided Halbach motor designed by optimization of $\hat{\epsilon}$, having an outside diameter of 25 mm, an overall length of 48 mm, and a stroke of 18 mm. To keep the individual magnet sizes reasonable, we chose a target pole pitch of 12 mm; while somewhat larger would be necessary to achieve bird-scale force densities, we expected this pole pitch to still provide considerably greater force density than commercially-available motors. We assumed high-performance square magnet wire would be used [61], giving $X = 0.75$, wound as a concentrated three-phase winding. To simplify manufacturing, we forced the radial and axial magnets to have equal widths; the optimal widths were not very different for motors with $kr_{mi,i} > 0$, in any event. Finally, we required that there be an air gap equal to 1% of the radius on both the inside and outside of the coil, to provide running clearance. These design constraints are summarized in Table 5.1 below.

From this point, numerical optimization for $\hat{\epsilon}$ was straightforward using Equation 3.66b, Equation 3.64, and Equation 3.65. Optimizing without accounting for Y gives the following values for the motor geometry: $kr_{mi,i} = 2.06$, $kr_{mi,o} = 4.11$, $kr_{c,i} = 4.15$, $kr_{c,o} = 5.07$, and $kr_{mo,i} = 5.12$. This geometry is shown to scale in

Table 5.1: The design constraints for the motor prototype are given here in dimensionless form, where applicable.

Parameter	Value or Constraint
Pole Pitch	$p = 12\,\text{mm}$ $k = 524\,\text{m}^{-1}$
Magnet Length	$L = 4p$
Coil Length	$Y = 0.625$
Outside Diameter	$kr_{mo,o} = 6.54$
Air Gaps	$kr_{c,i} = 1.01kr_{mi,o}$ $kr_{c,o} = 0.99kr_{mo,i}$
Magnet Width	$\delta_r i = \delta_r o = 0.5$

Figure 5-1. (Including the effect of the stroke-to-length ratio changes the geometry only slightly.) Let us assume that the magnets are made from VACODYM 633 HR material ($B_{rem} = 1.35\,\text{T}$ at $20\,^\circ\text{C}$) [66]; in this case, the expected motor constant is $\epsilon = 9.12\ \text{N}/\sqrt{\text{W}}$ ($\hat{\epsilon} = 0.322$). Furthermore, let us assume that the effective heat transfer coefficient on the exterior of the motor is very high, the coil thermal conductivity is $\kappa_c = 1.5\ \text{W}/(\text{m}\cdot\text{K})$, and the magnet thermal conductivity is $\kappa_m = 9\ \text{W}/(\text{m}\cdot\text{K})$ [42]; in this case the thermal resistance $R_{th} = 2.6\ \text{K/W}$ ($\hat{R}_{th} = 0.18$).

To calculate the thermal resistance for this motor, we neglect axial heat conduction and assume a stationary coil, which permits the dimensionless thermal resistance to be calculated using Equation 2.32a, with an added multiplicative factor of Y^{-1}. So long as the coil is driven with the current distribution in phase with the field produced by the magnets, the current itself has little tendency to demagnetize the magnets; the maximum operating temperature of the inner magnets is about $80\,^\circ\text{C}$, and of the outer magnets $60\,^\circ\text{C}$, before self-demagnetization becomes a problem. Fortunately, the cooling configuration ensures that the outer magnets will always be much cooler than the inner magnets, leaving the inner magnet limit as the effective coil temperature limit.

5.1.1 Manufacturing Changes

As the mechanical design of the motor was developed, and the parts of the motor went into manufacturing, it became apparent that certain changes to the magnet and coil dimensions were needed. First, as will be discussed in Section 5.2, we chose to have the inner magnets serve as the coil's linear motion bearing. Thus, the clearance inside the coil was reduced, such that $r_{c,i} = 7.88\,\text{mm}$. Using this dimension, we then chose the actual winding pattern. Rather than the square magnet wire assumed for the initial fill factor of $X = 0.75$, round magnet wire was used, with each phase group in the coil comprising 5 layers of 5 turns each, 28 AWG heavy-insulation magnet wire[1] rated for $200\,^\circ\text{C}$. This winding instead has a fill factor of $X = 0.55$. The coil structure also requires the removal of portions of the inner magnets, which can be

[1] McMaster-Carr 7588K73

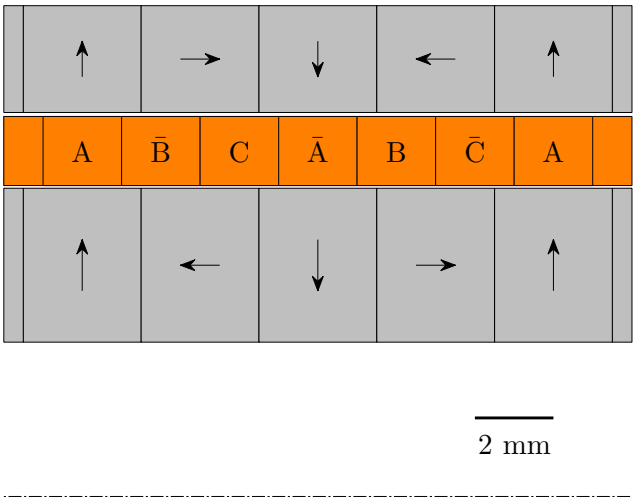

Figure 5-1: The optimum geometry for one period of the prototype motor is shown here, optimized for $\hat{\epsilon}$ but neglecting the effect of the stroke-to-length ratio. Letters denote the windings corresponding to each of the three phases, and windings labeled with an overbar are wound in the opposite direction of those without. The actual dimensions have the values $r_{mi,i} = 3.93\,\text{mm}$, $r_{mi,o} = 7.85\,\text{mm}$, $r_{c,i} = 7.92\,\text{mm}$, $r_{c,o} = 9.68\,\text{mm}$, $r_{mo,i} = 9.78\,\text{mm}$, and $r_{mo,o} = 12.50\,\text{mm}$.

approximated as reducing their remanence by the fraction of area removed, 15.4%. Also, for manufacturability the radial magnets must be constructed from discrete segments of uniform magnetization, rather than being purely radial in nature. Four segments were used, reducing the effective strength of the radial magnets by 10% as discussed in Section 3.4.5.

To ensure that the magnets and coil would fit together, the coil was wound and impregnated before cutting the magnets. It quickly became apparent that it was not possible to wind this coil without providing spacers between phase groups. Adding these spacers increased the pitch length of the winding to $p = 14.5\,\text{mm}$, and reduced the effective fill factor to $X = 0.44$. Once the coil was wound, its outside diameter was also found to be slightly oversize, with $r_{c,o}$ as large as 9.80 mm in places. While re-impregnation of the coil under pressure in a rigid mold reduced the radius to a consistent 9.78 mm, it was still necessary to slightly enlarge $r_{mo,i}$, to 9.84 mm. The change in pole pitch also necessitated a change in the overall dimensions to stay close to the original stroke and overall length; the magnet array would now only be 3.5 pitches long (50.8 mm), and the coil would be 2 pitches long (29 mm), resulting in $Y = 0.57$ and a stroke of $\ell_s = 21.8\,\text{mm}$. These changes in geometry do not appreciably change the self-demagnetization temperatures.

A summary of the changes in motor properties resulting from these geometry changes can be found in Table 5.2. After accounting for the design and manufacturing changes, the expected motor constant is about 33% lower, but the thermal resistance is expected to be 30% lower. The reduction in motor constant is primarily caused by the dramatic reduction in fill factor from that specified in the initial optimization; winding

Table 5.2: The predicted performance of the motor is given here under three sets of conditions: the theoretical performance, as given by the optimization; the nominal performance, accounting for the details arising in design; and the expected performance, also accounting for the changes in manufacturing. The maximum force is that corresponding to an 80 °C coil temperature and 20 °C coolant temperature, while all other properties are calculated with the motor at 20 °C.

Condition	$\hat{\epsilon}$	$\epsilon\ \left(\mathrm{N}/\sqrt{W}\right)$	$R_{th}\ \left(\mathrm{K/W}\right)$	M (g)	F_{max} (N)
Theoretical	0.322	9.12	2.6	141	39
Nominal	0.299	6.95	2.6	129	30
Expected	0.304	6.09	1.8	132	31

strategies that can improve the fill factor, such as square wire, edge-wound ribbon wire, or thinner inter-winding spacers would be highly beneficial. The improvement in thermal resistance is caused by the reduction in specified air gap, as the thermal resistance is dominated by the air even at very narrow gap widths. Note that the motor constants were calculated using only the first harmonics of magnetization and current, and therefore represent an average motor constant over the stroke.

5.2 Mechanical Design and Manufacturing

A functioning motor requires more than a set of magnet and coil dimensions—the magnets must be held in place, cooling must be provided, current must be delivered to the coil appropriately, and the force must be transferred from the coil to the load. For maximum performance, these provisions must be made using as little mass as possible and without infringing upon the electromagnetic geometry. At the same time, however, the motor components must be manufacturable, and the whole motor must be possible to assemble. We chose to design the motor so that the structural and cooling systems would be largely decoupled, with the cooling system only on the outer surface of the motor and the structural interfaces located primarily on the inner magnets.

5.2.1 Magnets and Coil

In order to keep the mass added by the structural components to a minimum, we chose to rely on the magnets and coil themselves to carry most of the loads in the system. This required adhesive assembly, with a careful choice of the adhesives used in each part of the system. As shown in Figure 5-2, the inner and outer magnets were each divided into four segments for manufacturing. Each segment was provided with features to keep the segments aligned in a circle, and a 100 micrometer gap was left between segments to allow space for the adhesive. A similar gap was left between magnets in the axial direction, maintained via the use of small (2 mm square) spacers made from office paper. To support the forces on the coil and transmit motion to the load, four carbon fiber rods (1.7 mm diameter) were located inside the coil; 2 mm wide

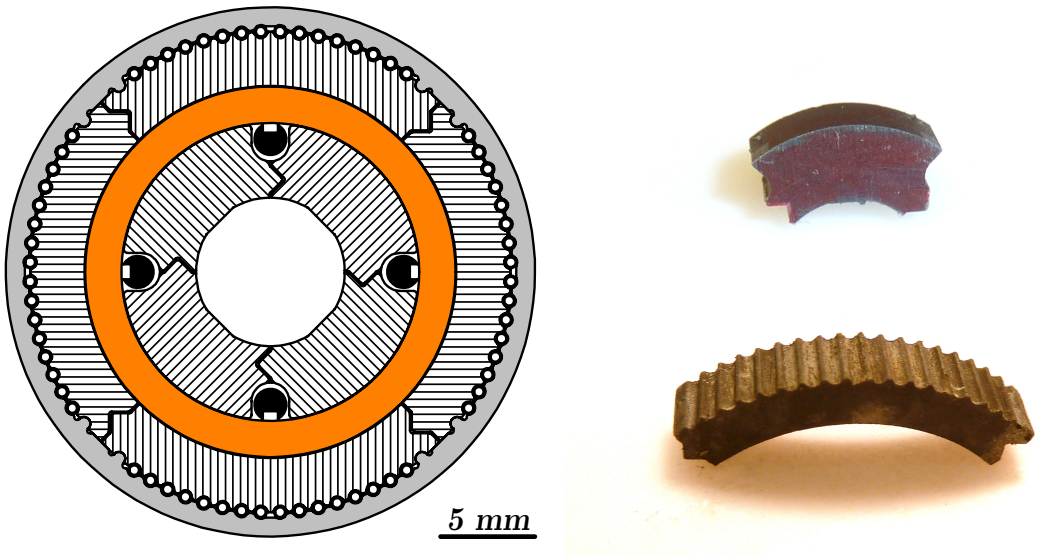

Figure 5-2: A cross-section of the as-built motor in the $r\theta$-plane (left) shows several differences from the optimum geometry (of Figure 5-1). The magnets (hatched parallel to magnetization) have been split into four segments to allow manufacturing, with alignment features on the end faces; grooves have been added to the outside of the magnets, to hold cooling tubes; and large channels have been removed from the inner magnets, to fit support rods (black) for the coil (orange). In addition to these changes, a magnesium sleeve (light gray) has been added outside the outer magnets for mechanical support. A photo of the actual magnet segments is shown on the right.

channels were removed from the inner magnets to fit these rods. The rods have milled channels (0.8 mm wide and 0.5 mm deep) to fit the wires between each phase group in the coil; as only three of the rods are needed to contain the phases, the fourth rod's groove instead contains a type T thermocouple, with its junction placed in the center of the coil. The outer magnets were given grooves to fit cooling channels, as will be discussed further in Section 5.2.2.

Rather than include an external bearing, we instead chose to use the magnet-coil interface as a bearing. To do this, the coil inside diameter was adjusted to be just larger (30 μm) than the inner magnets, and a thin layer of wear-resistant polymer (50 μm PEEK[2]) was used as a coil liner. This configuration is thermally stable, as the magnets have a thermal expansion coefficient an order of magnitude smaller than that of the copper in the coil.

The coil was wound on a precision mandrel of diameter 15.76 mm, which was cut by wire EDM to have grooves 1.9 mm wide for the support rods. The mandrel was first wrapped by the PEEK sheet, then the rods were slipped into place over the sheet. The coil was wound over the PEEK, with thermally-conductive urethane (Loctite US1150) applied to each layer of the winding, and each phase group allowed to cure for 12 hours before winding the next. The phases were connected in a wye topology at the

[2]McMaster-Carr 4671T11, treated with acetone to remove the adhesive.

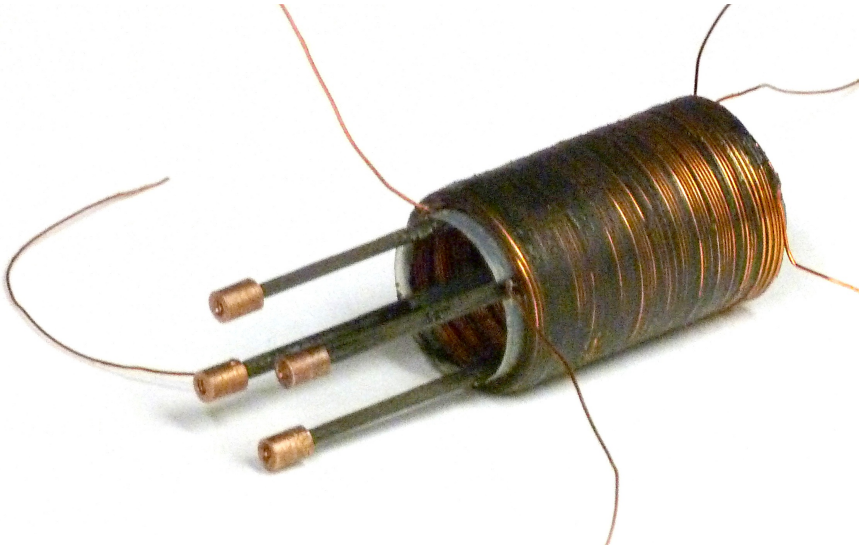

Figure 5-3: The coil is seen here with its support rods, before the wires were terminated. The copper ferrules on the ends of the carbon rods were used as attachment points for the motor's load.

bottom of the coil, and the coil wires were soldered to larger (18 AWG) leads at the top of the coil. The electrical connections at the ends of the coil added approximately 3 mm to the coil length, reducing the stroke accordingly. The coil can be seen in Figure 5-3, before the wires were terminated.

After winding the coil, it was found to have several loose wires, and the PEEK liner proved unable to survive removal from the mandrel. To compact the coil, and provide for a wear-resistant lining, the coil was placed on its mandrel in an aluminum mold (19.5 mm I.D.), and impregnated with Loctite E-30CL epoxy under 600 kPa air pressure. This process reduced the coil's outside diameter to 19.55 mm, eliminating the loose wires.

The magnets were wire EDM cut from a billet of VACODYM 633 HR.[3] After cutting, they were impulse magnetized at 3.2 T in a solenoid fixture, then prepared for assembly by scouring with a brass brush and cleaning with solvent. Magnets were first assembled into rings, using a fixture as shown in Figure 5-4; the rings were stacked to form the arrays in close-fitting sleeves that had been treated with a mold release. The outer magnets were assembled primarily with Loctite 331 acrylic adhesive, while the inner magnets were assembled primarily using Loctite 1C-LV epoxy.[4] It was determined that adhesive alone was unable to support the outer magnets against their own magnetic field, and a magnesium sleeve (alloy AZ80A) was fabricated by wire EDM and used to restrain the magnets without blocking the cooling channels (as shown in Figure 5-2). While the inner magnets were self-supporting, we chose to

[3]Vacuumschmelze GmbH & Co. KG

[4]Loctite 331 cures to a tougher bond more quickly than 1C-LV, but not as reliably under prototyping conditions. Several magnets in the inner array suffered adhesive failure with Loctite 331, and had to be replaced using 1C-LV.

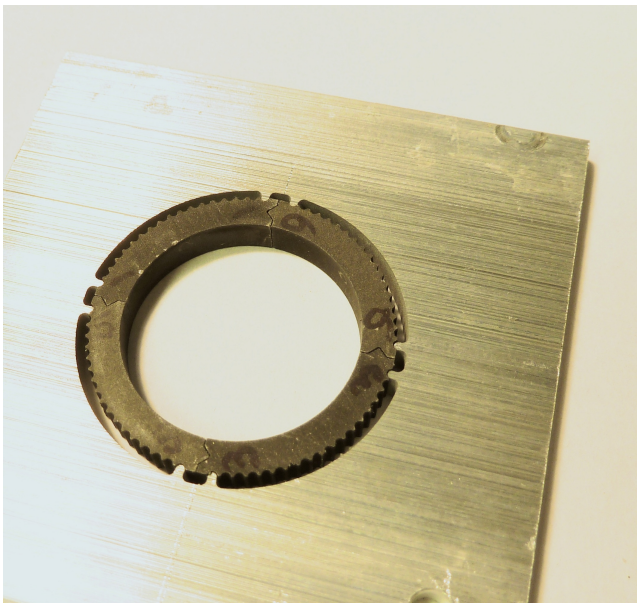

Figure 5-4: Magnets were assembled into rings using fixtures made by wire EDM; shown here is a ring of outer magnets in its fixture.

reinforce them by inserting a hypodermic tube[5] (5.16 mm O.D., 4.80 mm I.D.) in their central cavity and filling the gap between with 1C-LV epoxy.

One major problem that was discovered during magnet assembly was that the glue gaps left between the segments allowed for a substantial amount of diameter variation. While the bearing surface on the inner magnets was sanded smooth, one magnet protruded by too much to sand down and, as will be seen in Section 5.4.1, causes a substantial amount of friction during motor operation. The outer magnets were likewise diamond-filed to fit, but the axial magnets underwent significant radial expansion, leaving a larger-than-desired air gap. We suspect that it would be necessary to machine the magnet arrays after assembly to maintain the tolerances needed for very low thermal resistance.

5.2.2 Cooling System

To remove heat from the motor, we chose to employ water cooling via small-diameter tubing on the outside of the motor. A tube with an inside diameter of 500 μm, containing a laminar water flow and with a fixed wall temperature, would have a heat transfer coefficient[6] of about 4400 $\mathrm{W/(m^2 \cdot K)}$ [41]; if such tubes were to cover half of the outer surface of the motor, the resulting thermal resistance would be 0.12 K/W, small compared to that predicted for conduction alone in Table 5.2.

To provide this level of thermal performance, the tubes must be small and numerous, with as little thermal resistance presented between the fluid and the magnets as possible.

[5] McMaster-Carr 5560K414

[6] Assuming fully-developed flow and a temperature of 22 °C; relaxing these assumptions increases the heat transfer coefficient.

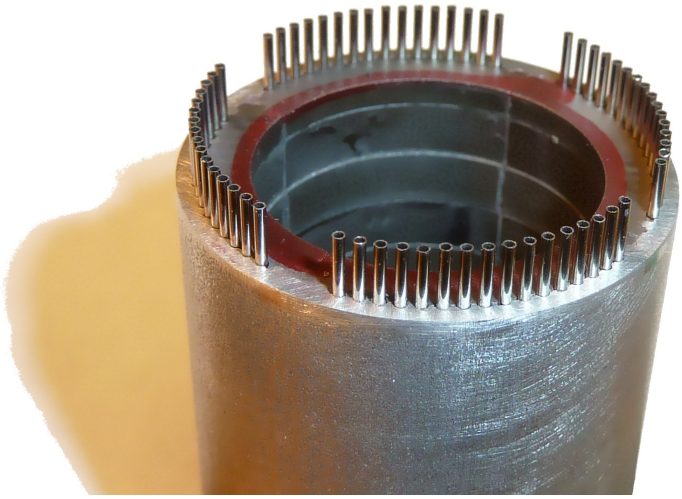

Figure 5-5: The outer magnet array is shown here with the cooling tubes installed in their grooves. Also visible is the slight variation in the magnets' inside diameters caused by the repulsive forces within the array.

Simple hypodermic tubing contributes little thermal resistance, with trade size 23XTW tubing[7] (635 μm O.D., 508 μm I.D.) contributing less than 2% of the thermal resistance due to convection. To provide for close thermal contact between the magnets and the tubing, semicircular channels were cut into the magnets' outer surface, with additional magnet material provided between tubes to keep the average outer diameter of the magnet at 25 mm. The channels were filled with Arctic Silver thermal compound prior to magnet assembly, to avoid introducing significant interface resistance. A total of 72 channels were placed around the periphery of the motor; eight of these were used to secure the magnet retention sleeve, leaving 64 cooling tubes spaced around the motor, as shown in Figure 5-5. The tubes were cut to length by wire EDM, to avoid burrs, and inserted between the magnets and the retention sleeve after magnet assembly. (During assembly, the channels were periodically cleared of excess adhesive and thermal compound.)

With the heat transfer surface designed, it remained necessary to choose the flow conditions and design the fluid manifold required. We chose to set the flow to allow a maximum of 10 °C temperature rise from inlet to outlet under a thermal load of 70,W, slightly more severe than the expected maximum operating conditions. The required flow under these conditions would be 1.67 mL/s, a modest flow rate easily provided by compact pumps. This flow, however, could pass through the tubes in any manner: a single pass through all the tubes in parallel, in series through all the tubes, or some series-parallel combination of them. A summary of the possible flow arrangements is given in Table 5.3; as the number of passes increases, the pressure drop and power requirements increase rapidly. The drawback to a small number of passes is the existence of larger thermal gradients in the motor, especially in the

[7] McMaster-Carr 5560K63, 304 stainless steel

Table 5.3: The flow conditions are summarized for the possible numbers of passes in the cooling jacket of the prototype motor. Pressure drop is given from inlet to outlet, and calculated assuming fully-developed flow; fluid power is the pumping power required by the flow. (Asterisks denote turbulent flow conditions, violating the model assumptions.)

Number of Passes	Flow Velocity (m/s)	Reynolds Number	Pressure Drop (kPa)	Fluid Power (mW)
1	0.13	68	0.82	1.4
2	0.26	140	3.3	5.5
4	0.51	270	13	22
8	1.0	540	52	87
16	2.0	1100	210	350
32	4.1	2200	840	1400
64	8.2	4400*	3400*	5600

single-pass case. Also, with low overall pressure gradients and many tubes in parallel, there may be uneven flow distribution if some tubes are slightly different in inside diameter. On the whole, a low but non-unity number of passes seemed best, and a four-pass strategy was chosen for the prototype.

To provide for the four-pass flow configuration, manifolds with passages connecting banks of 16 tubes on each end of the motor would be required. We sought to keep the parts count to a minimum and avoid complex sealing arrangements, and so the manifolds were designed as single-piece endcaps for the motor, as shown in Figure 5-6. The header for each bank of 16 tubes was formed by two intersecting holes, 1.6 mm in diameter, and banks were connected by extending one of the drilled holes. The manifolds were machined from alloy 6017 aluminum in a single setup, with the exception of the headers, which were drilled individually with a custom fixture. The manifolds were sealed to the tubes and to the magnets using Loctite E-30CL epoxy. The final assembly proved to have a higher fluid resistance than expected, needing 50 kPa to support 1.67 mL/s of flow rather than the expected 13 kPa. The discrepancy likely arose from a combination of pressure drops in the manifolds and contamination of the tube ends with adhesive during assembly; as pressure drop is proportional to the inverse fourth power of tube diameter under constant volume flow conditions, even very small constrictions can lead to large pressure drops.

5.2.3 Overall Structure and Assembly

With the magnets, coil, and cooling system designed, the parts of the motor simply need to be connected to each other and to the outside world, as appropriate. The expected actuation forces of 40-50 N pose no special structural challenge, but there are potentially very large forces attracting the inner magnet array to the outer magnets. Thus, the mechanical endcaps needed to resist large radial forces, or preferably to keep the inner magnets centered at the unstable equilibrium point to avoid the generation of

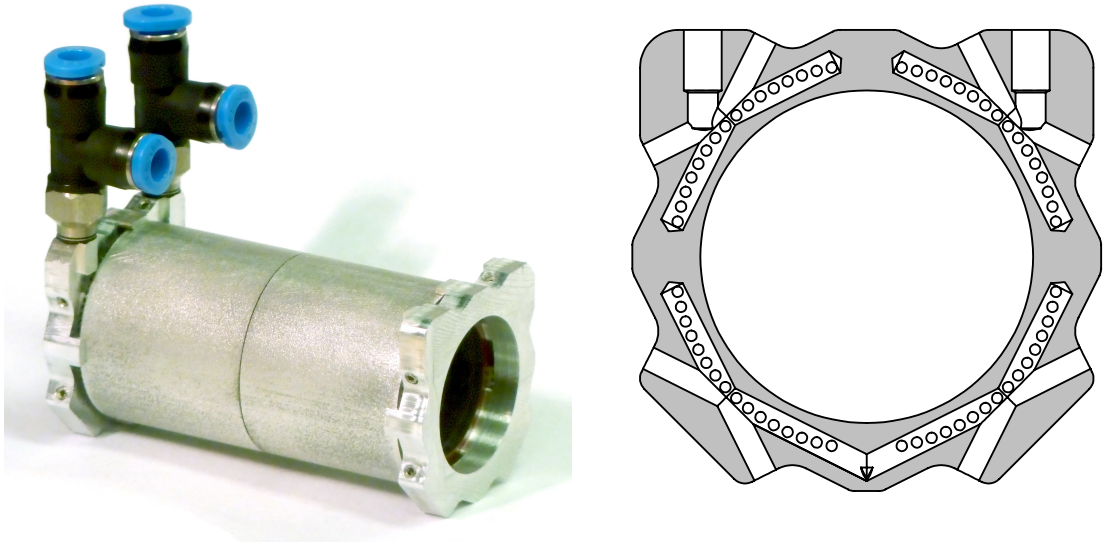

Figure 5-6: Cooling manifolds are shown installed on the ends of the outer magnet array (left), along with a cross-sectional view of the manifold (right). At one end of the motor, water is brought in and out via 4 mm push-to-connect tee fittings, which also serve as sites for thermocouple probes. The cross-drilled fluid passages are sealed with M2 set screws, several of which are visible on the front of the motor. Two passages suffice to connect all 16 tubes in a bank, and the holes are extended to connect banks of tubes.

radial forces in the first place. Furthermore, these forces also had to be avoided during motor assembly, as a single endcap would be unable to keep the opposite end of the magnets centered, and one endcap would have to be removed for coil installation. In addition to the problem of magnet centering, the structure ultimately had to prevent the coil "bearing" on the magnets from experiencing side or moment loads, to keep friction to a minimum.

The solution to the centering problem was straightforward—we placed a boss on each endcap that extends about 1 mm into the air gap. This reduced the stroke, but kept the parts simple and the size of the structural loop minimized. The resulting parts are shown in Figure 5-7. To keep the magnets centered during assembly, the endcaps were designed to allow a tool (also shown in the figure) to be inserted along the entire length of the air gap. As the coil was inserted, it could also provide the centering function and displace the centering tool. The endcaps are secured to the magnet arrays using an aluminum tie-rod, passing down the center of the inner magnets. Both endcaps are machined from FR-4 glass-epoxy composite, for strength and light weight.

We chose to leave the problem of off-axis forces to the application design, for now—the motor user must place suitable bearings and/or couplings on the motor mounts to avoid off-axis forces. In our test system, described further in Section 5.3.1, we used a spherical bearing on the motor output, moved the motor with a precision stage, and bolted the motor itself to an optical table. This arrangement depended on careful stage alignment to avoid off-axis forces, but the addition of a second spherical

Figure 5-7: The front (bottom left) and rear (top left) endcaps bear spacing rings to keep the inner magnets centered; the rear endcap also has cutouts to admit the motor assembly tool (right). The square feature on the rear endcap aligns it to the inner magnets, while the bowl-shaped indentation on the front endcap leaves space for a nut and washer below it, which keep the rear endcap attached while the front endcap is removed. The motor is mounted to the application by the two M3 threaded holes in the rear endcap.

bearing on the motor mount would eliminate them.

The motor output is connected to the ferrules on the coil by four M1.6 screws. For testing purposes, we provided the output with a 3/8"-24 female screw thread for connection to the load, as well as with a mating feature for the slider of a potentiometer position sensor.[8] Position sensing is a key feature in commutated motors like this one; while we chose to use an external potentiometer to measure coil position for expediency, we anticipate that linear hall effect sensors placed either outside the outer magnets or on one of the coil support rods inside the magnetic airgap could do the job without needing an external sensor mount. Slots were also provided to manage the wires leaving the motor, as shown in Figure 5-8.

With all of the components of the motor prepared, the assembly process was reasonably straightforward. A spacer sleeve was machined to fit between the inner and outer magnets, and used to support them through assembly in an arbor press. (Dual Halbach arrays act as very powerful magnetic springs [60], necessitating high forces for assembly.) The rear endcap was then attached to the inner magnets, with a nut and washer on the output end of the motor and the tie-rod passing through the length of the magnets. The spacer sleeve was then replaced by the assembly tool, which was pushed through the cutouts in the rear endcap. The assembly tool, in turn, was displaced by the coil, inserted from the front. Once the coil was fully inserted, the front endcap was fastened to the tie-rod using a nut, and finally the output coupler was fastened to the coil with socket head cap screws. A rendering of the as-assembled motor is given in Figure 5-8. The completed motor had a mass of 185 g, of which 27 g were moving mass (i.e. the coil and output coupler).

5.3 Experiment Design

Once we had a complete motor, we had to determine how to best evaluate its performance. The models developed in this thesis were intended to predict two major aspects of motor performance: heat transfer and static force capability. We therefore designed a simple testbed to measure these properties, without the complexity of a full dynamometer.

5.3.1 Force Measurement

To fully evaluate the force production in the motor, we needed to be able to measure force at every position along the stroke, while reliably measuring that position. To measure force, a threaded load cell (Futek LCM200, 250 lb. rating) was fastened to the motor output, to which a spherical joint rod end[9] was connected. The rod end, in turn, was connected to a precision lead-screw stage (Danaher Motion LM-200), which was used to move the motor over its stroke. The stage, though equipped with a stepper motor, was actuated by simply turning a knob by hand. The motor itself was fastened to a carrier plate, which also held the position sensor (Panasonic EVAJGTJ20B14

[8] Panasonic EVAJGTJ20B14

[9] McMaster-Carr 2458K341

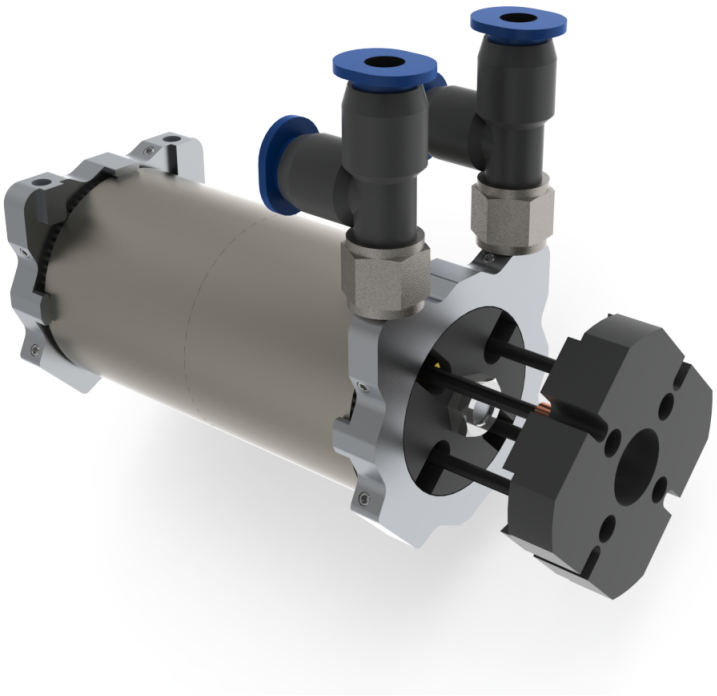

Figure 5-8: A rendering of the complete, as built motor shows the front endcap, motor output coupler, and overall layout of the motor.

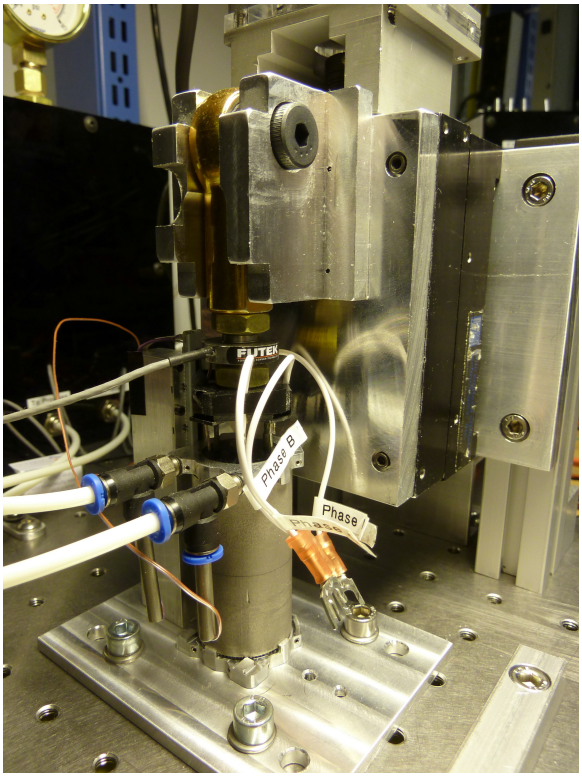

Figure 5-9: The motor was connected to a precision stage for force measurements. Visible here are also the load cell (center) and rod end (top center, golden color).

linear potentiometer) in the correct position. The stage and carrier plate were both fastened to an optical breadboard, completing the structural system. The resulting apparatus is depicted in Figure 5-9.

The load cell and potentiometer were driven by a simple signal conditioning circuit, and the resulting data were recorded using a data acquisition unit (DAQ) (National Instruments USB-6215) and National Instruments LabView SignalExpress software. The potentiometer was driven from a precision 5 V reference (Analog Devices AD586M), and its output was read directly by the DAQ. A linear calibration of the potentiometer was performed using a height gage (Mitutoyo HDS). The load cell was driven by a laboratory power supply (Agilent E3631A) at 10 V, and its output was amplified using a precision instrumentation amplifier (Analog Devices AD624) configured for a gain of 1000. The configuration of the load cell did not admit in-situ calibration; rather than calibrate it in a different system, we chose to use the datasheet sensitivity, and report its output as "uncalibrated". Our test protocol eliminated any offset error from the load cell reading.

To produce force, of course, current had to be applied to the motor windings. A laboratory power supply (Hewlett-Packard E3610A) was used as a controllable source, and a bank of switches was used to assign the current to the phases of the motor. Each phase of the motor could be powered, grounded, or left floating, and a switch was also provided to reverse the current. The voltage at each phase was directly recorded by the DAQ; current was measured on phase A and on the supply using

0.1 Ω resistors, read directly by the DAQ. The current measurements were calibrated using a benchtop multimeter (Agilent 34411A).

During all experiments, the DAQ was configured to record 6000 samples per second. The data were filtered with a 100-point moving average, to eliminate 60 Hz noise, and down-sampled to an effective sample rate of 10 samples per second. This process also reduced broadband noise, as well as noise induced by the tendency of the stage to move in discrete steps due to the stepper motor.

5.3.2 Coolant Loop

To evaluate the thermal performance of the motor, we needed to supply it with a continuous 1.67 mL/s flow of water, and reject the heat deposited in the water to the environment. At the same time, we sought to demonstrate that the major components of such a cooling system need not be large or heavy compared to the motor. Thus, we chose a very compact gear pump (Flight Works 2202-RM2B-SPBBXZ) to provide the water flow. This pump is rated to supply up to 7.5 mL/s at a pressure of up to 270 kPa, sufficient to supply cooling to 25 copies of the prototype motor simultaneously, yet has a mass of just 44 grams.

We were less concerned with the mass and size of the other parts of the cooling system, and so we used standard tubing and gauges. In brief, the loop includes a water reservoir, a 50 μm filter (Flight Works 6065-4), the pump, a rotameter for flow measurement (Key Instruments MR3L19SNVT), a pressure relief valve set for 100 kPa, and a pressure gage (15 psi / 100 kPa maximum) immediately upstream from the motor. Downstream from the motor, heat is passively rejected to ambient via a 15 m length of copper tubing (4.8 mm O.D., 3.2 mm I.D.) hung vertically in the room as a loose coil, before the water is returned to the reservoir. The heat rejection coil adds 10 kPa to the measured pressure at the motor inlet when running at 1.67 mL/s.

Temperature is measured at three points using type T thermocouples: the motor's water inlet, the water outlet, and on the coil itself. The water temperature is measured using 4 mm diameter probes, designed to place the thermocouple junction at the center of the tee fittings. The junctions themselves were encapsulated in Loctite E-30CL epoxy. The temperatures were read out and recorded using an Omega HH147U meter, sampling once every second.

5.3.3 Test Protocol and Data Reduction

Two different kinds of experiments were performed to determine the motor performance: thermal and force production. Before each test, the water pump was activated and adjusted to give the proper water flow rate. For the thermal test, the motor was configured with phase C powered and phases A and B grounded, and positioned at the mid-point of its stroke. Terminal currents of 0.5 A, 1 A, 1.5 A, and 2 A were applied for at least 5 minutes, until the temperature had reached close to steady state. The motor was also tested with the pump switched off, at a current of 1.5 A, until the temperature reached 45 °C, at which point the pump was reactivated. The power applied at each current level was determined from measurement of the motor's

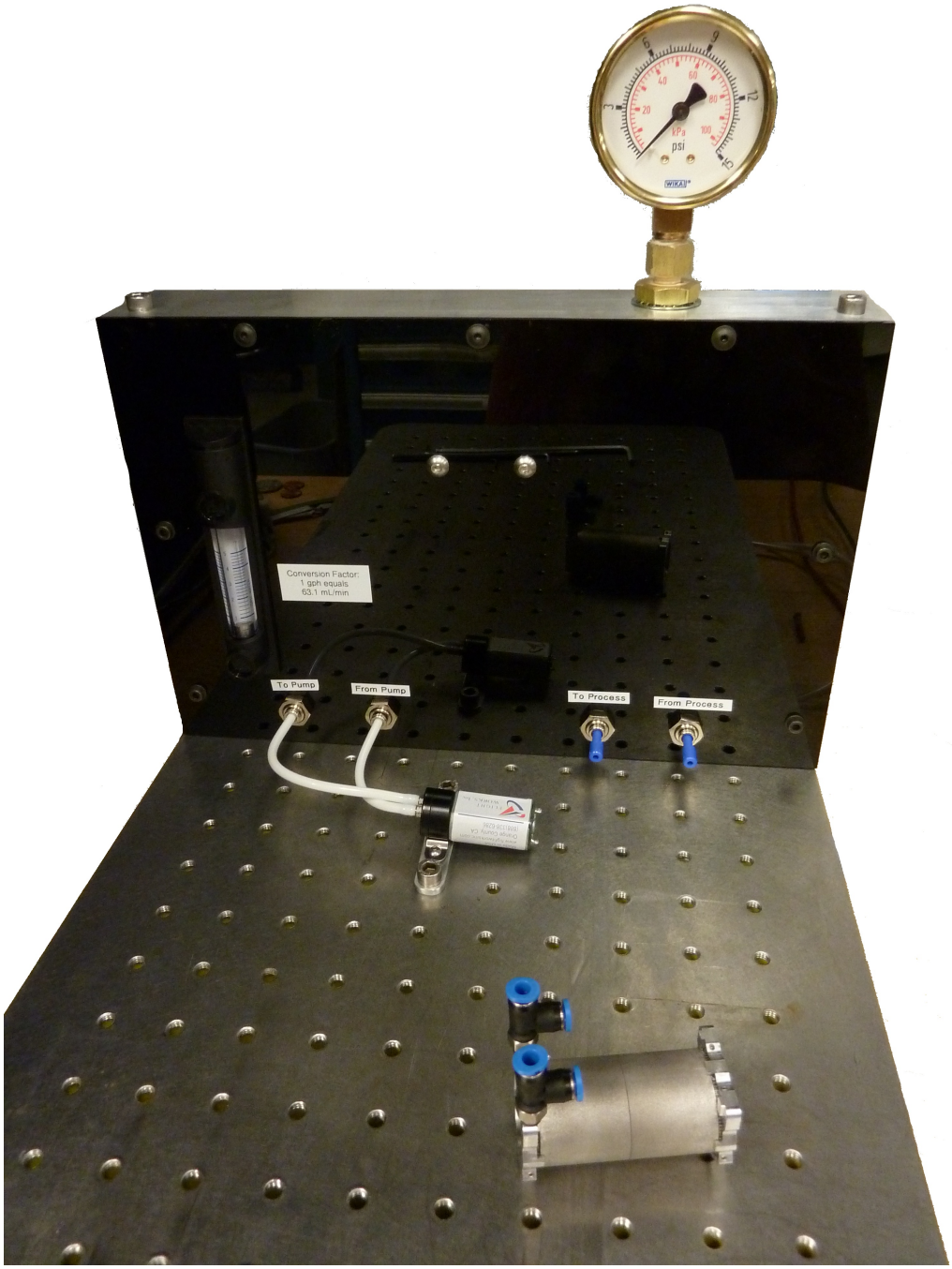

Figure 5-10: The cooling system can be seen clearly in this photo, taken before assembly of the force measurement system. The pump, flow meter, and pressure gage are visible here; the reservoir, filter, and pressure relief valve are located behind the panel. The heat rejection coil is not shown.

terminal voltage and current. The data were analyzed by isolating each period of current application, and fitting an exponential curve to the difference between the coil temperature and the water inlet temperature. Thermal resistance was determined by dividing the steady-state temperature difference (from the exponential fit) by the applied power for each current level.

To measure the motor's force production, applied power was held constant as the motor was moved between its stroke limits. Force was measured for each of the six possible winding configurations: A-B, A-BC, A-C, C-AB, B-C, and B-AC, where the phase before the dash is powered, the phases after the dash are grounded, and any phases omitted are left floating. At the beginning of each test, the motor was located approximately at the midpoint of its stroke. First, with the current off, the motor was moved up to the top of its stroke, down to the bottom, up to the top again, down to the bottom again, and back to the midpoint, providing two passes each in the upwards and downwards directions. A terminal current of 1.5 A was then applied, and the motion cycle repeated. Finally, the current was reversed, and the motion cycle repeated once more.

To analyze the motor force data, each experiment was broken into segments based on current level and motion direction. The data with no current were interpolated and averaged, to give a "friction function" for the upwards and downwards directions. This friction function was then subtracted from the data segments with current applied, to determine the force produced within the motor. Once all six configurations (yielding 48 passes total) were measured, the data were broken out into position bins, 0.2 mm in width. The forces and phase currents (calculated based on the phase A and terminal current measurements) within each bin were used to determine the force constants for each phase by constrained linear least squares minimization, according to

$$F = K_A I_A + K_B I_B + K_C I_C, \text{ with } K_A + K_B + K_C = 0, \tag{5.1}$$

where K_x denotes the force constant (in N/A) of phase x, and I_x denotes the phase current. The overall motor constant under optimum commutation in each bin could then also be determined, according to

$$\epsilon = \frac{1}{\sqrt{R_{ph}}} \sum_x K_x^2, \tag{5.2}$$

where R_{ph} is the resistance of one phase, measured via the phase voltage and current. The lack of connection to the star point of the windings in the motor ensured that the sum of the phase currents is always zero, but this made it impossible to measure any component of the phase force constants that would result in a nonzero mean force constant.

5.4 Motor Performance

Overall, the prototype motor performed well, exceeding the expected magnetic performance but falling short thermally and mechanically. A summary of the measured

Table 5.4: The measured performance parameters of the prototype motor are compared to the design performance and the expected performance. (Friction is excluded from the calculation of F_{max}.) The maximum force is that corresponding to an 80 °C coil temperature and 20 °C coolant temperature. The theoretical and expected motor constants are reported at the motor's experimental operating temperature of 40 °C.

Condition	$\epsilon \left(\mathrm{N}/\sqrt{\mathrm{W}}\right)$	R_{th} (K/W)	M (g)	F_{max} (N)
Theoretical	8.75	2.6	141	39
Expected	5.84	1.8	132	30
Actual	5.89	2.6	185	26

motor performance is given in Table 5.4.

5.4.1 Force Production

In general, the motor produced force slightly more efficiently than predicted by the model, as indicated in Table 5.4. This enhancement was likely due to the approximation of the magnet cutouts and coil spacers as being homogeneous reducers of magnet and copper density, when in reality the material was removed from portions of the magnets and coils with reduced contributions to force production. A major challenge, however, was posed by unexpectedly high friction within the motor. The friction measured during one run of the experiment is shown in Figure 5-11. Over much of the stroke, the friction force amounted to about 5 N, or 17% of the predicted maximum continuous output. While this is highly detrimental to the motor efficiency, commercially-available linear motors also can exhibit similarly high levels of friction. (See Section 5.5 for more details regarding extant motors.) About 4 mm from the bottom of the stroke, friction spikes to about 10 N. This location corresponds to that of the protruding magnet segment mentioned in Section 5.2.1.

Despite the high friction within the motor, the force production was still relatively repeatable. Data from one run of the experiment, with friction subtracted and normalized by power dissipation, are shown in Figure 5-12. The variation in motor constant for a fixed commutation pattern is nearly sinusoidal, as expected for a Halbach motor. Over the top half of the stroke, the force data are quite repeatable; repeatability is reduced in the bottom half of the stroke, where friction is increased. When the commutation pattern is well-matched to the magnetic field in the motor, the motor constant reaches approximately $6\,\mathrm{N}/\sqrt{\mathrm{W}}$.

To extend the results to describe the motor performance for an arbitrary current distribution, we processed the data from five of the commutation patterns with Equations 5.1 and 5.2. (The data for the A-BC commutation pattern did not allow for a unique determination of the currents in phases B and C, due to the use of a single phase current sensor.) The resulting estimated force constants, as well as the overall motor constant, are shown in Figure 5-13. The relatively wide tolerance bands on the phase force constants are induced by the low friction repeatability, but also

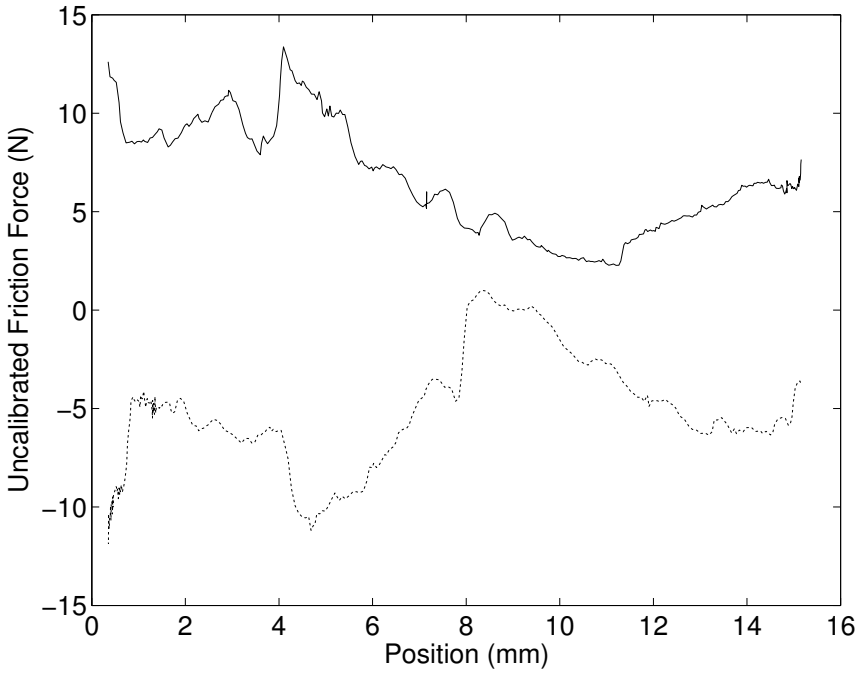

Figure 5-11: The measured friction from one experiment (phase connection A-B) is shown, for both inwards (dashed) and outwards (solid) motion of the coil. Positive force denotes tension, while negative denotes compression; the brief tensile excursion in the friction for inwards motion indicates the presence of a small offset in the load cell output.

depend strongly on the binning of positions. No confidence interval is given for the overall motor constant, as the errors in the phase force constants are correlated by the constraint. The estimated motor constant varies between $5.4\,\mathrm{N}/\sqrt{\mathrm{W}}$ and $6.6\,\mathrm{N}/\sqrt{\mathrm{W}}$, with the highest values occurring at the ends of the stroke and the lowest values mid-stroke. The value reported in the results table corresponds to the mean motor constant over the entire stroke. The elevated motor constant at the ends of the stroke is unexpected, and may be the result of a slight mismatch between the coil pitch and the magnet pitch.

5.4.2 Heat Rejection

The prototype motor exhibited a thermal resistance significantly higher than that predicted, an average of 2.6 K/W rather than the predicted 1.8 K/W. This discrepancy was most likely due to the poor dimensional tolerance of the outer magnet array, leaving a larger air gap than expected. This increase in thermal resistance corresponds to only an extra $40\,\mu$m of air gap between the coil and outer magnets. The use of this cooling strategy is critically dependent on maintenance of a precise, very small air gap. The high thermal resistance lowers the maximum force rating of the motor by the square root of the thermal resistance ratio, or about 17%.

The rest of the cooling system performed well; the course of one thermal experiment

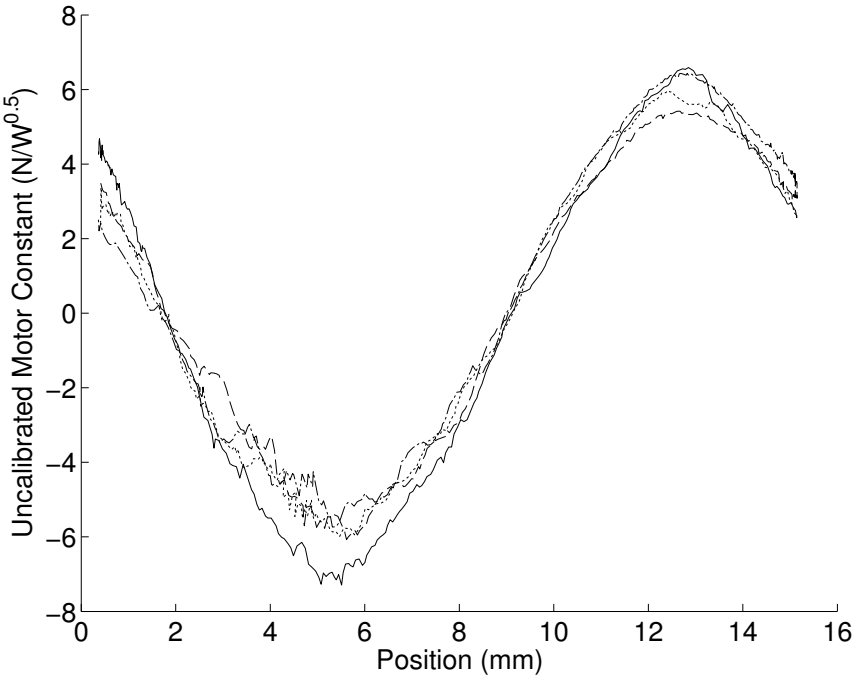

Figure 5-12: The measured motor constant is plotted against coil position for one phase connection scheme, A-B. The different lines correspond to the eight passes over the motor stroke made in one experimental run, illustrating the degree of friction repeatability.

is shown in Figure 5-14. The power steps generate clean first-order exponential temperature responses, as illustrated in Figure 5-15. For the four power levels of 0.47, 1.86, 4.33, and 8.05 W, the curve fits give thermal resistances of 2.6, 2.7, 2.7, and 2.6 K/W, respectively. The average time constant of approximately 100 seconds indicates a heat capacity of 38 J/K, while the heat capacity of the coil alone should be (based on copper mass) only about 5 J/K—the inner magnets are very closely coupled to the coil, with a time constant too short for this experiment to measure. The temperature difference between the water inlet and outlet is consistent with all of the dissipated power being removed by the flow; the thermocouple resolution is insufficient to give quantitative confirmation. The heat rejection coil also proved sufficient, though the heat capacity of the water in the loop was high enough to avoid significant heating over the length of the experiment.

5.5 Discussion and Comparison to Extant Motors

Our test results show that double Halbach tubular linear motors are, indeed, capable of very high electromagnetic performance. Furthermore, the close agreement between our model and the performance of the actual motor confirms the model's veracity and utility—checking the motor performance in the model takes less than one second, and optimizing the geometry for a particular topology only takes a few minutes, while

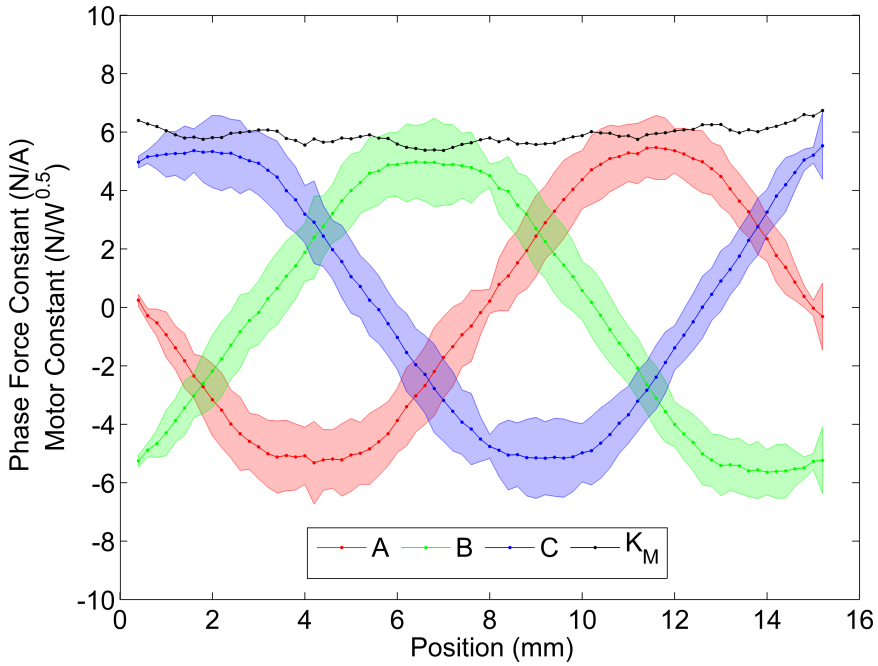

Figure 5-13: The estimated phase force constants (red, green, and blue) are plotted against coil position, along with the estimated motor constant (black) if an optimum set of phase currents are applied. The shaded bands around each force constant correspond to the 95% confidence interval; all parameters were estimated using 0.2 mm position bins.

finite element analysis of a motor takes several minutes just to check the performance of one configuration, and building and testing a prototype takes months and thousands of dollars. If manufacturing specifications, particularly achievable winding fill factor, can be known in advance, then analytical modeling alone should suffice to predict motor performance.

The main factor not accounted for in the model is the friction in the motor, which is exquisitely sensitive to the build quality and manufacturing tolerances. We suspect that post-magnetization grinding of the magnet arrays would be needed to get reliable, low-friction performance from a motor with this particular bearing and cooling design. While such grinding does not appear to be common industry practice, our experience attempting to smooth the arrays' surfaces suggests that it would not be unduly difficult to remove even magnetized grinding swarf from the magnets. Alternatively, a different bearing strategy could be used, such as an external conventional bearing, or a hydrostatic bearing built into the inner magnets. The hydrostatic bearing approach would have the additional benefit of providing cooling immediately on the coil surface, rather than requiring heat transfer across an air gap.

5.5.1 Comparison to Commercially Available Motors

It is instructive to compare the performance of this prototype to a range of commercially available linear motors with different geometries. Figures 5-16, 5-17, and 5-18

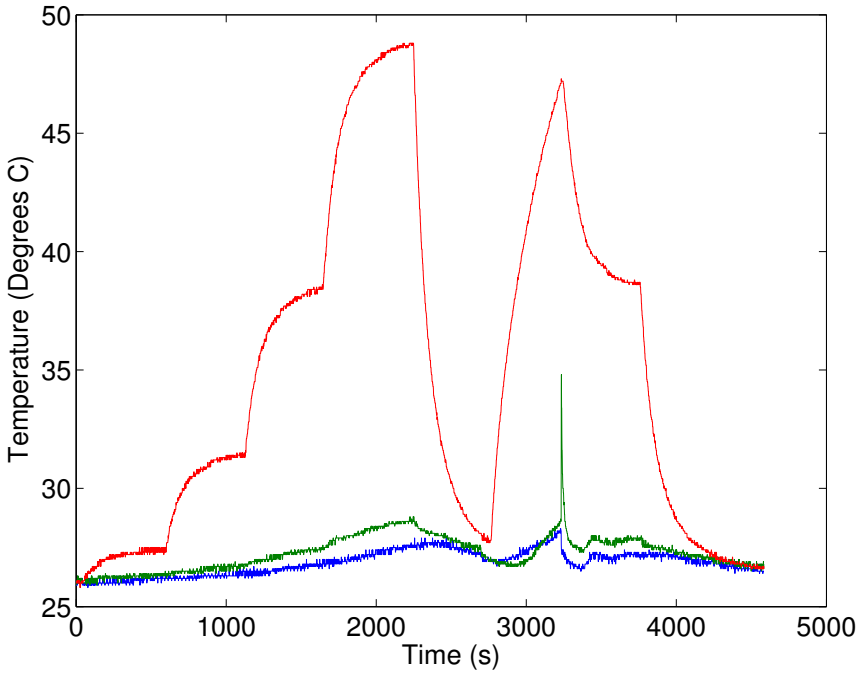

Figure 5-14: The water inlet (blue), water outlet (green), and coil (red) temperatures are plotted over the course of a thermal performance experiment. The first four temperature steps correspond to power dissipations of 0.47 W, 1.86 W, 4.33 W, and 8.05 W, respectively. The motor is then allowed to cool to ambient before the water flow is switched off, and 4.33 W are applied again. When the coil temperature reaches about 45 °C, the water is turned back on, generating a spike in water outlet temperature, and the motor is allowed to cool.

compare the performance of our motor to that of coreless double-sided flat linear synchronous motors (LSMs) from Rockwell Automation (LEM series [136], LEU series [137], and LZ-030 series [138]), coreless tubular motors from Dunkermotoren (STA11 series [139], STA25 series [140], and XTA38 series [141]), tubular motors with slotted stators from Moog [142], and ironless tubular motors from Faulhaber (LM Series [143–145]), as well as moving-coil voice coil actuators from BEI Kimco [134], H2W Technologies [146], Moticont [147], and Akribis [148], and moving-magnet voice coils from H2W Technologies [146]. Where the stroke of the motor would be configurable, the shortest option was chosen, so as to present its performance in the most favorable light possible. Several models of these motors support water cooling; specifications of motors with water cooling are shown separately from those for motors that are passively cooled. Two performance specifications are compared: the motor constant divided by the square root of the mass ("motor constant density") and the force density. The motor constant density evaluates both the materials choices and the electromangetic performance of the design, and in the absence of structural mass should be independent of mass; including structural mass, it might be expected to improve somewhat in larger motors. The force density is compared to the pitch length in synchronous motors, to check against the scaling relation of Equation 2.68; all

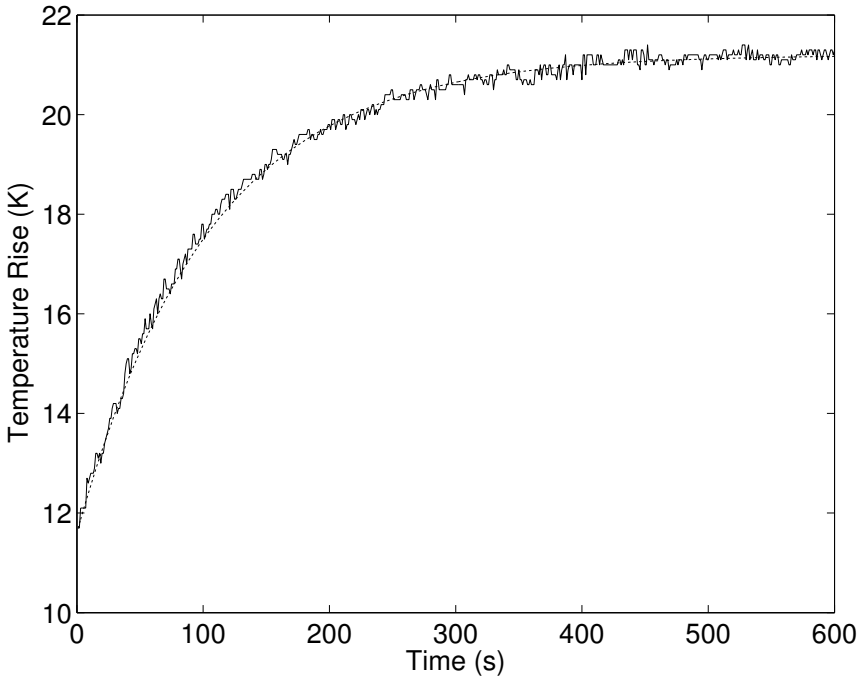

Figure 5-15: The coil temperature rise (over the inlet water temperature) is plotted during the transition from 4.33 W of power dissipation to 8.05 W. The actual temperature (solid) tracks a first-order exponential curve fit (dashed) very closely, with a final temperature rise of 21.2 °C and a time constant of 105 seconds.

else being equal, motors of shorter magnetic pitch length should support higher force densities.

Examining the motor constant density of the motors, it is clear that our motor performs very well compared with the commercial synchronous motors—only the Moog motors, which have 100 times the mass of our motor, offer comparable performance. One possible reason for this is form factor; most of the commercial tubular motors use small-diameter magnet rods with long magnetic pitches, which lead to inefficient magnetic structures. The Moog motors have a substantially larger rod compared to their pitch length, allowing the magnetic circuit to be more compact and thus more efficient. This fact is graphically illustrated in Figure 5-17, where it can be seen that most of the synchronous motors cluster at very low dimensionless magnet radii. (Compare to Figure 3-17, which expresses the theoretical performance of a double-sided Halbach motor as a function of dimensionless radius.) The penalty for larger magnets relative to pitch, however, is increased manufacturing cost.

Our motor's electromagnetic performance also compares well to commercially-available voice coils, with only the moving-magnet voice coils having a comparable motor constant density and size. These motors, however, have very short strokes relative to their sizes, limiting their range of applicability. As shown in Figure 5-17, the periodic structure of our motor allows high electromagnetic performance at small overall aspect ratios; short, large-diameter voice coils are needed to achieve comparable motor constant density. It is also useful to note that these voice coils are all based on

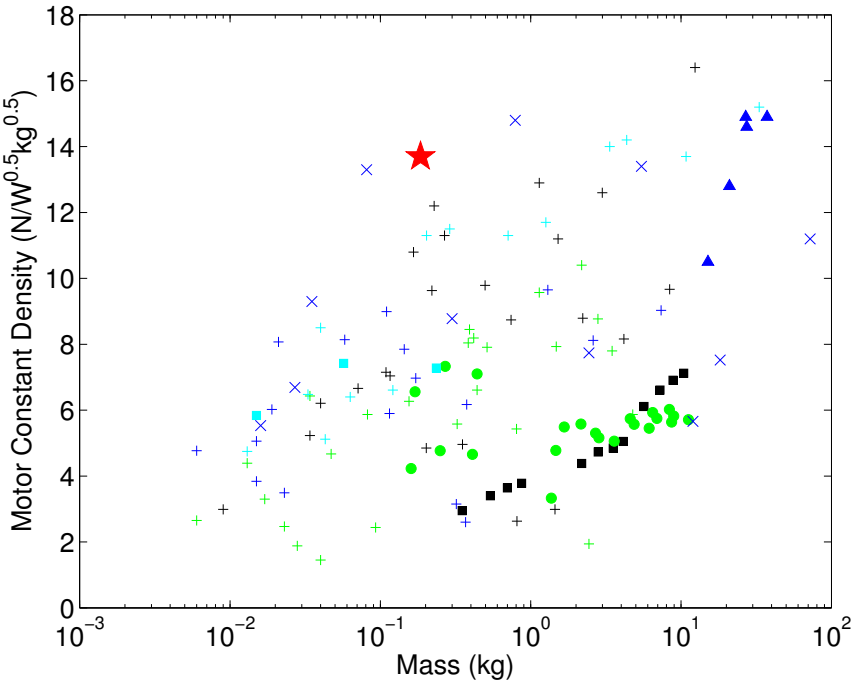

Figure 5-16: The motor constant density (motor constant divided by the square root of motor mass) is plotted against motor mass for 132 different commercially available linear permanent magnet motors. Coreless moving-magnet tubular LSMs are indicated by squares (black for Dunkermotoren and cyan for Faulhaber), slotted moving-magnet tubular LSMs with water cooling are indicated by triangles (Moog), double-sided coreless moving-coil planar LSMs are indicated by circles (Rockwell), moving-coil voice coils are indicated by crosses (black for BEI Kimco, blue for H2W, green for Moticont, and cyan for Akribis), and moving-magnet voice coils are indicated by diagonal crosses (H2W). The performance of our prototype motor is indicated by a red star.

magnetic circuits containing iron, and have limited peak force capability.

The force density of the synchronous motors shows roughly the expected behavior, with maximum force density inversely proportional to pitch length as shown in Figure 5-18. There is too much variation in performance to determine whether the observed scaling corresponds to convection-limited scaling ($F'_{max} \propto p^{-0.5}$) or conduction-limited scaling ($F'_{max} \propto p^{-1}$). The voice coil motors exhibit even greater scatter in their force density; different manufacturers appear to use wildly different standards for their continuous operating conditions. For instance, one of BEI Kimco's motors, the LA15-16-024A, is specified with a continuous force density of 107 N/kg, the highest among the 132 motors examined; this corresponds to an unusually high natural convection heat transfer coefficient, over $50\,\mathrm{W/(m^2 \cdot K)}$. Experimental study may be required to determine the practical force ratings of different manufacturers' motors under consistent environmental conditions.

In spite of the higher-than-expected thermal resistance of our prototype motor, it still achieves a higher force density than all of the commercial motors investigated,

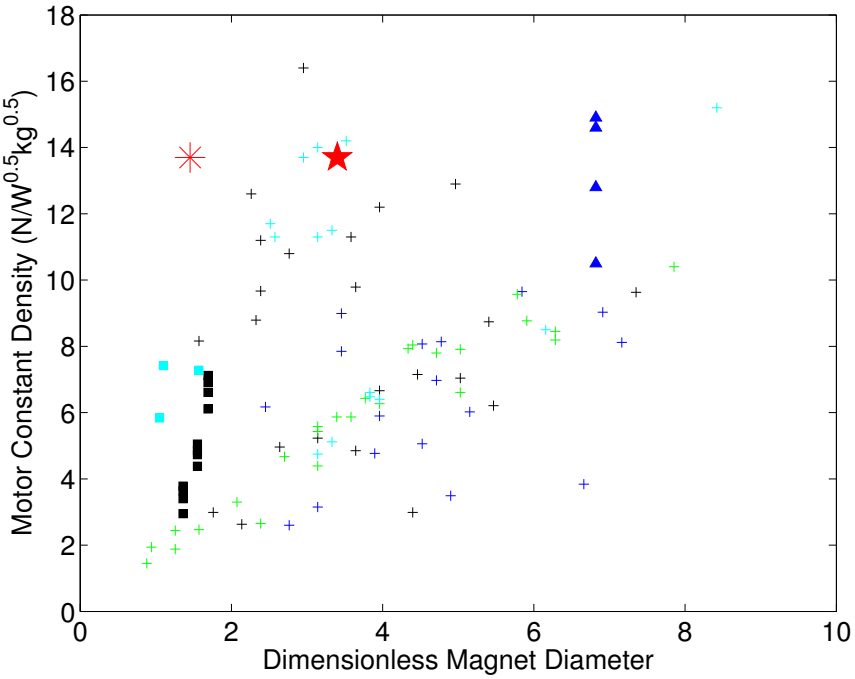

Figure 5-17: The motor constant density (motor constant divided by the square root of motor mass) is plotted against inner magnet radius times wavenumber (for synchronous motors) or 2π times outer magnet housing radius divided by magnet housing length (for voice coils) for a wide range of commercially available linear permanent magnet motors. Coreless moving-magnet LSMs are indicated by squares (black for Dunkermotoren and cyan for Faulhaber), slotted moving-magnet LSMs with water cooling are indicated by triangles (Moog), and moving-coil voice coils are indicated by crosses (black for BEI Kimco, blue for H2W, green for Moticont, and cyan for Akribis). The performance of our prototype motor is indicated by a red star, for dimensionless inner magnet radius, and a red asterisk, for magnet housing geometry. (Moving magnet voice coils and planar synchronous motors are omitted due to different appropriate geometric ratios.)

in most cases over twice as high. The thermal resistance of our motor could be directly reduced through the addition of ferrofluid to the air gap; improvement in manufacturing tolerance would help even further. More exotic heat transfer strategies, with heat removed directly from the coil rather than from the motor exterior, could yield substantial improvement. Note, however, that the maximum force is proportional to the inverse square root of the thermal resistance, so very large relative changes in thermal resistance are required to make large improvements in force capability.

While we did not experimentally verify it, the model predicts a one second peak force rating of 111 N for our motor, or 600 N/kg, based on heating the coil from 80 °C to 90 °C. This is over 50% greater than the next highest value among the motors tested, 390 N/kg, also for the BEI Kimco LA15-16-024A. More significantly, if this peak force is used to accelerate the moving element, the resulting acceleration is 4100 m/s^2, double that of the LA15-16-024A.

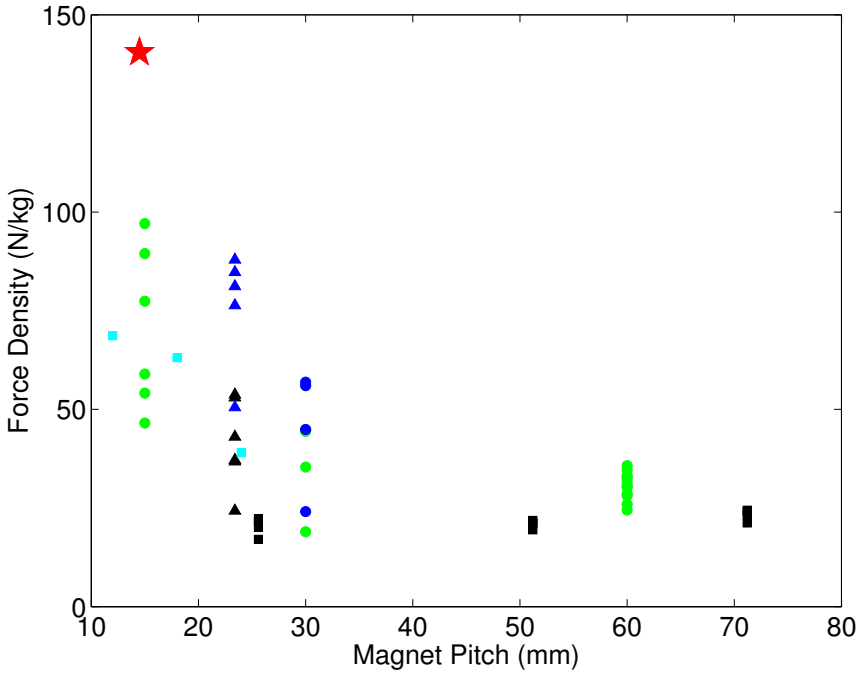

Figure 5-18: The force density is plotted against the magnetic pitch length for a variety of commercially available linear permanent magnet synchronous motors. Coreless moving-magnet tubular LSMs are indicated by squares (black for Dunkermotoren and cyan for Faulhaber), slotted moving-magnet tubular LSMs are indicated by triangles (Moog), and double-sided coreless moving-coil planar LSMs are indicated by circles (Rockwell). The data points correspond to passive cooling, except for several Moog and Rockwell models indicated with blue symbols. The performance of our prototype motor is indicated by a red star.

Beyond the specifications described by our theory, it is also helpful to look at the friction and cogging force levels in commercial motors. Of the motors compared, only the Moog specifications include friction; their model 50206 motors are specified with a friction force ranging between 120 N and 245 N, and a maximum continuous force output of 2002 N, allowing friction to consume up to 12% of the rated force. This motor uses a slotted stator and plain bearings, with the friction force generated by magnetic attraction between the magnets and stator. Festo's ironless linear motors [149] have an even higher level of friction as-specified; the DNCE-32-100 has 5.9 N of friction and a maximum continuous force of just 33.7 N, with friction consuming 18% of the rated force. Thus, if the protruding magnet in our motor causing the locally very high friction were eliminated, as it would be in any future versions, the residual friction would be well within the specifications of other common motors.

5.5.2 Comparison to Research-Grade Motors

Unlike motors offered for commercial sale, motors reported in the scientific literature rarely include full datasheet specifications. The most widely-available specification

is the volumetric force density, measured in N/m^3, sometimes based on the actual thermal resistance and maximum operating temperature and sometimes simply based on an arbitrary current density. Based on the exterior dimensions of our magnet array (including the cooling manifolds), our prototype motor exhibits a volumetric force density of $0.70\,MN/m^3$. Bianchi et al. in 2003 [150] predicted volumetric force densities of up to $0.24\,MN/m^3$ for linear synchronous motors with slotted stators under natural convection, and lower volume force densities for slotless motors; this value is exceeded by commercially available motors today.

More recently, Galea et al. [151] reviewed a variety of high-force-density linear permanent magnet motors, including their own efforts. They estimate the "typical" tubular linear permanent magnet motor as having a volume force density of $0.3\,MN/m^3$, presumably under natural convection conditions. Their own water-cooled slotted-stator tubular motor is reported as achieving $0.69\,MN/m^3$ and $106\,N/kg$, although they appear to only include the mass of the magnets, coils, and back-iron, and only the volume of the stator. They also discuss a design by Joseph and Cronje [73] for a very large generator with a double-sided slotted stator, with a volumetric force density of $0.46\,MN/m^3$, limited by strength of materials rather than thermal considerations; no version of this motor appears to have been built, however. Thus, our results are in line with the very best results reported in large, slotted tubular motors.

More interestingly, Galea et al. also discuss a family of multiple-airgap, "flux-switching" machines capable of very high force densities. These motors act as hybrids between permanent magnet synchronous motors and variable reluctance motors, with the position of an iron structure relative to a magnet array determining the magnitude of the flux linkage in a large coil. While relatively little information is available about the practical performance of these actuators, and measurements appear to have been made under pulsed conditions, Cavarec et al. [36] reported a volume force density of about $1\,MN/m^3$ for a multi-rod tubular flux switching motor, and Ziegler et al. [152] report the astonishing values of $5\,MN/m^3$ and $1000\,N/kg$ for their planar flux-switching actuator. Elsewhere, Wang et al. [153] describe a single-airgap flux-switching motor with a (modeled) volume force density of $1.4\,MN/m^3$ under reasonable ($40\,W/(m^2 \cdot K)$) natural convection conditions, though they have not constructed their motor.

These flux-switching motors offer intriguingly high force densities, but do have drawbacks. Besides having high friction [152] due to magnetic attraction between their iron and magnet elements, they also suffer from very poor power factors [91] and require high electrical drive frequencies. Thus, force density will rapidly decrease with velocity due to the power dissipation of the inductive current, and oversize power electronics may be required. Wound-field rotary versions of the flux-switching motor [154] have been well-characterized and are in commercial use in low-cost applications, though the design does not yet appear to be widely known. In all, this class of actuators has promising characteristics, but are held back by the challenges of analyzing their performance, the complexity of building them, and the challenges of electrically driving them.

Outside the synchronous motor literature, there have been reports of voice coil actuators with unusually high force densities and/or motor constant densities. Recasting the motor constant of our prototype in volumetric terms, we achieve a volumetric

motor constant density of $0.96\,\mathrm{kN}/\sqrt{\mathrm{W}\cdot\mathrm{m}^3}$. Mizuno et al. [155] report a value of $1.6\,\mathrm{kN}/\sqrt{\mathrm{W}\cdot\mathrm{m}^3}$ for their moving-magnet voice coil. Their design shares elements of the flux-switching motor, in that it redirects the magnet flux along the axis of the coil, and likely has a very high inductance relative to its permanent magnet flux linkage. (The force density reported reaches $0.5\,\mathrm{MN/m}^3$ before saturation becomes important.)

The research motors described thus far achieve high force densities primarily through electromagnetic design, with active cooling simply applied to the exterior of the motor. Others have instead approached the problem by strongly enhancing the heat transfer, if even at the expense of some electromagnetic performance. Liebman [156] explored cooling techniques based on expanding the end-turns of a planar motor, allowing the heat transfer in the motor to take place primarily along the wires in the coil rather than across air gaps. While no performance results are available for the motor as a whole, oil cooling of the end-turns was able to achieve a nearly six-fold improvement in current rating over simple natural convection cooling. Galea et al. [157] instead employed enhanced cooling in a tubular motor, by means of extending fins into the winding spaces. This increased the current rating twofold, though the authors did not explore the consequences of inserting an electrically-conductive plate into a winding carrying high-frequency currents. A further wide variety of cooling strategies have been explored in the patent literature, such as cooling by sprays [158] or jet impingement [159], though data on their performance are sparse.

On a final note, the most common approach to achieving high force density is of course to use a reduction drive. Mechanical gear reducers and leadscrews are standard in industrial practice; high-performance systems for space vehicles [160] achieve up to 4000 N/kg, albeit with very low accelerations. There have, however, been some novel attempts to integrate the reduction drive with the actuator. Fujimoto et al. [161] built a fascinating and extremely complex screw-shaped motor, with a design approximately equivalent to a moving-magnet, double-sided planar synchronous motor wrapped into a helical shape. This motor does not achieve a particularly high force density ($0.27\,\mathrm{MN/m}^3$ or 46 N/kg), but has the remarkably high motor constant density of $44\,\mathrm{N}/\sqrt{\mathrm{W}\cdot\mathrm{kg}}$, due to the influence of the effective reduction ratio of about 16:1. Fujimoto et al. also give properties for a wide variety of other linear motors, which exhibit passively-cooled force densities of 0.2 to $0.3\,\mathrm{MN/m}^3$, and ballscrew actuators with force densities up to $0.59\,\mathrm{MN/m}^3$. If muscle-like dynamic performance is not required, actuators incorporating some form of motion transformation offer very good force and efficiency properties.

Chapter 6

Conclusions and Future Outlook

6.1 Motor Modeling Approaches

We have developed a suite of scaling (Chapter 2) and magnetic field (Chapter 3) models capable of describing linear permanent magnet motors with high accuracy. While numerous other models have been developed over the long history of motor design, ours is the first set built to marry a field model to the overall motor scaling properties. Rather than employing rules of thumb for current density or for overall scaling [162], we model all aspects of motor performance from fundamental physical principles. This allowed us to determine the full range of capabilities that can be expected from such motors, with force densities of over 1000 N/kg achievable (Section 4.1.1) even using convection cooling on the motor exterior.

Further, our scaling model showed that the efficiency (Equation 2.9.1) of a motor operating on a simple work-loop does not depend on the scale or size of the motor, but only on the (dimensionless) geometry, the materials from which it is made, the force density required, and the velocity at which the load is driven. In turn, the thermal and electromagnetic performance constraints map to a relationship (Equation 2.68) between the motor's maximum allowable pole pitch and the required force density. The pole pitch sets an internal length scale that can differ from the overall size scale of the motor, allowing for multi-scale design that allows both electromagnetic and thermal performance to be optimized.

Our magnetic field model is essentially complete for ironless motors; all aspects of their behavior can be considered, and the results determined to within machine precision. For common motor aspect ratios, the field can be calculated to well over the 100^{th} harmonic order. This model can also be computed quickly enough to allow for the computation of extensive design databases, freeing the design process from the need to perform electromagnetic calculations at all. We found that the best performance among simple ironless motors is obtained from double-sided Halbach arrays, and the penalty incurred by forming this topology into a cylindrical (tubular) shape is small so long as the pole pitch is shorter than the coil diameter.

For iron-bearing motors, our model is by necessity approximate, though still very accurate. By iteratively accounting for saturation directly in the iron, we can determine

the fields without introducing any fictitious geometry. The price is computational cost, as the field calculations must be performed up to one hundred times more than in the ironless case. By making a further approximation of ideal iron behavior, and assuming a value for the saturation flux density based on the outcome of the model that accounts for saturation, this computational cost can be reduced with little loss in accuracy. Our model in this case accounts for the added mass and volume needed for the iron in the motor, allowing for a realistic comparison between iron-bearing and ironless motor designs. We find that iron-bearing motors cannot match the performance of their ironless brethren, except for when the pole pitch is much longer than the coil diameter.

Ultimately, our models suggest that the highest levels of raw electromagnetic performance (as measured by the mass-specific motor constant) are achievable in double-sided ironless motors, both in planar and in tubular configurations down to small aspect ratios. If we require that the repeating unit structure in the motor be very long relative to its diameter, it becomes advantageous to instead use an iron-bearing motor, with an iron rod inside the coil and a Halbach array outside the coil.

6.2 Motor Design

By applying our models to an iterative design process (Chapter 4), we have established a technique for the development of motors with excellent performance at the low speeds typical of direct-drive applications. Our design perspective for linear synchronous motors is unique compared to the precedent in the literature, and provides a very complete picture of the available design space. Significantly, we found that even at high performance levels the thermal constraints on motor performance were of little consequence, so long as active cooling strategies were employed.

Despite the implication of the scaling model (on its own) that the highest force densities can be achieved through the combination of numerous small motors, we found that for the design of a muscle-like motor it was preferable to use a single large motor structure. This was not necessarily a contradiction, however, as the best performance was found for long motors with short pole pitches—i.e. composed of many small "motor" segments. Unlike the situation in biological muscles, which are limited by their maximum developable stress regardless of the strain they generate, linear motors produce higher forces for smaller effective strains (i.e. stroke-to-length ratios). Thus, it is better to make a motor from many small segments lined up in series than to array them in parallel. It remains essential, however, to have a close connection between each segment and the mechanism for heat transfer out of the motor, just as a biological muscle has a close coupling to its own transport systems.

We were able to validate this design process (as well as our field models) by constructing a small ironless motor with a novel magnetic topology (Chapter 5). While there were some difficulties encountered in building the motor to the required geometric tolerances, we nonetheless achieved best-in-class force density and motor constant. In a mobile robotic system, a modest active cooling system could support

a network of these motors, with greatly enhanced dynamic performance [37] due to reduced motor mass.

6.3 Future Work

We have developed a very complete model and design strategy for ironless linear synchronous motors, but there remains work to be done both in modeling, for iron-bearing motors, and in construction, to improve the tolerances and resulting thermal performance of motors. As discussed in Section 5.5, we suspect it is possible to grind magnet arrays to size after they have been magnetized and assembled, which would lead to both improved geometric tolerances and to a simplified manufacturing process. Given the interest in high-force-density motors, at least within the robotics community as witnessed by the author, it would be useful to develop mass-production techniques for motors like our prototype so that they can be commercialized and made available to the community.

We also feel there is more work to be done in the modeling of iron-bearing motor structures. Our models were not able to capture all of the performance trends associated with voice coil motors, leading to designs with more iron than was actually required. Modeling of saturation in the iron used to enforce the periodic boundary condition at the end of a motor is not a problem that appears to have seen close scrutiny in the literature, though some of the classic results on the method of images [80, 163] may be applicable. In addition, the models developed in this work had a limited ability to account for structures with multiple iron layers, with the infinite-permeability models suffering from numerical instability and with no saturation algorithm developed for the finite-permeability models. We expect that such an algorithm could be developed without undue difficulty, and used to complete the suite of motor models.

Finally, our efforts have thus far been limited to quasi-static phenomena and performance properties in motors. The field modeling approach we have used can, however, be adapted to account for eddy current effects in the magnets and coils, which would allow for the modeling of dynamic performance as well.

6.4 Concluding Remarks

This thesis originally sprang from an attempt to answer a simple question: what is the maximum force density available from a linear permanent magnet motor? To our surprise, it happened that this question had not previously been addressed, and our model stands as a series of increasingly-nuanced answers regarding the maximum achievable performance in such a motor. In coming up with a satisfactory set of answers, the root of our contributions was in applying the modeling approach characteristic of heat transfer and fluid mechanics, dimensionless scaling analysis, to the problem of electromagnetic field modeling in motors. While both dimensionless scaling models and detailed field models have long been known for linear permanent magnet motors, the union of the two is a novel contribution that reveals new, previously unexploited trends in motor performance.

Our models are ultimately intended to reach outside the circle of electric machinery experts, and to be applied by members of motor user communities. As we found in our optimization studies, good designs of motors for different applications can look very different indeed, yet the range of design tools accessible to non-experts is typically limited to finite element analysis and simple magnetic circuit modeling. By calculating a set of optimized design libraries, we add a new tool to that list that allows for optimal design without tedious calculation or arcane mathematical derivations. Ultimately, the solutions to a wide variety of actuation problems may simply lie in the application of careful design optimization and scaling exploitation.

References

[1] "Annual energy review 2010," U.S. Energy Information Administration, Oct. 2011. [Online]. Available: http://www.eia.gov/totalenergy/data/annual/pdf/aer.pdf

[2] E. A. Avallone and T. Baumeister, III, Eds., *Marks' Standard Handbook for Mechanical Engineers*, 10th ed. New York: McGraw-Hill, 1996. ISBN 0-07-004997-1

[3] R. D. Stevenson and R. J. Wassersug, "Horsepower from a horse," *Nature* 364: 195, 1993. DOI: 10.1038/364195a0

[4] J. D. Madden, "Mobile robots: Motor challenges and materials solutions," *Science* 318(5853): 1094–1097, 2007. DOI: 10.1126/science.1146351

[5] M. H. Dickinson, C. T. Farley, R. J. Full, M. A. R. Koehl, R. Kram, and S. Lehman, "How animals move: An integrative view," *Science* 288: 100–106, 2000. DOI: 10.1126/science.288.5463.100

[6] R. Playter, M. Buehler, and M. Raibert, "BigDog," in *Unmanned Systems Technology VIII*, volume 6230, no. 1, Apr. 2006, paper 62302O. DOI: 10.1117/12.684087

[7] S. C. Jacobsen, E. K. Iversen, D. F. Knutti, R. T. Johnson, and K. B. Biggers, "Design of the Utah/M.I.T. dextrous hand," in *Proceedings of the 1986 IEEE International Conference on Robotics and Automation*, volume 3, Apr. 1986, pp. 1520–1532. DOI: 10.1109/ROBOT.1986.1087395

[8] J. M. Hollerbach, I. W. Hunter, and J. Ballantyne, "A comparative analysis of actuator technologies for robotics," in *The Robotics Review 2*, O. Khatib, J. J. Craig, and T. Lozano-Peréz, Eds. Cambridge, MA: MIT Press, 1992, pp. 299–342. ISBN 978-0-262-11171-3

[9] K. Amundson, J. Raade, N. Harding, and H. Kazerooni, "Hybrid hydraulic-electric power unit for field and service robots," in *Proceedings of the 2005 IEEE/RSJ International Conference on Intelligent Robots and Systems*, Aug. 2005, pp. 3453–3458. DOI: 10.1109/IROS.2005.1545452

[10] A. Zoss and H. Kazerooni, "Design of an electrically actuated lower extremity exoskeleton," *Advanced Robotics* 20(9): 967–988, 2006. DOI: 10.1163/156855306778394030

[11] B. P. Ruddy and I. W. Hunter, "Design and optimization strategies for muscle-like direct-drive linear permanent-magnet motors." *The International Journal of Robotics Research* 30(7): 834–845, 2011. DOI: 10.1177/0278364911404260

[12] F. E. Zajac, "Muscle and tendon: Properties, models, scaling, and application to biomechanics and motor control," *Critical Reviews in Biomedical Engineering* 17(4): 359–411, 1989.

[13] N. P. Smith, C. J. Barclay, and D. S. Loiselle, "The efficiency of muscle contraction," *Progress in Biophysics and Molecular Biology* 88(1): 1–58, 2005. DOI: 10.1016/j.pbiomolbio.2003.11.014

[14] J. D. W. Madden, N. A. Vandesteeg, P. A. Anquetil, P. G. A. Madden, A. Takshi, R. Z. Pytel, S. R. Lafontaine, P. A. Wieringa, and I. W. Hunter, "Artificial muscle technology: physical principles and naval prospects," *IEEE Journal of Oceanic Engineering* 29(3): 706–728, 2004. DOI: 10.1109/JOE.2004.833135

[15] R. H. Baughman, "Playing nature's game with artificial muscles," *Science* 308: 63–65, 2005. DOI: 10.1126/science.1099010

[16] R. Z. Pytel, E. L. Thomas, and I. W. Hunter, "*In situ* observation of dynamic elastic modulus in polypyrrole actuators," *Polymer* 49(8): 2008–2013, 2008. DOI: 10.1016/j.polymer.2008.01.053

[17] L. Odhner and H. Asada, "Equilibrium point control of artificial muscles using recruitment of many motor units," in *Proceedings of the 2nd IEEE/RAS-EMBS International Conference on Biomedical Robotics and Biomechatronics*, Oct. 2008, pp. 121–126. DOI: 10.1109/BIOROB.2008.4762884

[18] R. Wood, E. Steltz, and R. Fearing, "Optimal energy density piezoelectric bending actuators," *Sensors and Actuators A* 119: 476–488, 2005. DOI: 10.1016/j.sna.2004.10.024

[19] B. W. Tobalske and A. A. Biewener, "Contractile properties of the pigeon supracoracoideus during different modes of flight," *Journal of Experimental Biology* 211: 170–179, 2008. DOI: 10.1242/jeb.007476

[20] G. A. Pratt and M. M. Williamson, "Series elastic actuators," in *Proceedings of the 1995 IEEE/RSJ International Conference on Intelligent Robots and Systems*, volume 1, Aug. 1995, pp. 399–406. DOI: 10.1109/IROS.1995.525827

[21] T. W. Secord, J. Ueda, and H. H. Asada, "Dynamic analysis of a high-bandwidth, large-strain, PZT cellular muscle actuator with layered strain amplification," in *Proceedings of the 2008 IEEE International Conference on Robotics and Automation*, May 2008, pp. 761–766. DOI: 10.1109/ROBOT.2008.4543297

[22] E. R. Laithwaite, *A history of linear electric motors.* Basingstoke: Macmillan, 1987. ISBN 978-033339928-6

[23] ——, "Linear electric machines—a personal view," *Proceedings of the IEEE* 63(2): 250–290, 1975. DOI: 10.1109/PROC.1975.9734

[24] S. E. Schoenherr. (2001) Loudspeaker history. [Online]. Available: http://centroidworks.files.wordpress.com/2008/08/speaker1.pdf

[25] J. D. Seabert, "Electrodynamic speaker design considerations," *Proceedings of the Institute of Radio Engineers* 22(6): 738–750, 1934. DOI: 10.1109/JRPROC.1934.226380

[26] G. R. Slemon, P. E. Burke, and N. Terzis, "A linear synchronous motor for urban transit using rare-earth magnets," *IEEE Transactions on Magnetics* 14(5): 921–923, 1978. DOI: 10.1109/TMAG.1978.1059794

[27] V. V. Athani, *Stepper Motors : Fundamentals, Applications And Design.* New Delhi: New Age International, 1997. ISBN 8122410065

[28] B. A. Sawyer, "Magnetic positioning device," US Patent 3 457 482, Jul. 22, 1969.

[29] O. Cugat, J. Delamare, and G. Reyne, "Magnetic micro-actuators and systems (MAGMAS)," *IEEE Transactions on Magnetics* 39(6): 3607–3612, 2003. DOI: 10.1109/TMAG.2003.816763

[30] K. Halbach, "Strong rare earth cobalt quadrupoles," *IEEE Transactions on Nuclear Science* 26(3): 3882–3884, 1979. DOI: 10.1109/TNS.1979.4330638

[31] F. W. Merrill, "Permanent-magnet excited synchronous motors," *Transactions of the American Institute of Electrical Engineers Part III: Power Apparatus and Systems* 73(2): 1754–1760, 1955. DOI: 10.1109/AIEEPAS.1954.4499031

[32] K. Binns, M. Jabbar, and W. Barnard, "Computation of the magnetic field of permanent magnets in iron cores," *Proceedings of the IEE* 122(12): 1377–1381, 1975. DOI: 10.1049/piee.1975.0336

[33] K. Halbach, "Design of permanent multipole magnets with oriented rare earth cobalt material," *Nuclear Instruments and Methods* 169: 1–10, 1980. DOI: 10.1016/0029-554X(80)90094-4

[34] J. F. Gieras, Z. J. Piech, and B. Z. Tomczuk, *Linear synchronous motors: transportation and automation systems*, 2nd ed. Boca Raton, FL: CRC Press, 2012. ISBN 978-1-4398-4221-8. DOI: 10.1201/b11105

[35] E. R. Laithwaite, "The goodness of a machine," *Proceedings of the IEE* 112(3): 538–542, 1965. DOI: 10.1049/piee.1965.0091

[36] P.-E. Cavarec, H. B. Ahmed, and B. Multon, "New multi-rod linear actuator for direct-drive, wide mechanical bandpass applications," *IEEE Transactions on Industry Applications* 39(4): 961–970, 2003. DOI: 10.1109/TIA.2003.813705

[37] B. Hannaford, P.-H. Marbot, P. Buttolo, M. Moreyra, and S. Venema, "Scaling of direct drive robot arms," *The International Journal of Robotics Research* 15(5): 459–472, 1996. DOI: 10.1177/027836499601500503

[38] P. Chatzakos and E. Papadopoulos, "The influence of DC electric drives on sizing quadruped robots," in *Proceedings of the 1998 IEEE International Conference on Robotics and Automation*, May 2008, pp. 793–798. DOI: 10.1109/ROBOT.2008.4543302

[39] Integrated Magnetics. (2012) Magnetic properties & data sheets: Rare earth (neodymium & samarium cobalt), alnico, & ferrite. [Online]. Available: http://www.intemag.com/magnetic_properties.html

[40] M. R. Williamson, K. P. Dial, and A. A. Biewener, "Pectoralis muscle performance during ascending and slow level flight in mallards (*Anas platyrhynchos*)," *Journal of Experimental Biology* 204: 495–507, 2001. [Online]. Available: http://jeb.biologists.org/cgi/content/abstract/204/3/495

[41] J. H. Lienhard, IV and J. H. Lienhard, V, *A Heat Transfer Textbook*, 3rd ed. Cambridge, MA: Phlogiston Press, 2008. ISBN 0-9713835-3-1. [Online]. Available: http://web.mit.edu/lienhard/www/ahtt.html

[42] MMG MagDev. (2008, Mar.) Sintered neodymium iron boron (sintered ndfeb). [Online]. Available: http://www.magdev.co.uk/product/pm/pm_sintered_NdFeB.aspx?id=3

[43] Z. Deng, I. Boldea, and S. A. Nasar, "Fields in permanent magnet linear synchronous machines," *IEEE Transactions on Magnetics* 22(2): 107–112, 1986. DOI: 10.1109/TMAG.1986.1064280

[44] G. Xiong and S. A. Nasar, "Analysis of fields and forces in a permanent magnet linear synchronous machine based on the concept of magnetic charge," *IEEE Transactions on Magnetics* 25: 2713–2719, 1989. DOI: 10.1109/20.24513

[45] D. L. Trumper, W.-J. Kim, and M. E. Williams, "Design and analysis framework for linear permanent-magnet machines," *IEEE Transactions on Industry Applications* 32(2): 371–379, 1996. DOI: 10.1109/28.491486

[46] D. L. Trumper, M. E. Williams, and T. H. Nguyen, "Magnet arrays for synchronous machines," in *Conference Record of the 1993 IEEE Industry Applications Society Annual Meeting*, Oct. 1993, pp. 9–18. DOI: 10.1109/IAS.1993.298897

[47] F. M. d'Heurle, "Electromigration and failure in electronics: An introduction," *Proceedings of the IEEE* 59(10): 1409–1418, 1971. DOI: 10.1109/PROC.1971.8447

[48] M. T. Berhan, "Implementation of a Halbach array in a tubular linear motor," Master's Thesis, Massachusetts Institute of Technology, 1996. DOI: 1721.1/10931

[49] J. Wang and D. Howe, "Tubular modular permanent-magnet machines equipped with quasi-Halbach magnetized magnets—Part I: magnetic field distribution, EMF, and thrust force," *IEEE Transactions on Magnetics* 41(9): 2470–2478, 2005. DOI: 10.1109/TMAG.2005.854328

[50] L. Yan, J. Hu, Z. Jiao, I.-M. Chen, and C. K. Lim, "Magnetic field modeling of linear machines with double-layered halbach arrays," in *International Conference on Fluid Power and Mechatronics (FPM)*, Aug. 2011. DOI: 10.1109/FPM.2011.6045891

[51] J. Wang, G. W. Jewell, and D. Howe, "A general framework for the analysis and design of tubular linear permanent magnet machines," *IEEE Transactions on Magnetics* 35(3): 1986–2000, 1999. DOI: 10.1109/20.764898

[52] N. Bianchi, "Analytical field computation of a tubular permanent-magnet linear motor," *IEEE Transactions on Magnetics* 36(5): 3798–3801, 2000. DOI: 10.1109/20.908373

[53] Wijono and H. Arof, "Open circuit field distribution and induced voltage of a cylindrical permanent magnet linear generator," *American Journal of Applied Sciences* 4(11): 912–917, 2007. DOI: 10.3844/ajassp.2007.912.917

[54] G. R. Telle, "Radial magnetic bearing," U.S. Patent 3 958 842, May 25, 1976.

[55] J.-P. Yonnet, G. Lemarquand, S. Hemmerlin, and E. Olivier-Rulliere, "Stacked structures of passive magnetic bearings," *Journal of Applied Physics* 70(10): 6633, 1991. DOI: 10.1063/1.349857

[56] T. J. Devaney and C. Li, "High field voice coil motor," U.S. Patent 7 135 792, Nov. 14, 2006.

[57] M. B. Binnard, J.-M. Gery, and A. J. Hazelton, "High efficiency voice coil motor," U.S. Patent 7 368 838, May 6, 2008.

[58] G. Liang and D. Hao, "Character analysis of double side tubular linear generator with improved structure," in *Proceedings of the International Conference on Electrical Machines and Systems (ICEMS)*, Aug. 2011. DOI: 10.1109/ICEMS.2011.6073851

[59] C. R. Saha, P. H. Riley, J. Paul, Z. Yu, A. J. Jaworski, and C. M. Johnson, "Halbach array linear alternator for thermo-acoustic engine," *Sensors and Actuators A* 178: 179–187, 2012. DOI: 10.1016/j.sna.2012.01.042

[60] B. E. Paden, C. Chen, and O. J. Fiske, "Magnetic spring and actuators with multiple equilibrium positions," U.S. Patent 7 265 470, Sep. 4, 2007.

[61] MWS Wire Industries, "MWS tech book," Westlake Village, CA, 2005. [Online]. Available: http://www.mwswire.com/pdf_files/mws_tech_book/TechBook082011.pdf

[62] Lord Rayleigh, "LVI. On the influence of obstacles arranged in rectangular order upon the properties of a medium," *Philosophical Magazine Series 5* 34(211): 481–502, 1892. DOI: 10.1080/14786449208620364

[63] W. T. Perrins, D. R. McKenzie, and R. C. McPhedran, "Transport properties of regular arrays of cylinders," *Proceedings of the Royal Society of London. Series A, Mathematical and Physical Sciences* 369(1737): 207–225, 1979. DOI: 10.1098/rspa.1979.0160

[64] D. Golda and M. L. Culpepper, "Modeling 3D magnetic fields for precision magnetic actuators that use non-periodic magnet arrays," *Precision Engineering* 32(2): 134–142, 2008. DOI: 10.1016/j.precisioneng.2007.06.002

[65] M. G. Lee, S. Q. Lee, and D.-G. Gweon, "Analysis of Halbach magnet array and its application to linear motor," *Mechatronics* 14: 115–128, 2004. DOI: 10.1016/S0957-4158(03)00015-1

[66] Vacuumschmelze Gmbh. & Co. KG, "Rare-earth permanent magnets," Hanau, Germany, 2007. [Online]. Available: http://www.vacuumschmelze.com/fileadmin/documents/broschueren/dmbrosch/PD-002_e_310807.pdf

[67] G. A. Pratt, "Scaling of permanent magnet electromagnetic motors," May 2007, unpublished.

[68] J. E. Shigley, C. R. Mischke, and R. G. Budynas, *Mechanical Engineering Design*, 7th ed. Boston, MA: McGraw-Hill, 2004. ISBN 0-07-252036-1

[69] *Accuracy Classification System - Tangential Measurements for Cylindrical Gears*, ANSI/AGMA Std. 2015-1-A01, Aug. 2002.

[70] Dr. Fritz Faulhaber GmbH & Co. KG. (2012) Precision gearheads. [Online]. Available: http://www.faulhaber.com/servlet/com.itmr.waw.servlet.Anzeige?fremdaufruf=ja&kdid=40929&sprachid=1&htdigurl=/n170275/i91597.html

[71] S. Akbarzadeh and M. M. Khonsari, "Prediction of steady state adhesive wear in spur gears using the EHL load sharing concept," *Journal of Tribology* 131: 024503, 2009. DOI: 10.1115/1.3075859

[72] Y. Watanabe, M. Edo, H. Nakazawa, and E. Yonezawa, "A new fabrication process of a planar coil using photosensitive polyimide and electroplating," *Sensors and Actuators A* 54: 733–738, 1996. DOI: 10.1016/S0924-4247(97)80048-9

[73] D. M. Joseph and W. A. Cronje, "Design and analysis of a double-sided tubular linear synchronous generator with particular application to wave-energy conversion," in *IEEE Power Engineering Society Conference and Exposition in Africa*, Jul. 2007. DOI: 10.1109/PESAFR.2007.4498032

[74] H. T. Kim, Y. B. Kim, and G. A. Kapustin, "Effects of machining on the magnetic properties of sintered NdFeB magnets," *physica status solidi (a)* 201(8): 1913–1916, 2004. DOI: 10.1002/pssa.200304621

[75] H. Nakamura, K. Hirota, M. Shimao, T. Minowa, and M. Honshima, "Magnetic properties of extremely small NdFeB sintered magnets," *IEEE Transactions on Magnetics* 41(10): 3844–3846, 2005. DOI: 10.1109/TMAG.2005.854874

[76] A. Walther, C. Marcoux, B. Desloges, R. Grechishkin, D. Givord, and N. M. Dempsey, "Micro-patterning of NdFeB and SmCo magnet films for integration into micro-electro-mechanical-systems," *Journal of Magnetism and Magnetic Materials* 321: 590–594, 2009. DOI: 10.1016/j.jmmm.2008.09.028

[77] W. Trimmer and R. Jebens, "Actuators for micro robots," in *Proceedings of the IEEE International Conference on Robotics and Automation*, volume 3, May 1989, pp. 1547–1552. DOI: 10.1109/ROBOT.1989.100198

[78] S. E. Salcudean and J. Yan, "Towards a force-reflecting motion-scaling system for microsurgery," in *Proceedings of the IEEE International Conference on Robotics and Automation*, volume 3, May 1994, pp. 2296–2301. DOI: 10.1109/ROBOT.1994.350943

[79] J. Hopkinson and E. Hopkinson, "Dynamo-electric machinery," *Philosophical Transactions of the Royal Society of London* 177: 331–358, 1886. [Online]. Available: http://www.jstor.org/stable/109485

[80] B. Hague, *Electromagnetic problems in electrical engineering.* London: Oxford University Press, 1929.

[81] B. L. J. Gysen, K. J. Meessen, J. J. H. Paulides, and E. A. Lomonova, "General formulation of the electromagnetic field distribution in machines and devices using fourier analysis," *IEEE Transactions on Magnetics* 46(1): 39–52, 2010. DOI: 10.1109/TMAG.2009.2027598

[82] W.-J. Kim, M. T. Berhan, D. L. Trumper, and J. H. Lang, "Analysis and implementation of a tubular motor with Halbach magnet array," in *Conference Record of the 1996 IEEE Industry Applications Conference*, volume 1, Oct. 1996, pp. 471–478. DOI: 10.1109/IAS.1996.557069

[83] K. Halbach, "Physical and optical properties of rare earth cobalt magnets," *Nuclear Instruments and Methods* 187: 109–117, 1981. DOI: 10.1016/0029-554X(81)90477-8

[84] Wijono, H. Arof, and H. Ping, "Analysis of magnetic field distribution of a cylindrical discrete halbach permanent magnet linear generator," *IET Electric Power Applications* 4(8): 629–636, 2010. DOI: 10.1049/iet-epa.2009.0267

[85] L. Yan, J. Hu, Z. Jiao, J. Shi, I.-M. Chen, C. K. Lim, and G. Yang, "Parametric analysis of tubular linear machines," in *IEEE Conference on Robotics, Automation and Mechatronics (RAM)*, Sept. 2011, pp. 347–352. DOI: 10.1109/RAMECH.2011.6070509

[86] P. T. Konkola, "Magnetic bearing stages for electron beam lithography," Master's Thesis, Massachusetts Institute of Technology, Feb. 1998. DOI: 1721.1/9315

[87] W.-J. Kim and B. C. Murphy, "Development of a novel direct-drive tubular linear brushless permanent-magnet motor," *International Journal of Control, Automation, and Systems* 2(3): 279–288, 2004. [Online]. Available: http://www.ijcas.org/admin/paper/files/IJCAS_v2_n3_pp279-288.pdf

[88] R. Ravaud, G. Lemarquand, V. Lemarquand, , and C. Depollier, "Discussion about the analytical calculation of the magnetic field created by permanent magnets," *Progress in Electromagnetics Research B* 11: 281–297, 2009. DOI: 10.2528/PIERB08112102

[89] F. W. Carter, "Air-gap induction," *Electrical World and Engineer* 38(22): 884–888, 1901. [Online]. Available: http://archive.org/stream/electricalworld38newy#page/884/mode/2up

[90] ——, "The magnetic field of the dynamo-electric machine," *Journal of the Institution of Electrical Engineers* 64(359): 1115–1138, 1926. DOI: 10.1049/jiee-1.1926.0122

[91] E. Spooner and L. Haydock, "Vernier hybrid machines," *IEE Proceedings - Electric Power Applications* 150(6): 655–662, 2003. DOI: 10.1049/ip-epa:20030909

[92] B. L. J. Gysen, E. A. Lomonova, J. J. H. Paulides, and A. J. A. Vandenput, "Analytical and numerical techniques for solving Laplace and Poisson equations in a tubular permanent magnet actuator: Part II. Schwarz-Christoffel mapping," *IEEE Transactions on Magnetics* 44(7): 1761–1767, 2008. DOI: 10.1109/TMAG.2008.923438

[93] (2007) Lamination steels third edition—a CD-ROM. The Electric Motor Education and Research Foundation.

[94] R. Ravaud, G. Lemarquand, and V. Lemarquand, "Magnetic field created by tile permanent magnets," *IEEE Transactions on Magnetics* 45(7): 2920–2926, 2009. DOI: 10.1109/TMAG.2009.2014752

[95] M. G. Lee and D.-G. Gweon, "Optimal design of a double-sided linear motor with a multi-segmented trapezoidal magnet array for a high precision positioning system," *Journal of Magnetism and Magnetic Materials* 281(2-3): 336–346, 2004. DOI: 10.1016/j.jmmm.2004.03.052

[96] S.-Y. Jung, H.-K. Jung, and J.-S. Chun, "Analytic methodology for slotless permanent magnet linear synchronous motor considering end-effect," *International Journal of Applied Electromagnetics and Mechanics* 16(3-4): 219–223, 2002. [Online]. Available: http://iospress.metapress.com/content/vawk6p7kxu9blj89/fulltext.pdf

[97] J. R. Melcher, *Continuum Electromechanics*. Cambridge, MA: MIT Press, 1981. ISBN 978-0-262-13165-0. [Online]. Available: http://ocw.mit.edu/resources/res-6-001-continuum-electromechanics-spring-2009/

[98] MMG MagDev. (2008, Mar.) Bonded neodymium iron boron (bonded NdFeB). [Online]. Available: http://www.magdev.co.uk/product/pm/pm_bonded_NdFeB.aspx?id=4

[99] Applied Magnetic Materials (AMM). (2009, Jul.) Sintered isotropic NdFeB magnet specification. [Online]. Available: http://www.appliedmagnet.com/catalog.0.html4.0.html

[100] J. Wang and D. Howe, "Design optimization of radially magnetized, iron-cored, tubular permanent-magnet machines and drive systems," *IEEE Transactions on Magnetics* 40(5): 3262–3277, 2004. DOI: 10.1109/TMAG.2004.833424

[101] R. P. Brent, *Algorithms for Minimization without Derivatives*. Englewood Cliffs, NJ: Prentice-Hall, 1973. ISBN 0-13-022335-2

[102] R. W. Hamming, *Numerical Methods for Scientists and Engineers*, 2nd ed. New York: Dover, 1973. ISBN 0-486-65241-6

[103] M. Abramowitz and I. A. Stegun, Eds., *Handbook of Mathematical Functions with Formulas, Graphs, and Mathematical Tables*, 10th ed. New York: Dover, 1964. ISBN 0-486-61272-4. [Online]. Available: http://people.math.sfu.ca/~cbm/aands/

[104] W. E. Boyce and R. C. DiPrima, *Elementary Differential Equations and Boundary Value Problems*, 6th ed. New York: John Wiley & Sons, 1996. ISBN 978-0-471-08955-1

[105] E. W. Weisstein. Lommel differential equation. From MathWorld–A Wolfram Web Resource. Retrieved May 8, 2012. [Online]. Available: http://mathworld.wolfram.com/LommelDifferentialEquation.html

[106] G. N. Watson, *A Treatise on the Theory of Bessel Functions*, 2nd ed. Cambridge, U.K.: Cambridge University Press, 1944. ISBN 978-0-521-48391-9

[107] H. Struve, "XVIII. Beitrag zur Theorie der Diffraction an Fernröhren," *Annalen der Physik und Chemie* 17(13): 1008–1016, 1882, in German. DOI: 10.1002/andp.18822531319

[108] de Boer, J. J. M. Braat, and A. J. E. M. Janssen, "Scan density and resolution in a laser beam pattern generator," *Pure and Applied Optics: Journal of the European Optical Society Part A* 3(4): 623–641, 1994. DOI: 10.1088/0963-9659/3/4/026

[109] R. M. Aarts and A. J. E. M. Janssen, "Approximation of the struve function h1 ocurring in impedance calculations," *Journal of the Acoustical Society of America* 113(5): 2635–2637, 2003. DOI: 10.1121/1.1564019

[110] J. W. Nicholson, "Notes on Bessel functions," *The Quarterly Journal of Pure and Applied Mathematics* 42: 216–224, 1911.

[111] S. Zhang and J. Jin, *Computation of Special Functions*. New York: Wiley, 1996. ISBN 0-471-11963-6

[112] B. Barrowes. (2004) Computation of special functions. From the MATLAB Central File Exchange. Retrieved May 9, 2012. [Online]. Available: http://www.mathworks.com/matlabcentral/fileexchange/6218

[113] A. J. MacLeod, "Chebyshev expansions for modified Struve and related functions," *Mathematics of Computation* 60(202): 735–747, 1993. [Online]. Available: http://www.jstor.org/stable/2153112

[114] ——, "Algorithm 757: MISCFUN, a software package to compute uncommon special functions," *ACM Transactions on Mathematical Software* 22(3): 288–301, 1996. DOI: http://doi.acm.org/10.1145/232826.232846

[115] K. J. Meessen, J. J. H. Paulides, and E. A. Lomonova, "Analysis of 3-d effects in segmented cylindrical quasi-halbach magnet arrays," *IEEE Transactions on Magnetics* 47(4): 727–733, 2011. DOI: 10.1109/TMAG.2010.2101079

[116] User israelkk. (2005, Aug.) B-H curve for 1018 steel. Eng-Tips Forum. [Online]. Available: http://www.eng-tips.com/viewthread.cfm?qid=132964

[117] D. Mackenzie, "A flapping of wings," *Science* 335(6075): 1430–1433, 2012. DOI: 10.1126/science.335.6075.1430

[118] R. J. Wood, "Design, fabrication, and analysis of a 3DOF, 3cm flapping-wing MAV," in *Proceedings of the 2007 IEEE/RSJ International Conference on Intelligent Robots and Systems*, Oct. 2007, pp. 1576–1581. DOI: 10.1109/IROS.2007.4399495

[119] B. W. Tobalske, "Biomechanics of bird flight," *Journal of Experimental Biology* 210: 3135–3146, 2007. DOI: 10.1242/jeb.000273

[120] D. R. Warrick and K. P. Dial, "Kinematic, aerodynamic and anatomical mechanisms in the slow, maneuvering flight of pigeons," *Journal of Experimental Biology* 201: 655–672, 1998. [Online]. Available: http://jeb.biologists.org/cgi/content/abstract/201/5/655

[121] A. A. Biewener, W. R. Corning, and B. W. Tobalske, "*In vivo* pectoralis muscle force-length behavior during level flight in pigeons (*Columba livia)*," *Journal of Experimental Biology* 201: 3293–3307, 1998. [Online]. Available: http://jeb.biologists.org/cgi/content/abstract/201/24/3293

[122] A. Kvist, Å. Lindström, M. Green, T. Piersma, and G. H. Visser, "Carrying large fuel loads during sustained bird flight is cheaper than expected," *Nature* 413: 730–732, 2001. DOI: 10.1038/35099556

[123] A. Taberner, N. C. Hogan, and I. W. Hunter, "Needle-free jet injection using real-time controlled linear Lorentz-force actuators," *Medical Engineering & Physics*, 2012, in press. DOI: 10.1016/j.medengphy.2011.12.010

[124] A. J. Taberner, N. B. Ball, N. C. Hogan, and I. W. Hunter, "A portable needle-free jet injector based on a custom high power-density voice-coil actuator," in *Proceedings of the 28th Annual International Conference of the IEEE Engineering in Medicine and Biology Society*, Sep. 2006, pp. 5001–5004. DOI: 10.1109/IEMBS.2006.260243

[125] B. D. Hemond, D. M. Wendell, N. C. Hogan, A. J. Taberner, and I. W. Hunter, "A lorentz-force actuated autoloading needle-free injector," in *Proceedings of the 28th Annual International Conference of the IEEE Engineering in Medicine and Biology Society*, Sep. 2006, pp. 679–682. DOI: 10.1109/IEMBS.2006.259918

[126] I. W. Hunter, A. J. Taberner, B. D. Hemond, D. M. Wendell, N. C. Hogan, and N. B. Ball, "Controlled needle-free transport," U.S. Patent 7 833 189, Nov. 16, 2010.

[127] N. Howard-Jones, "A critical study of the origins and early development of hypodermic medication," *Journal of the History of Medicine and Allied Sciences* 2(2): 201–249, 1947. DOI: 10.1093/jhmas/II.2.201

[128] A. L. Panlilio, J. G. Orelien, P. U. Srivastava, J. Jagger, R. D. Cohn, D. M. Cardo, the NaSH Surveillance Group, and the EPINet Data Sharing Network, "Estimate of the annual number of percutaneous injuries among hospital-based healthcare workers in the united states, 1997-1998," *Infection Control and Hospital Epidemiology* 25(7): 556–562, 2004. DOI: 10.1086/502439

[129] S. J. Lilley, H. F. Taylor, D. R. Theobald, C. J. Carlson, D. I. Rosen, and T. R. Johnson, "Medical injection system and method, gas spring thereof and launching device using gas spring," U.S. Patent 5 599 302, Feb. 4, 1997.

[130] R. A. Hingson and J. G. Hughes, "Clinical studies with jet injection. a new method of drug administration." *Current Researches in Anesthesia & Analgesia* 26(6): 221–230, 1947. [Online]. Available: http://www.anesthesia-analgesia.org/content/26/6/221.short

[131] Y.-C. Kim and M. R. Prausnitz, "Enabling skin vaccination using new delivery technologies," *Drug Delivery and Translational Research* 1(1): 7–12, 2011. DOI: 10.1007/s13346-010-0005-z

[132] F. He, C. E. Woods, J. R. Litowski, L. A. Roschen, H. S. Gadgil, V. I. Razinkov, and B. A. Kerwin, "Effect of sugar molecules on the viscosity of high concentration monoclonal antibody solutions," *Pharmaceutical Research* 28(7): 1552–1560, 2011. DOI: 10.1007/s11095-011-0388-7

[133] S. Einmahl, S. Capancioni, K. Schwach-Abdellaoui, M. Moeller, F. Behar-Cohen, and R. Gurny, "Therapeutic applications of viscous and injectable poly(ortho esters)," *Advanced Drug Delivery Reviews* 53(1): 45–73, 2001. DOI: 10.1016/S0169-409X(01)00220-4

[134] BEI Kimco Magnetics. (2011) Linear voice coil actuators - cylindrical un-housed. [Online]. Available: http://www.beikimco.com/actuators_linear_CYL_unhoused.php

[135] A. Brown, "Modeling and characterization of a voice coil motor," Bachelor's Thesis, Massachusetts Institute of Technology, Jun. 2012.

[136] Rockwell Automation, "LEM brushless linear motor," Data Sheet, Shirley, NY, 2005. [Online]. Available: http://www.rockwellautomation.com/anorad/downloads/pdf/Anorad_LEM.pdf

[137] ——, "LEU-micro linear motor," Data Sheet, Rockwell Automation, Shirley, NY, Oct. 2006. [Online]. Available: http://www.rockwellautomation.com/anorad/downloads/pdf/LEUlinearmotor.pdf

[138] ——, "LZ brushless linear motor," Data Sheet, Shirley, NY, 2007. [Online]. Available: http://www.rockwellautomation.com/anorad/downloads/pdf/LZ_Family.pdf

[139] Dunkermotoren Linear Systems Limited, "Models STA1104-1116 servotube actuator," Data Sheet, Basildon, Essex, UK, Jul. 2011. [Online]. Available: http://www.dunkermotor.com/data/linearsysteme/downloads/DS01097_EN.pdf

[140] ——, "Models STA2504-2510 servotube actuator," Data Sheet, Basildon, Essex, UK, Jul. 2011. [Online]. Available: http://www.dunkermotor.com/data/linearsysteme/downloads/DS01088_EN.pdf

[141] ——, "Models XTA3804-3810 servotube actuator," Data Sheet, Basildon, Essex, UK, Jul. 2011. [Online]. Available: http://www.dunkermotor.com/data/linearsysteme/downloads/DS01093_EN.pdf

[142] Moog Components Group, "High performance linear servomotor," Data Sheet, Blacksburg, VA, May 2011. [Online]. Available: http://www.moog.com/literature/MCG/LinearServoMotorDtS.pdf

[143] Dr. Fritz Faulhaber GmbH & Co. KG, "Linear DC-servomotors series LM 0830 ... 01," Data Sheet, Schönaich, Germany, 2011. [Online]. Available: http://www.faulhaber.com/uploadpk/EN_LM0830-01_MIN.pdf

[144] ——, "Linear DC-servomotors series LM 1247 ... 01," Data Sheet, Schönaich, Germany, 2011. [Online]. Available: http://www.faulhaber.com/uploadpk/EN_LM1247-01_MIN.pdf

[145] ——, "Linear DC-servomotors series LM 2070 ... 01," Data Sheet, Schönaich, Germany, 2011. [Online]. Available: http://www.faulhaber.com/uploadpk/EN_LM2070-01_MIN.pdf

[146] H2W Technologies, Inc. (2012) Voice coil linear actuators. [Online]. Available: http://www.h2wtech.com/Pages/Voice-Coil-Linear-Actuators.aspx

[147] Moticont, "Linear DC motors," Data Sheet, 2011. [Online]. Available: http://www.moticont.com/pdf/lvcm-all.pdf

[148] Akribis Systems, "AVM series voice coil actuators," Data Sheet, 2011. [Online]. Available: http://www.akribis-sys.com/images/pptimg.jpg

[149] Festo Corp., "Electric cylinders DNCE-LAS, with linear motor," Data Sheet, Hauppauge, NY, Jan. 2012. [Online]. Available: http://www.festo.com/cat/en-us_us/data/doc_enus/PDF/US/DNCE-LAS_ENUS.PDF

[150] N. Bianchi, S. Bolognani, D. D. Corte, and F. Tonel, "Tubular linear permanent magnet motors: an overall comparison," *IEEE Transactions on Industry Applications* 39(2): 466–475, 2003. DOI: 10.1109/TIA.2003.809444

[151] M. Galea, C. Gerada, T. Raminosoa, and P. W. Wheeler, "Considerations for the design of a tubular motor for an aerospace application," in *International Conference on Electrical Machines and Systems (ICEMS)*, Aug. 2011. DOI: 10.1109/ICEMS.2011.6073431

[152] N. Ziegler, P. Enrici, J. Jac, and D. Matt, "Multiairgap friction direct drive linear actuator with permanent magnets," in *18th International Conference on Electrical Machines (ICEM)*, Sep. 2008. DOI: 10.1109/ICELMACH.2008.4799941

[153] J. Wang, W. Wang, K. Atallah, and D. Howe, "Design considerations for tubular flux-switching permanent magnet machines," *IEEE Transactions on Magnetics* 44(11): 4026–4032, 2008. DOI: 10.1109/TMAG.2008.2002773

[154] H. Pollock, C. Pollock, R. Walter, and B. Gorti, "Low cost, high power density, flux switching machines and drives for power tools," in *Conference Record of the 38th IAS Annual Meeting*, volume 3, Oct. 2003, pp. 1451–1457. DOI: 10.1109/IAS.2003.1257748

[155] T. Mizuno, M. Kawai, F. Tsuchiya, M. Kosugi, and H. Yamada, "An examination for increasing the motor constant of a cylindrical moving magnet-type linear actuator," *IEEE Transactions on Magnetics* 41(10): 3976–3978, 2005. DOI: 10.1109/TMAG.2005.855160

[156] M. K. Liebman, "Thermally efficient linear motor analysis & design," Master's Thesis, Massachusetts Institute of Technology, Feb. 1998. DOI: 1721.1/10078

[157] M. Galea, C. Gerada, T. Raminosoa, and P. Wheeler, "Design of a high force density tubular permanent magnet motor," in *XIX International Conference on Electrical Machines*, Sep. 2010. DOI: 10.1109/ICELMACH.2010.5608075

[158] C. L. Tilton, G. J. Wos, and R. J. Baddeley, "Spray cooled motor system," US Patent 7 397 154, Jul. 8, 2008.

[159] K. Chen, A. Masrur, S. Ahmed, and V. K. Garg, "Jet impingement cooling of electric motor end-windings," US Patent 6 639 334, Oct. 28, 2003.

[160] M. A. Davis. (2001, Jul.) Electromechanical actuation for launch vehicles. Moog Inc. [Online]. Available: http://www.moog.com/literature/Space_Defense/Technical_Bulletins/Electromechanical_Actuation_for_Launch_Vehicles.pdf

[161] Y. Fujimoto, T. Kominami, and H. Hamada, "Development and analysis of a high thrust force direct-drive linear actuator," *IEEE Transactions on Industrial Electronics* 56(5): 1383–1392, 2009. DOI: 10.1109/TIE.2009.2012419

[162] J. H. Marden, "Scaling of maximum net force output by motors used for locomotion," *Journal of Experimental Biology* 208: 1653–1664, 2005. DOI: doi:10.1242/jeb.01483

[163] P. Hammond, "Electric and magnetic images," *Proceedings of the IEE - Part C: Monographs* 107(12): 306–313, 1960. DOI: 10.1049/pi-c.1960.0047

Appendix A: Additional Field Solutions

This section contains several sets of expressions for field coefficients in iron-bearing motor configurations. The expressions for the fields are too lengthy for incorporation into the main text, but are necessary for the development of computer codes for performance prediction or design optimization. Expressions for the field coefficients of planar motors with saturable iron on both sides of the coil, tubular motors with saturable iron inside the coil, tubular motors with saturable iron outside the coil, and tubular motors with ideal iron on both sides of the coil are presented. Field coefficients for other motor configurations are given in the main text of Chapter 3.

A.1 Double-sided planar motor with back-iron

A.1.1 Magnet coefficents

$$a_{mn,1} = b_{mn,3} + \frac{1}{2}\left(\hat{M}_{yn} - \hat{M}_{zn}\right)\mathrm{e}^{nky_{mi}} \qquad b_{mn,1} = a_{mn,1}$$

$$a_{mn,2} = a_{mn,1} \qquad b_{mn,2} = a_{mn,1}$$

$$a_{mn,3} = \frac{\mu+1}{2\mu}a_{mn,4} + \frac{\mu-1}{2\mu}\,\mathrm{e}^{-2nky_{mo}}\,b_{mn,4} - \frac{1}{2}\left(\hat{M}_{yn} + \hat{M}_{zn}\right)\mathrm{e}^{-nky_{mo}}$$

$$b_{mn,3} = \frac{\mu-1}{2\mu}\,\mathrm{e}^{2nky_{mo}}\,a_{mn,4} + \frac{\mu+1}{2\mu}b_{mn,4} - \frac{1}{2}\left(\hat{M}_{yn} - \hat{M}_{zn}\right)\mathrm{e}^{nky_{mo}}$$

$$a_{mn,4} = -\frac{(\mu-1)\,\mathrm{e}^{-2nky_{fo}}}{2}b_{mn,5}$$

$$b_{mn,4} = \frac{(\mu+1)}{2}b_{mn,5}$$

$$a_{mn,5} = 0$$

$$b_{mn,5} = 4\mu\frac{\hat{M}_{yn}\Big(\sinh\left(nky_{mo}\right) - \sinh\left(nky_{mi}\right)\Big) - \hat{M}_{zn}\Big(\cosh\left(nky_{mo}\right) - \cosh\left(nky_{mi}\right)\Big)}{(\mu+1)^2 - (\mu-1)^2\,\mathrm{e}^{-2nkt_f} - \left(\mu^2-1\right)\left(\mathrm{e}^{-2nky_{mo}} - \mathrm{e}^{-2nky_{fo}}\right)} \tag{A.1a}$$

A.1.2 Coil coefficients

$$a_{cni,1} = a_{cni,3} - \frac{1}{2}\,\mathrm{e}^{-\frac{nkt_c}{2}} \qquad b_{cni,1} = a_{cni,1}$$

$$a_{cni,2} = a_{cni,3} \qquad b_{cni,2} = b_{cni,3}$$

$$a_{cni,3} = \frac{\mu+1}{2\mu} a_{cni,4} + \frac{\mu-1}{2\mu}\,\mathrm{e}^{-2nky_{mo}}\, b_{cni,4} \qquad b_{cni,3} = \frac{\mu-1}{2\mu}\,\mathrm{e}^{2nky_{mo}}\, a_{cni,4} + \frac{\mu+1}{2\mu} b_{cni,4}$$

$$a_{cni,4} = -\frac{(\mu-1)\,\mathrm{e}^{-2nky_{fo}}}{2} b_{cni,5} \qquad b_{cni,4} = \frac{(\mu+1)}{2} b_{cni,5}$$

$$a_{cni,5} = 0$$

$$b_{cni,5} = \frac{4\mu \sinh\left(\frac{nkt_c}{2}\right)}{(\mu+1)^2 - (\mu-1)^2\,\mathrm{e}^{-2nkt_f} - \left(\mu^2-1\right)\left(\mathrm{e}^{-2nky_{mo}} - \mathrm{e}^{-2nky_{fo}}\right)} \tag{A.1b}$$

A.2 Cylindrical array with inner iron

A.2.1 Magnet coefficients

$$a_{mn,1} = \frac{nkr_{fi,i}}{\mu}\left[a_{mn,2}\left(\mu\,\mathrm{I}_1\left(nkr_{fi,i}\right)\mathrm{K}_0\left(nkr_{fi,i}\right) + \mathrm{I}_0\left(nkr_{fi,i}\right)\mathrm{K}_1\left(nkr_{fi,i}\right)\right) + b_{mn,2}\,(\mu-1)\,\mathrm{K}_1\left(nkr_{fi,i}\right)\mathrm{K}_0\left(nkr_{fi,i}\right)\right]$$

$$b_{mn,1} = 0$$

$$a_{mn,2} = \frac{\mu}{nkr_{mi,i}}\left[\frac{a_{mn,6} + \hat{M}_{rni}\left(\mathcal{L}_{\mathrm{K}}\left(nkr_{mi,i}\right) - \mathcal{L}_{\mathrm{K}}\left(nkr_{mi,o}\right)\right) + \hat{M}_{zni}\left(nkr_{mi,i}\,\mathrm{I}_1\left(nkr_{mi,i}\right) - nkr_{mi,o}\,\mathrm{I}_1\left(nkr_{mi,o}\right)\right)}{\mu\,\mathrm{I}_1\left(nkr_{mi,i}\right)\mathrm{K}_0\left(nkr_{mi,i}\right) + \mathrm{I}_0\left(nkr_{mi,i}\right)\mathrm{K}_1\left(nkr_{mi,i}\right) - \frac{(\mu-1)^2\,\mathrm{I}_1\left(nkr_{fi,i}\right)\mathrm{I}_0\left(nkr_{fi,i}\right)\mathrm{K}_1\left(nkr_{mi,i}\right)\mathrm{K}_0\left(nkr_{mi,i}\right)}{\mathrm{I}_1\left(nkr_{fi,i}\right)\mathrm{K}_0\left(nkr_{fi,i}\right)+\mu\,\mathrm{I}_0\left(nkr_{fi,i}\right)\mathrm{K}_1\left(nkr_{fi,i}\right)}}\right]$$

$$b_{mn,2} = -a_{mn,2}\left[\frac{(\mu-1)\,\mathrm{I}_1\left(nkr_{fi,i}\right)\mathrm{I}_0\left(nkr_{fi,i}\right)}{\mathrm{I}_1\left(nkr_{fi,i}\right)\mathrm{K}_0\left(nkr_{fi,i}\right) + \mu\,\mathrm{I}_0\left(nkr_{fi,i}\right)\mathrm{K}_1\left(nkr_{fi,i}\right)}\right]$$

$$a_{mn,3} = a_{mn,6} - \hat{M}_{rni}\,\mathcal{L}_{\mathrm{K}}\left(nkr_{mi,o}\right) - \hat{M}_{zni} nkr_{mi,o}\,\mathrm{K}_1\left(nkr_{mi,o}\right)$$

$$
\begin{aligned}
b_{mn,3} &= \frac{nkr_{mi,i}}{\mu}\left[a_{mn,2}\,(\mu-1)\,\mathrm{I}_1\big(nkr_{mi,i}\big)\,\mathrm{I}_0\big(nkr_{mi,i}\big) + b_{mn,2}\left(\mathrm{I}_1\big(nkr_{mi,i}\big)\,\mathrm{K}_0\big(nkr_{mi,i}\big) + \mu\,\mathrm{I}_0\big(nkr_{mi,i}\big)\,\mathrm{K}_1\big(nkr_{mi,i}\big)\right)\right] + \\
&\quad - \hat{M}_{rni}\,\mathcal{L}_{\mathrm{I}}\big(nkr_{mi,i}\big) + \hat{M}_{zni} nkr_{mi,i}\,\mathrm{I}_1\big(nkr_{mi,i}\big) \\
a_{mn,4} &= a_{mn,6} \\
b_{mn,4} &= b_{mn,3} + \hat{M}_{rni}\,\mathcal{L}_{\mathrm{I}}\big(nkr_{mi,o}\big) - \hat{M}_{zni} nkr_{mi,o}\,\mathrm{I}_1\big(nkr_{mi,o}\big) \\
a_{mn,5} &= a_{mn,6} \\
b_{mn,5} &= b_{mn,4} \\
a_{mn,6} &= \hat{M}_{rno}\left(\mathcal{L}_{\mathrm{K}}\big(nkr_{mo,i}\big) - \mathcal{L}_{\mathrm{K}}\big(nkr_{mo,o}\big)\right) + \hat{M}_{zno}\left(nkr_{mo,i}\,\mathrm{I}_1\big(nkr_{mo,i}\big) - nkr_{mo,o}\,\mathrm{I}_1\big(nkr_{mo,o}\big)\right) \\
b_{mn,6} &= b_{mn,4} \\
a_{mn,7} &= -\hat{M}_{rno}\,\mathcal{L}_{\mathrm{K}}\big(nkr_{mo,o}\big) - \hat{M}_{zno} nkr_{mo,o}\,\mathrm{K}_1\big(nkr_{mo,o}\big) \\
b_{mn,7} &= b_{mn,4} - \hat{M}_{rno}\,\mathcal{L}_{\mathrm{I}}\big(nkr_{mo,i}\big) + \hat{M}_{zno} nkr_{mo,i}\,\mathrm{I}_1\big(nkr_{mo,i}\big) \\
a_{mn,9} &= 0 \\
b_{mn,9} &= b_{mn,4} + \hat{M}_{rno}\left(\mathcal{L}_{\mathrm{I}}\big(nkr_{mo,o}\big) - \mathcal{L}_{\mathrm{I}}\big(nkr_{mo,i}\big)\right) - \hat{M}_{zno}\left(nkr_{mo,o}\,\mathrm{I}_1\big(nkr_{mo,o}\big) - nkr_{mo,i}\,\mathrm{I}_1\big(nkr_{mo,i}\big)\right)
\end{aligned}
\tag{A.2a}
$$

A.2.2 Coil coefficients

$$
a_{cn,1} = \frac{nkr_{fi,i}}{\mu}\left[a_{cn,2}\left(\mu\,\mathrm{I}_1\big(nkr_{fi,i}\big)\,\mathrm{K}_0\big(nkr_{fi,i}\big) + \mathrm{I}_0\big(nkr_{fi,i}\big)\,\mathrm{K}_1\big(nkr_{fi,i}\big)\right) + b_{cn,2}\,(\mu-1)\,\mathrm{K}_1\big(nkr_{fi,i}\big)\,\mathrm{K}_0\big(nkr_{fi,i}\big)\right]
$$

$$
b_{cn,1} = 0
$$

$$
a_{cn,2} = \frac{\mu}{nkr_{mi,i}}\left[\frac{a_{cn,4}}{\mu\,\mathrm{I}_1\big(nkr_{mi,i}\big)\,\mathrm{K}_0\big(nkr_{mi,i}\big) + \mathrm{I}_0\big(nkr_{mi,i}\big)\,\mathrm{K}_1\big(nkr_{mi,i}\big) - \frac{(\mu-1)^2\,\mathrm{I}_1\big(nkr_{fi,i}\big)\,\mathrm{I}_0\big(nkr_{fi,i}\big)\,\mathrm{K}_1\big(nkr_{mi,i}\big)\,\mathrm{K}_0\big(nkr_{mi,i}\big)}{\mathrm{I}_1\big(nkr_{fi,i}\big)\,\mathrm{K}_0\big(nkr_{fi,i}\big) + \mu\,\mathrm{I}_0\big(nkr_{fi,i}\big)\,\mathrm{K}_1\big(nkr_{fi,i}\big)}}\right]
$$

$$
\begin{aligned}
b_{cn,2} &= -a_{cn,2}\left[\frac{(\mu-1)\,\mathrm{I}_1\big(nkr_{fi,i}\big)\,\mathrm{I}_0\big(nkr_{fi,i}\big)}{\mathrm{I}_1\big(nkr_{fi,i}\big)\,\mathrm{K}_0\big(nkr_{fi,i}\big)+\mu\,\mathrm{I}_0\big(nkr_{fi,i}\big)\,\mathrm{K}_1\big(nkr_{fi,i}\big)}\right]\\
a_{cn,3} &= a_{cn,4}\\
b_{cn,3} &= \frac{nkr_{mi,i}}{\mu}\left[a_{cn,2}\,(\mu-1)\,\mathrm{I}_1\big(nkr_{mi,i}\big)\,\mathrm{I}_0\big(nkr_{mi,i}\big)+b_{cn,2}\left(\mathrm{I}_1\big(nkr_{mi,i}\big)\,\mathrm{K}_0\big(nkr_{mi,i}\big)+\mu\,\mathrm{I}_0\big(nkr_{mi,i}\big)\,\mathrm{K}_1\big(nkr_{mi,i}\big)\right)\right]\\
a_{cn,4} &= \mathcal{L}_\mathrm{K}\big(nkr_{c,i}\big)-\mathcal{L}_\mathrm{K}\big(nkr_{c,o}\big) & b_{cn,4} &= b_{cn,3}\\
a_{cn,5} &= -\,\mathcal{L}_\mathrm{K}\big(nkr_{c,o}\big) & b_{cn,5} &= b_{cn,3}-\mathcal{L}_\mathrm{I}\big(nkr_{c,i}\big)\\
a_{cn,6} &= 0 & b_{cn,6} &= b_{cn,3}+\mathcal{L}_\mathrm{I}\big(nkr_{c,o}\big)-\mathcal{L}_\mathrm{I}\big(nkr_{c,i}\big)\\
a_{cn,7} &= 0 & b_{cn,7} &= b_{cn,6}\\
a_{cn,9} &= 0 & b_{cn,9} &= b_{cn,6}
\end{aligned}
\tag{A.2b}
$$

A.3 Cylindrical array with outer iron

A.3.1 Magnet coefficients

$$
\begin{aligned}
a_{mn,1} &= a_{mn,6}+\hat{M}_{rni}\left(\mathcal{L}_\mathrm{K}\big(nkr_{mi,i}\big)-\mathcal{L}_\mathrm{K}\big(nkr_{mi,o}\big)\right)+\hat{M}_{zni}\left(nkr_{mi,i}\,\mathrm{K}_1\big(nkr_{mi,i}\big)-nkr_{mi,o}\,\mathrm{K}_1\big(nkr_{mi,o}\big)\right)\\
b_{mn,1} &= 0\\
a_{mn,3} &= a_{mn,6}-\hat{M}_{rni}\,\mathcal{L}_\mathrm{K}\big(nkr_{mi,o}\big)-\hat{M}_{zni}nkr_{mi,o}\,\mathrm{K}_1\big(nkr_{mi,o}\big)\\
b_{mn,3} &= -\hat{M}_{rni}\,\mathcal{L}_\mathrm{I}\big(nkr_{mi,i}\big)+\hat{M}_{zni}nkr_{mi,i}\,\mathrm{I}_1\big(nkr_{mi,i}\big)\\
a_{mn,4} &= a_{mn,6}\\
b_{mn,4} &= \hat{M}_{rni}\left(\mathcal{L}_\mathrm{I}\big(nkr_{mi,o}\big)-\mathcal{L}_\mathrm{I}\big(nkr_{mi,i}\big)\right)-\hat{M}_{zni}\left(nkr_{mi,o}\,\mathrm{I}_1\big(nkr_{mi,o}\big)-nkr_{mi,i}\,\mathrm{I}_1\big(nkr_{mi,i}\big)\right)\\
a_{mn,5} &= a_{mn,6}\\
b_{mn,5} &= b_{mn,4}
\end{aligned}
$$

$$
\begin{aligned}
a_{mn,6} &= a_{mn,7} + \hat{M}_{rno}\,\mathcal{L}_{\mathrm{K}}\big(nkr_{mo,i}\big) + \hat{M}_{zno} nkr_{mo,i}\,\mathrm{K}_1\big(nkr_{mo,i}\big) \\
b_{mn,6} &= b_{mn,4} \\
a_{mn,7} &= \frac{nkr_{mo,o}}{\mu}\left[a_{mn,8}\left(\mu\,\mathrm{I}_1\big(nkr_{mo,o}\big)\,\mathrm{K}_0\big(nkr_{mo,o}\big) + \mathrm{I}_0\big(nkr_{mo,o}\big)\,\mathrm{K}_1\big(nkr_{mo,o}\big)\right) + b_{mn,8}\,(\mu-1)\,\mathrm{K}_1\big(nkr_{mo,o}\big)\,\mathrm{K}_0\big(nkr_{mo,o}\big)\right] + \\
&\quad - \hat{M}_{rno}\,\mathcal{L}_{\mathrm{K}}\big(nkr_{mo,o}\big) - \hat{M}_{zno} nkr_{mo,o}\,\mathrm{K}_1\big(nkr_{mo,o}\big) \\
b_{mn,7} &= b_{mn,4} - \hat{M}_{rno}\,\mathcal{L}_{\mathrm{I}}\big(nkr_{mo,i}\big) + \hat{M}_{zno} nkr_{mo,i}\,\mathrm{I}_1\big(nkr_{mo,i}\big) \\
a_{mn,8} &= -b_{mn,8}\left[\frac{(\mu-1)\,\mathrm{K}_0\big(nkr_{fo,o}\big)\,\mathrm{K}_1\big(nkr_{fo,o}\big)}{\mu\,\mathrm{I}_1\big(nkr_{fo,o}\big)\,\mathrm{K}_0\big(nkr_{fo,o}\big) + \mathrm{I}_0\big(nkr_{fo,o}\big)\,\mathrm{K}_1\big(nkr_{fo,o}\big)}\right] \\
b_{mn,8} &= \frac{\mu}{nkr_{mo,o}}\left[\frac{b_{mn,4} + \hat{M}_{rno}\left(\mathcal{L}_{\mathrm{I}}\big(nkr_{mo,o}\big) - \mathcal{L}_{\mathrm{I}}\big(nkr_{mo,i}\big)\right) - \hat{M}_{zno}\left(nkr_{mo,o}\,\mathrm{I}_1\big(nkr_{mo,o}\big) - nkr_{mo,i}\,\mathrm{I}_1\big(nkr_{mo,i}\big)\right)}{\mathrm{I}_1\big(nkr_{mo,o}\big)\,\mathrm{K}_0\big(nkr_{mo,o}\big) + \mu\,\mathrm{I}_0\big(nkr_{mo,o}\big)\,\mathrm{K}_1\big(nkr_{mo,o}\big) - \frac{(\mu-1)^2\,\mathrm{I}_1\big(nkr_{mo,o}\big)\,\mathrm{I}_0\big(nkr_{mo,o}\big)\,\mathrm{K}_1\big(nkr_{fo,o}\big)\,\mathrm{K}_0\big(nkr_{fo,o}\big)}{\mu\,\mathrm{I}_1\big(nkr_{fo,o}\big)\,\mathrm{K}_0\big(nkr_{fo,o}\big) + \mathrm{I}_0\big(nkr_{fo,o}\big)\,\mathrm{K}_1\big(nkr_{fo,o}\big)}}\right] \\
a_{mn,9} &= 0 \\
b_{mn,9} &= \frac{nkr_{fo,o}}{\mu}\left[a_{mn,8}\,(\mu-1)\,\mathrm{I}_0\big(nkr_{fo,o}\big)\,\mathrm{I}_1\big(nkr_{fo,o}\big) + b_{mn,8}\left(\mathrm{I}_1\big(nkr_{fo,o}\big)\,\mathrm{K}_0\big(nkr_{fo,o}\big) + \mu\,\mathrm{I}_0\big(nkr_{fo,o}\big)\,\mathrm{K}_1\big(nkr_{fo,o}\big)\right)\right]
\end{aligned}
\tag{A.3a}
$$

A.3.2 Coil Coefficients

$$
\begin{aligned}
a_{cn,1} &= a_{cn,7} + \mathcal{L}_{\mathrm{K}}\big(nkr_{c,i}\big) - \mathcal{L}_{\mathrm{K}}\big(nkr_{c,o}\big) & \qquad b_{cn,1} &= 0 \\
a_{cn,3} &= a_{cn,1} & b_{cn,3} &= 0 \\
a_{cn,4} &= a_{cn,1} & b_{cn,4} &= 0 \\
a_{cn,5} &= a_{cn,7} - \mathcal{L}_{\mathrm{K}}\big(nkr_{c,o}\big) & b_{cn,5} &= -\,\mathcal{L}_{\mathrm{I}}\big(nkr_{c,i}\big) \\
a_{cn,6} &= a_{cn,7} & b_{cn,6} &= \mathcal{L}_{\mathrm{I}}\big(nkr_{c,o}\big) - \mathcal{L}_{\mathrm{I}}\big(nkr_{c,i}\big)
\end{aligned}
$$

$$
\begin{aligned}
a_{cn,7} &= \frac{nkr_{mo,o}}{\mu}\left[a_{cn,8}\left(\mu\,\mathrm{I}_1\big(nkr_{mo,o}\big)\,\mathrm{K}_0\big(nkr_{mo,o}\big)+\mathrm{I}_0\big(nkr_{mo,o}\big)\,\mathrm{K}_1\big(nkr_{mo,o}\big)\right)+b_{cn,8}\,(\mu-1)\,\mathrm{K}_1\big(nkr_{mo,o}\big)\,\mathrm{K}_0\big(nkr_{mo,o}\big)\right]\\
b_{cn,7} &= b_{cn,6}\\
a_{cn,8} &= -b_{cn,8}\left[\frac{(\mu-1)\,\mathrm{K}_1\big(nkr_{fo,o}\big)\,\mathrm{K}_0\big(nkr_{fo,o}\big)}{\mu\,\mathrm{I}_1\big(nkr_{fo,o}\big)\,\mathrm{K}_0\big(nkr_{fo,o}\big)+\mathrm{I}_0\big(nkr_{fo,o}\big)\,\mathrm{K}_1\big(nkr_{fo,o}\big)}\right]\\
b_{cn,8} &= \frac{\mu}{nkr_{mo,o}}\left[\frac{b_{cn,7}}{\mathrm{I}_1\big(nkr_{mo,o}\big)\,\mathrm{K}_0\big(nkr_{mo,o}\big)+\mu\,\mathrm{I}_0\big(nkr_{mo,o}\big)\,\mathrm{K}_1\big(nkr_{mo,o}\big)-\frac{(\mu-1)^2\,\mathrm{I}_1\big(nkr_{mo,o}\big)\,\mathrm{I}_0\big(nkr_{mo,o}\big)\,\mathrm{K}_1\big(nkr_{fo,o}\big)\,\mathrm{K}_0\big(nkr_{fo,o}\big)}{\mu\,\mathrm{I}_1\big(nkr_{fo,o}\big)\,\mathrm{K}_0\big(nkr_{fo,o}\big)+\mathrm{I}_0\big(nkr_{fo,o}\big)\,\mathrm{K}_1\big(nkr_{fo,o}\big)}}\right]\\
a_{cn,9} &= 0\\
b_{cn,9} &= \frac{nkr_{fo,o}}{\mu}\left[a_{cn,8}\,(\mu-1)\,\mathrm{I}_0\big(nkr_{fo,o}\big)\,\mathrm{I}_1\big(nkr_{fo,o}\big)+b_{cn,8}\left(\mathrm{I}_1\big(nkr_{fo,o}\big)\,\mathrm{K}_0\big(nkr_{fo,o}\big)+\mu\,\mathrm{I}_0\big(nkr_{fo,o}\big)\,\mathrm{K}_1\big(nkr_{fo,o}\big)\right)\right]
\end{aligned}
\tag{A.3b}
$$

A.4 Cylindrical array with infinitely-permeable inner and outer iron

A.4.1 Magnet coefficients

$$
\begin{aligned}
a_{mn,3} &= a_{mn,6}-\hat{M}_{rni}\,\mathcal{L}_{\mathrm{K}}\big(nkr_{mi,o}\big)-\hat{M}_{zni}nkr_{mi,o}\,\mathrm{K}_1\big(nkr_{mi,o}\big)\\
b_{mn,3} &= b_{mn,6}-\hat{M}_{rni}\,\mathcal{L}_{\mathrm{I}}\big(nkr_{mi,o}\big)+\hat{M}_{zni}nkr_{mi,o}\,\mathrm{I}_1\big(nkr_{mi,o}\big)\\
a_{mn,4} &= a_{mn,6}\\
b_{mn,4} &= b_{mn,6}\\
a_{mn,5} &= a_{mn,6}\\
b_{mn,5} &= b_{mn,6}\\
a_{mn,6} &= a_{mn,7}+\hat{M}_{rno}\,\mathcal{L}_{\mathrm{K}}\big(nkr_{mo,i}\big)+\hat{M}_{zno}nkr_{mo,i}\,\mathrm{K}_1\big(nkr_{mo,i}\big)\\
b_{mn,6} &= b_{mn,7}+\hat{M}_{rno}\,\mathcal{L}_{\mathrm{I}}\big(nkr_{mo,i}\big)-\hat{M}_{zno}nkr_{mo,i}\,\mathrm{I}_1\big(nkr_{mo,i}\big)
\end{aligned}
$$

$$
\begin{aligned}
a_{mn,7} &= \frac{b_{mn,7} - \hat{M}_{rno}\,\Lambda_0\big(nkr_{mo,o}\big) - \hat{M}_{zno}}{\mathrm{I}_0\big(nkr_{mo,o}\big)} \\
b_{mn,7} = \quad & \hat{M}_{rno}\frac{\mathcal{L}_\mathrm{K}\big(nkr_{mo,i}\big)\,\mathrm{I}_0\big(nkr_{mi,i}\big)\,\mathrm{I}_0\big(nkr_{mo,o}\big) - \mathcal{L}_\mathrm{I}\big(nkr_{mo,i}\big)\,\mathrm{I}_0\big(nkr_{mo,o}\big)\,\mathrm{K}_0\big(nkr_{mi,i}\big) - \Lambda_0\big(nkr_{mo,o}\big)\,\mathrm{I}_0\big(nkr_{mi,i}\big)}{\mathrm{I}_0\big(nkr_{mo,o}\big)\,\mathrm{K}_0\big(nkr_{mi,i}\big) - \mathrm{I}_0\big(nkr_{mi,i}\big)\,\mathrm{K}_0\big(nkr_{mo,o}\big)} + \\
& + \hat{M}_{rni}\frac{-\mathcal{L}_\mathrm{K}\big(nkr_{mi,o}\big)\,\mathrm{I}_0\big(nkr_{mi,i}\big)\,\mathrm{I}_0\big(nkr_{mo,o}\big) + \mathcal{L}_\mathrm{I}\big(nkr_{mi,o}\big)\,\mathrm{I}_0\big(nkr_{mo,o}\big)\,\mathrm{K}_0\big(nkr_{mi,i}\big) + \Lambda_0\big(nkr_{mi,i}\big)\,\mathrm{I}_0\big(nkr_{mi,i}\big)}{\mathrm{I}_0\big(nkr_{mo,o}\big)\,\mathrm{K}_0\big(nkr_{mi,i}\big) - \mathrm{I}_0\big(nkr_{mi,i}\big)\,\mathrm{K}_0\big(nkr_{mo,o}\big)} + \\
& + \hat{M}_{zno}\frac{nkr_{mo,i}\,\mathrm{K}_1\big(nkr_{mo,i}\big)\,\mathrm{I}_0\big(nkr_{mi,i}\big)\,\mathrm{I}_0\big(nkr_{mo,o}\big) + nkr_{mo,i}\,\mathrm{I}_1\big(nkr_{mo,i}\big)\,\mathrm{I}_0\big(nkr_{mo,o}\big)\,\mathrm{K}_0\big(nkr_{mi,i}\big) + \mathrm{I}_0\big(nkr_{mi,i}\big)}{\mathrm{I}_0\big(nkr_{mo,o}\big)\,\mathrm{K}_0\big(nkr_{mi,i}\big) - \mathrm{I}_0\big(nkr_{mi,i}\big)\,\mathrm{K}_0\big(nkr_{mo,o}\big)} + \\
& + \hat{M}_{zni}\frac{-nkr_{mi,o}\,\mathrm{K}_1\big(nkr_{mi,o}\big)\,\mathrm{I}_0\big(nkr_{mi,i}\big)\,\mathrm{I}_0\big(nkr_{mo,o}\big) - nkr_{mi,o}\,\mathrm{I}_1\big(nkr_{mi,o}\big)\,\mathrm{I}_0\big(nkr_{mo,o}\big)\,\mathrm{K}_0\big(nkr_{mi,i}\big) + \mathrm{I}_0\big(nkr_{mo,o}\big)}{\mathrm{I}_0\big(nkr_{mo,o}\big)\,\mathrm{K}_0\big(nkr_{mi,i}\big) - \mathrm{I}_0\big(nkr_{mi,i}\big)\,\mathrm{K}_0\big(nkr_{mo,o}\big)}
\end{aligned}
\tag{A.4a}
$$

A.4.2 Coil coefficients

$$
\begin{aligned}
a_{cn,3} &= a_{cn,4} & b_{cn,3} &= a_{cn,4}\frac{\mathrm{I}_0\big(nkr_{mi,i}\big)}{\mathrm{K}_0\big(nkr_{mi,i}\big)} \\
a_{cn,4} &= a_{cn,7} + \mathcal{L}_\mathrm{K}\big(nkr_{c,i}\big) - \mathcal{L}_\mathrm{K}\big(nkr_{c,o}\big) & b_{cn,4} &= b_{cn,3} \\
a_{cn,5} &= a_{cn,7} - \mathcal{L}_\mathrm{K}\big(nkr_{c,o}\big) & b_{cn,5} &= b_{cn,3} - \mathcal{L}_\mathrm{I}\big(nkr_{c,i}\big) \\
a_{cn,6} &= a_{cn,7} & b_{cn,6} &= b_{cn,3} + \mathcal{L}_\mathrm{I}\big(nkr_{c,o}\big) - \mathcal{L}_\mathrm{I}\big(nkr_{c,i}\big) \\
a_{cn,7} &= \frac{\mathrm{I}_0\big(nkr_{mi,i}\big)\,\mathrm{K}_0\big(nkr_{mo,o}\big)\,\Big(\mathcal{L}_\mathrm{K}\big(nkr_{c,i}\big) - \mathcal{L}_\mathrm{K}\big(nkr_{c,o}\big)\Big)}{\mathrm{I}_0\big(nkr_{mo,o}\big)\,\mathrm{K}_0\big(nkr_{mi,i}\big) - \mathrm{I}_0\big(nkr_{mi,i}\big)\,\mathrm{K}_0\big(nkr_{mo,o}\big)} & b_{cn,7} &= b_{cn,6}
\end{aligned}
\tag{A.4b}
$$